Galaxy Populations in Distant, X-ray Selected Clusters of Galaxies

by

Ariane Trudeau
B.Sc., Université de Montréal, 2016
M.Sc., Université de Montréal, 2018

A Dissertation Submitted in Partial Fulfillment of the
Requirements for the Degree of

DOCTOR OF PHILOSOPHY

in the Department of Physics and Astronomy

Galaxy Populations in Distant, X-ray Selected Clusters of Galaxies

by

Ariane Trudeau
B.Sc., Université de Montréal, 2016
M.Sc., Université de Montréal, 2018

Supervisory Committee

Dr. Jon Willis, Supervisor
(Department of Physics and Astronomy)

Dr. J.J. Kavelaars, Departmental Member
(Department of Physics and Astronomy)

Dr. Julia Baum, Outside Member
(Department of Biology)

ABSTRACT

Galaxy clusters are the largest gravitationally bound structures in the Universe. Their masses are dominated by dark matter ($\sim$85% of the mass) with stars representing 1-4% of their masses. A hot, X-ray emitting gas called the intracluster medium makes most of their baryonic mass.

The presence of this gas and of numerous neighbouring galaxies prematurely stop the star formation in clusters. In other terms, more galaxies in clusters are passive than in the general population of galaxies. This effect is mass and position-dependant: high-mass galaxies are more likely to be passive than less massive ones; galaxies inhabiting the cluster core are also less likely to form stars than those in the outskirts. The fraction of passive galaxies is greater in local clusters than in high-redshift ones, because they had more time to evolve.

Much is unknown about the cessation of star formation, called quenching, in clusters. Thus, although many examples of infalling galaxies being stripped of their gas have been reported for low-mass galaxies, it is unclear if the most massive members became quenched before or after they become cluster members. The relationship between quenching and the cluster mass is also poorly understood.

Despite the variety of methods devised to find clusters of galaxies, most of what we know about quenching in $z \gtrsim 1$ clusters was discovered with optically/infrared-selected cluster samples (clusters found as overdensities of galaxies), or samples of mixed origin. Yet, there is tentative evidence that optically/infrared-selected samples are biased toward having more passive galaxies than those that were X-ray selected. In the present dissertation, quenching is explored in X-ray selected cluster samples. A sample of high-redshift, low-mass galaxy clusters is built by finding galaxy overdensities coincident with sources of extended X-ray emission. A photometry-based analysis reveals that the fraction of quenched galaxies in these clusters is very variable. Moreover, the brightest cluster galaxies are also diverse.

Yet, for all the information that photometry can provide, this sample candidate clusters need to be confirmed with spectroscopy. Spectroscopic observations obtained for four candidate clusters are reduced and analysed. The results show that three of them are clusters, the fourth candidate being a superposition of structures. Member spectra are examined to infer their star formation history, and the results shows the existence of an intermediary population of galaxies, where an old stellar population coexists with weak star formation.

Finally, the galaxies of a $z = 1.98$ X-ray selected cluster, XLSSC 122 are investigated in

detail. Photometric data in 12 bands are organized to perform spectral energy distribution fittings, a technique that allows a simplified reconstitution of the history of the star formation. Results show that the members were formed at diverse epochs, the oldest being about 2.5 Gyrs old. Simulations drawn from the Multi Dark Planck 2 are used to infer the mass-scale of the cluster when the oldest galaxies were formed, something that has never been done before. The oldest galaxies were probably formed when XLSSC 122 had accreted $<10\%$ of its $z = 1.98$ mass, i.e. the mass-scale of a galaxy group.

Table of Contents

List of Tables

List of Figures

ACKNOWLEDGEMENTS

I would like to thank:

Jon Willis for your support and encouragement through my bouts of self-doubt when the road was bumpy. Thank you for being there whenever I had questions about this or that technique or for suffering through many pages of typo spotting.

Jaclyn and Katie for their enthusiasm whenever I wanted to hitch a car ride to explore Vancouver Island. I wish we had more opportunities to do day trips.

Mallory for being available whenever I wanted to chat and for her advice on student life. Thanks also for offering to read the conclusion of this dissertation.

Isabel, Ondrea and Salvatore for your sample applications and advice during the difficult period of postdoc applications.

Stephenson Yang for solving all my computer issues and replying very quickly to my emails, even when they arrive at 9:00 pm on a Friday evening.

My parents for being a phone call away, whenever I needed someone to talk to during the pandemic.

The sea lions of Cowichan Bay for lifting my mood when I went to watch you in 2020 and 2021. Your antics are one of the best cures against pandemic languor.

DEDICATION

À mes amis et à ma famille,
Toujours présents malgré la distance

Chapter 1

Introduction

The visible Universe is dominated by galaxies. A century of galaxy studies (e.g. Hubble 1922) has revealed that galaxies not only host stars but also gas, dust (e.g. Hubble 1925), supermassive black holes (e.g. Kormendy & Ho 2013) and dark matter (e.g. Rubin et al. 1980). Although the latter represents most of the matter in the Universe, its nature is very poorly understood. Gravity drives galaxies to congregate in larger structures - groups and clusters - linked by filaments (Plionis et al. 2008).

Clusters of galaxies are the largest gravitationally bound structures. Their total masses range from 10^{13} $M_{\odot}$[1] to over 10^{15} $M_{\odot}$ (e.g. Sarazin 1986; McDonald et al. 2012; Menanteau et al. 2012), although the determination of a lower mass limit of what constitutes a cluster is generally arbitrary (e.g. Willis et al. 2018).

Clusters are dark matter-dominated objects (about 85 to 90% of the total mass, e.g. Gonzalez et al. 2013; Sanderson et al. 2013; Chiu et al. 2016). Most of the baryonic matter (i.e. normal matter as opposed to dark matter) is in the form of a hot, X-ray emitting gas called the intracluster medium (ICM). The stars populating galaxies in clusters represent 1 to 4% of their total masses (Gonzalez et al. 2013; Sanderson et al. 2013; Chiu et al. 2016).

For a long time, galaxies were considered to be the only component of galaxy clusters. Indeed, Abell (1958) mounted the first cluster catalogue by finding the richest 'clustering of galaxies' in the sky. Although such a method generates a sample neither very pure nor very complete, the Abell catalogue is still in use today, mainly because it identified most of the obvious local clusters. Furthermore, several cluster finding surveys such as SpARCS (Wilson et al. 2006, 2009) or the future EUCLID (e.g. Euclid Collaboration et al. 2019) use overdensities of galaxies as cluster probes, although with somewhat more refined selection

[1] $M_{\odot}$: Solar mass, a commonly used mass unit in astronomy

methods (see below).

It was not until the development of rockets equipped with X-ray detectors (e.g. Giacconi 2003) that galaxy clusters appeared to be more than mere gatherings of galaxies. Byram et al. (1966); Felten et al. (1966); Bradt et al. (1967) detected X-ray emission associated with the Coma and Virgo cluster. With the launch of UHURU, it soon became clear that X-ray emitting gas (Forman et al. 1972; Gursky et al. 1972) is a major component of galaxy clusters. Several successors of UHURU including Einstein (Gioia et al. 1990), ROSAT (Böhringer et al. 2001) and recently XMM Newton (Pierre et al. 2004, 2016) have been used to find galaxy clusters via their X-ray emission. It is worth mentioning that the ICM can be detected indirectly, via its effect on the Cosmic Microwave Background: a fraction of the Cosmic Microwave Background photon gain energy by their interaction with the intracluster medium. This increase in energy result in a shift toward higher frequencies, a phenomenon that is now known as the Sunyaez-Zel'dovich effect (Zel'dovich & Sunyaev 1969; Sunyaev & Zel'dovich 1970, 1972, 1980a,b).

In parallel to the development of X-ray astronomy, Rubin et al. (1980) found from the analysis of galaxy rotational curves that a significant mass must be located in some kind of 'halo' extending beyond the optical extent of the galaxies. This was the first evidence of the existence of dark matter, which dominates the masses of the vast majority of galaxies, and, at larger scale, groups and clusters (e.g. Plionis et al. 2008; Gonzalez et al. 2013; Sanderson et al. 2013; Chiu et al. 2016). A few years later, the idea of measuring the 'total' mass of an astronomical object by its gravitational lensing effect on background galaxy images was developed, first for galaxies (Tyson et al. 1984) and then for clusters (Tyson et al. 1990). Each of these probes of the nature of galaxy clusters will be discussed in more details in Section 1.1.

Galaxy clusters evolve from protoclusters, which are gravitationally bound overdensities of dark matter haloes hosting large amounts of cold gas and intense star formation activity (e.g. Muldrew et al. 2015, 2018; Lovell et al. 2018). A key property that differentiates a cluster from a protocluster is the achievement of a gravitational equilibrium as defined by the virial theorem. This equilibrium is accompanied by the appearance of a dense core of galaxies and hot intracluster medium emission (e.g. Papovich et al. 2010; Gobat et al. 2011; Andreon et al. 2014; Muldrew et al. 2015; Hung et al. 2016; Overzier 2016; Lovell et al. 2018). Once formed, clusters grow by accretion of smaller structures, ranging from isolated galaxies to other clusters (e.g. Roettiger et al. 1997; Barrena et al. 2002; Berrier et al. 2009; McGee et al. 2009; Bilton et al. 2019). This growth by accretion is called hierarchical assembly and was first theorized by Gunn & Gott (1972); Press &

Schechter (1974) and then further developed by White & Rees (1978). A key concept of this theory is self-similarity, which explains that after the perturbation, the cluster will re-virialize and becomes a more massive version of its previous self (Press & Schechter 1974; White & Rees 1978).

Galaxy clusters represent ideal laboratories in which to observe the physics that governs star formation. Of particular interest is the physics that causes star formation to stop, referred to as 'quenching'. Galaxies in all environments may be quenched by internal processes (also called mass processes, Peng et al. 2010), but environmental quenching processes are enhanced in denser environments (Peng et al. 2010). These processes include ram pressure stripping, which affects infalling galaxies (intergalactic gas interacts with the intracluster medium and is thus left behind as the galaxy falls, Poggianti et al. 2016) and harassment which is the effect of multiple galaxy interactions (Farouki & Shapiro 1981; Treu et al. 2003). As they occupy some of the densest galaxy environments, cluster members are on average more quenched than field galaxies.

The idea of studying the galaxy population in clusters is not new: Butcher & Oemler (1978, 1984) compared the evolution of the fraction of blue galaxies (as a proxy for star-forming galaxies) in clusters with redshift, and found it to be increasing with the cluster redshift. Recent studies suggest that environmental quenching processes started to operate very early in galaxy clusters (e.g. Balogh et al. 2016; Nantais et al. 2017; Foltz et al. 2018) but that their effect increased around a redshift of 1 (about 7.85 Gyrs ago, e.g. Nantais et al. 2017; Lemaux et al. 2019), and were more effective at transforming low-mass galaxies (e.g. Lemaux et al. 2019). Two of the important questions addressed in this dissertation are: What physical processes are required to reconcile the quenched star formation in galaxy clusters with active star formation in the proto-clusters that preceded them? What physics occurred in galaxy clusters approximately 8 Gyrs ago, giving rise to widespread quenching?

The Brightest Cluster Galaxy (BCG), typically the central and most massive galaxy in a cluster, represent a unique galaxy environment. BCGs are massive elliptical galaxies – they are among the most massive galaxies in the universe – and they represent a separate class of galaxies with distinct light profiles and metallicities [2] (e.g. Tremaine & Richstone 1977; Dressler 1978; Schombert 1986, 1987, 1988; Von Der Linden et al. 2007) whose supermassive black holes play a major role in regulating the ICM (McNamara & Nulsen 2007, 2012).

[2] In astronomy, metallicity refers to the abundance of elements heavier than hydrogen and helium. Such elements are generated in stars. Thus their presence indicates that there has been more than one generation of stars.

BCGs were initially believed to have formed via multiple mergers of previously quenched galaxies, with active star formation having taken place at early cosmic times (De Lucia & Blaizot 2007). While this idea remains valid for their late-time evolution, recent studies have found evidence of significant star formation inside BCGs at $z \gtrsim 1$ (Webb et al. 2015b; McDonald et al. 2016; Bonaventura et al. 2017; Cooke et al. 2019). The physical process responsible for this star formation remains unknown and another aim of this dissertation is to understand the life history of BCGs by studying their properties in galaxy clusters observed at early times.

1.1 Finding galaxy clusters

The first systematic studies of galaxy clusters (e.g. Abell 1958) relied on visual identification of galaxy clustering (hence the name cluster of galaxies). However, such a method has significant caveats, both in terms of purity and completeness. Several rich fields might be mere projection effects and not clusters (i.e. the sample might be impure, Abell 1958). Additionally, the galaxies in more distant clusters appear less bright (because they are farther away) and won't be as conspicuous as more nearby ones (i.e. the sample is not complete).

The cluster identification methods presented here each target a particular physical component of clusters: the red sequence method is sensitive to a subset of the galaxy population which has ceased to form stars, while the shear lensing method is sensitive to the cluster mass, largely dominated by dark matter. Two of the methods presented below rely on a detection of the intracluster medium, either indirectly via the Sunyaev-Zel'dovich effect, or directly with X-ray observations. However, both methods generate different cluster samples, as one is sensitive to the ICM density along the line of sight and the second to the square of the density. Figure 1.1 illustrates this difference for the Coma cluster – a massive (1.5×10^{15} $M_{\odot}$, Łokas & Mamon 2003), fairly nearby ($z = 0.023$) cluster of galaxies (see e.g Lutovinov et al. 2008; Planck Collaboration et al. 2013).

Note also that there is a broad division among clusters between those that exhibit peaked X-ray profiles characterized by bright cores (Lea et al. 1973) and those that don't. The former are called cool core clusters and the latter, non-cool core clusters (e.g. Hudson et al. 2010). Each method has its own advantages, bias and blind spots (e.g. Rossetti et al. 2017; Willis et al. 2018). Therefore, we must often compare several detection methods in order to achieve an unbiased view of galaxy cluster properties.

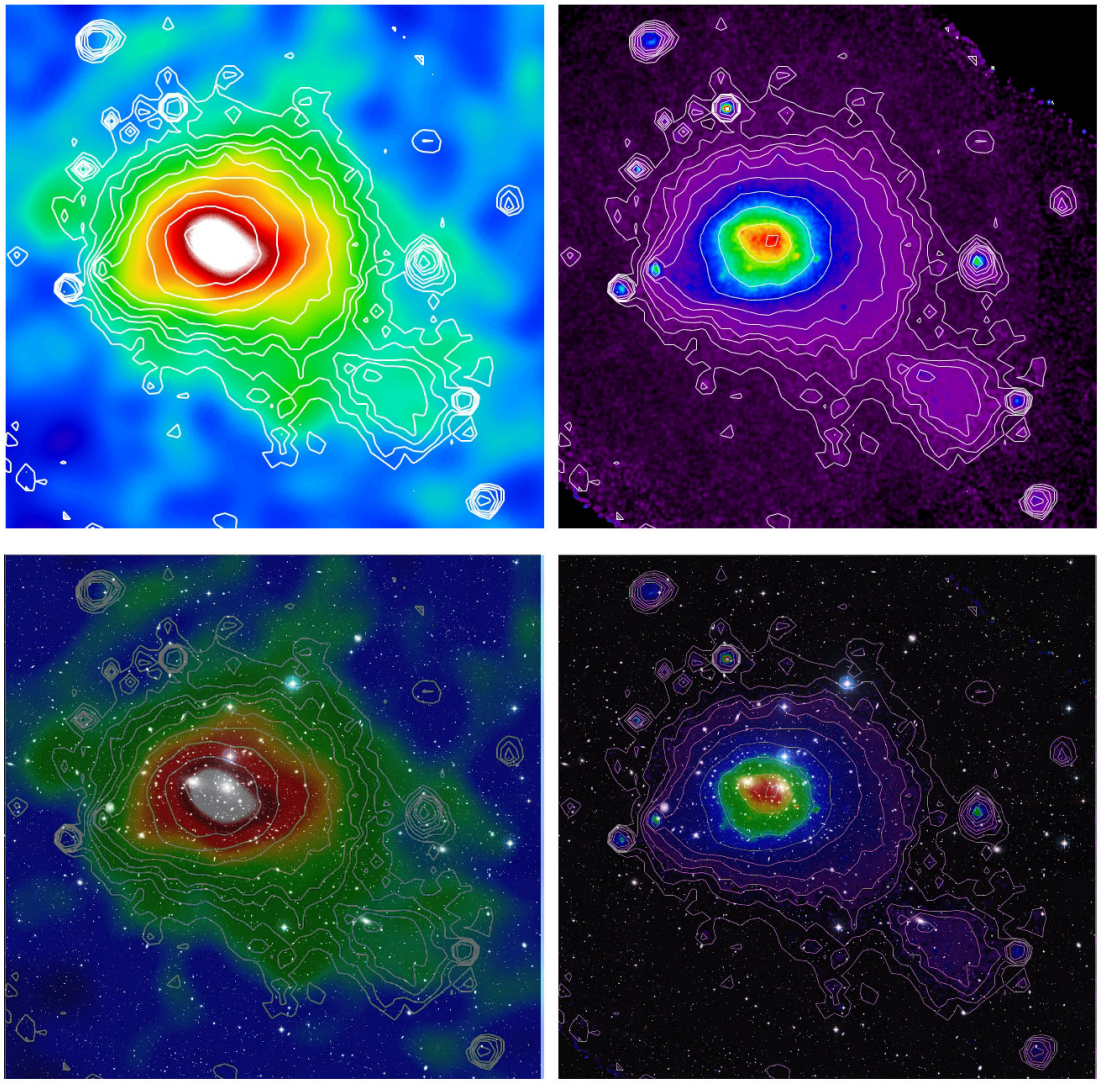

Figure 1.1: This figure from the Planck collaboration website (`http://planck.cf.ac.uk/results/coma-cluster`), displays two different views of the Coma cluster intracluster medium. Top Left: Suyaev-Zel'dovich effect map of the intracluster medium, from the Planck observatory, with X-ray contours overlaid. Top right: X-ray image from ROSAT observatory. Note how the two maps show different views of the outer, less dense regions of the intracluster medium: the Sunyaez-Zel'dovich map shows a greater extent of the ICM, but regions with different gas densities are more contrasted in the X-ray emssion map.

1.1.1 The red sequence method

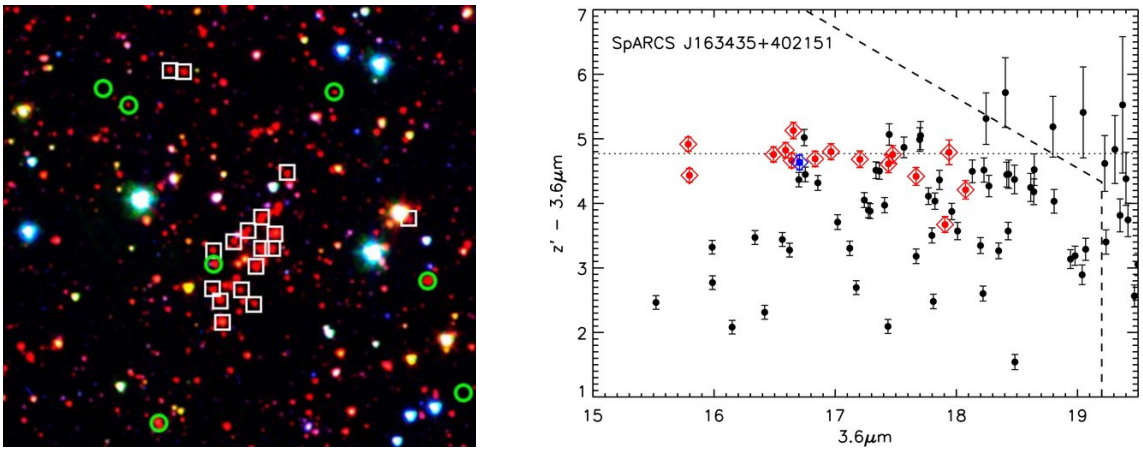

Figure 1.2: Figure adapted from (Muzzin et al. 2009). Left: Three filters image (R, z' and 3.6 μm) of SpARCS J163435+402151, a z=1.1798 cluster found by the red sequence method. Squares indicate the spectroscopically confirmed members and circles highlight the foreground and background galaxies. Right: Colour-magnitude diagram for the centre of SpARCS J163435+402151. Confirmed members are in red and foreground/background galaxies in blue. The other galaxies with a projected distance to the centre of the cluster smaller than R_{200} are represented by black dots. The dotted line indicates the best fit to the colours of confirmed members. Note that in this case, the red sequence corresponds to this dotted line.

In astronomy, 'colour' refers to the difference of magnitude when an object is observed in two photometric filters. When a galaxy is actively forming stars, its light is dominated by the emission from hot stars (types O and B), whose blackbody emission results in blue colours. These blue stars are the first to evolve off the main sequence, which means that when star formation ceases, the light of a galaxies becomes dominated by long-lived, cool stars (types G, K and M) whose blackbody emission results in red colours. Additionally, a ubiquitous spectral feature of stellar populations characteristic of passive galaxies is a significant drop in intensity at wavelengths below 4000 Å (in the galaxy frame), named the 4000 Å break (e.g. Gladders & Yee 2000). Thus, in the colour-magnitude diagram of a galaxy cluster, passive galaxies tend to cluster along a line, called the red-sequence (see the dotted line in the right panel of Figure 1.2), while the star-forming population is found in a region called the blue cloud (the region below the dotted line in Figure 1.2). The exact colour of the red sequence depends on the cluster redshift (see the first figure of Gladders & Yee 2005).

The fraction of passive galaxies tends to be higher in a galaxy cluster than in the field

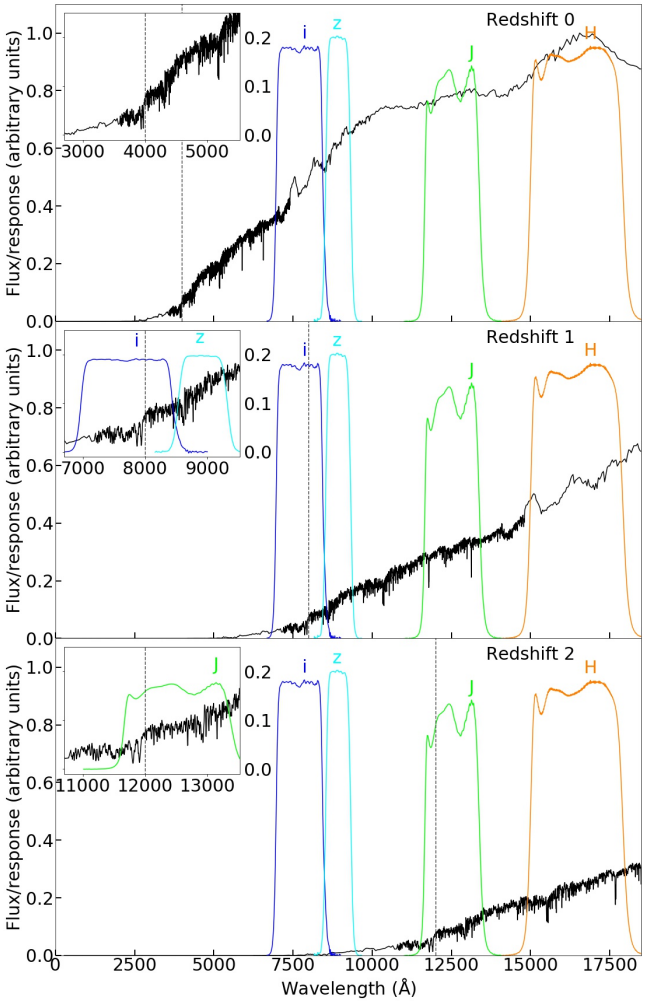

Figure 1.3: The effect of redshift on a typical quenched galaxy spectrum. The spectrum presented here is a fsps-generated synthetic model (Conroy et al. 2009; Conroy & Gunn 2010; Foreman-Macke et al. 2014), based on the best fit characterizing the red sequence of the galaxy clusters presented in Trudeau et al. (2020). A dashed grey line indicates the location of the 4000 Å break in each panel. Insets show enlargements of the main panels centred on the 4000 Å break. Top: Unredshifted spectrum, with the HSC-i and z filters, as well as VISTA J, H and K_s filters. Middle: Spectrum at a redshift of 1, with the same filters overplotted. Bottom: Spectrum at a redshift of 2, with the same filters.

(i.e. the general population of galaxies, Balogh et al. 2004; Wetzel et al. 2012, 2013; Nantais et al. 2017; Pintos-Castro et al. 2019, see also Section 1.3.1). Thus, the red-sequence method consists of observing a field in two filters suitably chosen to sample the 4000 Å break over a wide redshift interval (Gladders & Yee 2000, 2005). If there is a greater than usual concentration of red, passive galaxies toward a particular sky location, the field likely hosts a galaxy cluster. Figure 1.3 shows a selection of filters and three evolved spectra: one at a redshift of 0, one at a redshift of 1 and one at 2[3]. Note how a redshifted spectrum stretches, rather than simply shifting. Thus, if one is interested in finding galaxy clusters with the red-sequence method, the i and z filters would represent a sensible choice at $z \sim 1$ and the z and J filters at $1 \lesssim z \lesssim 2$.

The red-sequence method constitutes an interesting choice to select galaxies clusters with a wide variety of X-ray properties (Willis et al. 2018). However, there is tentative evidence that this method is biased toward a greater amount of passive galaxies in the cluster population (e.g. Donahue et al. 2002; Willis et al. 2018). Additionally, the cluster optical richness (i.e. the number of galaxies above a certain luminosity threshold contained within the cluster; e.g. Webb et al. 2015b) is correlated with its mass (e.g. Angulo et al. 2012; Webb et al. 2015b). Thus, optical methods tend to be sensitive to more massive clusters.

1.1.2 Shear selected clusters

Shear refers to the statistical distortion of background galaxy images created by a foreground space-time deformation. Space-time is sensitive to mass and thus the photon trajectories depend on the mass distribution of the foreground object, in this case a galaxy cluster (e.g. Mo et al. 2010). Near the structure, the shortest path for the photon (referred to as null geodesic) appears no longer as a straight line but instead as a curve following the space-time deformation (e.g. Einstein 1936; Carroll & Ostlie 2007; Mo et al. 2010). Depending on the mass distribution and on the quality of the alignment, background sources could be magnified, form multiple images on the sky, or arc-like images (e.g. Carroll & Ostlie 2007; Mo et al. 2010, see also Figure 1.4). These are all examples of strong lensing.

Shear lensing is a subtler version of gravitational lensing where background galaxy images tend to be distorted along lines of gravitational equipotential, forming 'mini-arcs' (e.g. Tyson et al. 1990; Kaiser et al. 1995; Schneider 1996; Wittman et al. 2001). Thus, by a

[3]Because of the universe expansion, all lengths are stretched, including wavelength. Thus, the redshift (z) is a measurement of how much the observed spectrum is 'stretched' compared to the emitted one. See Section 1.2 for a mathematical description

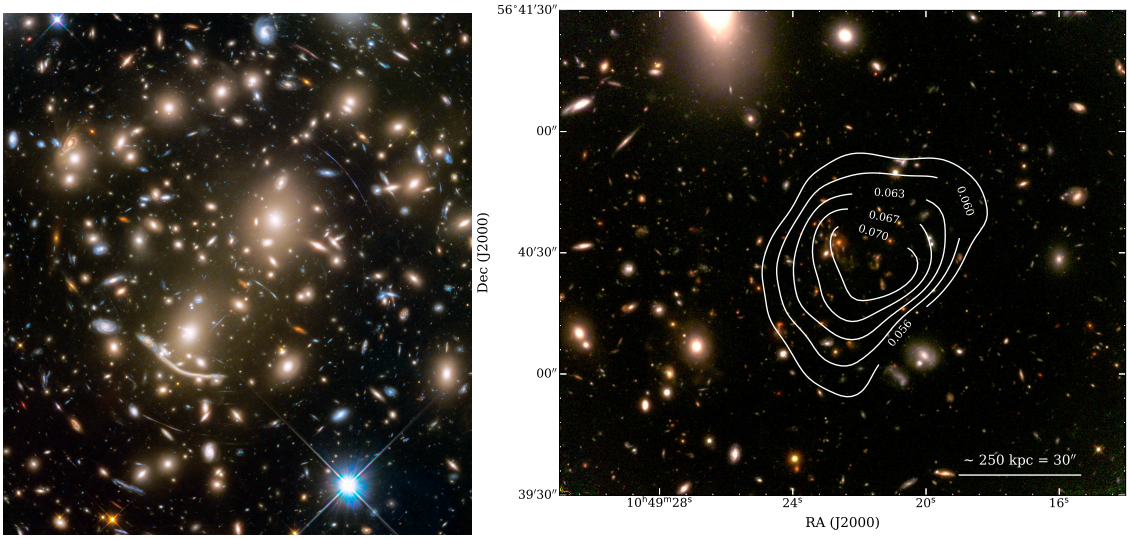

Figure 1.4: Left: Optical/near infrared Hubble image of the core of Abell 370, a nearby galaxy cluster displaying multiple arcs due to strong lensing. From `https://hubblesite.org/image/4024/gallery`. Right: Shear lensing map showing the mass profile of SpARCS104922.6+564032.5 (aka SpARCS1049), a $z = 1.71$ cluster of galaxies. From Finner et al. (2020).

statistical analysis of the shape of the galaxies in a field-of-view, one can determine the presence of a dark matter halo associated with a galaxy cluster (e.g. Kaiser et al. 1995; Miyazaki et al. 2002) and reconstruct its mass profile (e.g. Wittman et al. 2006, see also Figure 1.4).

In addition to providing an accurate evaluation of the cluster mass (e.g. Miyazaki et al. 2002; Gavazzi & Soucail 2007; Tudorica et al. 2017; Finner et al. 2020), this method does not rely upon a measurement of the stellar or ICM component of the cluster (e.g. Wittman et al. 2001, 2003; Miyazaki et al. 2002). However, weak lensing requires sensitive, high spatial resolution images, in order to perform a reliable analysis as well as the presence of a certain amount of background sources (Miyazaki et al. 2002).

1.1.3 The Sunyaev-Zel'dovich effect method

First proposed by the two physicists who gave it their names (Zel'dovich & Sunyaev 1969; Sunyaev & Zel'dovich 1970, 1972, 1980a,b), the Sunyaev-Zel'dovich effect method employs the inverse Compton scattering of cosmic microwave background (CMB) photons to detect indirectly the intracluster medium of a galaxy cluster. The CMB emission is characterised by a near-perfect blackbody with a temperature equal to 2.725 K (Carroll & Ostlie

2007). As the CMB photons pass through the intracluster medium of a galaxy cluster, a tiny fraction (10^{-3} to 10^{-2} according to Carlstrom et al. 2002; Carroll & Ostlie 2007; Mo et al. 2010) gains energy by interacting with the electrons of the intracluster medium and thus shift to a higher frequency. This results in the distortion of the CMB, illustrated in Figure 1.5.

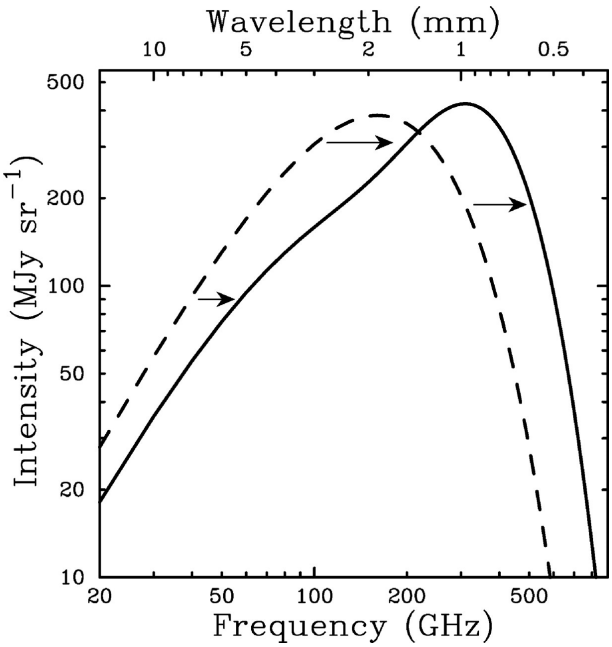

Figure 1.5: This figure from Carlstrom et al. (2002) illustrates, exaggerated by a factor of about a thousand, the distortion of the CMB spectrum due to the presence of a cluster of galaxies in the line-of-sight. The dashed and full lines represent respectively the original and altered spectra.

When viewed in the CMB normal frequency-emitting window, the cluster reveals its presence as an apparent decrement of the CMB emission compared to the nearby sky. The importance of the alteration due to the thermal effect is often expressed in term of temperature (Zel'dovich & Sunyaev 1969; Sunyaev & Zel'dovich 1980a; Carlstrom et al. 2002; Bleem et al. 2015), which depends on the electron density (n_e) and on the electron temperature (T_e) along the line of sight (l), with usually little or no relativistic effect:

$$\begin{aligned} \Delta T &= T_{CMB} f_{sz}(x) \int n_e \frac{k_B T_e}{m_e c^2} \sigma_T dl \\ f_{sz}(x) &= \left(x \frac{e^x + 1}{e^x - 1} - 4 \right) (1 - \delta_{rc}) \\ x &= \frac{h\nu}{k_B T_{CMB}}. \end{aligned} \tag{1.1}$$

In these equations, T_{CMB} is the CMB temperature, 2.725 K, k_B is the Boltzmann constant, m_e the electron mass, c the speed of light and σ_T the Thomson constant. δ_{rc} are the relativistic effects, important at $T_e \gtrsim 8$ keV (Bleem et al. 2015), h the Planck constant and ν the frequency considered. A derivation of this equation can be found in (Zel'dovich & Sunyaev 1969).

Although the angular scale of the affected region diminishes with redshift, the effect itself is insensitive to redshift (Carlstrom et al. 2002; Bleem et al. 2015; Rossetti et al. 2017), which is one of its most interesting properties as a cluster-finding tool. However, Suynaev-Zel'dovich detected samples are mass-limited (Motl et al. 2005) and sensitive to cluster orientation and projection effects (e.g. Angulo et al. 2012).

Furthermore, the effect of a cool core bias (i.e. if clusters with peaked, bright cores in X-ray tend to be overrepresented in a cluster sample) in Sunyaev-Zel'dovich selected samples is unclear: the gas density increase toward the cool core of some clusters might make them easier to detect (Lin et al. 2015) but the frequent presence of bright radio-galaxies at the centre of those clusters might counteract the apparent brightness decrement that is the signature of Sunyaev-Zel'dovich effect in radio (Lin et al. 2015; Rossetti et al. 2017).

1.1.4 The X-ray method

Like the Sunyaev-Zel'dovich effect, the X-ray method consists of detecting of the intra-cluster medium, this time directly, via its X-ray emission. There are two main populations of extragalactic X-ray emitters: point sources (AGN) and extended sources (group and clusters, e.g. Forman et al. 1972; Gursky et al. 1972; Pierre et al. 2016). Hence, the X-ray method consists of searching for extended X-ray sources.

In clusters, X-ray emission arises from the interactions between electron and ions. When a electron encounters an ion, it loses energy radiatively, an effect called thermal bremsstrahlung (Mo et al. 2010). The emissivity of a plasma via thermal bremsstrahlung is

given by (e.g. Sarazin 1986; Mo et al. 2010)[4]:

$$\varepsilon_{ff}(\nu) = \frac{32\pi q_e^6}{3m_e^2c^4}\left(\frac{2\pi Z^2 m_e c^2}{3k_B T_e}\right)^{\frac{1}{2}} Z^2 n_i n_e g(\nu, T_e) e^{-\left(\frac{h\nu}{k_B T_e}\right)}, \tag{1.2}$$

where q_e is the electrical charge of an electron, Z is the charge number, n_i and n_e the density number of ions and electron. The gaunt factor, $g(\nu, T_e)$, encodes quantum mechanical effects (near unity according to Mo et al. 2010). Typical temperatures for the intracluster medium are $10^7 - 10^8$ K (Mo et al. 2010; Eckert et al. 2011), so the bulk of the emission is in the X-ray. The dependence of emissivity on the square of the plasma density is one of the advantages of X-ray, as it makes the source detection less susceptible to projection effects (Pierre et al. 2016). Tentative evidence suggests that X-ray selection of galaxy clusters is better suited to galaxy populations studies compared to optical selection, as X-ray selected clusters do not all have large red-sequences (Donahue et al. 2002; Willis et al. 2018).

However, X-ray selected clusters tend to be more relaxed (i.e. more in gravitational equilibrium) than those selected optically (Willis et al. 2018) or by Sunyaev-Zel'dovich effect (Rossetti et al. 2017). To mitigate this bias, it has been suggested to exclude the core flux when selecting candidate clusters (Pratt et al. 2009; Arnaud et al. 2010; Eckert et al. 2011).

1.1.5 XMM Newton telescope and the XXL survey

UHURU ('freedom' in Swahili, see e.g. Giacconi et al. 1971), launched in December 1970, was the first space-based X-ray telescope (e.g. Giacconi 2003). It was little more than an X-ray detector with a collimator (for the general direction) and an anti-coincidence shield (to avoid spurious detections, e.g. Giacconi 2003). Unlike their ancestors, modern X-ray observatories include mirrors to concentrate the X-rays onto the detector (e.g. Weisskopf 1999; Giacconi 2003; Lumb et al. 2012). Given the targeted wavelength range, any system based on low incidence angles, such as the refractive or reflective system used in optical observatories, would result in the photons passing through the material entirely. X-rays can only be reflected at shallow, grazing-like incidence angles (e.g. Giacconi 2003). Based on an idea originally developed by Hans Wolter in 1958, modern designs consist of several coaxial paraboloidal mirrors, paired with hyperboloidal mirrors (see Figure 1.6).

The X-ray Multi-Mirrors Mission (XMM) Newton is an X-ray observatory developed

[4]See also `http://kestrel.nmt.edu/~lyoung/426/Chap4.pdf` for a partial derivation of this formula.

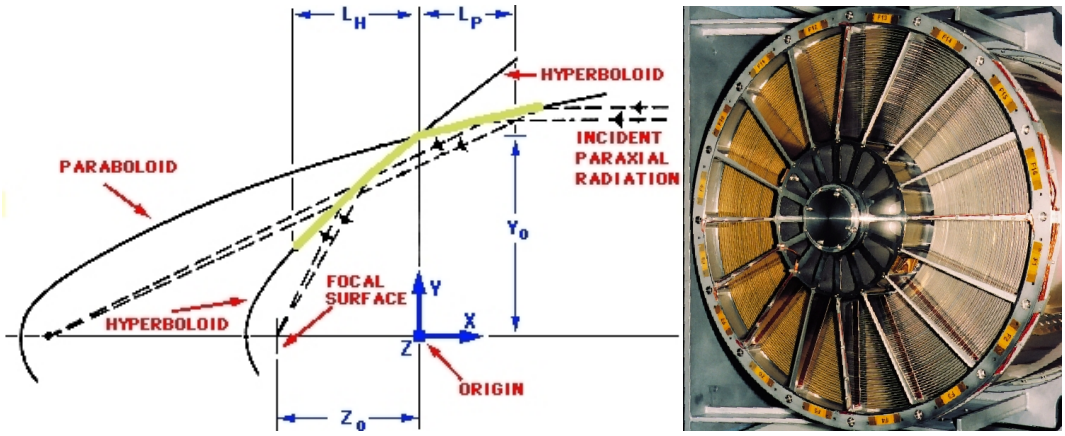

Figure 1.6: Left: Schema of a Wolter I mirror pair, as used in XXM Newton (or Chandra). Incoming X-ray photons are reflected twice, first by a paraboloidal mirror and then by an hyperboloidal mirror. From `https://sci.esa.int/web/xmm-newton/-/31318-x-ray-mirrors?section=optical-design`. Right: a view of one of the three mirror sets used in XMM Newton. Each set contains 58 coaxial and confocal mirrors. Retrieved from `https://www.cosmos.esa.int/web/xmm-newton/technical-details-mirrors`.

by the European Space Agency (ESA) and launched in 1999 (Lumb et al. 2012). It consists of six instruments (including three CCD cameras) organised around three parallel mirror sets, each containing 58 mirrors (e.g. Lumb et al. 2012, see also Figure 1.6). Despite not being designed as a survey facility, the large field-of-view (30 arcminutes – about the size of the full moon) and good sensitivity of XMM Newton make it suitable for X-ray surveys (Pierre et al. 2004). Hence, it has been used for the XMM Large Scale Structure (XMM-LSS) survey and for its successor the X-ray X-tra Large (XXL) survey (Pierre et al. 2004, 2016).

The XXL survey targets two 25 deg^2 sky areas, named XXL-North and XXL-South. Those two areas were selected because of the presence of archival X-ray, optical and infrared observations, low galactic absorption and easy access for eventual follow-up observations with the European Southern Observatory (ESO) facilities (Pierre et al. 2016). Indeed, data from the overlapping Visible and Infrared Survey Telescope for Astronomy (VISTA) Deep Extragalactic Observations (VIDEO, see Jarvis et al. 2013) and from the Hyper Suprime-Camera (HSC) Subaru Strategic Program (HSC-SSP, see Aihara et al. 2018a,b) surveys were used in the first project of this dissertation (see Chapter 2). Each field is observed in series of 10 ks observations. Note that while the bulk of XXL observations are executed with 10 ks exposure, deeper exposures exist for a 4.5 square degree field

called the XMM-SERVS field (Chen et al. 2018) and will be used in this dissertation.

The Xamin pipeline (Pacaud et al. 2006; Faccioli et al. 2018) is employed to process the observations. This software creates an event file (event means detected photon) for each of the three XMM cameras, in each of the three bands (think of a band as the X-ray or radio equivalent of a filter). Of particular interest for detecting clusters are the 0.5-2 keV energy event files, which, after being filtered for solar flares, are turned into images and then organised in $68' \times 68'$ slightly overlapping mosaics called 'tiles' (Pacaud et al. 2006; Pierre et al. 2016; Faccioli et al. 2018). After being corrected for different exposure times and smoothed using a wavelet filtering technique (see Pacaud et al. 2006; Faccioli et al. 2018, for a detailed explanation), the X-ray sources are extracted using a software called SExtractor (Bertin & Arnouts 1996; Valtchanov et al. 2001; Pacaud et al. 2006; Faccioli et al. 2018). Different models are then fitted to each identified source: a point source (AGN), an extended emission model, a point-source contaminated extended emission and a double point source model (Pacaud et al. 2006; Faccioli et al. 2018). The general idea is that point sources are more likely to originate from Active Galactic Nuclei (AGNs) and extended sources are more likely to be bremsstrahlung emission from an intracluster medium. Extended sources are further classified into C1, C2 and a recently added category called AC. The C1 class is an almost pure sample of extended sources while up to 50% of the C2 might be point sources (Pacaud et al. 2006; Pierre et al. 2016; Faccioli et al. 2018). The AC class contains potentially AGN-contaminated extended sources.

1.2 Spectroscopic confirmation of clusters

Extended X-ray sources, while dominated by galaxy cluster ICM emission, require further observations to unambiguously confirm their nature. In practice this is achieved by studying deep optical and infrared (IR) imaging observations to identify any galaxy overdensity associated with the X-ray emission. Further observations can then be obtained of individual galaxies believed to be located within the cluster, in order to confirm the cluster redshift (e.g. Valtchanov et al. 2004; Willis et al. 2005; Miyazaki et al. 2007; Hamana et al. 2009; Muzzin et al. 2009). Redshift is defined as:

$$z = \frac{\lambda_{observed\,frame} - \lambda_{rest\,frame}}{\lambda_{rest\,frame}} = \frac{\lambda_{observed\,frame}}{\lambda_{rest\,frame}} - 1, \tag{1.3}$$

where $\lambda_{rest\,frame}$ is one of the wavelengths emitted by the galaxies and $\lambda_{observed\,frame}$ is the corresponding observed wavelength.

Redshift is necessary to compute the distance and the lookback time of galaxies. One can estimate a galaxy redshift without spectroscopic information by fitting the existing optical and near infrared photometric data with several galaxy spectrum templates (in the case of Ilbert et al. 2006, their templates set includes one elliptical galaxy template, two different types of spirals, an irregular galaxy template and two starbursts) at different redshifts, and then choose the statistical best fit (e.g. Arnouts et al. 1999). One can also train a neural network to do the same (e.g. Fotopoulou & Paltani 2018). This estimate of the redshift is called a 'photometric redshift'. Galaxy photometric redshifts can be used to estimate the redshifts of candidate clusters and provide a reasonable sense that the cluster 'is really there', but this method is not as accurate or precise as spectroscopic redshifts (e.g. Jarvis et al. 2013). What appears to be a single overdensity in photometric redshift space might be two independent overdensities with close (but not identical) redshifts that happen to be along the same line-of-sight (see e.g. Valtchanov et al. 2004; Willis et al. 2020).

Hence, to confirm a cluster, one needs to measure the spectroscopic redshift of several galaxies. Typically, a candidate cluster is considered confirmed if it is associated with at least five galaxies with similar redshifts ($\pm$3500 km s^{-1} or less in terms of velocities, see e.g. Lubin et al. 2002; Valtchanov et al. 2004; Willis et al. 2005; Hamana et al. 2009). However, the presence of an extended, spatially coincident X-ray source makes the candidate cluster detection more secure. Thus, the XXL collaboration considers that the presence of three cluster members within the X-ray contour is sufficient to confirm a cluster (Adami et al. 2018; Guglielmo et al. 2018). The link between cluster member redshifts and their velocity differences is given by (Lubin et al. 2002; Willis et al. 2005):

$$\Delta v = c\frac{z-\bar{z}}{1+\bar{z}}, \tag{1.4}$$

where z is the spectroscopic redshift of a member and $\bar{z}$ the median redshift of the cluster.

Not every galaxy is suitable for spectroscopic observations: priority is given to the bright galaxies (because they need less observing time, e.g. Willis et al. 2005) with colours consistent with the red sequence (e.g. Valtchanov et al. 2004; Muzzin et al. 2009). Once the spectra are measured, one would ideally identify several spectral features. Among the often-used features are the [O II] emission line doublet at 3727 Å and the calcium H and K absorption lines at 3933 and 3969 Å (e.g. Willis et al. 2001; Valtchanov et al. 2004; Hamana et al. 2009; Muzzin et al. 2009). The wavelengths at which these features occur in the spectrum allow one to calculate the redshift, using Equation 1.3.

1.3 Galaxy populations in clusters

1.3.1 Quenching

The volume-averaged star-forming rate of the Universe has varied throughout its history: peaking at $z \sim 2$ and then decreasing to the present day (e.g. Madau & Dickinson 2014). Thus, one of the key concepts of galaxy evolution that presently lacks an explanation is the cessation of star formation, referred to as 'quenching'. The causes of quenching are multiple and subject to debate (e.g. Woo et al. 2015, 2017; Quai et al. 2019), but can be divided into two broad categories: internal processes (sometimes called mass processes), such as AGN feedback, and environmental processes, such as ram pressure stripping (e.g. Peng et al. 2010, 2012). Internal processes occur in all environments, but environmental processes tend to take place in dense environments like clusters or large groups of galaxies (Peng et al. 2010, 2012).

When star formation stops, the galaxy colour evolves and becomes redder on a short timescale, as the most massive and luminous (and thus bluer) stars quickly evolve off the main sequence and then explode as supernovae. Thus, the colour distribution of galaxies tends to be bimodal, with a peak of blue star-forming galaxies and another of red, quiescent ones (Strateva et al. 2001; Blanton et al. 2003; Baldry et al. 2004; Balogh et al. 2004). This bimodality is also observed in galaxy morphology, although with some scatter: spiral galaxies tend to be star-forming and elliptical galaxies, quiescent (Blanton et al. 2003; Hogg et al. 2003; Bell et al. 2012).

Internal quenching processes

Two general quenching processes are related to the internal properties of the galaxy: stellar and AGN feedback. Stellar feedback is a consequence of the presence of massive stars and of the winds they generate either during their time on the main sequence or as supernovae (e.g. Hopkins et al. 2012). The latter are generally the most important contributor of stellar feedback, massive stars being important only in metal-rich starbursts, younger than 10 Myrs (e.g. Veilleux et al. 2005). Stellar and supernova-driven outflows generally follow the empirical scaling relation $\frac{\dot{M}_{wind}}{M_*} \propto V_c^{-1}$ where $\dot{M}_{wind}$ is the wind-driven mass loss rate, M_* is the galaxy stellar mass and V_c is the galaxy circular velocity (Oppenheimer & Davé 2006; Oppenheimer et al. 2010; Hopkins et al. 2012). The quantity $\frac{\dot{M}_{wind}}{M_*}$ tends to be larger in the lowest mass galaxies (e.g. Veilleux et al. 2005; Hopkins et al. 2012). Furthermore, although the escape fraction is a poorly constrained quantity, most of these outflows are not powerful

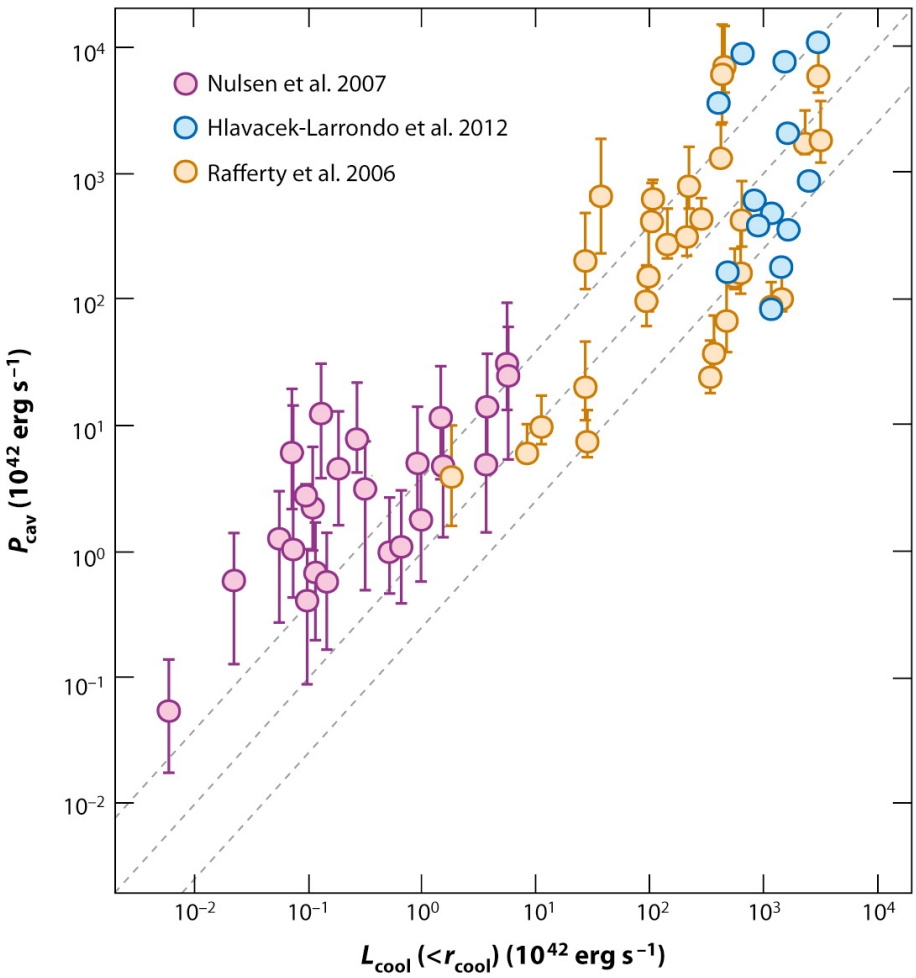

Fabian AC. 2012.
Annu. Rev. Astron. Astrophys. 50:455–89

Figure 1.7: Figure from Fabian (2012, publisher version), based on data from Rafferty et al. (2006); Nulsen et al. (2007); Hlavacek-Larrondo et al. (2012a). This graphic compares cavity power with the intracluster medium X-ray luminosity measured within the cooling region (defined as the region for which the cooling time would be less than 7 Gyrs if there was no feedback) for different systems, ranging from isolated elliptical galaxies to luminous, cool-core clusters.

enough to escape the galaxy and they end up being recycled (e.g. Oppenheimer et al. 2010; Davies et al. 2019). Thus, although they act as an important growth factor for medium-sized galaxies (stellar masses of 10^9 to 5×10^{10} $M_\odot$, according to Oppenheimer et al. 2010), stellar winds are an important quenching factor only in starburst dwarf galaxies, where shallow gravitational potentials allow powerful outflows to drive the gas away (e.g. Veilleux et al. 2005).

The other main internal quenching process, AGN feedback, can be divided into several categories: e.g. radio-galaxies, Seyfert galaxies type 1, Seyfert galaxies type 2, AGNs type 1, AGNs type 2, blazars. Some of these divisions are essentially historical (Seyfert and the other AGNs, see e.g. Mo et al. 2010). Others may arise from different lines of sight (type I, type II and blazars, see e.g. Mo et al. 2010; Fabian 2012) although a few time-variable objects (e.g. Raimundo et al. 2019) suggests that the observing angle might not be the only difference. In the present dissertation, a simpler and more physically motivated classification in two modes is adopted: radiative mode (i.e. quasar mode) and kinetic mode (i.e. radio mode).

The difference between these modes is believed to originate from within the accretion disk. At low accretion rates, the accretion disk is radiatively inefficient and advection-dominated (Fabian 2012; McNamara & Nulsen 2012): this is the radio mode, dominated by collimated outflows called jets. At higher accretion rates (above 1% of the Eddington luminosity[5], according to Fabian 2012) the disk becomes radiatively efficient: this is the quasar mode, where outflows tend to be in the form of less collimated winds.

The most massive outflows tend to be powered by quasars, although it is not easy to distinguish stellar from quasar outflows as both can be present at the same time (Veilleux et al. 2005; Fabian 2012; Förster Schreiber et al. 2019). As for stellar feedback, quasar winds are believed to quench a galaxy by removing its gas (e.g. Veilleux et al. 2005). Some recent high-redshift studies tend to agree with this picture (e.g. Genzel et al. 2014; Förster Schreiber et al. 2019; Herrera-Camus et al. 2019), while lower redshift studies raise doubts about the efficiency of quasar outflows to quench star formation (Fluetsch et al. 2019; Scholtz et al. 2020) or even suggest that quasars winds can induce star formation (Cresci et al. 2015).

The kinetic mode is also associated with collimated outflows called jets. Jets likely form within the accretion disk: the presence of a magnetic field forming an angle with the disk (less than 60° according to Blandford & Payne 1982) will result in the ejection of

[5]The Eddington luminosity is the maximal luminosity that an object can have in order from the radiation pressure not to overcome the gravity.

some of the disk material. This material transports angular momentum away from the disk, allowing the remaining disk material to infall and eventually feed the black hole. Away from the disk, the magnetic field becomes toroidal (i.e. affecting the shape of a gigantic corkscrew), which collimates the jet (Blandford & Payne 1982; Mignone et al. 2010).

Jets may quench a galaxy in a different way than winds: rather than expelling the gas, they prevent it from cooling, condensing and forming stars (e.g. McNamara & Nulsen 2007, 2012). The power of jets is visible in the hot X-ray emitting haloes of groups and clusters where they form 'cavities' (also called 'bubbles') that appear as regions depleted of X-ray emission (e.g. Rafferty et al. 2006, 2008; Dunn & Fabian 2008; Jetha et al. 2008; Randall et al. 2009; Fabian 2012; Hlavacek-Larrondo et al. 2012a,b, 2013, 2015; Randall et al. 2015). The power required to form those cavities is of the same order of magnitude as the energy radiated away by bremsstrahlung emission (or even greater in the case of groups), thus preventing the halo from cooling (e.g. Rafferty et al. 2006, 2008; Dunn & Fabian 2008; Jetha et al. 2008; Randall et al. 2009; Fabian 2012; Hlavacek-Larrondo et al. 2012a, 2015). This apparent tuning between the power injected by jets and the power radiated away by X-ray luminosity is illustrated in Figure 1.7. Some systems show more than one pair of cavities (see e.g. Fabian et al. 2002; Randall et al. 2009, 2015). The extra features are typically further out and devoid of radio counterparts. These 'ghost bubbles' are interpreted as old cavities that have detached from the jet and risen buoyantly. They can be used to estimate the power of past outbursts (e.g. McNamara & Nulsen 2007, 2012).

Environmental quenching processes

Environmental quenching processes can be divided into two categories: collisional interactions between intergalactic and intracluster media and gravitational interactions. One of the most common interactions between the galaxy and the cluster gas is referred to as ram pressure stripping. Ram pressure stripping occurs when the gas of an infalling galaxy encounters the intracluster medium (e.g. Gunn & Gott 1972; Poggianti et al. 2004, 2016; Steinhauser et al. 2016; Aguerri et al. 2018; Tonnesen 2019). As the stellar content of the galaxy continues to fall in, most of the gas is apparently left behind, removed from the galaxy, because of the collisions between the intergalactic and intracluster media particles. The most extreme cases of gas-stripping are galaxies with long ionized gas tails, named jellyfish galaxies after their suggestive shape (Poggianti et al. 2016; Jaffé et al. 2018). Jellyfish galaxies and gas stripping have been observed at a wide range of projected cluster-centric distances (e.g. Poggianti et al. 2004; Tonnesen 2019), although it has been suggested (Jaffé

et al. 2018) that jellyfish galaxies with the longest tails are found near the cluster core. The dominant gas ionization mechanism seems to be starlight from newly formed stars in the tail (Poggianti et al. 2019). These stars contribute to the formation of the intracluster light (Poggianti et al. 2016), i.e., stars within the cluster that are not part of an individual galaxy.

Gravitational interactions, in particular galaxy encounters, can trigger starbursts (e.g. Mihos & Hernquist 1994) and/or quenching (Moore et al. 1996, 1999; McIntosh et al. 2014). In particular, quenching by many fast gravitational encounters is called 'harassement' (e.g. Farouki & Shapiro 1981; Moore et al. 1996, 1999; Treu et al. 2003). The removal of the galaxy gas halo by any of the above mechanisms is sometimes called strangulation of starvation depending whether it is fast or slow (e.g. Larson et al. 1980; Balogh et al. 2000; Treu et al. 2003; Peng et al. 2015; Garling et al. 2020; Trussler et al. 2020). In both cases, the galaxy eventually runs out of gas to fuel star formation and thus becomes quenched.

Gravitational interactions, in particular galaxy encounters, can trigger starbursts (e.g. Mihos & Hernquist 1994) and/or quenching (Moore et al. 1996, 1999; McIntosh et al. 2014). In particular, quenching by many neighbouring galaxies approaching close enough to generate tidal tails is called 'harassement' (e.g. Farouki & Shapiro 1981; Moore et al. 1996, 1999; Treu et al. 2003). The removal of the galaxy gas halo by any of the above mechanisms is sometimes called strangulation or starvation depending whether it is fast or slow (e.g. Larson et al. 1980; Balogh et al. 2000; Treu et al. 2003; Peng et al. 2015; Garling et al. 2020; Trussler et al. 2020). In both cases, the galaxy eventually runs out of gas to fuel star formation and thus becomes quenched.

Measuring quenching in clusters

As seen in previous subsections, internal quenching processes occur in all environments, but environmentally-driven processes are more frequent in dense environments (Peng et al. 2010, 2012). Thus, clusters of galaxies are a good environment to study quenching.

The first step of a statistical quenching study is to segregate the quenched galaxies from the star-forming ones. If deep photometric data are available in several filters, this can be done by SED fitting (i.e. fitting a collection of star-forming and quenched galaxy spectral templates to each galaxy and choosing the best fit, e.g. Strazzullo et al. 2013; Pintos-Castro et al. 2019). Otherwise, this task is performed by the mean of some colour cut (e.g. Strazzullo et al. 2013, 2019; Cerulo et al. 2017; Foltz et al. 2018; Willis et al. 2020). Strazzullo et al. (2013) used both methods and found that they are in good agreement with

each other, except for a few objects near the star-forming/quenched colour divide.

During most of their history, clusters tend to be more quenched than the field (e.g. Nantais et al. 2016, 2017; Kawinwanichakij et al. 2017; Pintos-Castro et al. 2019). The quenched fraction varies within a cluster, with galaxies in the core being more quenched than in the outskirts (e.g. Pintos-Castro et al. 2019; Strazzullo et al. 2019). At the same time, however, the quenched fraction is greater for more massive galaxies, as a result of internal quenching processes (e.g. Visvanathan & Sandage 1977; Kawinwanichakij et al. 2017; Pintos-Castro et al. 2019). As the more massive galaxies tend to reside in the cluster core (e.g. Lavoie et al. 2016), it is difficult to determine if the galaxies in the cluster core are more quenched because they are more massive or if they are more quenched because they inhabit a denser environment (Kawinwanichakij et al. 2017; Pintos-Castro et al. 2019).

Even though quenching has been studied in different environments, its relations with redshift or with cluster physical properties such as mass are poorly understood. Furthermore, most of the studies devoted to quenching in high redshift clusters are based on optically/infrared-selected samples (e.g. Brodwin et al. 2013; Cerulo et al. 2016; Nantais et al. 2016, 2017; Foltz et al. 2018), a selection method that may be biased toward more quenched clusters (see Section 1.1.1). So far, very few studies explore quenching in X-ray selected clusters at $z \gtrsim 1$, with the exception of Nantais et al. (2013). Thus, this dissertation intends to study quenching in high redshift, X-ray selected clusters and compare and contrast with quenching in optically/infrared-selected clusters.

1.3.2 Brightest Cluster Galaxies

The term 'Brightest Cluster Galaxy' (BCG) refers to the dominant galaxy in size and mass within the cluster and usually, but not always, the brightest. BCGs are interesting not only because they represent the high-mass end of the galaxy population, but also because they display distinct light profiles and metallicities (e.g. Tremaine & Richstone 1977; Dressler 1978; Schombert 1986, 1987, 1988; Von Der Linden et al. 2007) compared to other galaxies in the cluster. Furthermore, as explained in Sections 1.3.1 and 1.3.1, they play a major role in the cluster gas cycle and core quenching via past or present outbursts of their supermassive black holes (e.g. Best et al. 2007; Hlavacek-Larrondo et al. 2012a,b, 2013; Vantyghem et al. 2017; Webb et al. 2017; Gendron-Marsolais et al. 2018). Despite that, their formation and evolution are not very well constrained (e.g. De Lucia & Blaizot 2007; Webb et al. 2015b; McDonald et al. 2016), especially at high redshift.

BCG properties and stellar population

BCGs tend to have a steeper surface brightness profile than other early-type galaxies, indicating that though they are massive, they are very compact. However, it is often difficult to fit a single profile to a BCG (e.g. Bernardi et al. 2007; Donzelli et al. 2011) because some (but not all) BCGs are cD galaxies, a type of giant elliptical galaxy characterized by the presence of an extended envelope composed of the stellar remains of multiple mergers (e.g. Lauer et al. 2014). In the most extreme cases, this envelope can extend up to 2 Mpc away from the BCG core (Oemler 1976). At their very heart, some BCGs are less luminous than predicted by standard luminosity profiles (e.g. Laine et al. 2003). This 'missing light' problem seems to be related to the presence of extremely massive central black holes and to their gravitational effect on stellar orbits (e.g. McNamara et al. 2009).

Supermassive black holes hosted by BCGs tend to be more active than those hosted by non-cluster galaxies of similar masses (e.g. Best et al. 2007; Stott et al. 2012). Indeed radio-mode AGN feedback is believed to be the main factor preventing the condensation of the intracluster medium onto the BCG (see McNamara & Nulsen 2007, 2012, for a review, see also the previous section). However, as AGN feedback sometimes fails to entirely shut down cooling flows (cooling of the intracluster medium resulting in an accumulation of gas onto the cluster core), several BCGs at low to moderate redshifts have been reported to form stars (e.g. Bildfell et al. 2008; O'Dea et al. 2008, 2010; Rafferty et al. 2008; Pipino et al. 2009; Donahue et al. 2011; McDonald et al. 2014; Loubser et al. 2016). Yet, with the exception of the massive cooling flow reported at the centre of the Phoenix cluster (e.g. McDonald et al. 2012, 2013, 2015), new stars represent less than 3% of the stellar population of star-forming BCGs (Pipino et al. 2009; Loubser et al. 2016).

Excepting this occasional small population of young stars, the stellar population and metallicities of local BCGs are very similar to other massive elliptical galaxies (Brough et al. 2007; Von Der Linden et al. 2007): they host very old stars with supersolar metallicities. The main difference between non-BCGs and local BCGs is in the relative abundances of metals, the latter displaying slightly larger $[\alpha/\mathrm{Fe}]$ ratios (i.e. the abundance of α-elements[6] compared to iron). This might indicate that star formation in BCGs occurred over a shorter timescale (e.g. Brough et al. 2007; Von Der Linden et al. 2007; Loubser et al. 2009; Groenewald & Loubser 2014; Edwards et al. 2020) as, in a long star-formation episode, supernovae type Ia tend to increase the amount of iron in the gas fuelling the star formation (Granato et al. 2004).

[6] such as helium, carbon, oxygen, etc.

BCG formation and evolution

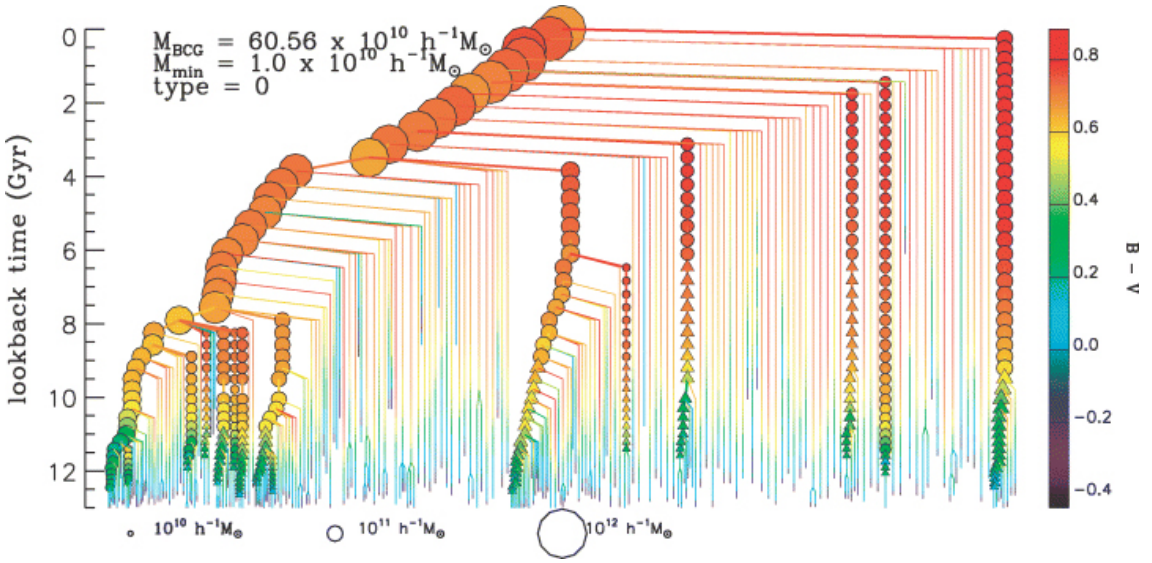

Figure 1.8: Figure from De Lucia & Blaizot (2007), showing the merger tree of a simulated BCG. B-V magnitudes are colour-coded and symbol sizes correlate with the stellar masses. Symbols are used only for progenitors more massive than 10^{10} $M_\odot$ h^{-1} (h refers to the value of the Hubble constant). The symbol shapes indicate if the merger was part of the field-of-view of main group (circle) or not (triangle).

One of the first ideas advanced to explain the evolution of BCGs was that they grew by cannibalizing their satellites and neighbours (Ostriker & Tremaine 1975; White 1976). This idea was then dismissed because the growth powered by this mechanism is insufficient to explain the luminosity of modern cD galaxies (Merritt 1985). Another idea was growth by cooling flows (Silk 1976; Fabian 1994), but such growth would create blue, star-forming BCGs rather than evolved ones. Furthermore, observed cooling flows, when present, are insufficient to be the main growth mechanism (McNamara & O'Connell 1989; Fabian 1994).

The scenario that prevailed until recently was one of very early star formation quickly suppressed by AGN feedback, followed by a progressive assembly by successive gas-poor mergers (Springel et al. 2001; Croton et al. 2006; De Lucia & Blaizot 2007). Figure 1.8 presents the merger tree of a BCG according to this model. In this hierarchical model, 50% of the stars are formed at $z \sim 5$ and 80% at $z \sim 3$ (De Lucia & Blaizot 2007). Although the exact growth rate of BCGs is under debate (Stott et al. 2011; Lidman et al. 2012), the hierarchical scenario is generally consistent with observations below $z \sim 1$ (Stott et al. 2008; Bellstedt et al. 2016; Edwards et al. 2020).

However, recent surveys have produced evidence of in-situ star-formation above a redshift of $z \sim 1$ (Webb et al. 2015b; McDonald et al. 2016; Bonaventura et al. 2017; Cooke et al. 2019). Bonaventura et al. (2017) noted that the specific star formation rates (i.e. star formation rate divided by the stellar mass) transition, from similar to the average of the galaxies at the same redshift (referred to as the galaxy main sequence) to below the average at $z \sim 1$. For their part, McDonald et al. (2016) suggest that a transition in the fuel source powering star formation occurred at $z \sim 0.8$: at low redshift, the main cause of star formation in BCGs is suggested to be residual cooling flows, while at high redshift, the cause is something else, possibly gas-rich mergers. Similarly, Cooke et al. (2019) suggest that early BCG growth is dominated by in-situ star formation and their later growth by gas-poor mergers, with an intermediary phase at $1.25 < z < 2.25$ where both contribute to the growth. This in-situ star formation is part of the most recent BCG simulations (e.g. Ragone-Figueroa et al. 2018; Rennehan et al. 2020), although studies disagree on its timescale.

Thus, there is a tension between the local BCGs observations, which suggest an evolution conform to the prescriptions of De Lucia & Blaizot (2007) and high redshift observations, which point toward a scenario with significant amounts of in-situ star formation at early epochs, with a transition at $z \sim 1$. Therefore, a part of Chapter 2 is devoted to a photometric study of BCGs stellar population at $z \sim 1$, to determine whether their colours are consistent with passive evolution or recent star formation.

1.4 Cluster formation and growth

1.4.1 Protoclusters

A protocluster is a gravitationally bound collection of dark matter haloes that will eventually collapse and virialize, at which point it becomes a cluster of galaxies (e.g. Overzier 2016). Most protoclusters exhibit prolate, irregular shapes (e.g. Muldrew et al. 2015; Lovell et al. 2018) and host large amounts of cold gas and intense star formation (Cucciati et al. 2014; Oteo et al. 2018; Muldrew et al. 2018).

However, defining a protocluster as a cluster progenitor it not practical from an observational point of view: to determine if a given overdensity is a protocluster, one would have to let it evolves for several million years. Hence, observationally the divide between protoclusters and clusters is drawn at the appearance of one or several cluster characteristics: e.g. the appearance of a cluster core (e.g. Andreon et al. 2014; Muldrew et al. 2015), a red sequence (e.g. Hung et al. 2016; Lovell et al. 2018) and/or a sufficiently hot intracluster

medium to be detected by X-ray (e.g. Papovich et al. 2010; Gobat et al. 2011; Andreon et al. 2014; Hung et al. 2016) or by the Sunyav-Zel'dovich effect (e.g. Mantz et al. 2014). Protoclusters have been detected up to a redshift of 6 (e.g. Jian et al. 2018; Harikane et al. 2019), and the transition between protoclusters and clusters seems to happen around $z \sim 2$ for massive clusters (e.g. Gobat et al. 2011; Hung et al. 2016; Darvish et al. 2020; Willis et al. 2020). However, the virialization can occur at significantly lower redshifts (as low as $z \sim 0.2$ or $z \sim 0.4$ for low-mass clusters, see Chiang et al. 2013; Overzier 2016).

Because protoclusters lack some of the commonly accepted observational signatures of galaxy clusters, new methods have been devised to find them. Several of these methods are variations over the same idea: using high-redshift radio-galaxies or quasars as over-density tracers (e.g. Venemans et al. 2007; Hatch et al. 2011a,b; Kuiper et al. 2011, 2012; Champagne et al. 2018). Another technique attempts to identify the large amounts of gas and dust in protoclusters: overdensities are detected as Lyman-α absorption features in the spectra of bright background galaxies (e.g. Lee et al. 2014a,b; Stark et al. 2015; Cai et al. 2016; Miller et al. 2019). Several protoclusters have also been found as a by-product of surveys of the large-scale structures of the Universe (e.g. Harikane et al. 2019) or even serendipitously (e.g. Pavesi et al. 2018).

As the likely progenitors of clusters, protoclusters give insights on galaxy evolution in clusters. Several studies suggest that star formation in protoclusters peaks at $z \sim 3$, earlier than in the field (e.g. Tanaka et al. 2010; Hatch et al. 2011b; Muldrew et al. 2018) and that by $z \sim 2$ the more massive galaxies are already quenched (e.g. Kodama et al. 2007; Tanaka et al. 2010; Hatch et al. 2011b). This idea of an earlier and faster star formation is consistent with the presence of a developed red sequence in several high-redshift clusters (e.g. Papovich et al. 2010; Andreon et al. 2014; Willis et al. 2020). However, Dannerbauer et al. (2017) found that the gas content, properties and star formation efficiency is similar in field galaxies and in protocluster members. They suggest that environmental processes such as ram-pressure stripping or harassment (see Section 1.3.1) are not as efficient in protoclusters, compared to clusters.

1.4.2 Hierarchical assemby

Massive structures accrete less massive ones: this is the essence of hierarchical assembly. Gunn & Gott (1972) together with (Press & Schechter 1974) were the firsts to suggest that clusters start as ovendensities and then grow by accreting isolated galaxies or galaxy groups (e.g. Berrier et al. 2009; McGee et al. 2009) with the occasional smaller galaxy cluster (e.g.

Roettiger et al. 1997; Barrena et al. 2002; Bilton et al. 2019). The idea of hierarchical assembly applies at all mass scales, and can thus be applied to explain the formation of massive elliptical galaxies (e.g. Cole et al. 1994; Gottlöber et al. 2001; McIntosh et al. 2008, 2014), especially of BCGs (e.g. De Lucia & Blaizot 2007, see also Section 1.3.2 for more information).

Multiple observations support this growth model for clusters. These include the presence of substructures in several galaxy clusters (e.g. West et al. 1995; Bekki 1999; De Lucia et al. 2004; Adami et al. 2005; Lee et al. 2016), the mass and luminosity segregation in clusters (Adami et al. 1998, 2007; Andreon 2002; Lee et al. 2016). The presence of residual substructures can be interpreted as an indication that the cluster is merging or has undergone a merger in a recent past. As the cluster returns to virial equilibrium, such features will be erased (e.g. White & Rees 1978).

Thus, most of the cluster members were formed in groups of galaxies. This leads to the idea that the cluster environment alone might not be entirely responsible for the larger quenching fraction in clusters compared to the field (see Section 1.3.1, see also e.g. Nantais et al. 2016, 2017; Kawinwanichakij et al. 2017; Pintos-Castro et al. 2019) but that quenching might start in groups. Indeed, several studies find evidence of 'preprocessing' by the group environment (e.g. McGee et al. 2009; De Lucia et al. 2012; Dressler et al. 2013), although there is no definitive agreement on that point (e.g. Berrier et al. 2009). In the present dissertation, the link between cluster assembly and quenching is further explored in Chapter 4.

The impact of mergers on the intracluster medium

The merger history of a galaxy cluster also affects the state of the intracluster medium. Some clusters exhibit a distinctive X-ray profile with a bright, very peaked core, called a cool core. Despite its name, the core is maintained hot by AGN feedback (see section 1.3.1, see also e.g. Fabian 2012; McNamara & Nulsen 2007, 2012). Other clusters, with less peaked profiles, are called non-cool core. When a cool core cluster experiences a merger with a low-mass satellite halo, the encounter induces an oscillation of the ICM called 'sloshing motion' (e.g. Markevitch & Vikhlinin 2007; Sanders et al. 2016). The effect of sloshing motion on the cluster is shown on the left panel of Figure 1.9. In cases of major encounters, the cool core remnants remain discernable during their first passage through each other (see the right panel of Figure 1.9), but eventually coalesce during the final stages of the merger (e.g. O'Hara et al. 2004; Springel et al. 2005; Markevitch &

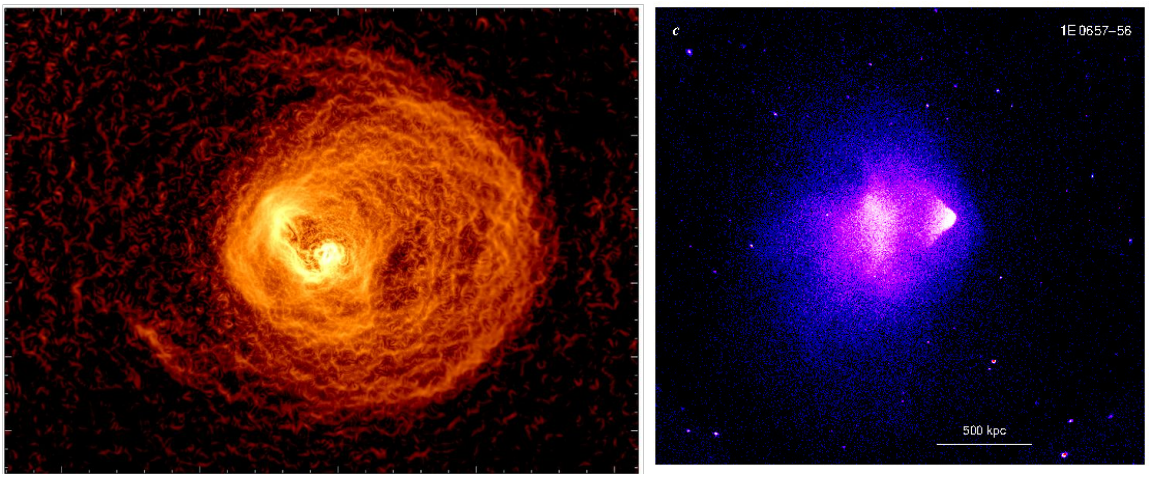

Figure 1.9: Left: Chandra X-ray image, with luminosity scale calculated with a Gaussian Gradient Magnitude filter in order to enhance the luminosity gradient. This image shows the sloshing motion of the ICM in the main Centaurus cluster, at $z = 0.0104$. From Sanders et al. (2016). Right: Chandra X-ray Observatory image of the bullet cluster, a merging cluster at $z = 0.296$, showing the remnants of two cool cores. Retrieved from Markevitch & Vikhlinin (2007).

Vikhlinin 2007). The result is a disturbed, non-cool core cluster that will take a few Gyrs to virialize and revert to a relaxed cluster (Markevitch & Vikhlinin 2007).

Although one way to disrupt a cool core is with a merger, the link between a cluster's current dynamical state and its classification as a cool core or non-cool core is weak: Barnes et al. (2018) found no evidence that cool cores are more relaxed than non-cool cores. There is an ongoing debate about how merger history shapes the cluster ICM profile (e.g. Burns et al. 2008; Hudson et al. 2010) and if mergers are the only thing that can disrupt a cool core (e.g. Barnes et al. 2018).

1.5 Dissertation outline

This dissertation is organized around the main steps of cluster analysis: build a candidate cluster sample, confirm the clusters and then try to better understand them via follow-up studies. Chapter 2 details the construction of a sample of X-ray selected candidate clusters and the work done to characterize their properties: they appear to be low-mass clusters, with diverse levels of quenching. For each candidate cluster, a candidate BCG was selected. A comparison of the photometric colours of these candidate BCGs suggests that some of them might have experienced either an extended or more than one star-forming episode.

This Chapter was originally published in 2020 in Astronomy & Astrophysics under the title *The XXL Survey. XLII. Detection and characterisation of the galaxy population of distant galaxy clusters in the XXL-N/VIDEO field: A tale of variety*.

To confirm four of the candidate clusters detected in (Trudeau et al. 2020), multi-object spectroscopic observations were performed by the Gemini Observatory in 2019. Chapter 3 describes the data reduction process that resulted in the confirmation of three of the four targeted candidate clusters, and the perspective that spectroscopic information gives onto the star formation histories of the member galaxies.

An example of a follow-up study of an interesting object is presented in Chapter 4. At $z = 1.98$, XLSSC 122 is a galaxy cluster with a well-defined mass that appears to possess an evolved galaxy population. This Chapter presents a detailed characterization of the stellar population of its 37 spectroscopically confirmed members, based on photometric data in 12 broad-band filters. The cluster accretion history is investigated with simulated dark matter haloes drawn from the MultiDark Planck 2 cosmological simulations, and the results are compared to its member star formation histories, which has never been done before. This Chapter has been accepted for publication in Monthly Notices of the Royal Astronomical Society under the name *The XXL Survey: XLIX. Linking the members star formation histories to the cluster mass assembly in the* $z = 1.98$ *galaxy cluster XLSSC 122*. The conclusion (Chapter 5) summarises the main realizations presented in this dissertation and briefly describes ideas of future work.

Chapter 2

Detection and characterisation of the galaxy population of distant galaxy clusters in the XXL-N/VIDEO field: A tale of variety

The material in this Chapter was originally published in Astronomy and Astrophysics Volume 642, page A124, 2020 under the title *The XXL Survey. XLII. Detection and characterisation of the galaxy population of distant galaxy clusters in the XXL-N/VIDEO field: A tale of variety*. The authors were A. Trudeau, C. Garrel, J. Willis, M. Pierre, F. Gastaldello, C. Chiappetti, S. Ettori, K. Umetsu, C. Adami, N. Adams, R. A. A. Bowler, L. Faccioli, B. Häußler, M. Jarvis, E. Koulouridis, J.P. Le Fevre, F. Pacaud, B. Poggianti and T. Sadibekova. I made the data analysis, except for section 2.3.3, which comes from the work of Fabio Gastaldello, Stephano Ettori and Keiichi Umetsu. The X-ray data were reduced by Christian Garrel.

Abstract

Context. Distant galaxy clusters provide an effective laboratory in which to study galaxy evolution in dense environments and at early cosmic times.
Aims. We aim to identify distant galaxy clusters as extended X-ray sources that are coincident with overdensities of characteristically bright galaxies.
Methods. We used optical and near-infrared (NIR) data from the Hyper Suprime-Cam

(HSC) and VISTA Deep Extragalactic Observations (VIDEO) surveys to identify distant galaxy clusters as overdensities of bright, $z_{phot} \geq 0.8$ galaxies associated with extended X-ray sources detected in the ultimate XMM extragalactic survey (XXL).
Results. We identify a sample of 35 candidate clusters at $0.80 \leq z \leq 1.93$ from an approximately 4.5 deg^2 sky area. This sample includes 15 newly discovered candidate clusters, ten previously detected but unconfirmed clusters, and ten spectroscopically confirmed clusters. Although these clusters host galaxy populations that display a wide variety of quenching levels, they exhibit well-defined relations between quenching, cluster-centric distance, and galaxy luminosity. The brightest cluster galaxies (BCGs) within our sample display colours that are consistent with a bimodal population composed of an old and red sub-sample together with a bluer, more diverse sub-sample.
Conclusions. The relation between galaxy masses and quenching seem to already be in place at $z \sim 1$, although there is no significant variation in the quenching fraction with the cluster-centric radius. The BCG bimodality might be explained by the presence of a younger stellar component in some BCGs, but additional data are needed to confirm this scenario.

Keywords: Galaxies: clusters: general – Galaxies: distances and redshifts – Galaxies: evolution – Galaxies: high-redshift – Galaxies: photometry – X-rays: galaxies: clusters

2.1 Introduction

Galaxy clusters are the most massive gravitationally bound structures at any epoch. Clusters are dark matter dominated ($\sim 85\%$ of the total mass), while a hot X-ray emitting intracluster medium (ICM) accounts for most of the baryonic mass of the cluster (Plionis et al. 2008). Stars and galaxies correspond to less than 5% of the total mass (Plionis et al. 2008). Clusters provide one of the most extreme environments in the Universe: Infalling galaxies are stripped of their gas by the intracluster medium ram pressure (e.g. Poggianti et al. 2004, 2008, 2016, 2019; Jaffé et al. 2018; Tonnesen 2019), while the centre is one of the densest environments found in space.

The formation and evolution of the most massive giant elliptical galaxies, the brightest cluster galaxies (BCGs), is intimately related to the cluster environment. The BCGs are located near the gravitational centre of their host galaxy clusters and they exhibit unique properties, such as distinct luminosity and surface brightness profiles, and/or supersolar metallicities (e.g. Oemler 1976; Tremaine & Richstone 1977; Dressler 1978; Von Der Lin-

den et al. 2007; Loubser et al. 2009). The classical formation scenario of these galaxies, proposed by De Lucia & Blaizot (2007), is one of early star formation (mostly before $z \sim 3$), which is quickly suppressed by active galactic nuclei (AGN) feedback (e.g Croton et al. 2006), and of progressive, late assembly via gas-poor mergers.

At low redshifts, BCG properties are generally consistent with this picture (e.g. Stott et al. 2008, 2011; Lidman et al. 2012; Bellstedt et al. 2016; Edwards et al. 2020); although, several examples of low to moderately star-forming BCGs have been reported in individual, X-ray bright clusters (e.g. Egami et al. 2006; Bildfell et al. 2008; Stott et al. 2008; Pipino et al. 2009; Loubser et al. 2009, 2016; Rawle et al. 2012; Green et al. 2016). However, there is gathering evidence against the classical scenario at $z \gtrsim 1$: Webb et al. (2015b) and McDonald et al. (2016) report evidence of significant in-situ star formation in $\sim 20\%$ and $\sim 90\%$ of their $z > 1$ samples, respectively. The triggering mechanism of this star formation remains unknown; although, McDonald et al. (2016) have suggested galaxy interactions, which is a possibility that is supported by recent simulations (Rennehan et al. 2020).

The cessation of star formation activity, referred to as quenching, plays an important role in the evolution of galaxies – both for the BCG and within the cluster environment as a whole. Indeed, galaxies appear to evolve at an accelerated rate in clusters as opposed to in the field at all redshifts (e.g. Alberts et al. 2014; Nantais et al. 2017; Foltz et al. 2018; Jian et al. 2018; Pintos-Castro et al. 2019; Strazzullo et al. 2019), although it is unclear at which redshift the passive fraction in clusters becomes greater than in the field (e.g. Strazzullo et al. 2013, 2019; Brodwin et al. 2013; Alberts et al. 2014; Nantais et al. 2017). Quenching also depends on galaxy mass in the sense that higher mass galaxies are more quenched than those of a lower mass (e.g. Muzzin et al. 2012; Balogh et al. 2016; Kawinwanichakij et al. 2017; Jian et al. 2018; Pintos-Castro et al. 2019). Since the most massive galaxies typically reside in the cluster core, mass and environmental effects are difficult to disentangle (e.g. Balogh & McGee 2010; Muzzin et al. 2012; Kawinwanichakij et al. 2017; Jian et al. 2018; Pintos-Castro et al. 2019) and they require large samples of well-characterised galaxy clusters.

Galaxy clusters may be identified by employing a range of techniques. Optical and infrared (IR) imaging surveys identify clusters as overdensities of galaxies (e.g. Postman et al. 1996; Gladders & Yee 2000, 2005; Euclid Collaboration et al. 2019). The red-sequence algorithm (Gladders & Yee 2000, 2005), as was used in the recent Spitzer Adaptation of the Red-sequence Survey (SpARCS; e.g. Wilson et al. 2006, 2009), identifies overdensities exhibiting colours that are consistent with the red-sequence at a given redshift. However, this red-sequence selection may introduce a bias towards clusters with

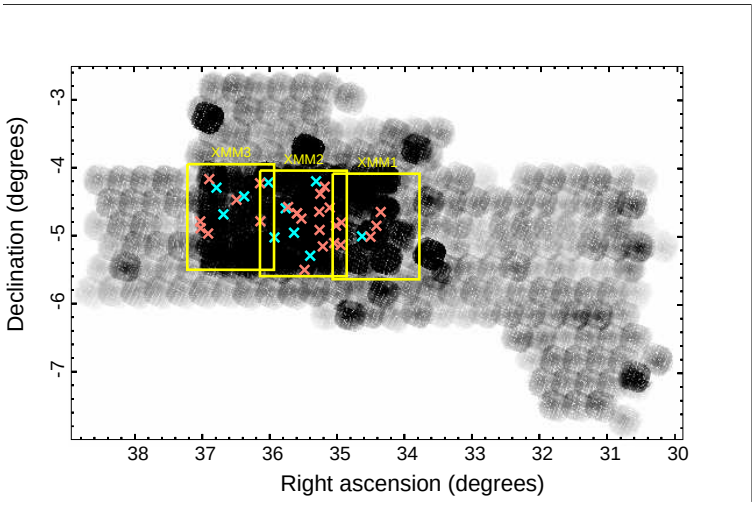

Figure 2.1: VIDEO footprints overlaid on XXL-N exposure map. VIDEO covers eight VISTA footprints, the following three of them are within the XXL-N field: XMM1, XMM2, and XMM3. The darker part of the exposure map corresponds to the 46 ks exposure of the XMM-SERVS field. The cyan and salmon crosses correspond to the respective locations of the confirmed clusters and candidate clusters in our sample.

enhanced red galaxy populations (e.g. Donahue et al. 2002; Willis et al. 2018). An alternative approach is to identify clusters using the properties of the intra-cluster medium, either indirectly via the Suyaev-Zel'dovich effect (e.g. Zel'dovich & Sunyaev 1969; Sunyaev & Zel'dovich 1970, 1972, 1980a,b; Carlstrom et al. 2002; Bleem et al. 2015) or directly via X-ray bremsstrahlung emission (e.g. Gursky et al. 1972; Sarazin 1986; Pierre et al. 2004, 2016, hereafter XXL Paper I; Willis et al. 2018). X-ray selection has been successfully used in the past to find clusters of galaxies, either alone (e.g. Vikhlinin et al. 1998; Clerc et al. 2012) or with the aid of optical data (e.g. Gioia et al. 1990; Böhringer et al. 2001; Willis et al. 2013). There is tentative evidence that such clusters sometimes display smaller red-sequence galaxy populations than optically selected clusters (Donahue et al. 2002; Willis et al. 2018), but a drawback is that X-ray selected samples can exhibit a bias towards relaxed, cool-core clusters (e.g. Eckert et al. 2011; Rossetti et al. 2017; Willis et al. 2018) and lower BCG-X-ray peak distances (e.g. Lavoie et al. 2016, hereafter XXL Paper XV; Rossetti et al. 2016), hence the need for cluster studies with various, complementary selected samples (e.g. Donahue et al. 2002; Sadibekova et al. 2014; Bleem et al. 2015; Willis et al. 2018).

In this Chapter, we employ a multi-wavelength data set constructed as part of the XMM-XXL survey to identify distant galaxy clusters and study their galaxy populations. The XMM-XXL survey covers 50 deg^2 divided into two equal fields: XXL-North and XXL-

South (XXL-N and XXL-S; XXL Paper I). Each field is constructed from a mosaic of 10 ks XMM pointings. The present Chapter focuses on a contiguous sub-area of the XXL-N field covering 5.3 deg^2, XMM-SERVS, which has been observed with an exposure time of 46 ks per pointing (Chen et al. 2018). This deeper sub-area of XMM data is accompanied by a range of multi-wavelength optical and IR data (see XXL Paper I), including a high-quality data set generated by the *Visible and Infrared Survey Telescope for Astronomy* (VISTA) *Deep Extragalatic Observations* (VIDEO) survey (Jarvis et al. 2013). We refer to the 4.5 deg^2 field with overlapping deep XMM and VIDEO data as the XXL-N/VIDEO field (see Fig. 2.1).

This Chapter presents the identification and characterisation of a sample of distant galaxy clusters selected from the XXL-N/VIDEO field. In Sects. 2.2 and 2.3, we describe the identification and composition of the cluster sample. In Sect. 2.4, we compute the fraction of quenched galaxies within the cluster sample and as a function of salient properties, such as the cluster-centric distance and galaxy luminosity. In Sect. 2.5 we identify a sample of BCGs from the cluster sample and investigate the properties of their stellar populations and their star formation histories. In Sect. 2.6 we discuss the possible causes of the variety of observed cluster quenching fractions and of the BCG colour bimodality before summarising our main conclusions in Sect. 2.7. We employ a WMAP9 cosmology characterised by $H_0 = 69.32$ km s^{-1} Mpc^{-1}, $\Omega_m = 0.2865$, and $\Omega_\Lambda = 0.7135$ (Hinshaw et al. 2013). At redshifts of 1 and 1.5, an angular scale of 1 arcminute corresponds to 489 and 518 kpc, respectively. All photometry is quoted in the AB magnitude system. The present Chapter relies on the new version of the XXL-XMM pipeline (V4), which is still in development, and on the related X-ray parameters and images. Compared to the V3 pipeline dealing with individual XMM observations on which all previous XXL publications were based, the V4 pipeline processes coadded observations that are assembled into 1×1 deg^2 mosaics. By dealing with pointing overlaps, V4 ensures reaching the ultimate sensitivity at any position (Faccioli et al. 2018, hereafter XXL Paper XXIV). This is especially important for the VIDEO region, which is characterised by a high level of redundancies.

Throughout this Chapter, we consider that a cluster is confirmed if at least three galaxies within the X-ray emission have matching spectroscopic redshifts or if an obvious BCG has a spectroscopic redshift (Adami et al. 2018, hereafter XXL Paper XX). The expression 'unconfirmed clusters' is used to refer to candidate clusters with insufficient information in order to be spectroscopically confirmed. Cluster names with the prefix 'XLSSC' pertain to spectroscopically confirmed clusters only and they may be found in XXL Paper XX. The prefix '3XLSS' refers to X-ray sources that are a part of the Chiappetti et al. (2018, XXL

Paper XXVII) catalogue. New V4 detections are labelled by the prefix 'XLSSU'.

2.2 Observations and cluster detection

In this Chapter, we attempt to identify significant galaxy overdensities observed in optical-IR imaging data associated with extended X-ray sources. We employed the galaxy photometric redshift (from the VIDEO catalogue) distribution of positive matches to select candidate distant clusters at $z_{phot} \geq 0.8$.

2.2.1 X-ray data

In short, the XAMIN pipeline tests four models to characterise the detected sources, which generate likelihood estimates for point, extended, and double point sources, as well as an extended plus point source. This latter model, denoted AC, is intended to flag extended sources that are significantly contaminated by a central AGN. The coordinates of the X-ray source presented in Sect. 2.3 are based on the centre of the best-fit model. Cluster sources are further classified into C1 and C2 on the basis of pipeline parameters `extent` and `extent_likelihood`. The C1 sample corresponds to an almost pure sample of bright clusters, while the C2 sample, which is fainter, allows for up to 50% of the sample to be misclassified point sources (see Pacaud et al. 2006; XXL Paper XXIV). False C2 are routinely excluded by the examination of X-ray and optical overlays for cluster candidates below z=1.

It is important to mention that the choice of the numerical pipeline parameter values used to define the C1 and C2 criteria are still those that are based on the detections performed with the V3 pipeline from simulated individual XMM observations. These criteria will be revised when the final V4 is fully validated and applied to mosaic simulations. However, we do not expect drastic changes in the class parameters since they are based on likelihoods. This situation does not impact the current study because it does not explicitly involve the cluster selection function at any stage.

2.2.2 Optical and near infrared photometry

The VIDEO observations consist of IR imaging undertaken with the VISTA telescope in the YJHK$_s$ photometric bands. In the XMM-SERVS field, these observations reach 5σ depths of at least 25.1, 24.7, 24.2, and 23.8 mag within 2 arcsecond circular apertures for

$YJHK_s$, respectively (Adams et al. 2020). The VIDEO catalogue also contains additional imaging data consisting of the *Canada-France-Hawaii Telescope Legacy Survey Deep-1* field (CFHTLS-D1) and of the deep 'layer' of the *Hyper Suprime-Camera* (HSC) *Subaru Strategic Program* (HSC-SSP, Aihara et al. 2018a,b). The ultra-deep 'layer' of HSC-SSP overlaps with the XMM1 field. The photometric redshift analysis included in the catalogue employs an i-band selected source list where photometry in additional bands is obtained by applying `SExtractor` to astrometrically-matched pixel data at other wavelengths. In addition, we employed HSC-SSP iz and VIDEO JK_s photometry from this catalogue to study the properties of candidate cluster member galaxies directly. The HSC-SSP deep data have 5σ limiting magnitudes of 25.4 and 24.6 in the i and z bands, respectively, and the ultra-deep data have limiting magnitudes of 26.4 and 26.3 (Adams et al. 2020).

Photometric redshifts for sources in the VIDEO catalogue are computed using the LE-PHARE photometric redshift code (Ilbert et al. 2006). The code employs the COSMO template set (Ilbert et al. 2009), including 32 templates from Polletta et al. (2007) and from Bruzual & Charlot (2003). Dust attenuation follows a Calzetti et al. (2000) law, and the intergalactic medium absorption treatment is based on Madau (1995). Further details are provided by Adams et al. (2020).

2.2.3 Identification of galaxy clusters

We performed four steps to select candidate clusters from our X-ray sample and followed a similar procedure to that of Willis et al. (2013). Each step is summarised below:

1. Convolve the photometric redshift histogram for bright galaxies with a matched Gaussian filter chosen to match the properties of redshift peaks of spectroscopically confirmed clusters. Galaxies are selected to be brighter than the characteristic luminosity, L^*, along the line-of-sight of each X-ray source (i.e. a 1 arcmin radius aperture centred on the X-ray best-fit model centre).

2. Identify overdensities corresponding to a bright galaxy excess of $\gtrsim 4$ and display the position of potential members on colour images together with X-ray emission contours.

3. Examine the $i-z$ and $z-J$ colour-magnitude diagrams of each candidate cluster.

4. Employ a Gaussian model of the photometric redshift distribution of selected overdensities to estimate a refined mean cluster redshift and its standard deviation.

Figure 2.2 presents a visual summary of these four steps. Similar images of the other candidate clusters are presented in Appendix 2.7.

The first step of the identification process is to select galaxies and AGN that might be associated with each X-ray source. We selected the galaxies and AGN sources by employing their goodness-of-fit when compared to stellar, galactic, and AGN templates (see Jarvis et al. 2013). Because galaxies in clusters are more likely to host radio-loud AGN than field galaxies (Best et al. 2007), we kept AGN and discarded only the star-like objects. Then, we selected objects within 1 arcmin of the considered X-ray detection. We refer to these objects as the 'field-of-view'galaxies.

We selected bright galaxies in the field-of-view by employing luminosity function arguments: We computed the apparent magnitude of M^*[1], assuming $M^* = -22.26$ in the K_s band using Cirasuolo et al. (2010) with no evolution from $z \sim 3$ to $z \sim 0$ and a k-correction described by the bandwidth term. Galaxies brighter than the expected apparent m^* magnitude at their photometric redshift were retained. We applied a further photometric cut based on the 5σ depth of the VIDEO K_s band, discarding any galaxy fainter than 23.8. The latter cut is important beyond $z \sim 1.4$, where m^* is fainter than the VIDEO 5σ limit.

Selected field-of-view galaxies were then binned in photometric redshift space, over the interval $0.2 < z_{phot} < 3.2$. Galaxies were sampled in bins of 0.04 in photometric redshift since this is the redshift iteration step employed in the photometric redshift analysis. We then used the catalogue distribution to perform a background subtraction by applying the same selection steps described above and by scaling the number distribution by the relative size of our field-of-view compared to that of the full the catalogue, that is to say

$$N_{excess} = N_{FOV} - N_{cat}\left(\frac{\pi r_{FOV}^2}{A_{cat}}\right), \tag{2.1}$$

where N_{FOV} is the number of galaxies in a particular redshift bin in our field-of-view, N_{cat} is the number of galaxies listed in the catalogue in the corresponding redshift bin after applying the same cuts, r_{FOV} is the 1 arcminute radius we used to select galaxies associated with an X-ray detection, and A_{cat} is the catalogue area.

To identify structures in the photometric redshift histogram along the line-of-sight to each extended X-ray source, we employed a matched Gaussian filter with a full width at half maximum (FWHM) that is equal to 0.12 in redshift (i.e. three bins). The properties of the Gaussian profile are based on the unfiltered redshift peaks associated with spectroscopically confirmed clusters.

[1] the characteristic luminosity, a parameter of the Schechter function

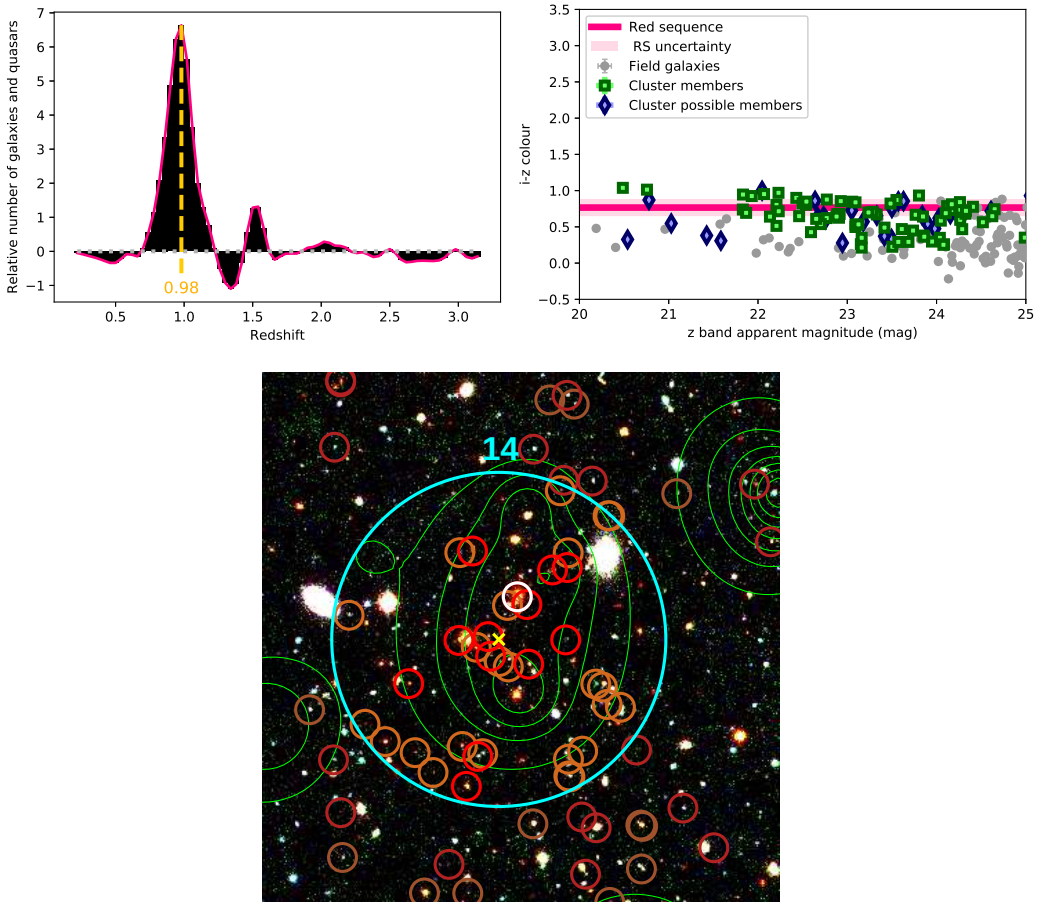

Figure 2.2: Visual summary of the cluster identification process. Top left: Background subtracted and Gaussian filtered photometric redshift distribution of the bright galaxies within the central arcmin of candidate 14. The dashed line indicates the highest bin in the redshift spike. Top right: i-z CMD plot of the galaxies above the VIDEO 5σ limit within 1 arcmin of the centre. The green squares indicate the galaxies with photometric redshifts that are consistent with the mean redshift plus or minus 1.5 times the standard deviation of the most accurate Gaussian modelling of the redshift spike. The blue lozenges indicate galaxies with redshifts that are consistent with the sidewings of the most accurate Gaussian model, up to three times the standard deviation. The deep pink line indicates where the red sequence should be at this redshift, based on the best fit calculated in Sect. 2.4.1. The light pink region indicates the uncertainty on this red-sequence model, which is also calculated in Sect. 2.4.1. Bottom panel: Example of a Megacam r and i filter as well as a VIDEO H filter image for candidate 14, which is one of our candidate clusters. The cyan circle delimits the region within 1 arcmin of the X-ray best fit model centre, which is marked by a yellow cross. The red and brown circles highlight the bright galaxies with a redshift corresponding to the cluster photometric peak redshift ± 0.02 and to the cluster redshift ± 0.06, respectively. Darker circles indicate the galaxies outside the central region. The BCG is circled in white. The X-ray contours in green are logarithmically distributed in ten levels between the maximum and minimum emission observed in a 7×7 arcmin^2 box around the X-ray source.

Table 2.1: List of detections above $z \sim 0.8$. Every detection is presented with its official designation, X-ray characterisation model, X-ray coordinates, photometric redshift from VIDEO, and redshift from the literature (z_{lit}) when available. The sixth column corresponds to the significance of the detection in terms of the numbers of galaxies in the highest bin. The ninth column displays the [0.5-2] keV band X-ray luminosities in the central 300 kpc of the candidate clusters, while the tenth column provides an X-ray luminosity based estimate of the cluster mass.

#	Nearest object[a]	Flags[b]	RA (degrees)	Dec (degrees)	Sign.	z^{c}_{phot}	z^{de}_{lit}	L_X[f] (10^{43} erg s^{-1})	M_{500} (10^{13} $M_\odot$)	Notes
1	3XLSS J022222.9-044043	US	35.595	-4.679	3.9	0.80	0.77	-	-	[g]
2	XLSSC 184	C	35.312	-4.207	7.4	0.80	0.81	1.9 ± 0.2	7 ± 2	-
3	XLSSC 071	C	35.639	-4.966	6.4	0.83	0.83	2.8 ± 0.2	8 ± 3	-
4	3XLSS J022432.9-044742	U	36.137	-4.796	5.1	0.83	0.90	4.3 ± 0.3	9 ± 3	-
5	3XLSS J022135.2-051811	C	35.399	-5.305	8.4	0.85	0.84	2.9 ± 0.2	7 ± 3	-
6	XLSSU J021947.4-050841	U	34.948	-5.145	5.0	0.86	0.89	1.2 ± 0.3	6 ± 2	-
7	XLSSC 015	C	35.928	-5.034	8.2	0.87	0.86	1.3 ± 0.2	6 ± 2	-
8	XLSSC 064	C	34.632	-5.018	9.2	0.89	0.87	6.9 ± 0.3	10 ± 4	-
9	3XLSS J022557.1-042845	U	36.489	-4.480	4.0	0.90	1.05	1.9 ± 0.3	6 ± 2	-
10	3XLSS J022156.1-053049	U	35.483	-5.513	3.8	0.91	0.95	1.4 ± 0.3	6 ± 2	-
11	3XLSS J021945.5-044831	U	34.935	-4.814	4.9	0.91	0.92	1.1 ± 0.2	5 ± 2	[h]
12	XLSSU J022530.3-042544	C	36.376	-4.429	5.9	0.87	0.92	0.8 ± 0.2	5 ± 2	-
13	3XLSS J022804.6-045351	U	37.020	-4.898	4.3	0.93	0.86	2.5 ± 0.4	7 ± 3	-
14	XLSSU J022051.0-050958	N	35.213	-5.166	6.6	0.97	-	2.5 ± 0.5	7 ± 3	[h]
15	3XLSS J022103.0-045524	U	35.260	-4.924	5.1	0.97	1.10	4.7 ± 0.3	8 ± 4	-
16	3XLSS J022739.0-045830	N	36.909	-4.976	3.9	0.99	-	10.0 ± 0.6	10 ± 5	-

Table 2.1: List of detections above $z \sim 0.8$. Every detection is presented with its official designation, X-ray characterisation model, X-ray coordinates, photometric redshift from VIDEO, and redshift from the literature (z_{lit}) when available. The sixth column corresponds to the significance of the detection in terms of the numbers of galaxies in the highest bin. The ninth column displays the [0.5-2] keV band X-ray luminosities in the central 300 kpc of the candidate clusters, while the tenth column provides an X-ray luminosity based estimate of the cluster mass.

#	Nearest object[a]	Flags[b]	RA (degrees)	Dec (degrees)	Sign.	z^{c}_{phot}	z^{de}_{lit}	L_X[f] (10^{43} erg s^{-1})	M_{500} (10^{13} $M_\odot$)	Notes
17	3XLSS J022044.7-041713	N	35.185	-4.287	4.1	1.00	-	6.2 ± 0.4	9 ± 4	-
18	XLSSC 044 ($z_f = 0.27$)	US	36.141	-4.235	4.9	1.00	1.13	-	-	-
19	XLSSC 124 ($z_f = 0.52$)	NS	34.419	-4.862	3.9	1.00	-	-	-	[h]
20	XLSSC 029	C	36.016	-4.225	8.3	1.06	1.05	13.1 ± 0.3	11 ± 5	-
21	XLSSC 005	C	36.785	-4.300	5.6	1.04	1.06	4.5 ± 0.4	7 ± 4	-
22	XLSSC 192 ($z_f = 0.35$)	NS	34.507	-5.023	4.6	1.08	-	-	-	[h]
23	3XLSS J022027.0-043538	N	35.111	-4.595	4.7	1.09	-	13.4 ± 0.8	11 ± 6	-
24	3XLSS J022222.9-044043	US	35.595	-4.679	4.0	1.12	-	-	-	[g]
25	XLSSC 141 ($z_f = 0.20$)	NS	34.356	-4.659	4.9	1.21	-	-	-	-
26	XLSSC 046	C	35.762	-4.605	9.0	1.18	1.21	3.5 ± 0.5	6 ± 4	-
27	3XLSS J022003.6-045142	N	35.016	-4.861	5.1	1.44	-	1.9 ± 0.5	4 ± 3	-
28	3XLSS J022255.1-043508	N	35.726	-4.587	4.5	1.45	-	16.4 ± 0.9	9 ± 6	-
29	3XLSS J022100.4-042327	N	35.250	-4.392	4.2	1.48	-	9 ± 1	7 ± 5	-
30	3XLSS J022207.4-044532	N	35.529	-4.758	3.9	1.49	-	9 ± 1	7 ± 5	-
31	XLSSU J022105.6-043935	N	35.265	-4.656	4.1	1.54	-	13.2 ± 0.9	8 ± 6	-
32	3XLSS J022010.3-050701	N	35.043	-5.117	5.5	1.57	-	4.0 ± 0.8	5 ± 4	-

Table 2.1: List of detections above $z \sim 0.8$. Every detection is presented with its official designation, X-ray characterisation model, X-ray coordinates, photometric redshift from VIDEO, and redshift from the literature (z_{lit}) when available. The sixth column corresponds to the significance of the detection in terms of the numbers of galaxies in the highest bin. The ninth column displays the [0.5-2] keV band X-ray luminosities in the central 300 kpc of the candidate clusters, while the tenth column provides an X-ray luminosity based estimate of the cluster mass.

#	Nearest object[a]	Flags[b]	RA (degrees)	Dec (degrees)	Sign.	z^{c}_{phot}	z^{de}_{lit}	L_X[f] (10^{43} erg s^{-1})	M_{500} (10^{13} $M_\odot$)	Notes
33	3XLSS J022806.4-044803	N	37.025	-4.797	4.9	1.79	-	8 ± 2	6 ± 5	-
34	JKCS 041	C	36.683	-4.694	8.2	1.63	1.80	16 ± 1	7 ± 6	-
35	3XLSS J022734.1-041021	N	36.891	-4.174	4.0	1.93	-	10 ± 1	6 ± 5	-

[a] Nearest confirmed cluster or X-ray source. If the nearest object is a confirmed foreground cluster, its spectroscopic redshift, z_f, is given.

[b] C: spectroscopically confirmed cluster; U (for unconfirmed): not spectroscopically confirmed, but listed as a candidate cluster in the literature; N: new candidate cluster; S: superposition with a low redshift confirmed cluster or with another candidate.

[c] The uncertainties on the photometric redshifts were estimated to 0.02 at $z < 1.4$ and 0.14 at $z \gtrsim 1.4$.

[d] Spectroscopic redshifts (flag C) reported from Pierre et al. (2006), Willis et al. (2013), Andreon et al. (2014), and XXL Paper XX.

[e] Tentative or photometric redshifts (flag U) reported from Finoguenov et al. (2010), Durret et al. (2011), Wen & Han (2011), Licitra et al. (2016), and XXL Paper XX.

[f] We did not compute the X-ray luminosity for clusters marked S (superposition) because their X-ray emission might be a blend of foreground and background emission.

[g] Archival spectroscopic observations available.

[h] Gemini GMOS observations under proprietary time.

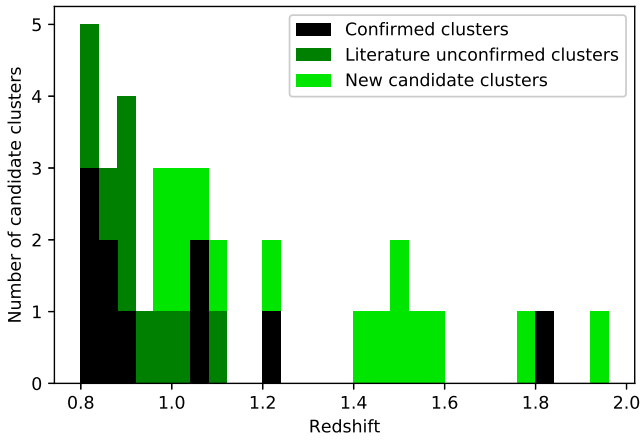

Figure 2.3: Histogram of the candidate cluster redshifts. The black bars correspond to the spectroscopic redshifts of the confirmed clusters and the green bars represent the photometric redshifts of the candidate clusters, which were either previously observed (dark green) or newly detected (lighter green).

2.2.4 Overdensity assessment

We performed a visual inspection of all C1, C2, and AC X-ray sources that display a signal that is consistent with > 4 galaxies at a single photometric redshift. We typically employed *riH* images from CFHTLS and VIDEO with the candidate members indicated in addition to X-ray emission contours (see Fig. 2.2). We further generated $i-z$ and $z-J$ colour magnitude diagrams of each candidate cluster in order to determine if a red sequence is present.

The overdensity finding method provides a first estimate for the candidate cluster redshift based on the median redshift of the bin with the highest count (see Fig. 2.2, top left panel). To refine this estimate, we modelled each candidate redshift signal as a Gaussian and employed the 13 central bins of the non-filtered redshift signal. We then used the Gaussian mean as the cluster redshift and the standard deviations as an estimate of the uncertainty.

2.3 The cluster sample

2.3.1 Sample selection

We processed a total of 284 extended X-ray detections within the XXL-N/VIDEO region. This parent sample generated a sample of 35 candidate distant galaxy clusters. Table 2.1 and Fig. 2.3 present these clusters, each of which represents a detection with a significance

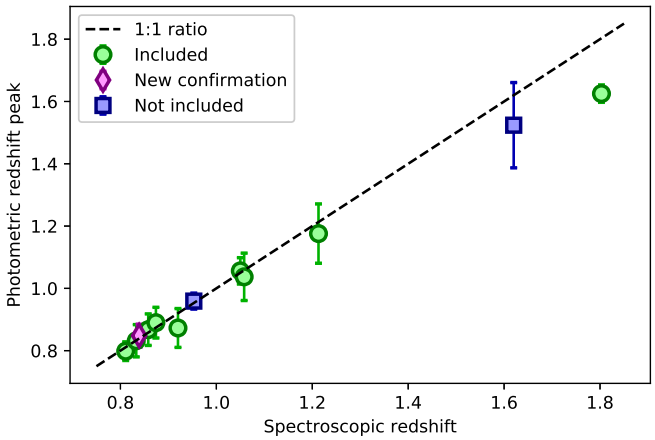

Figure 2.4: Comparison between the spectroscopic redshifts of confirmed clusters within the XXL-N/VIDEO overlap and the corresponding photometric overdensities in the VIDEO catalogue. The error bars correspond to the standard deviation of the Gaussian model that fits the photometric spike best. All clusters, except two (not included), were detected in optical. The green dots are the clusters that are a part of our sample, while the blue squares are not included in our sample since they do not meet our X-ray selection criteria. The magenta diamond is the newly confirmed candidate 3. The dashed line represents the ideal case, where $z_{phot} = z_{spec}$.

of approximately four galaxies or more in a photometric redshift bin satisfying $z_{phot} \geq 0.8$ (see also Fig. 2.1). Of these 35 candidate clusters, ten have been spectroscopically confirmed while 15 are presented here for the first time. Ten additional candidates have been previously identified as distant clusters; however, to our knowledge, they have never been spectroscopically confirmed (see Olsen et al. 2007; Finoguenov et al. 2010; Durret et al. 2011; Wen & Han 2011; Licitra et al. 2016; XXL Paper XX).

Nine of the confirmed cluster detections were confirmed by prior spectroscopy (e.g. Pierre et al. 2006; Willis et al. 2013; XXL Paper XX), including one at $z = 1.803$ (Andreon et al. 2014). With the spectroscopic redshifts listed in the CESAM database[2] (XXL Paper XX), we were able to confirm one additional cluster (candidate 3), bringing the total number of confirmed clusters to ten. All of these X-ray detections meet our criteria for candidate clusters.

Four confirmed distant clusters in this area (Pierre et al. 2006; Papovich et al. 2010; XXL Paper XX) are not a part of our sample because their coordinates do not correspond to a V4 C1, C2, or AC detection. This is the case for a $z = 1.62$ cluster (Papovich et al. 2010). Although IRC-0218A and our detections at similar redshifts possess comparable

[2] `http://cesam.lam.fr/xmm-lss/`

masses (IRC-0218A M_{200} is $7.7 \pm 3.9 \times 10^{13}$ $M_{\odot}$), IRC-0218A X-ray emission is completely dominated by a point source (Pierre et al. 2012).

We nevertheless applied our optical and IR detection criteria to those four clusters. Two clusters satisfied these criteria, including IRC-0218A, and were included in our photometric redshift accuracy assessment (see the following section). The clusters XLSS J022609.9-043120 and XLSSC 203 (see Pierre et al. 2006; XXL Paper XX) located at $z = 0.82$ and $z = 1.077$, respectively, did not satisfy them. Since V4 works on co-added and thus deeper images, we expect its source characterisation to be more reliable.

2.3.2 Photometric redshift accuracy

To estimate the reliability of our photometric redshift estimates for the candidate clusters, we compared the spectroscopic redshift of 12 confirmed clusters in the field (six clusters listed in XXL Paper XX, four from Pierre et al. 2006; Papovich et al. 2010; Willis et al. 2013; Andreon et al. 2014, and two other confirmed clusters in the XXL-N/VIDEO area) to the photometric redshift generated by the cluster finding procedure. Figure 2.4 shows the result of this comparison. At $z \sim 1$, the differences between the photometric and spectroscopic redshifts fall well within the photometric redshift error estimates. These error bars represent the standard deviation of the best-fitting Gaussian model. For the two high redshift clusters, the photometric redshifts seem to underestimate the spectroscopic values. Therefore, we calculated the root mean square (RMS) of the $z \sim 1$ and $z \gtrsim 1.5$ clusters separately. We obtained 0.02 and 0.14, respectively. From now on, we use these RMS values as the uncertainties on the photometric redshifts.

2.3.3 Clusters' estimated masses

Following a similar methodology as the second data release of XXL, we used scaling relations to provide an estimate of the mean parameters for clusters for which the data quality is not sufficient enough to perform a direct spectral fit. A detailed description is provided in Sect. 4.3 of XXL Paper XX, and we provide a brief overview here. We estimated count-rates in the pn data in the [0.5-2] keV band within 300 kpc of the cluster centre, using the Bayesian approach to the fixed aperture photometry measurement outlined in Willis et al. (2018). We then converted this count-rate to the corresponding X-ray luminosity by adopting an initial gas temperature, a metallicity fixed to 0.3 times the solar value (as tabulated in Anders & Grevesse 1989), and the cluster spectroscopic (when available) or photometric redshift. With the same initial guess as to the temperature, we estimated $r_{500,scal}$ from the

mass-temperature relation constrained from a subset of 105 XXL clusters that have both measured HSC lensing masses and X-ray temperatures (see Umetsu et al. 2020). We stress that here we use a $M_{500} \mid T_X$ relation, which was obtained using the Bayesian regression scheme implemented in the LIRA package (Sereno 2016; Sereno et al. 2016), and not the $T_X - M_{500}$ relation reported in Umetsu et al. (2020). The luminosity was then extrapolated from 300 kpc to $r_{500,scal}$, assuming a β-model for the cluster emissivity with parameters $(r_c, \beta) = (0.15 r_{500,scal}, 2/3)$. Then a new temperature was evaluated using the best-fit result for the luminosity-temperature relation quoted in Table 6 of XXL Paper XX (XXL fit). The iteration on the gas temperature was stopped when the input and output values agreed within 5%, and in general the process converges after 2-3 steps. The uncertainties on the derived parameters, and in particular the masses, are obtained by the propagation of errors on the scaling parameters, including the measured correlation among them.

2.3.4 Other clusters in XXL-N/VIDEO

There are 54 previously confirmed clusters that are either within or overlap with the XXL-N/VIDEO field (XXL Paper XX). Of these, 47 are located at $z < 0.8$ with the remaining seven clusters located at $z \geq 0.8$. These seven clusters correspond to a surface density of 1.6 distant clusters per square degree. This number represents a lower limit because some known clusters associated with an extended X-ray detection (e.g. JKCS 041, a z=1.803 confirmed cluster Andreon et al. 2014) were excluded from XXL Paper XX compilation.

Adding all of our detections would bring this number up to approximately 8.2 clusters per square degree, with a flux limit of 1.7×10^{-15} erg cm-2 s^{-1} in the [0.5-2] keV band (Chen et al. 2018). This represents 3.6 times and 0.51 times the surface densities reached by Willis et al. (2013) and Finoguenov et al. (2010) with depths of 1×10^{-14} erg cm-2 s^{-1} and 2×10^{-15} erg cm-2 s^{-1} in the [0.5-2] keV band, respectively.

2.4 Quenching and star formation in clusters

The fraction of quenched galaxies in a sample of distant, X-ray selected galaxy clusters has the potential to provide an unbiased view of the star formation conditions in massive, virialised structures. In this section, we compute the fraction of quenched galaxies within the XXL-N/VIDEO distant cluster sample, focussing on the clusters at $z < 1.4$, because the catalogue 5σ magnitude limit restricts the number of selected galaxies beyond that redshift. We achieved this by employing four related analysis techniques, while intending

to investigate whether each provides consistent results. Only the galaxies brighter than the 5σ limit in J and K_s are used in these computations.

1. The first employs the $i-z$ colour histogram of background corrected galaxies in the field of each candidate cluster. This colour space distribution is then modelled using two Gaussian functions to represent the red sequence and the blue cloud (see Fig. 2.5).

2. The second method employs the same background corrected colour distribution as above, but it employs a single colour cut to divide the distribution into quenched and star-forming galaxies.

3. The third method selects cluster galaxies using photometric redshift and then applies the boundary method used in the method above (2).

4. The fourth method is similar to method 2 with the additional constraint that each galaxy, including the background, must be brighter than L^* at the candidate cluster redshift. The L^* evolutionary k-correction is computed using the results from method 1 (see Fig. 2.6).

2.4.1 First quenching method

The first step consists of defining the appropriate area within which one can select field-of-view galaxies for each cluster. Some previous studies (e.g. Wetzel et al. 2012; Pintos-Castro et al. 2019) analyse the quenched and star-forming fraction up to several virial radii. However, since several of our fields appear to contain secondary overdensities, we chose to restrict our analysis to closer to the cluster centre, namely within a radius of 1.35 Mpc around the X-ray coordinates. A radius of 1.35 Mpc corresponds to approximately 1.5 times the value of r_{500} for a 1×10^{14} $M_\odot$ galaxy cluster (Chen et al. 2007) and to an angle of 2.76 arcminutes at $z = 1$. We further selected galaxies with a photometric redshift between 0.60 and 2.04, both in the cluster field and background catalogue, and sampled the resulting distributions into 0.04 wide bins in $i-z$ colour.

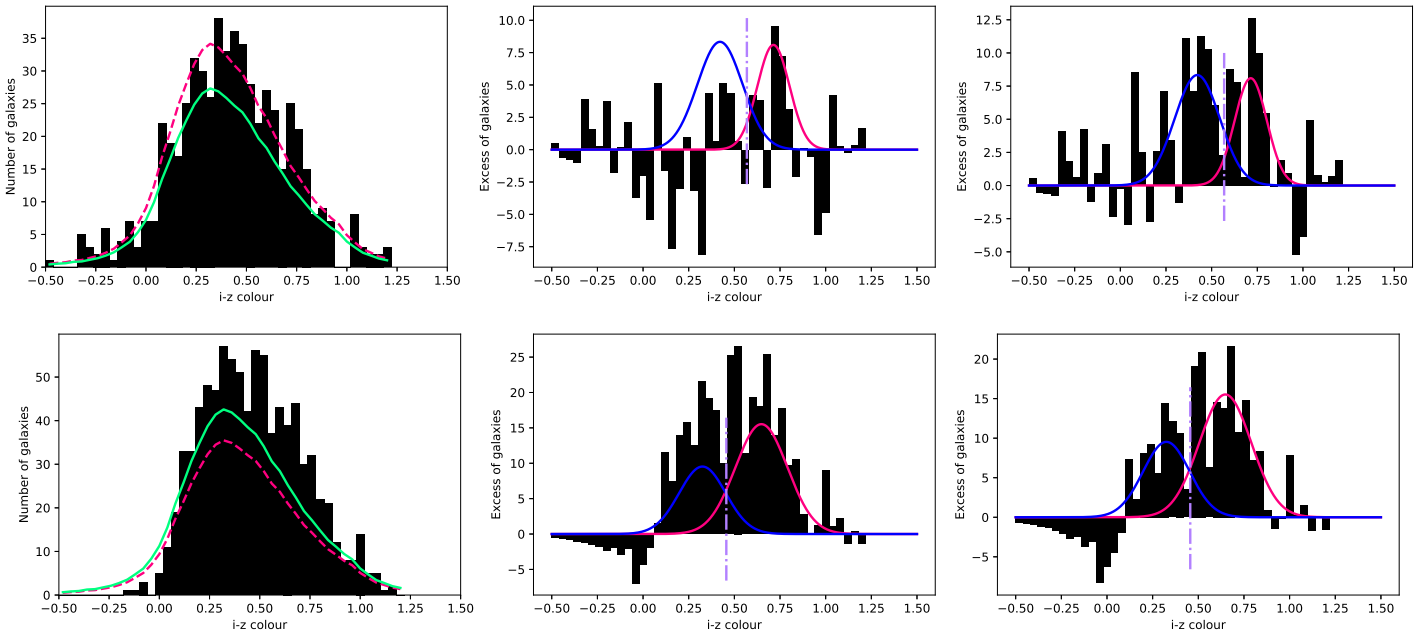

Figure 2.5: Illustration of two steps of the first method. Left panels: i-z colour histograms in two fields-of-view (candidate 13 and candidate 8) where the default background (pink line) is either too high or too low. The adjusted background is overplotted in green. Middle panels: Resulting colour distribution is the background is left unadjusted. For comparison purposes, the Gaussian models of the red sequence and the blue cloud are shown in pink and blue, respectively; although, they were computed with an adjusted background. The mauve dash-dotted line is the 'boundary' used in method 2, 3, and 4. Right panels: Colour distribution once the background was adjusted.

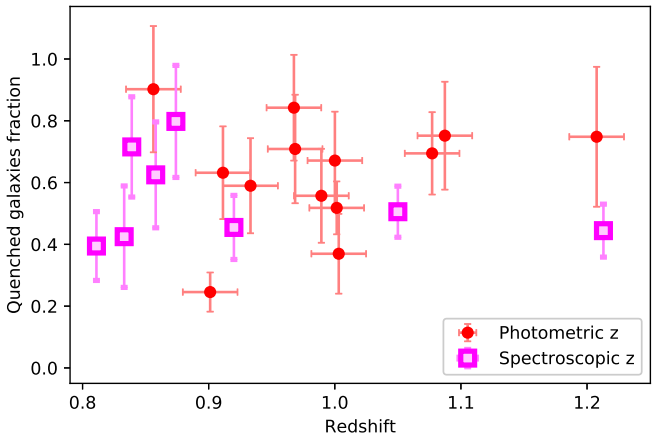

Figure 2.6: Fraction of quenched galaxies as a function of the redshift, according to method 4, for each VIDEO candidate, excluding candidates 1, 4, 10, 21, and 24 and the candidate clusters above z=1.4. Spectroscopically confirmed clusters are indicated by squares, and circles are used to show the other ones. The error bars are the propagation on the Poissonian uncertainties on the integrals of the red sequence and the blue cloud models.

We then corrected this field-of-view distribution using the same method as applied in Eq. 2.1. A visual inspection reveals that the resulting colour distribution is bimodal (see Fig. 2.5). We modelled this bimodal colour distribution using two Gaussian functions – one representing the red sequence and the other the blue cloud. In some fields, we note that the background correction is either too large or too small to yield to a clear bimodal distribution, resulting in poor fits or even in a non-convergent fitting algorithm (candidate 7). In such cases, we adjusted the background correction by up to 20% before determining whether the adjusted background results in an improved fit. Figure 2.5 presents the effect of an unadjusted background on the colour distribution on two typical fields. Although both cases that are too high and too low are presented, the former concerns only four clusters. One of these clusters is confirmed (candidate 3) and two others (including the case presented in Fig. 2.5) are among the sample of other photometric studies (see Olsen et al. 2007; Wen & Han 2011; Licitra et al. 2016). Thus, most of them are unlikely to be false detections.

Three out of the eight clusters with an increased background lie in overlaps between two VIDEO footprints and thus have, according to Jarvis et al. (2013) longer exposure times. Moreover, two additional clusters are in the XMM1 field, which is a part of the ultra-deep layer of the HSC-SPP survey, and they thus possess 1 to 1.5 mag deeper photometry in the i and z band (see Adams et al. 2020).

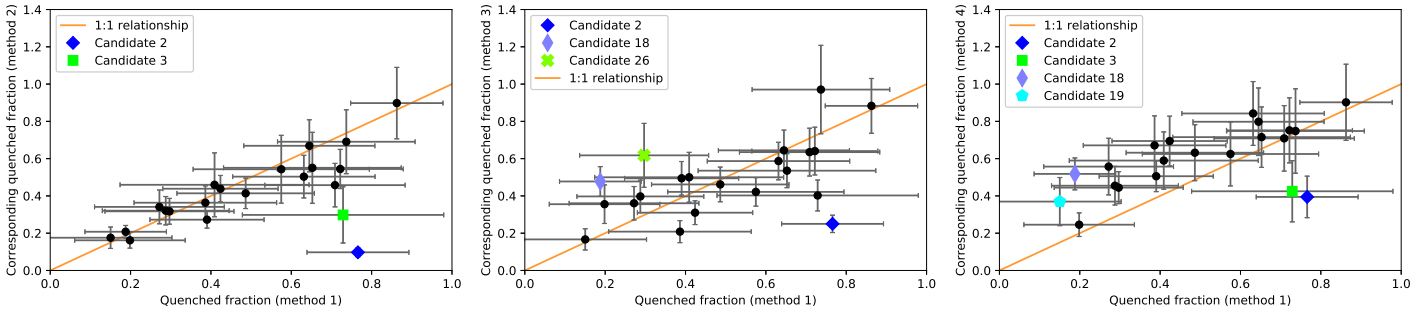

Figure 2.7: Comparison between the quenched fractions obtained by methods 1 and 2 (left panel), methods 1 and 3 (middle panel), or methods 1 and 4 (right panel). The error bars are based on the Poissonian uncertainties on the number of quenched galaxies in the cluster and on the number of galaxies in the considered field-of-view. The background uncertainty included is estimated to 5% of the unscaled background subtraction since we adjusted the subtracted background by steps of 10%. Clusters that have quenching ratios above or below 1.5 times the standard deviation of $\frac{Q_i}{Q_1}$ are highlighted.

The quenched fraction was then computed as the integral of the best-fitting red sequence Gaussian profile, divided by the sum of the integrals of the blue cloud and red sequence Gaussian profiles. Some clusters were removed from the analysis. We removed 1, 4, 10, 21, and 24 since there are indications of more than one overdensity along the line-of-sight to each of these X-ray sources. Candidate clusters at $z \geq 1.4$ were also removed, resulting in a sample of 21 candidate clusters.

Next, we investigate whether the Gaussian modelling produces consistent average star formation histories, that is whether the red sequence colour can be adequately described by a simple stellar population model. We used Flexible Stellar Population Models (FSPS; see Conroy et al. 2009; Conroy & Gunn 2010; Foreman-Macke et al. 2014), modelling the red sequence stellar population with an exponentially decreasing star formation rate characterised by an *e*-folding timescale τ, displaying solar metallicity and no dust. We generated a grid of models with two free parameters: We tested 100 formation redshifts between 4 and 16, and 100 τ values between 0.1 and 2.5 Gyr for a total of 10000 models. The model providing the best fit has a formation redshift of 16 with a characteristic time of 1.19 Gyr and a reduced $\chi^2_\nu = 0.76$, corresponding to a rejection probability of 24%. The red sequence displayed on the colour-magnitude diagram (CMD) plot in Fig. 2.2 is based on this model. The associated uncertainty is the standard deviation of the difference of red sequence colours, as predicted by the model, and the Gaussian modelling results. We also used this fit to compute the evolutionary and K-correction associated with the characteristic luminosity used in method 4.

2.4.2 Other quenching methods

The second method to identify quenched galaxies employs the same colour binning and background subtraction procedure as the one used by the Gaussian method described above. We specified the colour where the blue and red Gaussian models are equal as the boundary between the red sequence and the blue cloud. We further restricted the colour interval by rejecting any galaxy that is redder than 2.5 times the standard deviation of the red Gaussian or bluer than 2.5 times the standard deviation of the blue Gaussian. We performed a fractional calculation within the affected bins where those boundaries fall within a colour bin.

The third method does not include the area-corrected background subtraction used in the first two methods, but it instead selects cluster members based on their photometric redshift. Any galaxy within the field-of-view and with a redshift consistent with the cluster

mean redshift plus or minus 1.5 times its standard deviation (calculated in Sect. 2.2.4) is considered as a cluster member. We then selected the red sequence and blue cloud members using the colour boundaries defined in method 2.

All the methods described above employ the 5σ limit of the VIDEO catalogue in J and K_s bands as a magnitude selection threshold. The fourth quenching method is essentially the same as method 2, yet with an evolving magnitude limit based on the values of L^* in J and K_s bands computed using our best-fitting FSPS model for the red sequence, that is, including both an evolutionary and *k*-correction (see Fig. 2.6). As in Sect. 2.2.3, we assume a characteristic absolute magnitude of -22.26 at $z = 0$ (see also Cirasuolo et al. 2010).

A comparison between method 1 and the other methods is presented in Fig. 2.7. Each method generates similar quenched fractions compared to method 1. Within the limited variation of the approaches taken by each method, this indicates that the quenched fractions are robust from method to method. The few clusters for which the quenched fractions obtained by method 1 are more than 1.5 times the standard deviation above or below the mean are identified and highlighted. From now on, we focus on the results from method 4.

2.4.3 Quenching results

Figure 2.6 shows the quenched fraction results of the fourth method and indicates that there are a wide variety of quenching levels within the interval $0.8 \leq z \leq 1.2$. The wide range of computed quenched fractions is nominally consistent with the expectation expressed in Sect. 2.1 that the X-ray selection of galaxy clusters should be less biased to the properties of their member galaxies than optical and IR overdensity methods.

Next, we test, despite the range of quenched fractions, whether there is a consistent variation in the quenched fraction as a function of cluster-centric distance within the sample of clusters as a whole. We computed the quenched fraction for each cluster within three equal radial annuli out to 1.35 Mpc. We then computed the mean cluster quenched fractions as a function of the radius into two groups based upon the total quenched fraction, that is, we stacked those clusters that are quenched at the level greater than the median quenched fraction into one group and those quenched at less than the median level into another.

We then investigated if the quenched fraction depends on the galaxy luminosity. We computed the quenched fraction in three bins of J/K_s luminosities (0.5 to 1 L^*, 1 to 2 L^*, and 2 to 4 L^*). Once again, the results for each cluster were stacked on the basis of their overall quenching level. This test is limited to $z < 1.4$, because beyond this, 0.5 L^* falls below the 5σ magnitude cut.

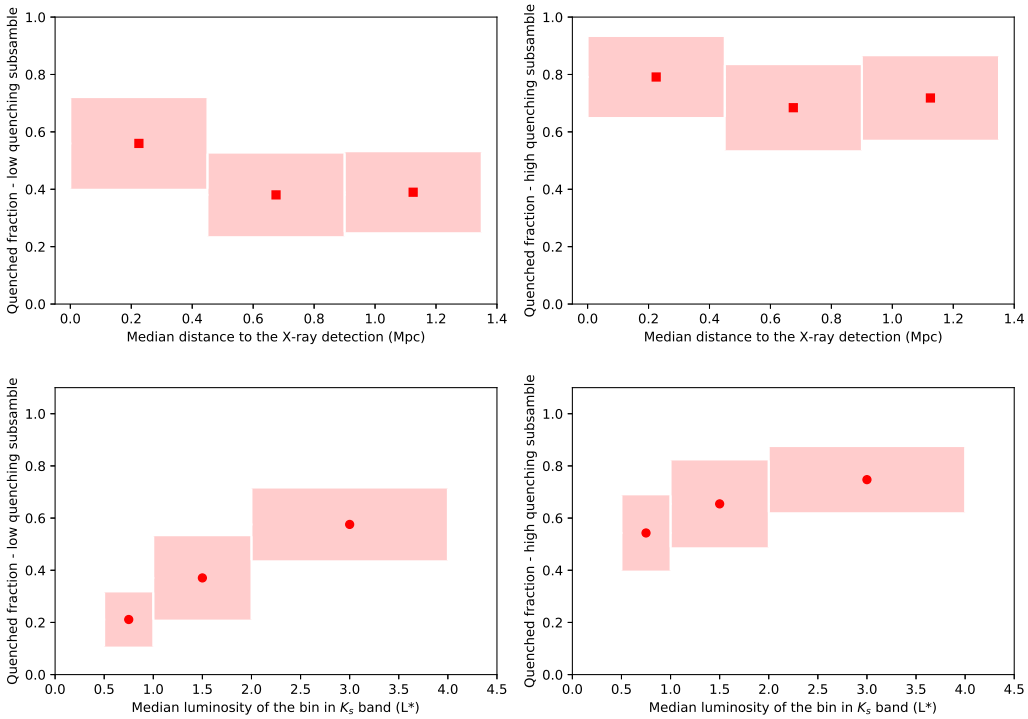

Figure 2.8: Top row: Mean quenched fraction for each distance bin, for the low quenching (left) and high quenching (right) candidate clusters. Symbols mark the mean quenched fraction, while the shaded regions represent the bin size (x axis) and the standard deviation (y axis) of the quenched fraction. Bottom row: Mean quenched fraction for each luminosity bin according to method 2/4 (method 2 is equivalent to method 4 in this context). Luminosities are expressed in terms of L^*. We stress that L^*, expressed in absolute magnitudes, changes with the redshift to reflect the passive evolution of a quenched galaxy. In the interval $0.8 \leq z < 1.4$, the absolute magnitude M^* varies from -22.87 to -23.14 in the K_s band and the corresponding stellar masses from 1.45×10^{11} $M_\odot$ to 1.47×10^{11} $M_\odot$. Again, clusters are divided into low quenching (left) and a high quenching (right) groups. These plots only include clusters below $z = 1.4$ in order to mitigate the selection effects of the catalogue 5σ limit.

Figure 2.8 displays no significant trend between the mean quenched fraction and the cluster-centric radius, especially for the highly quenched half of the sample. We note, however, a slight increase in the quenched fraction towards the centre of the lowly quenched cluster subsample, suggesting a weak dependence of the quenched fraction with the distance. The bottom panels of Fig. 2.8 show that more luminous galaxies are more quenched, although the variation is less pronounced in highly quenched clusters.

2.5 Brightest cluster galaxies

To identify candidate BCGs within each galaxy cluster, we initially noted that 80% of BCGs are located within 0.1 virial radii of the cluster's X-ray emission peak (Lin & Mohr 2004). They are usually, but interestingly not always (e.g. Lange et al. 2018), the most luminous galaxy in the cluster. We, therefore, selected galaxies within 225 kpc of the X-ray detection coordinates where this distance corresponds to approximately 15% of the virial radius of a 1×10^{14} $M_{\odot}$ cluster (we added an extra 5% to account for possible offsets between the X-ray best-fit model centres and the X-ray emission peaks). We then applied a luminosity cut to select galaxies brighter than 3 L^{*} in J and K_s bands (using the model computed in Sect. 2.4.1 to compute evolutionary effects and a full *k*-correction). If the luminosity cut resulted in less than three candidate BCGs, we extended the cut to 2.5 L^{*}. If there still remained less than three galaxies, we enlarged our search radius to 450 kpc. We implemented this three candidate limit because we noticed that some fields contained faint stars that were misclassified as galaxies or quasars in the VIDEO catalogue.

To identify spurious candidates, we subsequently performed a visual check of the BCG candidates, while paying special attention to the brightest and second brightest candidates. We also flagged, but did not remove, candidates with unreliable photometry, such as candidates within the halo of a star or blended sources. We then created $i-z$, $z-J$, and $J-K_s$ colour magnitude diagrams of the central 225 kpc of each cluster to determine which candidate BCGs possess colours that are consistent with the cluster redshift. This step also resulted in the benefit that it identified galaxies with magnitudes and colours comparable to the two most luminous candidates that might have been missed by the previous cuts. We then selected up to three potential BCGs within each cluster. In most of the clusters considered, a single BCG candidate is prominent. In cases with more than one candidate BCG, we used the K_s band luminosities to select the most likely BCG, followed by the projected cluster-centric distance if K_s band magnitudes were similar. When possible, we used the CESAM spectroscopic database to check the redshift of our selected BCG candidates and

made adjustments in the case of obvious inconsistencies with the estimated cluster redshift.

We compared our BCG list to Wen & Han (2011), XXL Paper XV, and Ricci et al. (2018, hereafter XXL Paper XXVIII), even though we have only 15, 1, and 5 clusters in common, respectively. Those three studies have slightly different BCG selection criteria: Wen & Han (2011) used the i, i^*, or the r band depending on the data available, while XXL Paper XV and XXL Paper XXVIII used z and i' band photometry as their main selection criterion, respectively. Each of them used larger search radii and, in the case of XXL Paper XXVIII, a stricter photometric redshift cut.

We found the same BCGs for 11 of the 15 shared candidates with Wen & Han (2011). When our selection disagrees, the BCG from Wen & Han (2011) is either fainter than our selected candidate (candidates 13 and 18), it possesses an incompatible spectroscopic redshift (candidate 12), or it is an obvious foreground galaxy (candidate 1). For candidate 20, which is the only candidate we have in common with XXL Paper XV, our BCG selection agrees. In the case of clusters that we have in common with XXL Paper XXVIII, four of the five common clusters have matching BCGs (candidates 3, 8, 20, and 21). For candidate 2, they selected our second-best BCG candidate, which, unlike our chosen candidate, possesses a spectroscopic redshift. However, the preferred candidate of XXL Paper XXVIII is fainter than our chosen candidate in the i, z, J, and K_s band.

As a final step, we employed FSPS to generate a suite of stellar population models, which we compared to the $J-K_s$ colours of our total sample of BCGs as a function of redshift. We tested 100 different formation redshifts between three and 16, in combination with 100 different metallicities between 0.1 and 5 $Z_\odot$. We assumed an instantaneous starburst, no dust extinction, and a Salpeter initial mass function (Salpeter 1955). We then tested the effect of including a third free parameter, using ten different formation redshifts and 50 metallicities within the same intervals as above. We first tested the effect of dust, which was calculated as a power law with a -0.7 index, with 25 dust obscuration percentages covering 0 to 99.3%. We also investigated the effect of permitting a dust-free, exponentially decreasing star formation rate (SFR) employing 25 τ values between 0.004 and 1 Gyr.

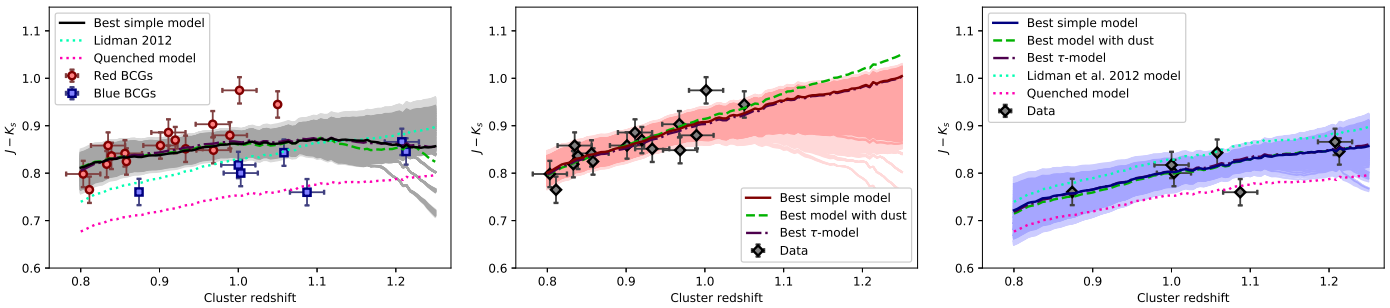

Figure 2.9: Best fits for different sub-samples. In each case, three fits were tested: A simple model, in which the metallicity and the formation redshift, assuming an instantaneous starburst, were allowed to vary; and two other models where an additional parameter was allowed to vary, which is the dust content in one case (green dashed line) or the characteristic timescale of the star formation, assuming an exponentially decreasing star formation rate, instead of an instantaneous starburst (purple dash-dotted line). For comparative purposes, we also display the best fit model of Lidman et al. (2012) and our red sequence fit on two panels (the dotted cyan and dotted magenta lines, respectively; see Sect. 2.4.1). The shaded region corresponds to the 95% confidence region for the simplest model tested and the darker zone corresponds to the 68% confidence region. Left panel: Best fits for all BCGs at $0.8 \leq z \leq 1.2$, except candidate 10 and three BCGs with known photometric problems. Red galaxies are a part of the red sample and blue galaxies are a part of the blue sample. Middle panel: Best fits for the red BCGs sub-sample. Right panel: Best fits for the blue sub-sample.

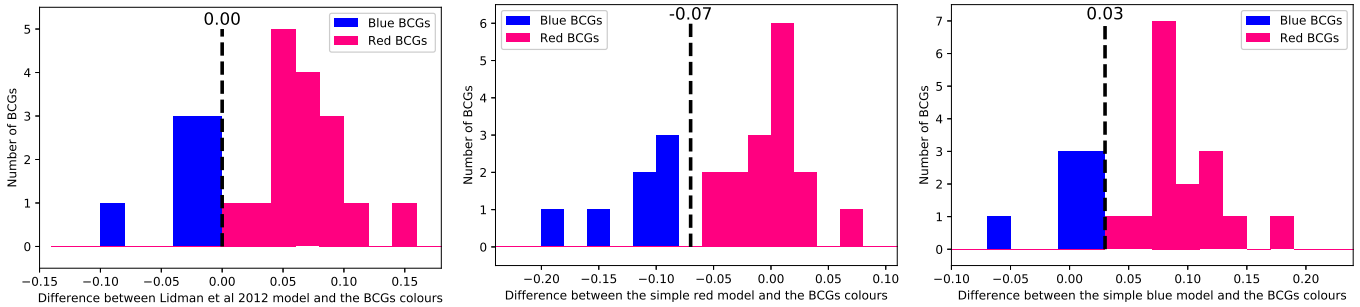

Figure 2.10: Division of the blue and red BCGs based on their colour difference with a reference model; the dashed line represents the limit between the two groups. Left: Division based on the Lidman et al. (2012) model. Middle: Assessment of our sample bimodality based on the red BCGs best fit. Right: Same as the left side, but based on the best fit of blue BCGs.

We limited the stellar population modelling to BCGs drawn from clusters in the interval $0.8 \leq z < 1.4$ and also removed BCGs with unreliable photometry. We also excluded candidate 10 because no suitable BCG candidate was identified. We thus performed our fits with a sample of 23 BCGs. The models described above generate fits that are characterised by reduced χ^2 (hereafter noted χ^2_ν), which is approximately equal to 3.5 in each case. The left panel of Fig. 2.9 presents these best fitting models and their associated confidence intervals. An examination of that figure indicates that the single model fits might well be averaging two groups of BCGs, namely a group with red $J - K_s$ colours and a comparatively bluer group. We refer to these groupings as red and blue BCGs. None of the BCGs in the blue sample are bluer than the red sequence model, which is displayed as a magenta dotted line in Fig. 2.9. This discrepancy is discussed further in Sect. 2.6.2.

We find that none of the fitted stellar population models appear to capture the overall slope of colour versus redshift for the combined BCG sample. However, we noted with interest that the stellar population model of Lidman et al. (2012) appears to provide an effective method to segregate the red and blue BCGs. We therefore segregated the red and blue BCGs by employing the colour difference with respect to the Lidman et al. (2012) model colours as a function of redshift (see Fig. 2.10, left panel). Having split the BCGs into red and blue on the basis of this criterion, we then applied the FSPS fitting procedure described above to both populations and performed a final check of the BCG colour evolution versus redshift with respect to the best-fitting red and blue models (Fig. 2.10, centre and right panels). All three approaches generate the same division between red and blue BCGs.

Table 2.2: Summary of the stellar population fits obtained for the red BCGs.

Fit	χ^2_ν	z_0	Dust absorption[a] (%)	Metallicity ($Z_\odot$)	τ[b] (Gyr)
No dust, varying z_0 and Z	1.140	14.214	0	1.44	0
Varying z_0, Z, and dust	1.155	11.030	61.28	0.40	0
No dust, varying z_0, Z, and τ	1.250	11.030	0	1.40	0.010

[a] Fraction of starlight absorbed by dust.
[b] Characteristic timescale for an exponentially decreasing star formation rate.

Treating the red and blue BCGs as separate populations provides a significant improvement to the quality of the stellar population fits (see Fig. 2.9, middle and right panels). Tables 2.2 and 2.3 give the χ^2_ν and best parameter fits for every model tested. The uncertainties are based on the 1σ photometry errors. Despite relatively good χ^2_ν (1.140 for the simplest model), none of the red BCG fits seem to be able to capture the slope of the J-K_s

Table 2.3: Summary of the stellar population fits obtained for the blue BCGs.

Fit	χ^2_ν	z_0	Dust absorption[a] (%)	Metallicity ($Z_\odot$)	τ^b (Gyr)
No dust, varying z_0 and Z	1.497	4.426	0	1.24	0
Varying z_0, Z, and dust	1.920	3.613	6.67	1.10	0
No dust, varying z_0, Z, and τ	1.954	5.241	0	1.20	0.317

[a] Fraction of starlight absorbed by dust.
[b] Characteristic timescale for an exponentially decreasing star formation rate.

colours of the high-redshift half of the sample. Both the simple and dusty models perform similarly, but the plausibility of the latter seems questionable since it features a starlight dust absorption percentage of 61% (assuming grey dust).

For the blue BCGs, there is no visible slope discrepancy between the data and the model. However, the χ^2_ν are larger than in the case of red BCGs, which is probably because none of the applied models include a term for intrinsic scatter. In fact, the 95% confidence interval of the simplest model, which also has the minimum χ^2_ν, is barely spawning the variety of colours observed in the blue BCGs. This may indicate that the blue BCG population is too diverse to be represented by a single stellar population model.

Nevertheless, we computed the BCG stellar masses for the red and the blue BCGs, using the parameters from the simple model (i.e the instantaneous starburst model with no dust). We adopted a similar approach as in Lidman et al. (2012) by computing the mass as the quotient between the observed and the modelled flux density in the K_s band, correcting with the model stellar mass. To estimate the uncertainties, we computed the K_s band fluxes of every model enclosed in the 68% χ^2 confidence region. We then considered their standard deviation as the uncertainty on the flux and propagated this error to the mass.

The results are presented in Tables 2.4 and 2.5. The mean masses are $5 \pm 1 \times 10^{11}$ $M_\odot$ and $2.8 \pm 0.6 \times 10^{11}$ $M_\odot$ for the red and blue BCGs, respectively.

2.6 Discussion

2.6.1 Cluster quenched fractions

Figure 2.7 presents a wide variety of quenched fractions, with no clear trend; despite this, only the most luminous (massive) galaxies are visible at higher redshifts. The fourth method of computing the quenched fraction incorporates a luminosity cut specifically intended to mitigate this bias. However, although this method generates slightly higher

Table 2.4: Positions and stellar masses of the red BCGs.

#	Candidate name	BCG RA & Dec (degrees)	z	BCG stellar masses (10^{11} $M_{\odot}$)
1	3XLSS J022222.9-044043	35.5854 -4.6857	0.80[a]	2.6 ± 0.4
2	XLSSC 184	35.3169 -4.2079	0.81	3.5 ± 0.6
3	XLSSC 071	35.6420 -4.9655	0.83	7 ± 1
4	3XLSS J022432.9-044742	36.1398 -4.7940	0.83[a]	4.6 ± 0.8
5	3XLSS J022135.2-051811	35.3985 -5.3052	0.84	5.6 ± 0.9
6	XLSSU J021947.4-050841	34.9458 -5.1399	0.86[a]	6 ± 1
7	XLSSC 15	35.9273 -5.0336	0.86	8 ± 1
9	3XLSS J022557.1-042845	36.4802 -4.4804	0.90[a]	3.8 ± 0.7
11	3XLSS J021945.5-044831	34.9362 -4.8124	0.91[a]	5 ± 1
12	XLSSU J022530.3-042544	36.3738 -4.4295	0.92	4.1 ± 0.8
13	3XLSS J022804.6-045351	37.0203 -4.9056	0.93[a]	7 ± 1
14	XLSSU J022051.0-050958	35.2108 -5.1620	0.97[a]	8 ± 2
15	3XLSS J022103.0-045524	35.2634 -4.9222	0.97[a]	3.4 ± 0.7
16	3XLSS J022739.0-045830	36.9073 -4.9698	0.99[a]	3.9 ± 0.8
18	XLSSC 044	36.1345 -4.2287	1.00[a]	6 ± 1
20	XLSSC 029	36.0175 -4.2240	1.05	6 ± 1

[a] Photometric redshift. The uncertainties are ± 0.02.

Table 2.5: Positions and stellar masses of the blue BCGs

#	Candidate name	BCG RA & Dec (degrees)	z	BCG stellar masses (10^{11} $M_{\odot}$)
8	XLSSC 064	34.6335 -5.0165	0.87	2.6 ± 0.5
17	3XLSS J022044.7-041713	35.1953 -4.2900	1.00[a]	2.5 ± 0.5
19	XLSSC 124	34.4272 -4.8658	1.00[a]	3.7 ± 0.8
21	XLSSC 005	36.7872 -4.2988	1.06	2.0 ± 0.4
23	3XLSS J022027.0-043538	35.1173 -4.6041	1.09[a]	3.7 ± 0.8
25	XLSSC 141	34.3478 -4.6696	1.21[a]	1.6 ± 0.4
26	XLSSC 046	35.7636 -4.6043	1.21	3.7 ± 0.9

[a] Photometric redshift. The uncertainties are ± 0.02.

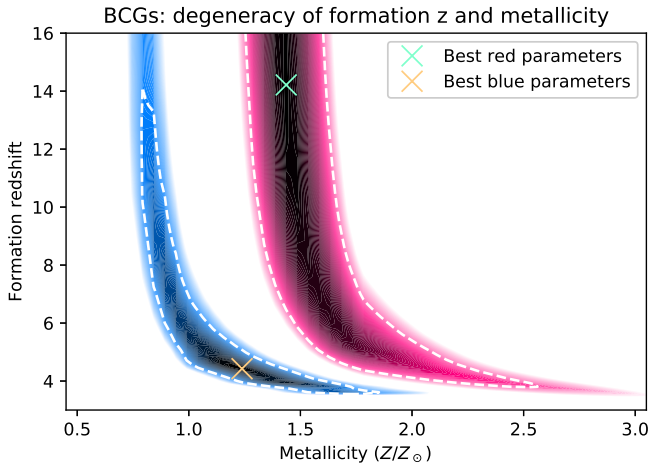

Figure 2.11: Contour plots for the red and blue BCG sub-samples showing the χ^2_ν value as a function of the two varying parameters (formation redshift and metallicity). Dashed white curves correspond to the 68% confidence limit. The coloured regions correspond to the 98% confidence interval. The tested metallicity range is $Z = 0.1\ Z_\odot$ to $Z = 5\ Z_\odot$, but here it is restricted to $Z = 0.5\ Z_\odot$ to $Z = 3.5\ Z_\odot$. The tested formation redshift range is $z_{form} = 3$ to $z_{form} = 16$. The cross displays the location of the best fit parameters.

quenched fractions (except for the two lowest redshift clusters in our sample; see Fig. 2.7), it does not otherwise affect the apparent diversity of quenched fractions. There is thus no evidence of evolution with redshift in Fig. 2.6.

The results presented in Sect. 2.4.3 demonstrate a link between the quenched fraction and the K_s band luminosity, although the link seems weaker for the highly quenched half of our sample. The K_s band luminosities are a proxy for galaxy stellar masses, assuming dust extinction is negligible. This type of link has been observed before (e.g. Peng et al. 2010, 2012; Muzzin et al. 2012; Balogh et al. 2016; Kawinwanichakij et al. 2017; Jian et al. 2018; Pintos-Castro et al. 2019); however, whether this is due to mass-dependent galaxy evolution and/or to the environment remains an open question.

We observe no significant evidence that the quenching fraction varies with the cluster-centric distance, although the quenched fraction is slightly higher towards the centre of the lowly quenched clusters in our sample – an observation that is in agreement with previous studies (e.g. Muzzin et al. 2012; Pintos-Castro et al. 2019). The more quenched half of our sample possesses levels of quenching above 70% in all bins, which might be because only galaxies above L^* are included in this profile and since bright galaxies tend to be slightly more quenched at all radii.

2.6.2 Potential bimodal brightest cluster galaxy population

The $J - K_s$ colours of the candidate BCGs in the distant cluster sample are not consistent with the properties of a single, passively-evolving stellar population. There is tentative evidence for a bimodal distribution of BCG colours. In separating the sample employing the fiducial stellar population model of Lidman et al. (2012), we find that the colours of the redder BCGs in our sample are consistent with an older, instantaneous burst of metal-rich stars, whereas the bluer BCG colours are more diverse and they are possibly related to a younger component in the stellar population.

Despite the variety of colours, only one of the BCGs is bluer than the red sequence model computed in Sect. 2.4.1 (see also Fig. 2.9). This might indicate that BCG stellar populations have different properties (such as metallicity) than the average quenched galaxies in the cluster, as suggested by some low-redshift studies (e.g. Von Der Linden et al. 2007; Loubser et al. 2009).

Figure 2.11 shows the degeneracy between metallicity and formation redshift as applied to the stellar population models describing the two BCG samples. We observe that the 98% confidence regions of the two BCG samples do not overlap, supporting the idea that the stellar populations of the blue and red BCGs are indeed different. The confidence intervals for the blue sample are centred on lower metallicities than the red sample regions, while formation redshift also tends to be lower; although, the confidence regions of both models extend over a wide range of redshifts.

Based on the stellar population analysis, one might infer that blue BCGs have formed more recently than the red ones. However, Li & Han (2007) reported that when more than one stellar population is present, the age and metallicity obtained by colours alone might be biased towards the younger and more metal-rich stars. Therefore, the blue BCGs might be bluer because they have experienced either an extended star formation episode or more than one bursts in the past. In these types of scenarios, differences in the duration of the star formation or in the relative importances and epochs of the secondary bursts would account for the spread in colour observed in the bluer BCGs.

One factor that may trigger a star formation episode is a cooling flow. Several studies have reported the existence of blue, moderately star-forming BCGs in cool-core clusters at low to moderate redshifts (e.g. Egami et al. 2006; Bildfell et al. 2008; Stott et al. 2008; Loubser et al. 2009, 2016; Pipino et al. 2009; Rawle et al. 2012; Green et al. 2016). Since X-ray selected clusters are biased towards relaxed clusters (Rossetti et al. 2017), this might partially explain why the blue BCGs represent a significant part of our sample.

Alternatively, statistical studies based on IR- (e.g. Webb et al. 2015b; Bonaventura et al. 2017) or SZ-selected clusters (e.g. McDonald et al. 2016) have shown that in-situ star formation is an important mechanism at $z \gtrsim 1$, which is possibly triggered by galaxy interactions (McDonald et al. 2016). This suggests that a range of BCG colours might be a part of every high-redshift sample, regardless of the sample selection.

One limitation of the current analysis is that the fitted stellar population models are unable to accommodate the slope of the high-redshift end of the red sample J-K_s colour variation with redshift (see Fig. 2.9) and that no BCGs are red beyond $z = 1.05$. This suggests that the stars making up the red BCGs formed later or evolve faster than predicted by our model. The former is supported by the degeneracy between formation redshift and metallicity. The best-fitting formation redshift, $z_{form} \sim 12$, might be considered high compared to the predictions of the most recent simulations (e.g. Ragone-Figueroa et al. 2018; Rennehan et al. 2020); however, it is consistent with recent observations (Hashimoto et al. 2018; Willis et al. 2020).

Dust extinction might be evoked to explain why these objects are so red. Indeed, a fit including dust provides an equivalent statistical description of the red BCGs (see Table 2.2), although we note that the colour of a model stellar population is degenerate between the star formation history, metallicity, and dust obscuration. For this reason, we prefer a simple, dust free model for the analysis of the red BCG population.

Ultimately, the current data available for the BCGs sample are unable to provide a definitive explanation as to the blue and red dichotomy. The acquisition of rest-frame optical spectroscopy of several BCGs of both groups is needed in order to get a more accurate and thorough picture of the star formation history of these objects (e.g. Lonoce et al. 2015, 2020; Belli et al. 2017; Saracco et al. 2019).

2.7 Summary

We have identified a sample of 35 X-ray-selected distant galaxy clusters in the XXL-N/VIDEO field and performed a preliminary analysis of their galaxy populations. Clusters were selected as extended X-ray sources (C1, C2, or AC) coincident with overdensities of bright galaxies in photometric redshift space. Of the 35 candidate clusters at $z_{phot} \geq 0.8$, ten are spectroscopically confirmed clusters, and a further 15 are presented here for the first time. The ten remaining clusters have been detected previously but never confirmed.

The sample of clusters displays a wide variety of quenched fractions, a result that is nominally consistent with the assertion made in Sect. 1 that selecting clusters on the ICM

properties is insensitive to the star formation history of their member galaxies. The relationship between the galaxy luminosity and quenched fraction appears to be in place at $z \sim 1$, although we do not observe a significant variation in the quenched fraction with the cluster-centric radius.

The sample of BCGs is inconsistent with a single stellar population model. The observed distribution is bimodal in colour and is consistent with an old, passive population and a possibly younger, relatively bluer, and more diverse population. Although we are unable to provide a definite explanation for this split, we suggest that the blue BCGs may have experienced either an extended or more than one star-formation episode.

Acknowledgements

AT is supported by the Natural Sciences and Engineering Research Council of Canada (NSERC) Postgraduate Scholarship-Doctoral Program. JPW acknowledges support from the NSERC Discovery Grant program. The Saclay group acknowledges long-term support from the Centre National d'Etudes Spatiales (CNES). This work was supported by the Programme National Cosmology et Galaxies (PNCG) of CNRS/INSU with INP and IN2P3, co-funded by CEA and CNES. NA acknowledges funding from the Science and Technology Facilities Council (STFC) Grant Code ST/R505006/1. RAAB is supported by the Glasstone Foundation, MJJ and RAAB acknowledge support from the Oxford Hintze Centre for Astrophysical Surveys which is funded through generous support from the Hintze Family Charitable Foundation and the award of the STFC consolidated grant (ST/N000919/1). XXL is an international project based around an XMM Very Large Programme surveying two 25 deg^2 extragalactic fields at a depth of $\sim$ $6 \times 10{-}15$ erg cm^{-2} s^{-1} in the [0.5-2] keV band for point-like sources. The XXL website is `http://irfu.cea.fr/xxl`. Multiband information and spectroscopic follow-up of the X-ray sources are obtained through a number of survey programmes, summarised at `http://xxlmultiwave.pbworks.com/`. This work is based on data products from observations made with ESO Telescopes at the La Silla Paranal Observatory under ESO programme ID 179.A- 2006 and on data products produced by the Cambridge Astronomy Survey Unit on behalf of the VIDEO consortium. This research has made use of the NASA/IPAC Extragalactic Database (NED), which is funded by the National Aeronautics and Space Administration and operated by the California Institute of Technology.

Notes on individual objects

Candidate 1/24

Candidate 1/24 was observed by Gemini South in 2010 and classified as a distant cluster (John Stott, personal communication), but, to our knowledge, the results were never published. We observed two spikes in the photometric redshift space of this source, one at $z_{phot} = 0.80 \pm 0.02$ and one at $z_{phot} = 1.19 \pm 0.02$. Furthermore, the X-ray emission associated with this detection is complex with several brighter spots. This suggests that there might be two distant clusters in the same line-of-sight.

Candidate 5

The BCG of this $z = 0.84$ cluster has a possible companion that is 0.454 magnitudes less luminous in the K_s band. The optical centre of both galaxies lie at a projected separation of 58.2 kpc (7.48 arcsec). The projected separation between the BCG and the X-ray coordinates is 27.4 kpc and 43.6 kpc for the companion. Neither the BCG nor the companion exhibit signs of interactions. We were able to confirm this cluster with archival spectroscopic observations stored in the CESAM database (XXL Paper XX).

Candidates 6 and 27

Both candidates 6 and 27 are faint detections (compared to the other X-ray sources discussed in this Chapter) in the vicinity of bright point sources. Thus, in these two fields, we increased the number of X-ray contours from 10 to 25. Candidate 6 is at $z = 0.86 \pm 0.02$ and candidate 27 is at $z = 1.44 \pm 0.14$.

Candidate 10

Despite appearing as an isolated spike in the redshift space, candidate 10 seems to be constituted of two or more overdensities: The background subtracted colour diagram of candidate 10 exhibit four 'bumps' rather than two. Similarly, none of our BCG candidates seem reliable: The best one exhibits a very red J-K_s colour, which is more consistent with $z \sim 1$ than $z \sim 0.9$ and indeed has a photometric redshift of z 0.98. The two other BCG candidates both sit at more than 750 kpc of projected separation with the X-ray coordinates. Since candidate 10 meets our detection criteria, we included it in our list of candidate clusters, but not in our analysis.

Candidate 30

Candidate 30 has a photometric redshift of 1.48 ± 0.14, which makes it one of our newly discovered, very high-z clusters. Unfortunately, the photometry of the BCG and of another central galaxy are unreliable because they are in the halo of a foreground star.

Candidate 33

Among the candidate clusters presented here for the first time, candidate 33 is probably the second most distant one, with a photometric redshift of 1.79 ± 0.14. This is again a robust (significance between 4.5 and 5.5 galaxies) detection in the photometric space. X-ray emission is regular, and the distance between its coordinates and the BCG is 60.8 kpc. The BCG is extremely red: Its Z-J and J-K_s colours are 2.45 and 1.59, respectively, while the mean colours of the other $z \gtrsim 1.5$ BCGs with reliable photometry (i.e. excluding candidate 31) are 1.45 and 0.90. Interestingly, the i-z colour discrepancy between candidate 33 and the other high-z BCGs is smaller in i-z: 0.88 for candidate 33 compared to 0.63. These types of colours might originate from the presence of dust in this object, but more data are needed to confirm this.

Candidate 35

This candidate cluster is probably the farthest object in our sample, with a photometric redshift of 1.93 ± 0.14. This X-ray detection is associated with multiple spikes in the photometric redshift space. Since the photometric redshift does not perform very well at $z \sim 2$, some of these spikes might be associated with the main overdensity. However the presence of a significant spike at $z \sim 1$ suggests the presence of at least another overdensity along the line-of-sight.

Other candidate clusters at $z \gtrsim 1.4$

There are four other new candidate clusters at $z \gtrsim 1.4$ in our sample: candidates 28, 29, 31, and 32 sitting at redshifts of 1.45 ± 0.14, 1.48 ± 0.14, 1.54 ± 0.14, and 1.57 ± 0.14. Candidate 32 is a weaker X-ray detection than the three others, but it also features the most significant photometric redshift spike.

Candidate clusters

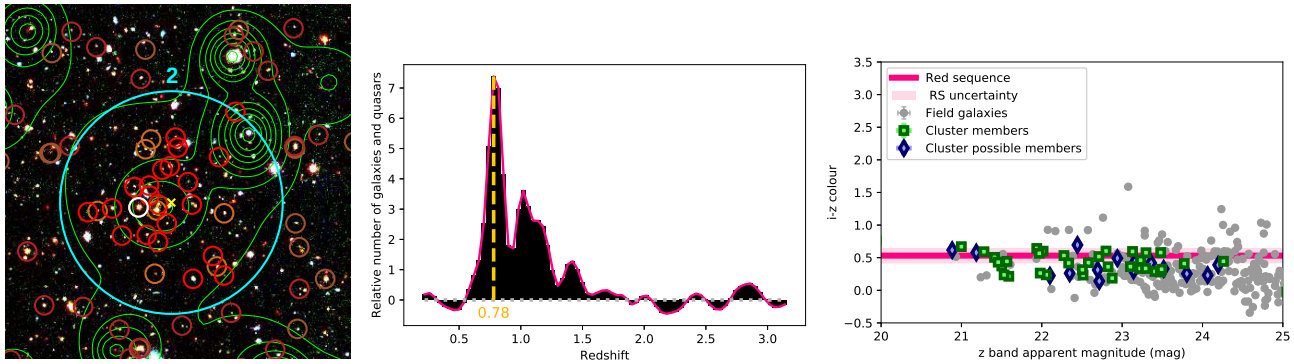

Figure 2.12: Left columns: Megacam R and I filter and VIDEO H filter images for each confirmed cluster at $z \geq 0.8$ meeting our selection criteria, classified by increasing redshifts. The cyan circles delimit regions within 1 arcmin of the X-ray best fit model centres, which are marked by yellow crosses. The red and brown circles highlight the bright galaxies with a redshift corresponding to the cluster peak redshift ± 0.02 and to the cluster redshift ± 0.06, respectively. Darker circles indicate the galaxies outside of the central region. The BCGs are circled in white. The X-ray contours in green are logarithmically distributed in ten levels between the maximum and minimum emission observed in a 7×7 arcmin^2 box around the X-ray source. Middle columns: Background subtracted and Gaussian filtered redshift distribution of the bright galaxies within the central arcmin, for the corresponding candidates. The dashed line highlights the median redshift of the highest bin in the redshift spike. Its colour assesses the importance of the overdensity and, therefore, our confidence in the detection: gold for the most reliable candidates (the highest bin height is above 5.5), grey for the reliable one (above 4.5), and beige for the other. Right columns: i-z ($0.8 \leq z < 1.2$) or z-J ($z \geq 1.2$) CMD plot of the galaxies above the VIDEO 5σ limit within 1 arcmin of the centre. The green squares indicate the galaxies with photometric redshifts that are consistent with the mean redshift plus or minus 1.5 times the standard deviation of the most accurate Gaussian modelling of the redshift spike. The blue lozenges indicate the galaxies with redshifts that are consistent with the sidewings of the most accurate Gaussian model, up to three times the standard deviation. The deep pink lines indicate the colours predicted by the stellar population model computed in Sect. 2.4.1. The light pink region is the standard deviation of the difference of this model with method 1 red sequences.

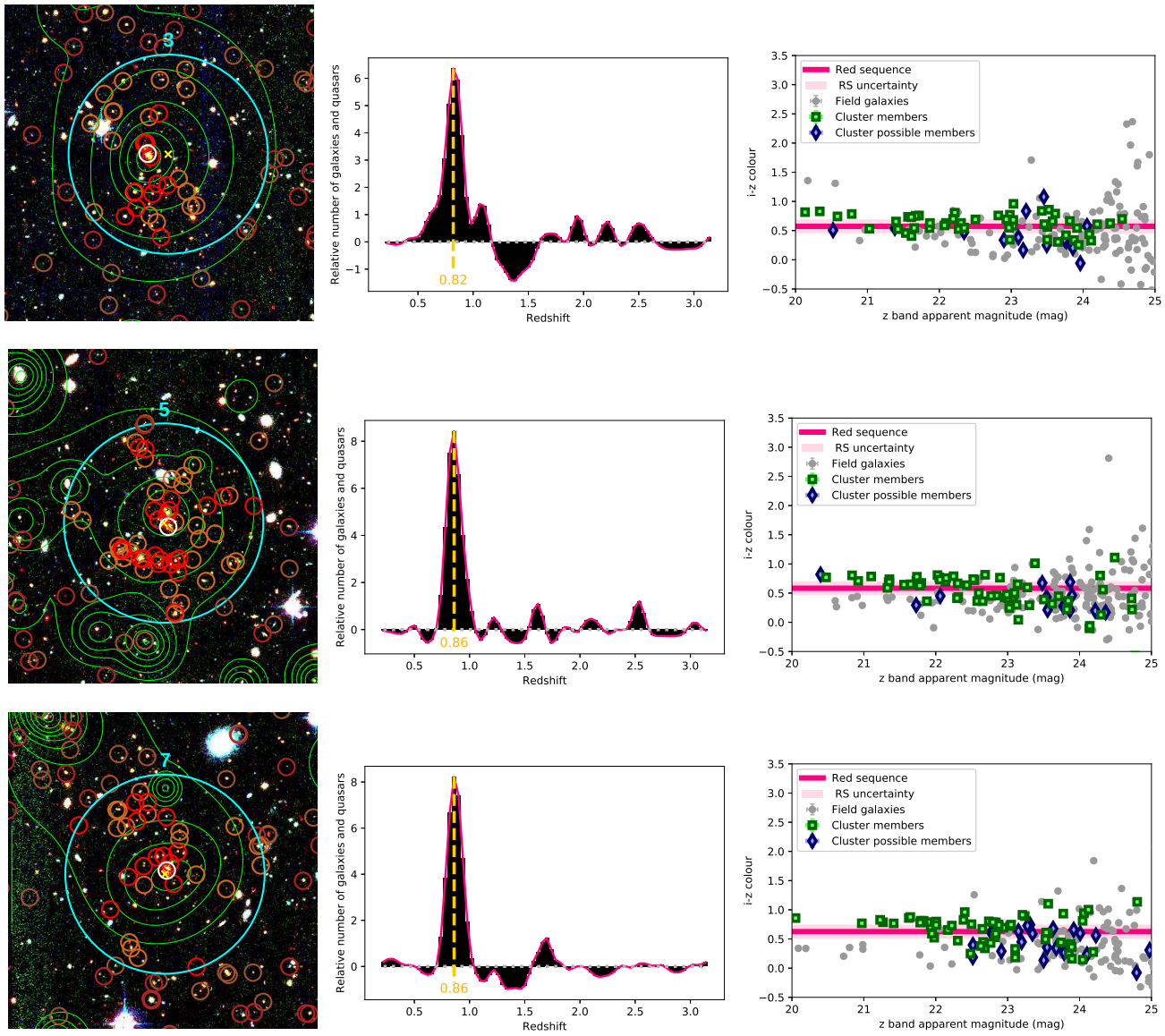

Figure 2.12: *continued*

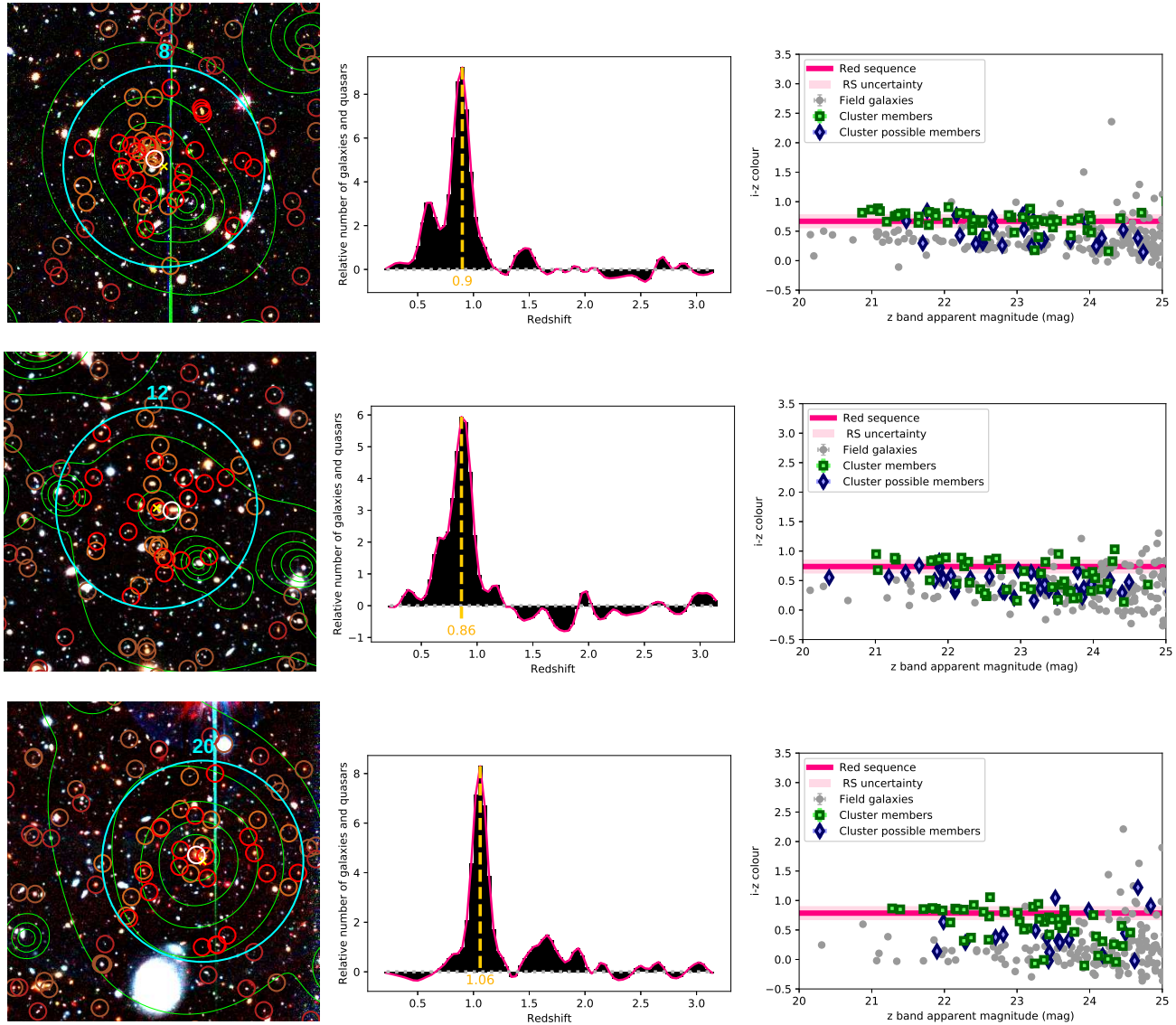

Figure 2.12: *continued*

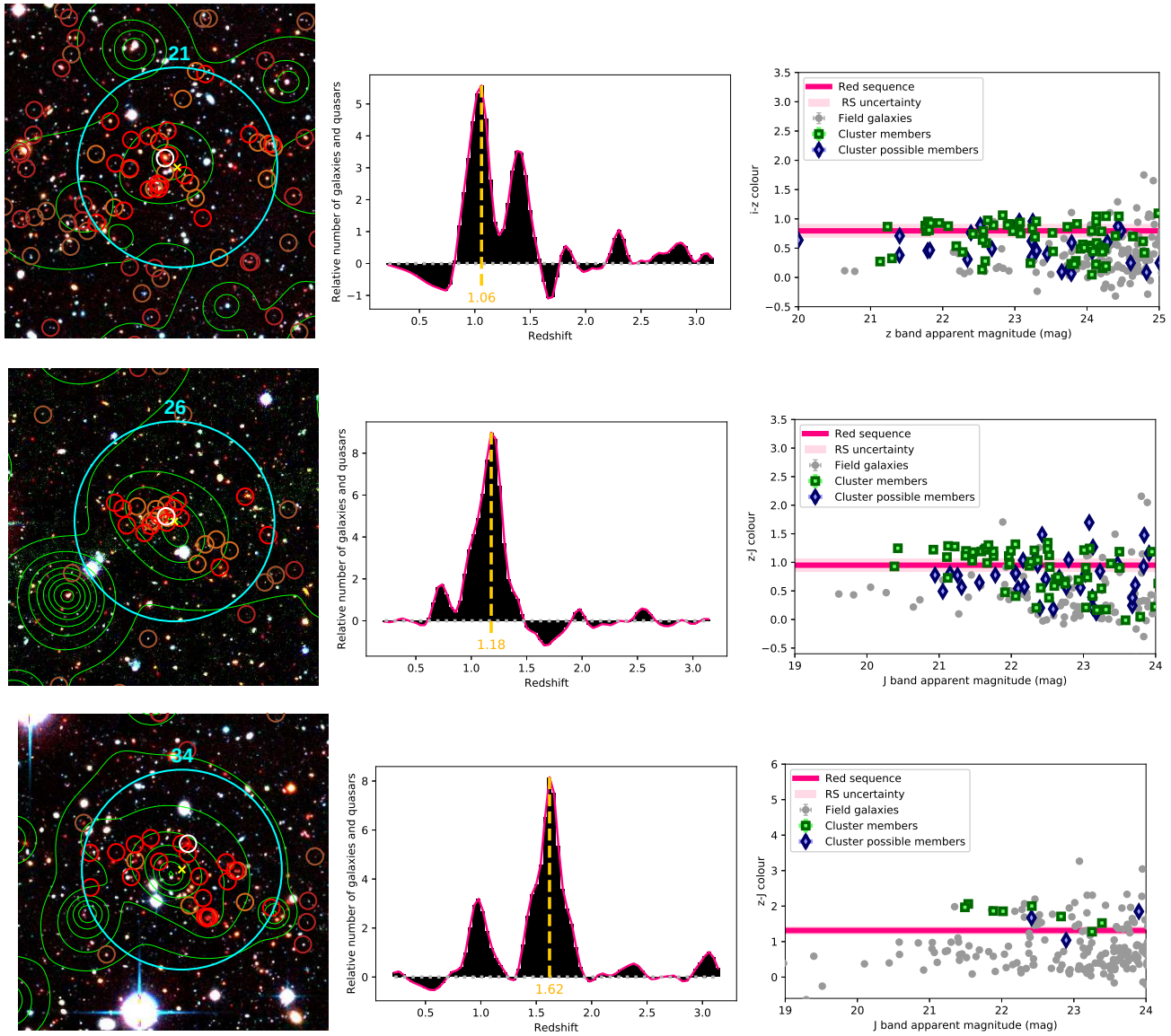

Figure 2.12: *continued*

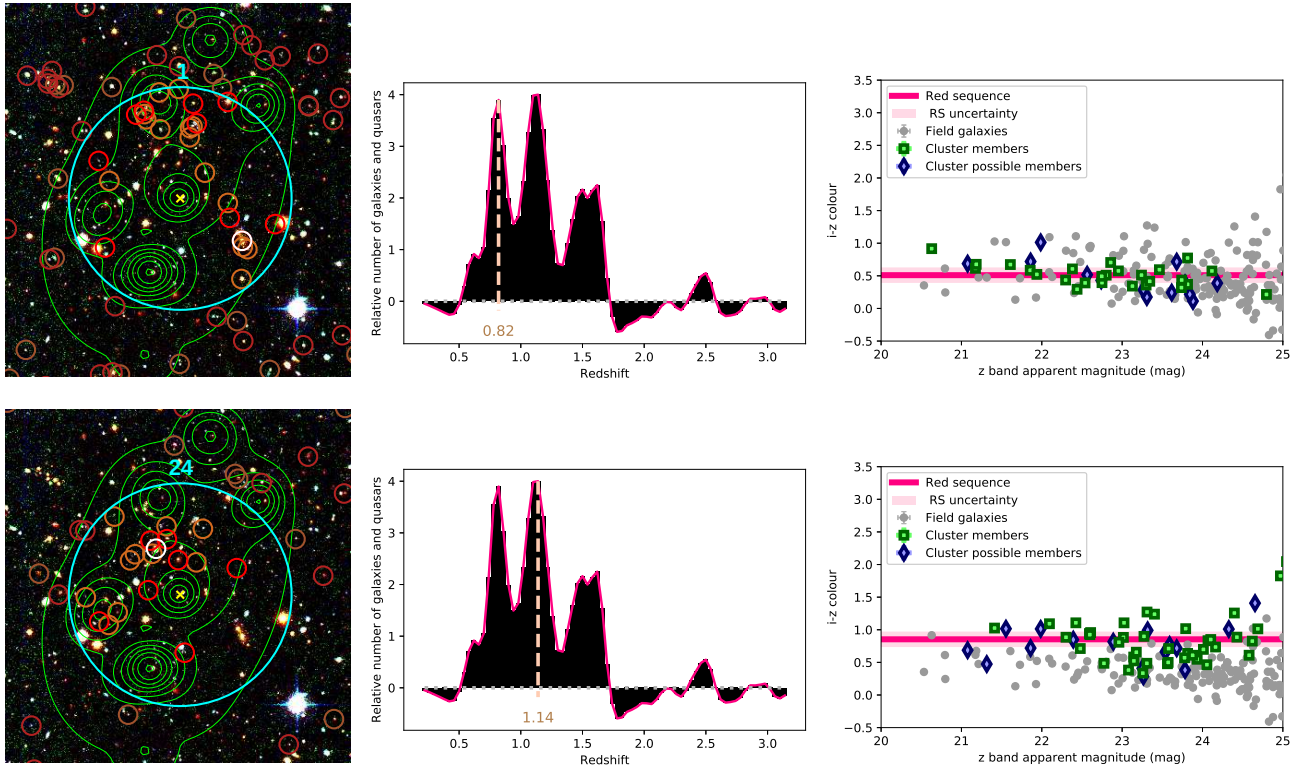

Figure 2.13: Left columns: Megacam R and I filter and VIDEO H filter images for the two candidate clusters along the same line-of-sight. Definitions of symbols and contours are given in Fig. 2.12. Middle columns: Background subtracted and Gaussian filtered redshift distribution of the bright galaxies within the central arcmin for the corresponding candidates. Bottom columns: i-z ($0.8 \leq z < 1.2$) or z-J ($z \geq 1.2$) CMD plot of the galaxies above the VIDEO 5σ limit within 1 arcmin of the centre.

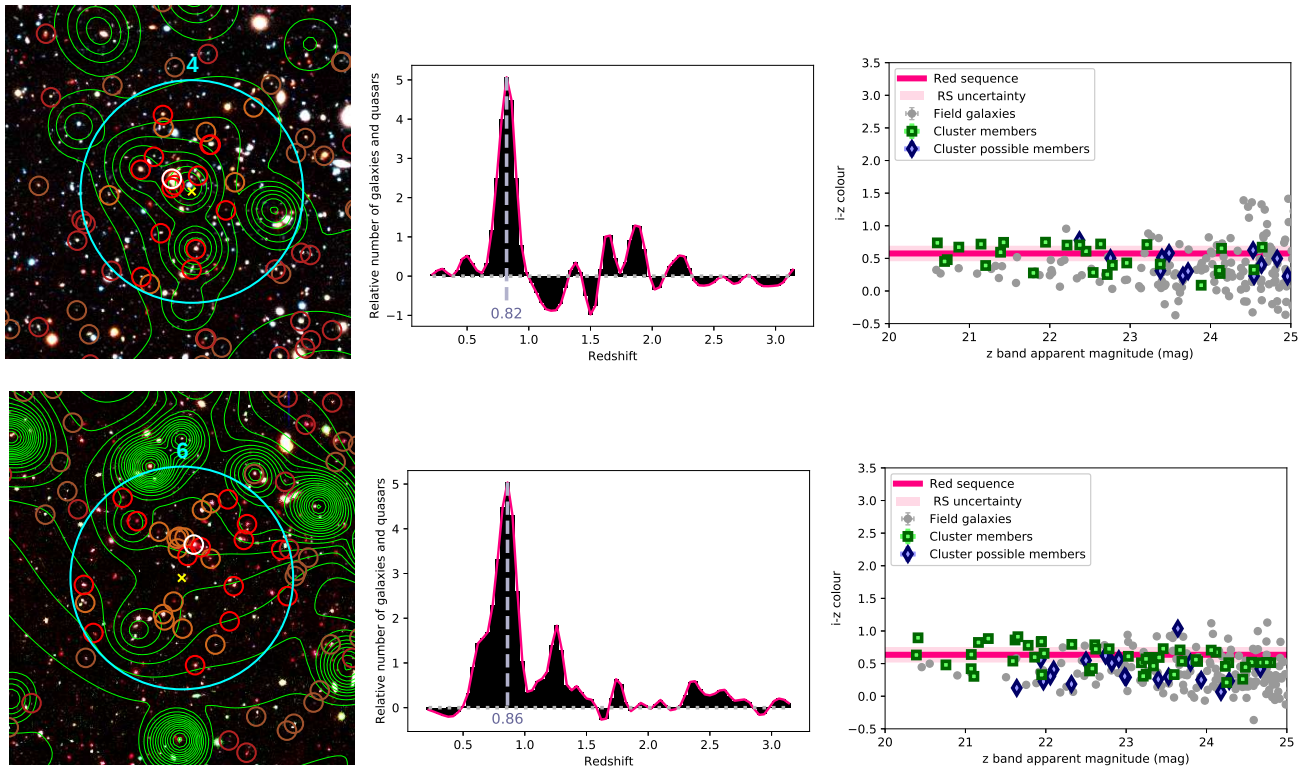

Figure 2.14: Left columns: Megacam R and I filter and VIDEO H filter images for the previously detected but unconfirmed candidate clusters at $z \geq 0.8$, which are classified by increasing redshifts. The X-ray contours in green are logarithmically distributed in ten levels between the maximum and minimum emission observed in a 7×7 arcmin^2 box around the X-ray source, except for candidate 6 which displays 25 levels based on a 4×4 arcmin^2 box. Definitions of symbols are given in Fig. 2.12. Middle columns: Background subtracted and Gaussian filtered redshift distribution of the bright galaxies within the central arcmin for the corresponding candidates. Bottom columns: i-z ($0.8 \leq z < 1.2$) or z-J ($z \geq 1.2$) CMD plot of the galaxies above the VIDEO 5σ limit within 1 arcmin of the centre.

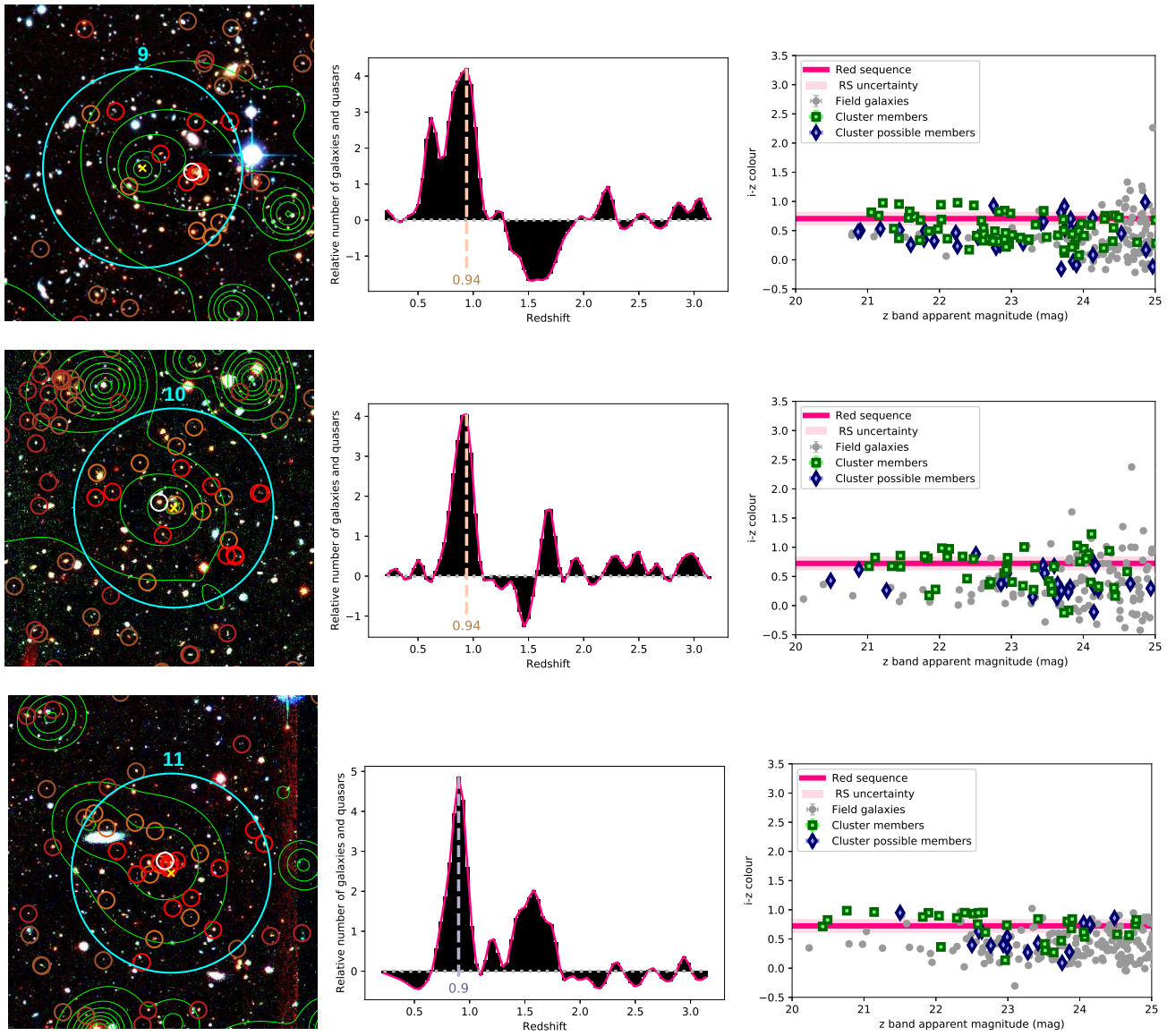

Figure 2.14: *continued*

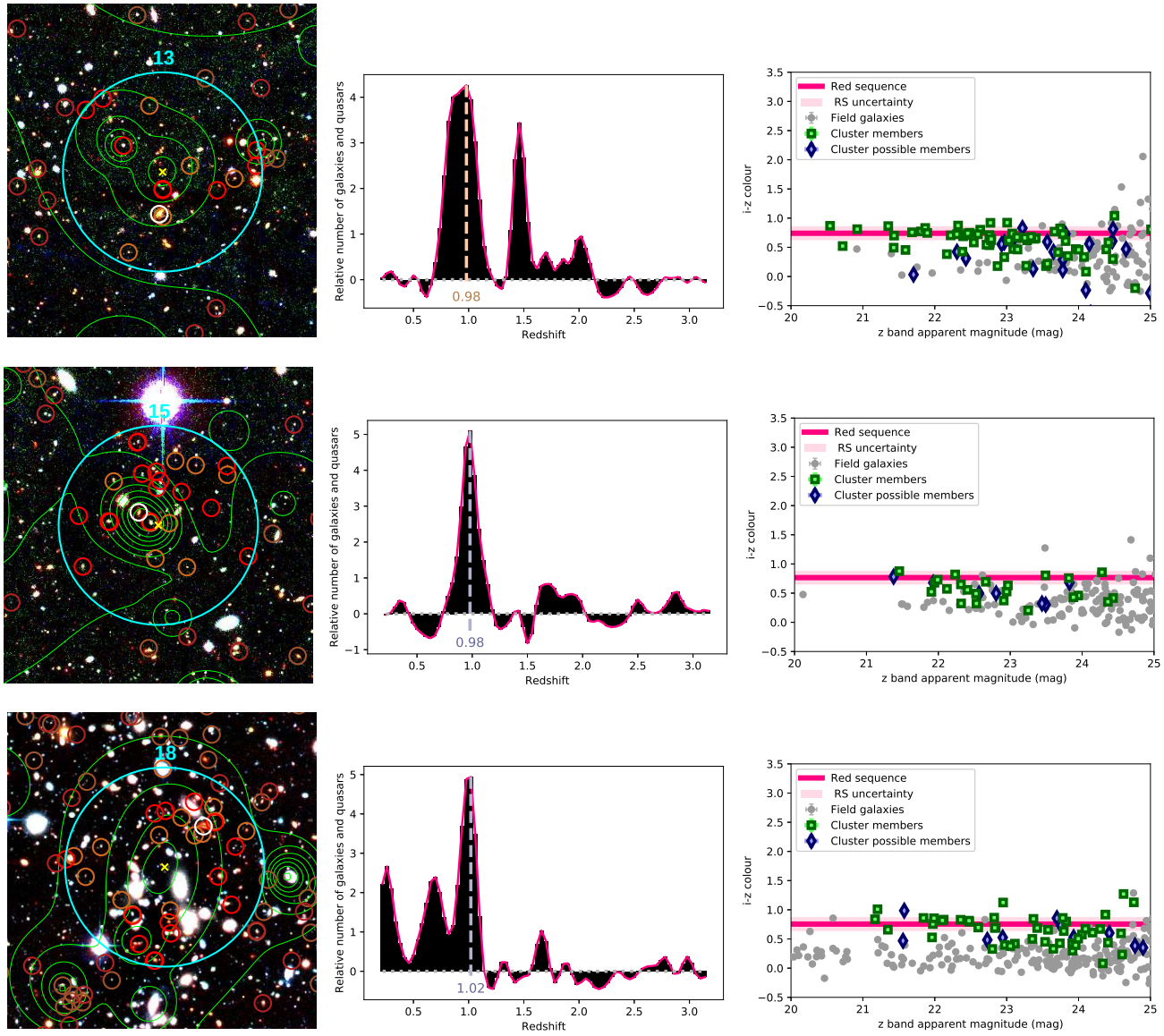

Figure 2.14: *continued*

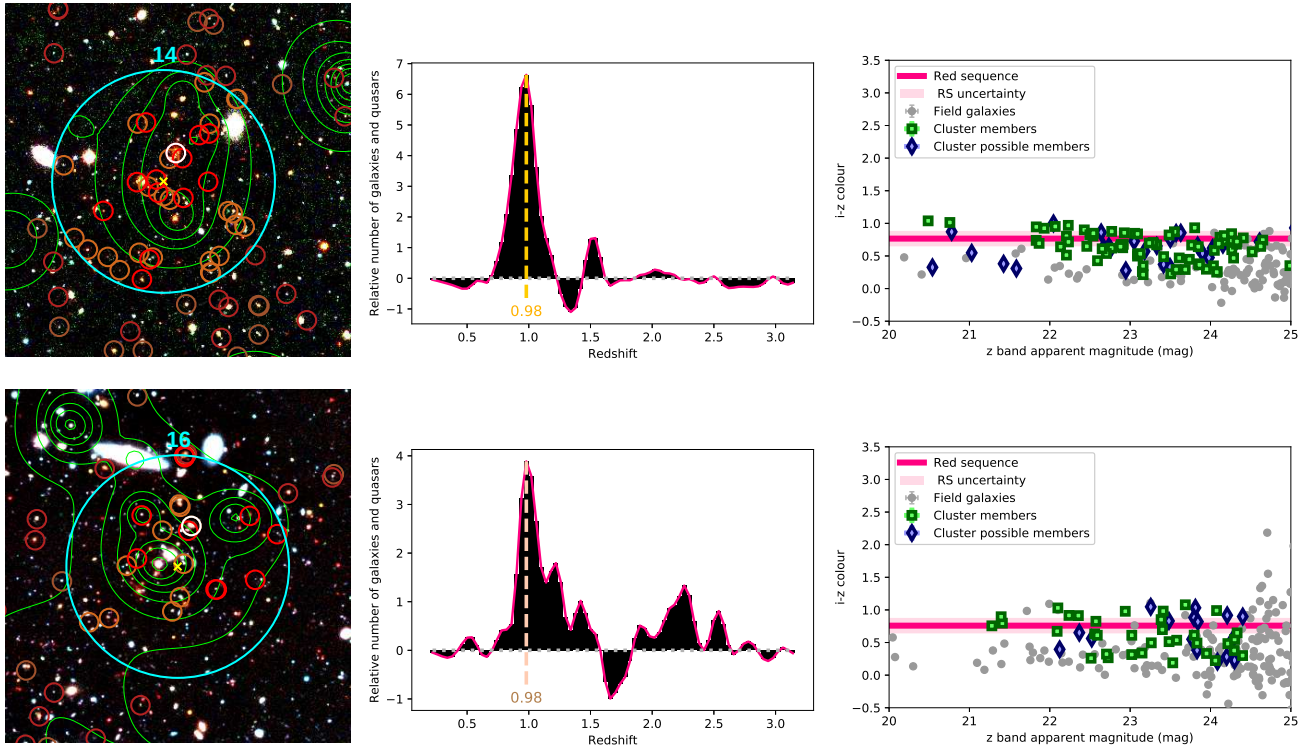

Figure 2.15: Left columns: Megacam R and I filter and VIDEO H filter images for the new candidate clusters at $z \geq 0.8$, which are classified by increasing redshifts. The X-ray contours in green are logarithmically distributed in ten levels between the maximum and minimum emission observed in a 7×7 arcmin^2 box around the X-ray source, except for candidate 27 which displays 25 levels based on a 4×4 arcmin^2 box. Definitions of symbols are given in Fig. 2.12. Middle columns: Background subtracted and Gaussian filtered redshift distribution of the bright galaxies within the central arcmin for the corresponding candidates. Bottom columns: i-z ($0.8 \leq z < 1.2$) or z-J ($z \geq 1.2$) CMD plot of the galaxies above the VIDEO 5σ limit within 1 arcmin of the centre.

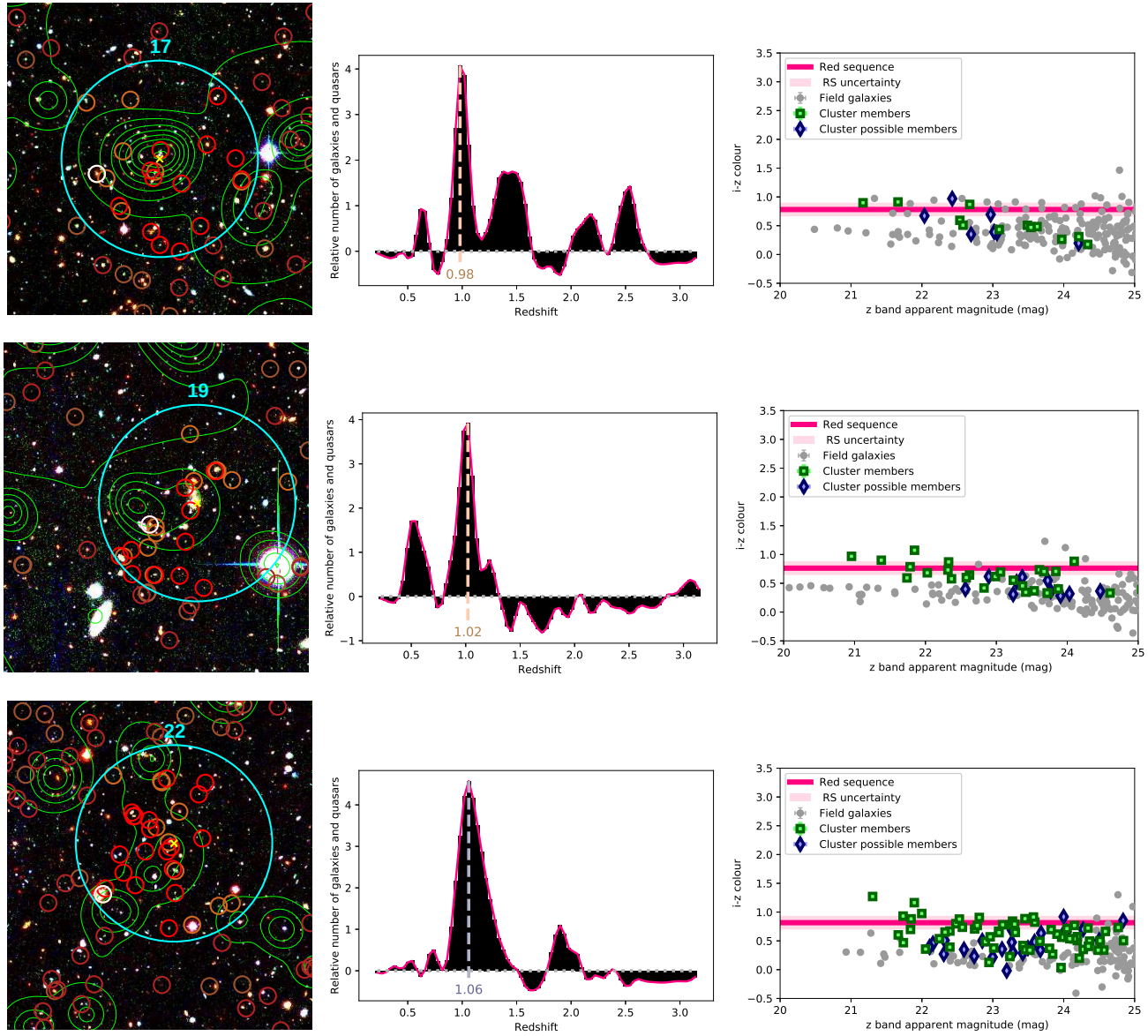

Figure 2.15: *continued*

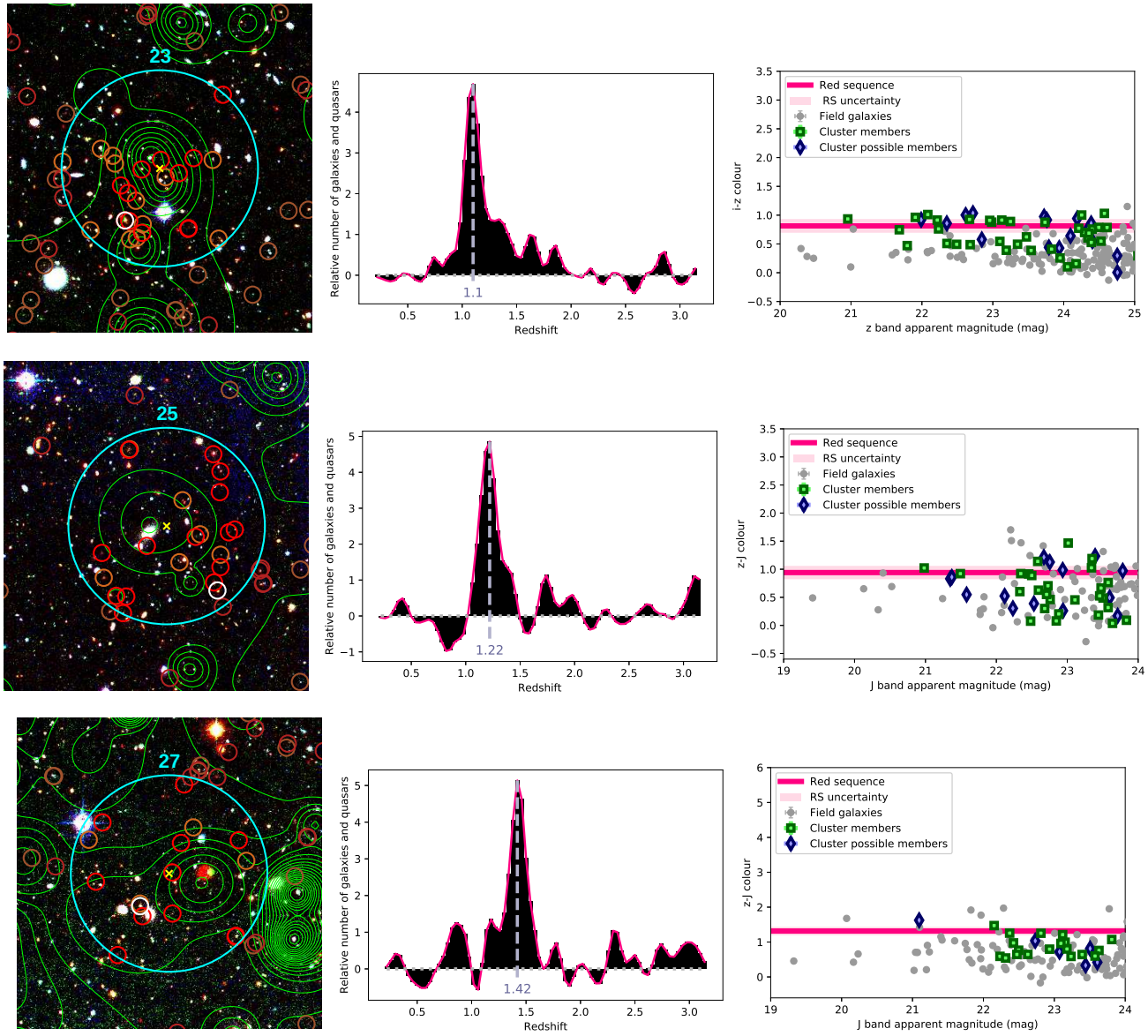

Figure 2.15: *continued*

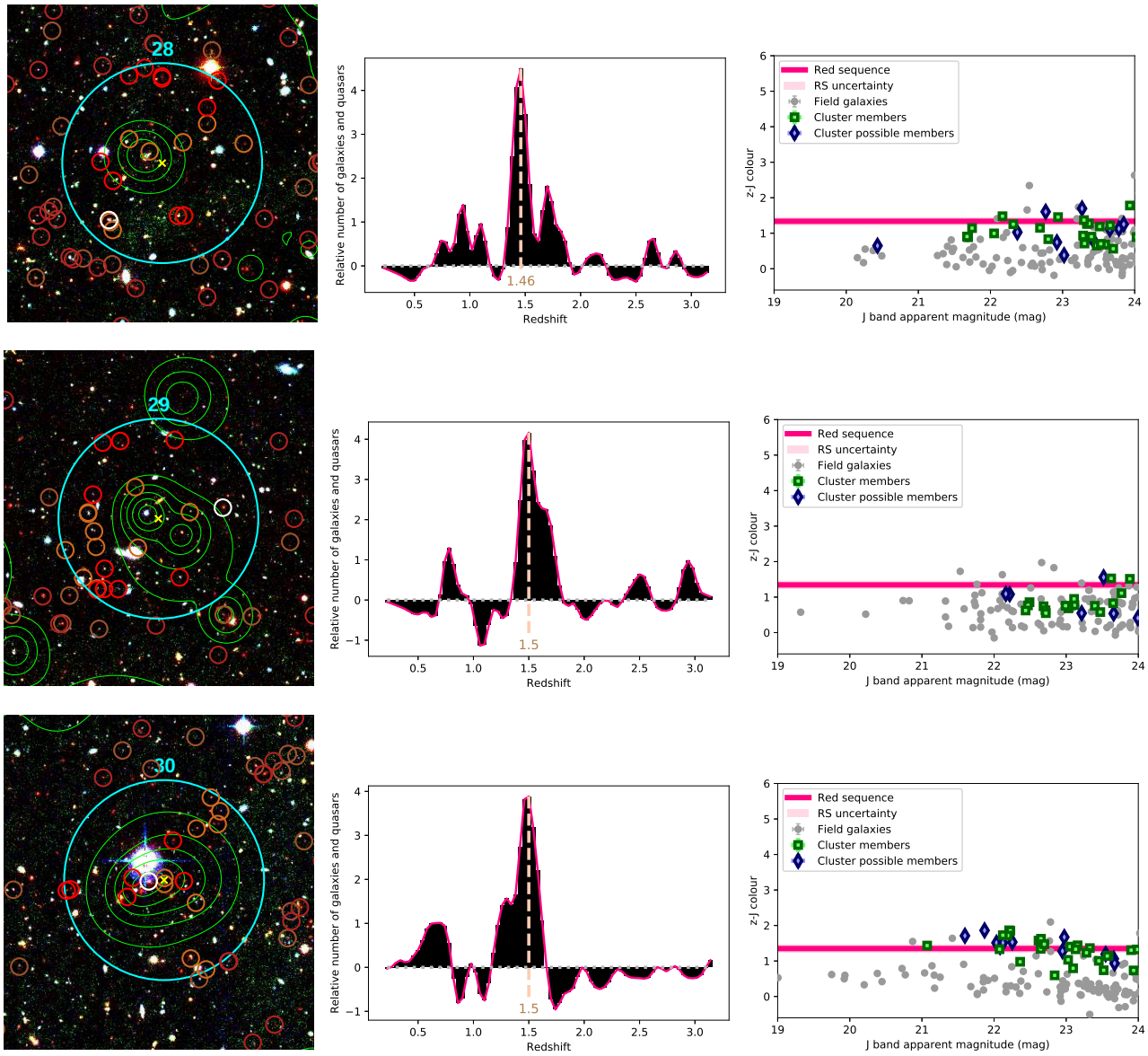

Figure 2.15: *continued*

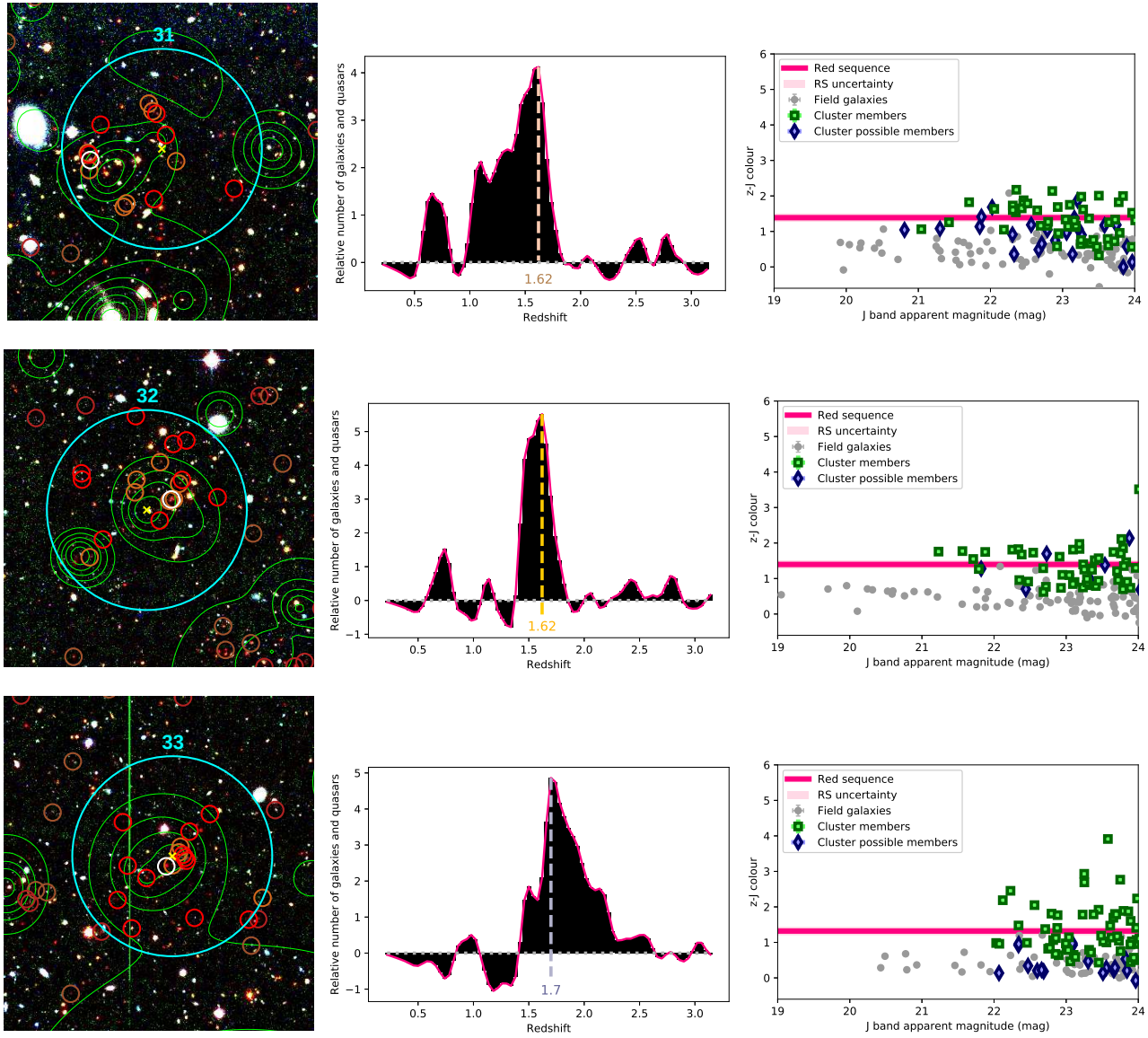

Figure 2.15: *continued*

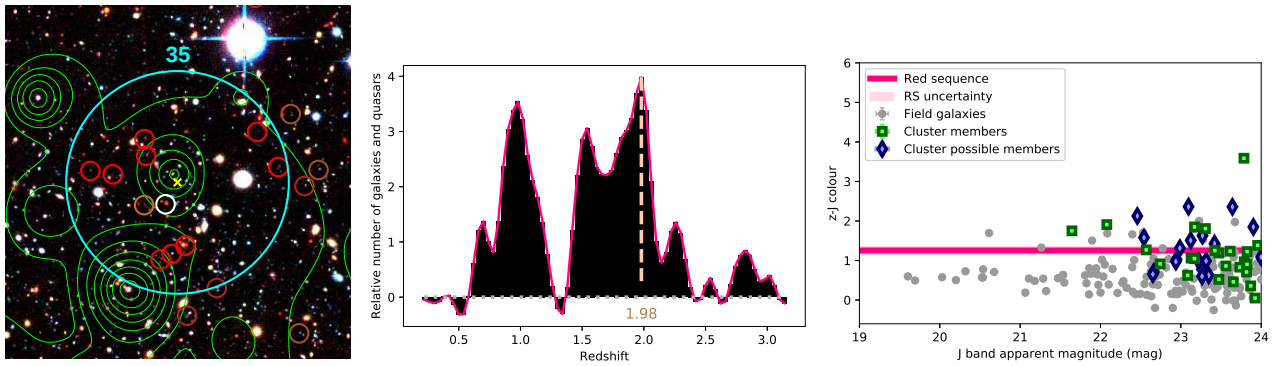

Figure 2.15: *continued*

Chapter 3

Spectroscopic confirmation of four z$\sim$1 clusters

3.1 Science rationale

Observationally, virialized galaxy clusters are differentiated from protoclusters (bound but unviralized structures) and line-of-sight galaxy overdensity by two characteristics: the presence of a galaxy red-sequence and a hot, x-ray emitting intracluster medium (Papovich et al. 2010; Gobat et al. 2011; Andreon et al. 2014; Muldrew et al. 2015). Most of the extended X-ray emission in the sky is generated by intracluster or intragroup medium (e.g. Pierre et al. 2016). Thus, the presence of an overdensity of galaxies spatially coincident with an extended X-ray emission is a good indicator of the presence of a galaxy cluster (e.g. Andreon et al. 2005; Logan et al. 2018).

In Trudeau et al. (2020, chapter 2 of the present dissertation), I followed this approach to detect 35 distant candidate clusters, using photometric redshifts to select candidate clusters at $z \gtrsim 0.8$. Although photometric redshifts are accurate to about $\Delta z \sim 0.03(1+z)$ (e.g. Ilbert et al. 2006, see also section 2.3.2 of Trudeau et al. (2020)), they remain an approximation. In particular, photometric redshifts are unable to distinguish between a single cluster and two (or several) close, but unassociated structures (e.g. Hamana et al. 2009; Willis et al. 2020). Another possible problem is that the accuracy of photometric redshifts decrease for fainter (and thus more distant) galaxies (Ilbert et al. 2006, 2009; Fotopoulou & Paltani 2018).

Thus, in order to secure the redshifts of these candidate clusters, spectroscopic observations are needed. Furthermore, spectroscopic redshifts of candidate BCGs selected in

Trudeau et al. (2020) will ensure that they belong to the candidate clusters.

This chapter is organised as follow: Section 3.2 describes the observational set up and how Nod-and-Shuffle spectroscopy operates. The main data reduction and calibration steps are presented in Section 3.3, while Section 3.4 and 3.5 highlight the main science results and their implications. Section 3.6 provides a brief summary of the main results and presents ideas for future work.

3.2 Observations design

3.2.1 Instrument and targets

Four candidate clusters were observed with the Gemini Multi-Objects Spectrograph (GMOS), between September 2019 and January 2020. Gemini Observatory consists of two 8.1-meter telescopes. Gemini South is located in Chile (Cerro Pachón), and Gemini North is in Hawaii (Mauna Kea; gem 2022a). For better chances of success observed cluster were selected on the basis of:

1. photometric redshift (should be close to one in order to place several suitable spectral lines within the obseved wavelength window)

2. presence of about 10 or more bright photometric members

Thus candidate clusters 11, 14, 19 and 22 (IDs from Trudeau et al. 2020) were selected. As each candidate cluster could be observed by either observatories, two clusters were observed by Gemini South (11 and 14, in the program GS-2019B-Q-314) and two by Gemini North (19 and 22, program GN-2019B-Q-326). A summary of each observation is provided in Table 3.1.

Table 3.1: Information on the observed fields: IDs, right ascensions and declinations, photometric redshifts and number of targeted galaxies

ID	RA (Deg)	Dec (Deg)	z_{phot}	numbers of slits[a]
11	34.935	-4.814	0.91	14
14	35.213	-5.166	0.97	13
19	34.419	-4.862	1.00	10
22	34.507	-5.023	1.08	10

[a] Exclude the three guide star slits.

As its name indicates, GMOS allows the observer to obtain the spectra of several galaxies at once, assuming the targeted objects all fit within the instrument 5.5 $\times$ 5.5 arcmin^2 field-of-view. To avoid contaminating the spectra with the light of untargeted objects or with the sky background, a plate with rectangular slits at the positions of the target, called a mask, is placed before the detectors during observations. To allow a fine positioning of the telescope, three square apertures are made in the mask for guide stars. Masks were made by Jon Willis using GMMPS version 1.5.1, selecting 10 to 14 photometric members of the candidate clusters (including the candidates BCG whenever possible). To minimize observing time, only member brighter than 23 AB magnitudes in the z band were targeted. Each galaxies was placed in a 1 $\times$ 3 arcsecond^2 slit.

Each candidate cluster was observed nine times, with 900 sec (i.e. 15 minutes) exposures. The observing time and the overheads correspond to a total time of about 5 hours 48 minutes per cluster. For candidate cluster 22, a tenth science frame is available but unusable because the observation was interrupted by clouds. For Gemini South, spectra were dispersed with a R150_+G5326 grating with the blocking filter RG610_G0331, resulting in an effective spectral coverage from 6000 to 11000 Å. For Gemini North observations, a grating and filter combination with similar resolution and wavelength coverage was used: grating R150_+G5308 with RG610_G0307.

3.2.2 Nod-and-Shuffle

In the near infrared, the night sky atmospheric emission is characterised by strong emission lines (e.g. Glazebrook & Bland-Hawthorn 2001; Davies 2007; Trinh et al. 2013; Hart 2019), that must be subtracted from the science spectra. The sky emission changes on a few minutes timescale (Davies 2007), so any sky observation must be made contemporaneously to the object spectroscopy.

One way of doing it is to use long slits, so the edges of a slit record the sky spectrum while the centre records the combined object and sky spectrum (Colless et al. 1990; Lilly et al. 1991; Cuillandre et al. 1994; Davies 2007). However, two different pixels can have slightly different responses to the same illumination (e.g. Colless et al. 1990; gem 2022a). Difference in pixel sensitivities can be computed and corrected by measuring the pixel responses with a calibration lamp (i.e. a flat-field; more information on them are given in Section 3.3.2). However, flat-field and sky subtraction errors are multiplicative, which make classical spectroscopy especially challenging for faint targets (Cuillandre et al. 1994).

An alternative way of performing the sky subtraction is to use nodding, also called

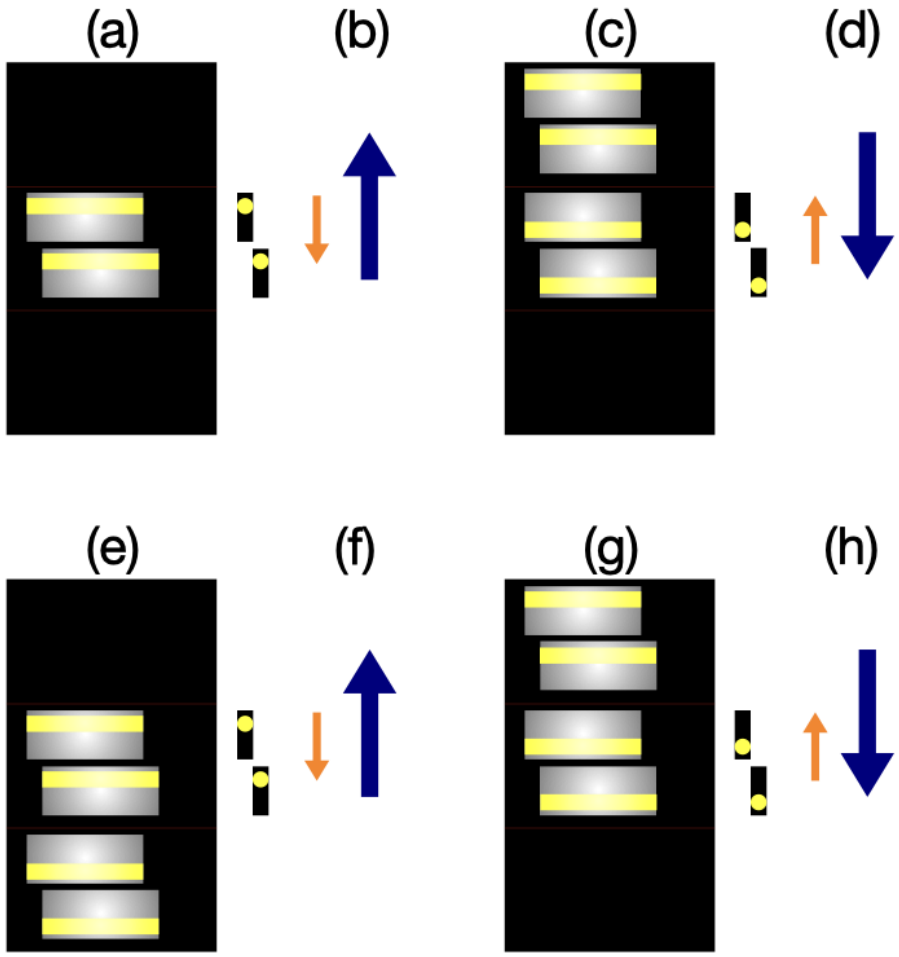

Figure 3.1: Illustration of the Nod-and-Shuffle observing method from as I use it in this dissertation a) One or several objects are observed, using the central portion of a large CCD detector. They are positioned at the top of their slits, and the bottom of the slits record the sky spectrum. b) While the telescope moves along the slits (orange arrow), the detector charges are shuffled to the top (navy blue arrow). c) In that new position, objects are at the bottom of the slits and the top of the slits record the sky spectrum. d) All the charge are shuffled to the bottom, while the telescope moves back to its previous position. e) The telescope then observe again. On the detector the charge generated by this new observation add up to the ones generated in a). f) All the charges are shuffled upward, while the telescope moves to its position in c). g) New observation with the objects at the bottom of the slits. the charge generated by this observation add up to the ones generated in c). h) Charges are shuffled downwards while the telescope moves along the slits. The cycle can be repeated as long as desired.

dithering or beam shifting. Nodding consist of changing slightly the position of the targeted objects on the detector (Glazebrook & Bland-Hawthorn 2001). The portions of the detector that are not occupied by objects can count as sky observation. By moving the objects around, this method allows one to use the same pixels for both object and sky observations, significantly mitigating the impact of pixel-to-pixel sensitivity variations. However, to retain the advantages of nodding, one must make sure that the time between the different observations does not exceed a few minutes, which is difficult to achieve if one has to read out the detector between each observation.

A CCD detector exposed to illumination acquires a charge. This charge can be shifted across to an unused portion of the detector much quickly than it can be read out (Glazebrook & Bland-Hawthorn 2001), a process called 'shuffling'. When charges are shuffled, the storage pixels sensitivities do not impact the detector response: only the observation pixels do (Glazebrook & Bland-Hawthorn 2001). Therefore, one can alternate object and sky observations, using the time needed to shift the telescope to move the charge up or down onto a unilluminated part of the CCD used for storage. This technique, called Nod-and-Shuffle spectroscopy was first proposed by Cuillandre et al. (1994) and Sembach & Tonry (1996). It was then characterised in real conditions by Glazebrook & Bland-Hawthorn (2001).

The main disadvantages of this technique are a smaller available field-of-view, since parts of the CCD are used for storage, and an increase of the overhead compared to classical observations, despite the time gained by shuffling the charge rather than reading the CCD after each exposure (gem 2022a). One way to effectively double the science exposure time is to use longer slits and to move the objects up and down the slits, rather than making separate object and sky observations. This variation of the Nod-and-Shuffle technique, presented in Figure 3.1, is the one used in the present dissertation. The steps of the cycle are thus:

1. First observation: the objects are aligned with the top of the slits; the bottom parts of the slits observe the nearby sky.

2. The telescope shutter is closed. While the telescope is moving to its second position, the charges are shuffled toward the top of the detector.

3. The shutter is opened. Now the objects are aligned with the bottom of the slits and their top parts observe the sky.

4. The shutter is closed anew. While the telescope moves back to its original position, the charges are shuffled toward the bottom of the detector.

5. The shutter is opened and the cycle repeats as often as desired.

During the data reduction one block of charge is subtracted from the other resulting in two 'half-traces': one positive trace where the sky is subtracted from the object+sky and a negative one where the object+sky is subtracted from the sky (gem 2022b).

3.3 Data reduction

3.3.1 Science mosaics

Data reduction was performed with pyRAF 2.1.15. The pyRAF environment supports python-like syntax for Gemini reduction tasks and allows for the integration of non-Gemini-related python commands within the same script.

As summarized in Section 3.2.1, for each cluster, science data consist of 9 science frames of 900 seconds each. Each frame presents two charge blocks covering two thirds of the detector, generated by eight Nod-and-Shuffle cycles. In addition to the routine calibrations such as biases, several calibrations were taken during this science program: flat-fields (six per clusters) and arc exposures (one per night of observations).

Biases are zero second exposures of the CCD, taken with the shutter closed (gem 2022a,b). They are used to characterize and subtract the read noise from science data and/or other calibration data. Flat-fields are exposures of a surface illuminated by a calibration lamp with a smoothly varying spectrum (i.e. no emissions or absorption lines). They are used to correct pixel-to-pixel variations in response to illumination. For GMOS multi-object spectroscopy, flat-fields are taken through the mask used to observe science spectra, and can thus be used to locate slit traces. Finally, arc exposures are generated by dispersing through the mask slits the light of a reference copper-argon lamp. They are used to determine the wavelength correspondence and correct the traces distortions (gem 2022a,b).

The first step of the data reduction was to combine biases taken close to the observing times using a task called GSREDUCE. The averaged bias frame was then subtracted from the science data using GBIAS.

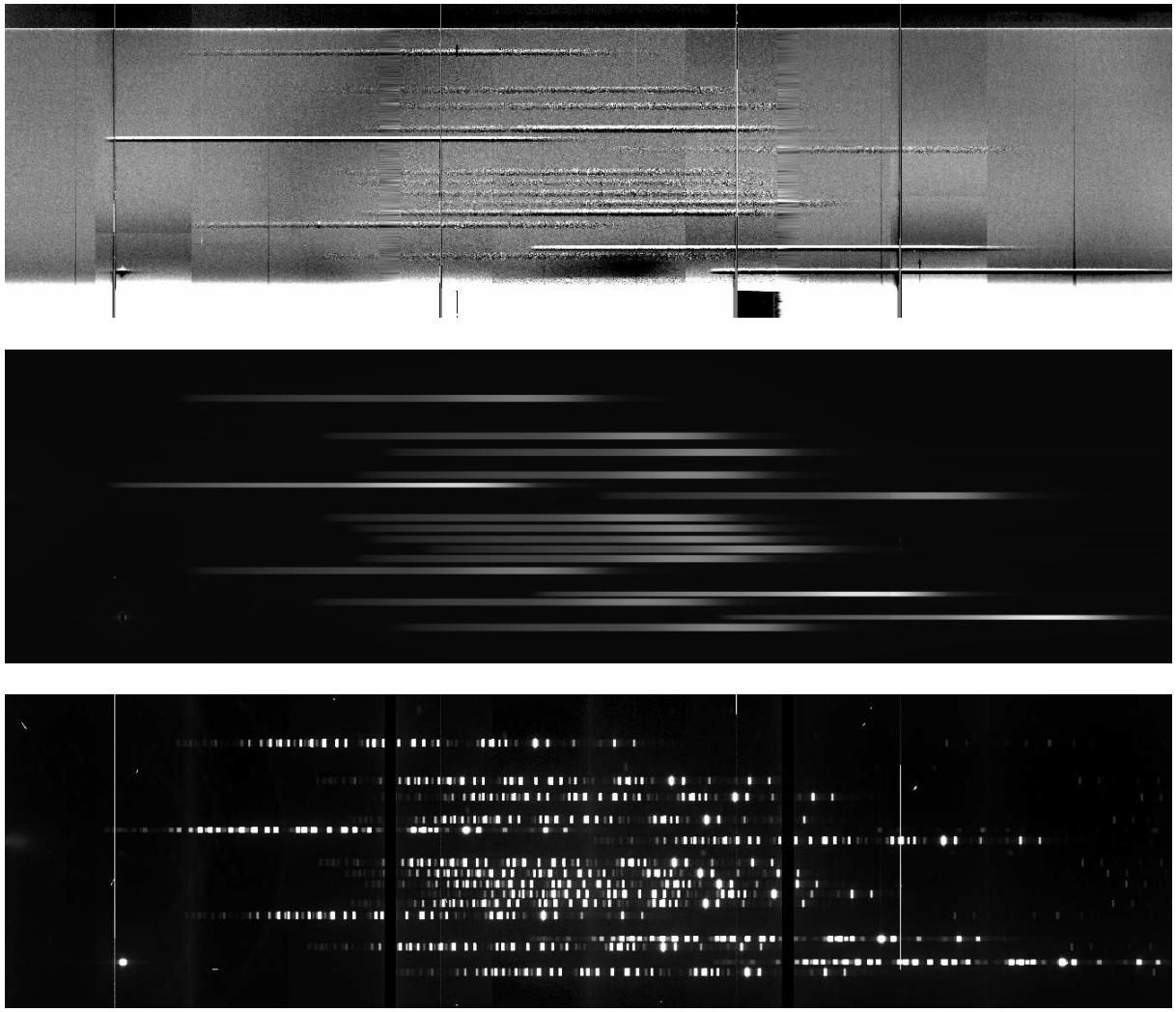

Figure 3.2: Top: Central tier of the image generated by GNSCOMBINE (mosaicked), for candidate cluster 14. The white and black stripes are the positive and negative trace associated with each object. The two bright traces at the top right and the one a the bottom left are produced by guide stars and are not used in the data reduction. Centre: central tier of the mosaicked gradient image, for candidate cluster 14. Light dispersed through the slits illuminate the regions containing spectra in the science image. Bottom: An example of a mosaicked CuAr arc exposure for candidate cluster 14. Bright vertical lines correspond to the emission lines of copper and argon.

Once this was done,GNSCOMBINE was executed on the science data to add the science frames together and then subtract one block of charges from the other. As explained in Section 3.2.2, the result of this operation is two traces per slit: a negative and a positive trace. The image is then mosaicked with GSREDUCE: its twelve science extensions, each corresponding to a twelfth of the detector, are stitched together into a single frame. GMOS detector has three gaps: each are replaced in the mosaic by an interpolation of the nearby pixel values. Fits image extensions corresponding to the variance and to a map of the bad pixels are similarly assembled. The top panel of Figure 3.2 shows the centre of the mosaicked science frame (the top and bottom edges of the image correspond to the regions of the detector used for storage during the observations and are thus irrelevant).

3.3.2 Flat-fields and gradient images

Each pair of positive/negative traces must be individually wavelength-calibrated and extracted. To do so, each spectrum must be detected and cut with the task GSCUT. However, this task tends to focus on the positive trace and often remove half or more of the negative one. To ensure an adequate selection, it is necessary to use a gradient image. A example of such an image is shown on the central panel of Figure 3.2.

Gradient images are generated by the combination of un-normalised flat-field images, and are an intermediate step in the flat-field processing done by GSFLAT. Normalized and combined flat-fields are used to detect and correct variation in the pixel sensitivity across the detector.

However, because the sky and the object flux densities are measured using the same pixels (see Section 3.2.2), the variation of sensitivity between pixels does not impact the sky subtraction. Moreover, the consequences of sensitivity variation between pixels on the final reduced spectrum is minimal, which means that normalised flat-fields are unlikely to reduce significantly the noise level in the spectra.

To prove this, I measured the pixel-to-pixel variations in the fourth trace from the top in the gradient image of Figure 3.2. I measured the counts of each pixel and then estimated and removed the continuum of the lamp used for the flat-field to get the noise. This noise is made of two components: the photon noise and the pixel sensitivity fluctuations. The noise behaves in a Poissonian manner and its standard deviation can thus be estimated as the square root of the signal. Assuming both noise sources follow a Gaussian distribution, a property of the sum of two Gaussians can be used to estimate the contribution of the photon noise to the total noise:

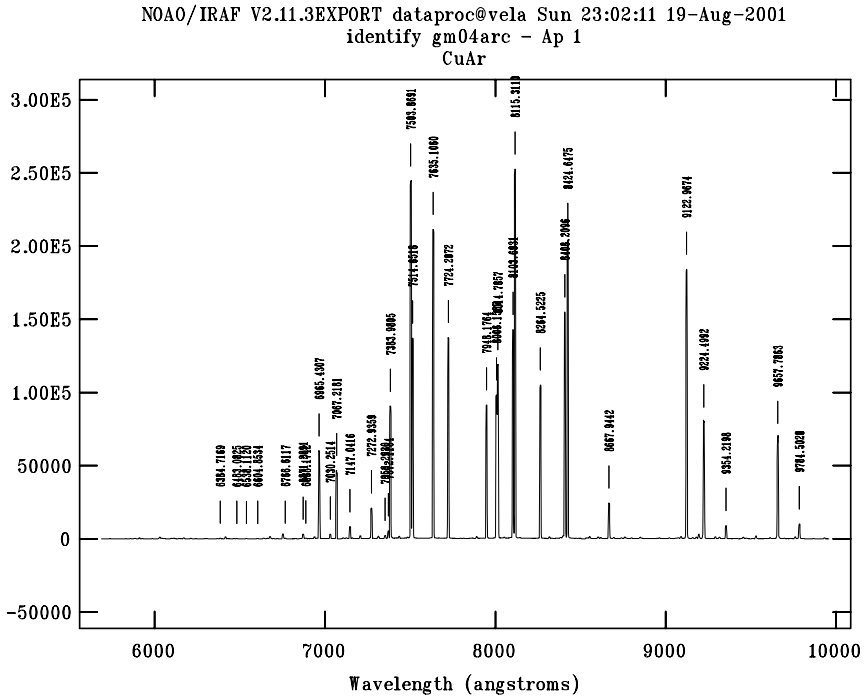

Figure 3.3: Comparison CuAr spectrum used for identifying the main emission lines by hand. Retrieved from gem (2022b).

$$\sigma^2_{sum} = \sigma^2_{photons} + \sigma^2_{ff}, \tag{3.1}$$

where σ is the standard deviation. I estimated the total standard deviations across each vertical line of pixels in the trace (each pixel in a vertical line within a trace will measure the same wavelength), and used Equation 3.1 to estimate the standard deviation of the noise due to the variation of response from one pixel to another. The mean standard deviation correspond to 0.67% of the continuum and the maximal σ to 1.5%. As reduced spectra typically have signal-to-noise ratios close to 5, (i.e. the noise corresponds to 20% of the median continuum level), a flat-field contributed error of 1.5% is not significant.

3.3.3 Wavelength calibration

The wavelength calibration is performed with arc images, i.e. exposures of a gas discharge lamp as seen through the dispersing grating and mask used for the observations. For

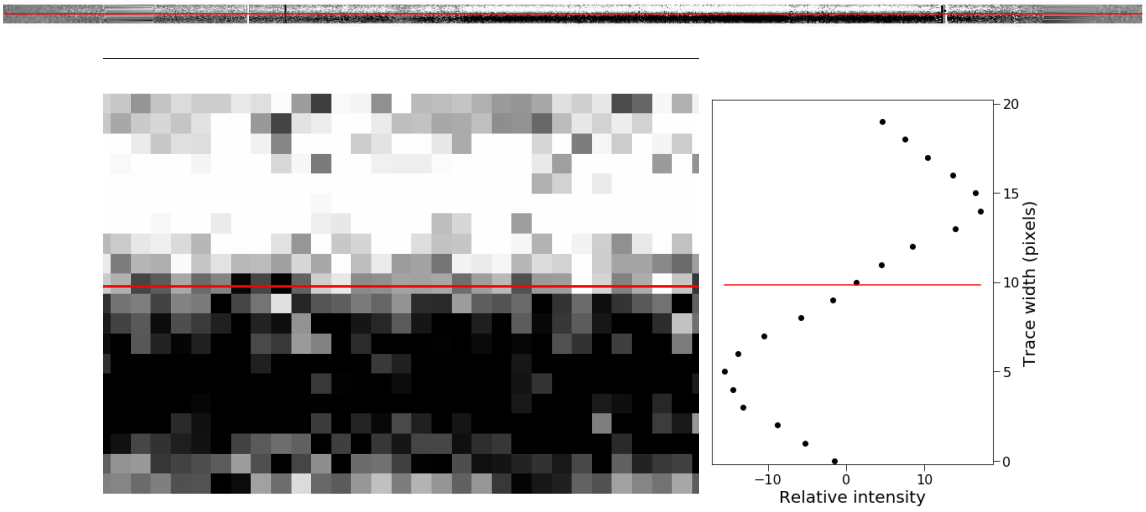

Figure 3.4: Top: Fourth trace in cluster 14. The separation between the positive and negative trace is indicated in red. Bottom left: Zoom-in on the same trace. Bottom right: Median profile of the trace.

GMOS, the gas used is a mix of copper and argon. In common with the combined science exposures, arc exposures are mosaicked and the CuAr spectra are located with the gradient image and are cut. The bottom panel of Figure 3.2 displays an example of a mosaicked arc exposure.

GSWAVELENGTH is used to determine precisely which pixel is associated with which wavelength and to account for trace distortion. Light exiting a narrow aperture (like a slit) forms a curved wavefront. When projected onto an approximately flat detector, this curved wavefront results in a smoothly varying, yet non-linear relationship between wavelength and position on the detector.

This relationship was approximated by a five-degree polynomial and the fit was performed interactively, with a manual identification of the principal emission lines in the CuAr spectra. To help with the process, plots with labelled lines are available on the (gem 2022b) website. Figure 3.3 presents the plot that covers the observed wavelength range.

Once the wavelength calibrations are computed, GSTRANSFORM applies them to the science spectra to linearise their wavelength dispersion. The spectra are now ready to be extracted.

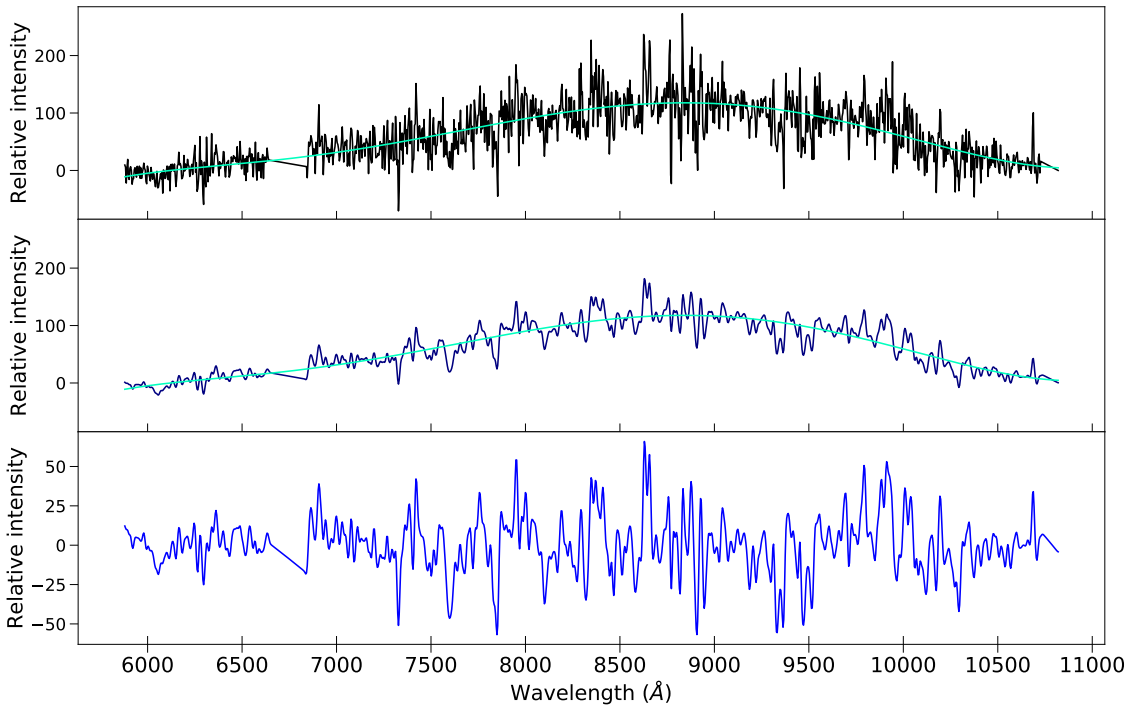

Figure 3.5: Top: Raw spectra for the fifth slit of candidate cluster 14, with the the modelled continuum superimposed on blue-green. Centre: Gaussian filtered spectrum, and modelled continuum. Bottom: Continuum-subtracted, Gaussian filtered spectrum. In theses spectra and the following ones, 'wavelength' refers to the observed wavelength.

3.3.4 Spectra extraction

Gemini pyRAF GSEXTRACT task generates 1D spectra from the linearised 2D spectral traces of each slit. However, this task is not optimized for the extraction of the negative traces. A custom routine was therefore written to efficiently extract and sum the positive and negative traces.

For each trace pair, the code computes the median vertical section of the trace pair to determine where to separate the positive and negative traces. An example of a linearised trace and its vertical section is presented in Figure 3.4. Pixel values belonging to the negative trace are multiplied by -1, and then the pixels corresponding to the same wavelength in both traces are summed together.

The extraction routine was able to generate unidimensional spectra for 43 of the 47 targeted objects observed across the sample of four candidate clusters.

To suppress the level of pixel-to-pixel noise without removing spectral features larger than the spectral resolution, extracted spectra were smoothed with a 2 pixels wide (full

width at half maximum) Gaussian filter. Examples of a raw and Gaussian filtered spectrum are shown respectively in the top and middle panels of Figure 3.5. Several absorption lines, previously hard to find in the noise, are now visible.

Finally to ease the identification of those features and compute a signal-to-noise ratio, the continuum of the spectra is modelled as a sixth degree polynomial and removed. In Figure 3.5, the blue-green curve in the top and middle panels is the continuum model. The bottom panel of the Figure shows the continuum-subtracted spectrum. Note that the removal of the continuum was done solely for identification purposes. In the following figures, spectra are plotted prior to continuum subtraction.

3.4 Results

3.4.1 Redshifts determination

Redshift were assigned via visual inspection of smoothed, continuum subtracted spectra. Using photometric redshifts as an initial guess, spectroscopic redshift were assigned following a strategy similar to the one described in Muzzin et al. (2009): The H and K CaII lines or the unresolved [OII] doublet were identified first. The input redshift was then modified until there was an agreement between the position of the lines and the wavelength predicted by the input redshift. The spectroscopic redshift was then further refined by identifying the Balmer lines and, when present, the G line and the [OIII] emission line doublet. Finally, in the spectra with the highest signal-to-noise ratios, a few calcium and iron absorption lines were identified: Fe4383, Ca4455, Fe4531 and a blended line at 4921 Å (Willis et al. 2001). Figure 3.6 presents examples of spectra with absorption lines only, while Figure 3.7 displays spectra where both type of lines are present.

A redshift is considered reliable if at least two of the following features are reliably identified: [OII], H, K, G or any member of [OIII] doublet. Balmer lines are not part of this list because their strength as absorption lines is widely variable, depending on the age of the stellar population (e.g. Rabin 1982; Dressler & Gunn 1983; Poggianti & Barbaro 1997). Furthermore, in galaxies containing few young stars, the Balmer absorption lines can be partially filled by a weak emission component (e.g. Trager et al. 2000; Dressler et al. 2004; Poggianti et al. 2004). This effect is especially visible in the galaxy spectrum displayed in the bottom panel of Figure 3.7. Additionally, any redshift based on four or more identified lines is also considered reliable.

Following these criteria, 39 of the 43 extracted spectra possess reliable spectroscopic

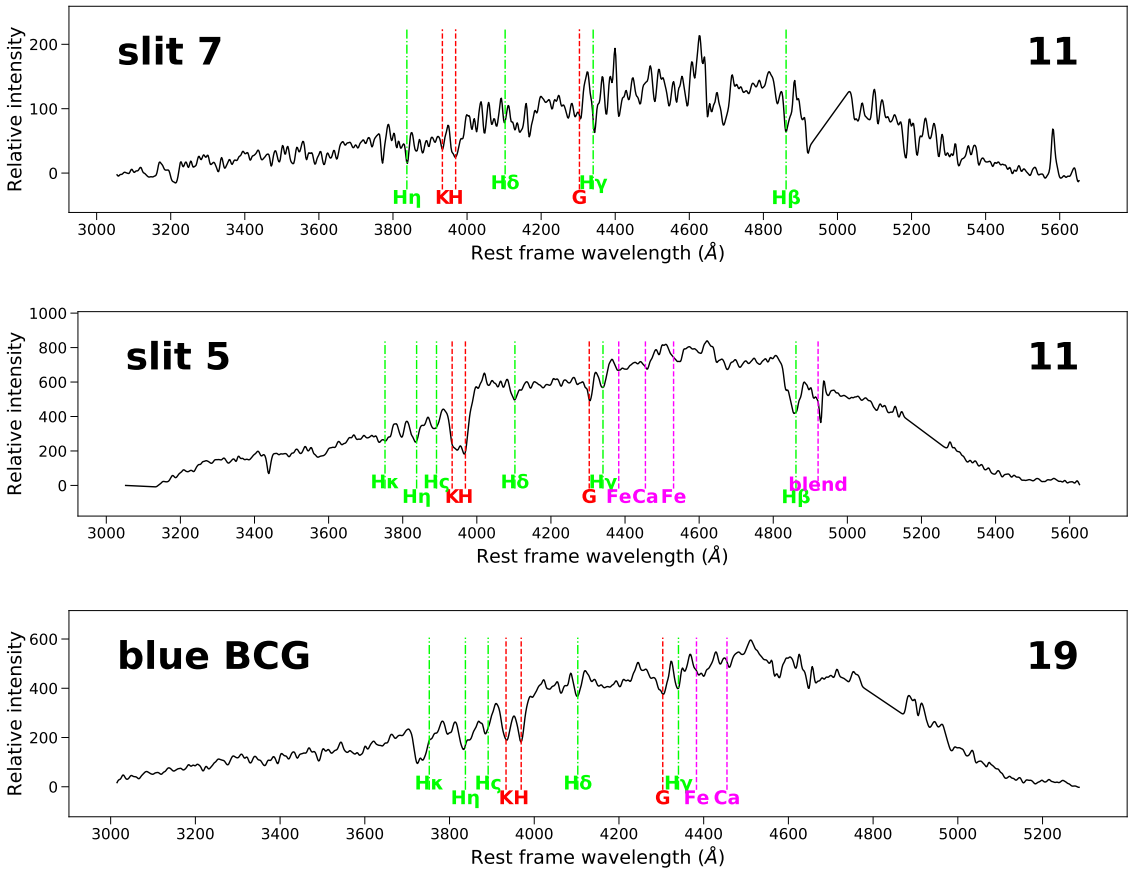

Figure 3.6: Several examples of galaxy spectra displaying the spectral features used to identify quiescent galaxies. The [Ca II] H and K and the G lines are in red, the Balmer lines are in green. The magenta lines correspond to a set of fainter absorption lines that can be located in the spectra with good signal-to-noise ratios. Top: Spectrum of slit 7 in cluster 11. Slit 7 is a class 2 member at $z = 0.92$. Middle: Spectrum of slit 5 in cluster 11, a class 1 member ($z = 0.927$). Bottom: The BCG of cluster 19, i.e. slit 10 ($z = 1.043$).

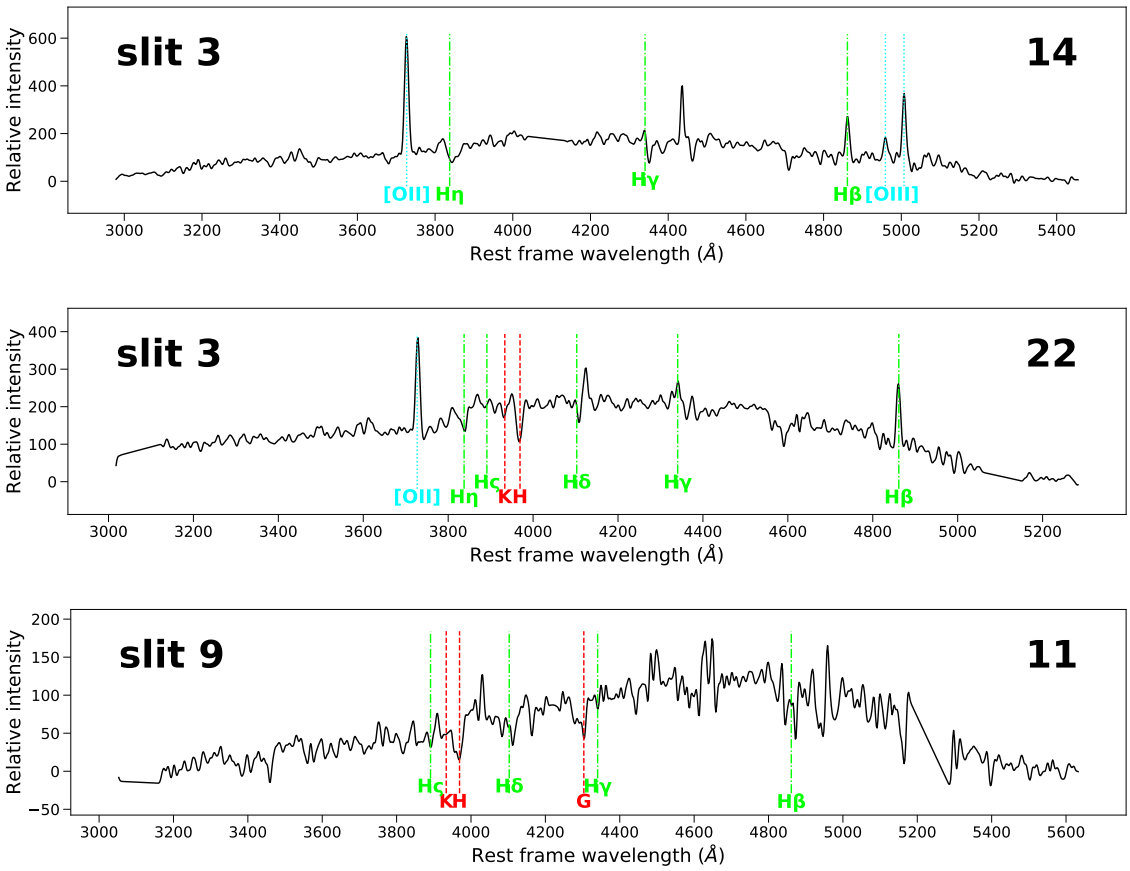

Figure 3.7: Several examples of galaxy spectra displaying emission lines associated with star formation. The [OII] (not resolved) and [OIII] emission line doublets are highlighted in cyan and Balmer lines are in green. When present, features associated with and older stellar population (H, K and G lines) are in red. Top: Spectrum of slit 3 in cluster 14 (class 2, $z = 0.9775$). Note that Hβ and Hγ are now emission lines. Middle: Spectrum of slit 3 in candidate cluster 22 (class 1, $z = 0.925$). H and K lines are present alongside the [OII] emission line. Bottom: Spectrum of slit 9 in cluster 11 (class 1, $z = 1.043$). Hβ and Hδ are half emission, half absorption lines.

redshifts. Of the four remaining spectra, three appear to be foreground stars and only one is unidentified. To further assess the results reliability, these 39 good spectra were divided into two categories: class 1 with a signal-to-noise ratio over five between 8000 and 9000 Å and class 2 for every other spectrum.

3.4.2 Confirmed candidates

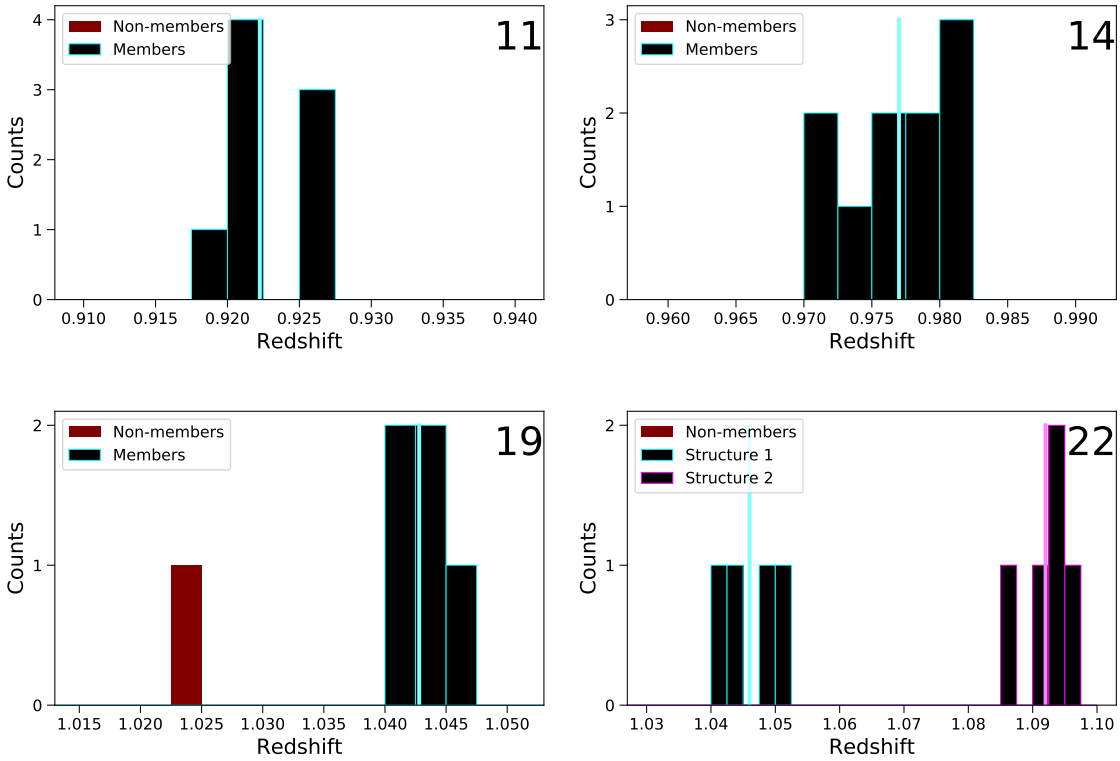

Figure 3.8: Top left: Spectroscopic redshift histogram of cluster 11, cropped around the cluster spike. The cyan line indicates the cluster mean redshift. Top right: Redshift histogram of cluster 14. Bottom left: Histogram of cluster 19. Bottom right: Redshift histogram of candidate cluster 22. The redshift spike around $z = 1.046$ is highlighted by a cyan outline and the one at $z = 1.092$ by a magenta outline.

The recursive approach adopted to confirm the clusters was inspired by Lubin et al. (2002); Willis et al. (2005): for each galaxy with a reliable redshift, I compute $\Delta v = c(z - \bar{z})/(1 + \bar{z})$ (i.e. Equation, 1.4 in Chapter 1), where $\bar{z}$ is the median redshift of the field. If the maximal $|\Delta v|$ is greater than 3500 km s^{-1}, I then remove it and I repeat.

Redshift estimate were then further refined by computing the bi-weight scale as defined in (Beers et al. 1990). The bi-weight scale provides a similar measurement to the standard

Table 3.2: Redshift and related information for the members of each cluster or structure.

Slit	RA (Deg)	Dec (Deg)	z_{spec}	Δv (km s^{-1})	SNR	Class
Cluster 11 ($< z >= 0.922$)						
1 (BCG)	34.9361	-4.8124	0.920	-156	12.1	1
3	34.9306	-4.8373	0.925	625	7.8	1
5	34.9389	-4.8128	0.927	937	13.6	1
7	34.9318	-4.8186	0.920	-156	4.9	2
8	34.9270	-4.8136	0.921	0	3.6	2
9	34.9342	-4.8123	0.925	625	5.5	1
10	34.9489	-4.8464	0.921	0	4.7	2
12	34.9420	-4.8095	0.919	-312	9.7	1
Cluster 14 ($< z >= 0.977$)						
2	35.2163	-5.1769	0.980	417	5.9	1
3	35.2316	-5.1733	0.9775	38	4.9	2
4	35.2109	-5.1718	0.977	-38	10.5	1
5	35.2149	-5.1670	0.977	-38	5.2	1
6 (BCG)	35.2108	-5.1620	0.9775	38	9.9	1
8	35.2153	-5.1574	0.982	721	6.5	1
9	35.1808	-5.1644	0.982	721	4.2	2
11	35.2022	-5.1707	0.974	-493	7.0	1
12	35.2116	-5.1683	0.972	-797	3.6	2
13	35.2092	-5.1695	0.971	-948	5.6	1
Cluster 19 ($< z >= 1.043$)						
2	34.4261	-4.8672	1.044	147	6.0	1
3	34.4203	-4.8634	1.040	-441	2.9	2
4	34.4197	-4.8584	1.042	-147	8.0	1
6	34.4158	-4.8566	1.045	294	5.0	2
10 (BCG)	34.4272	-4.8658	1.043	0	8.0	1
22 – Structure 1 ($< z >= 1.046$)						
1	34.5371	-5.0414	1.042	-587	6.7	1
3	34.5142	-5.0182	1.043	-440	8.5	1
9	34.5338	-5.0159	1.049	440	8.8	1
10	34.5068	-5.0281	1.050	587	6.5	1
22 – Structure 2 ($< z >= 1.092$)						
2	34.5069	-5.0319	1.094	0	5.0	1
4	34.5062	-5.0181	1.085	-1289	9.8	1
5	34.5080	-5.0232	1.091	-430	3.7	2
7	34.5082	-5.0248	1.094	0	6.0	1
8	34.5318	-5.0176	1.096	287	9.1	1

deviation, but unlike it the bi-weight scale does not rely on the assumption that the redshift distribution is Gaussian. If any galaxy velocity deviates from the median more than three times this scale, it was removed from the cluster member list and the calculation was done again, until the most discrepant velocity was below that threshold. The resulting redshift histograms are shown is Figure 3.8 and the main characteristics of each member are presented in Table 3.2.

This process works well for every targeted candidate cluster. However, as the bottom right panel of Figure 3.8 suggests, candidate cluster 22 appears to be a superposition of two redshift spikes, while our recursive computation resulted in only one structure with a mean redshift of 1.092 (median redshift of 1.094).

To test weather there is another structure in candidate cluster 22, the five galaxy discarded during the first computation were gathered. Their median redshift and their Δv were computed and used as the primary input of another recursive bi-weight calculation. Four of these galaxies indeed belong to an additional structure, with a mean redshift of 1.046 (the median redshift is also 1.046). This structure is presented as structure 1 in Table 3.2, and the other structure is called structure 2.

The XXL collaboration criteria to confirm a cluster can be summarized as follow: three or more galaxies displaying concordant spectroscopic redshifts should be spatially located within the X-ray source. Failing that, a single massive elliptical galaxy likely to be the BCG (and with a spectroscopic redshift) should be located near the X-ray centroid (Adami et al. 2018; Guglielmo et al. 2018).

Figure 3.9 shows the spatial positions of each candidate cluster members in a three colour image, with the X-ray contours are overlaid in green. Following the XXL criteria, three clusters can be confirmed: cluster 11, 14 and 19. By following strictly XXL criteria, the farthest of the two structures in candidate cluster 22 should also be confirmed, as there are three concordant redshifts within the X-ray contours. However, most authors are especially careful when there are more than one structure in a same line-of-sight (e.g. Hamana et al. 2009; Adami et al. 2018; Guglielmo et al. 2018). Candidate cluster 22 and the reasons why it is not considered as a confirmed cluster are discussed in greater details in Section 3.5.1.

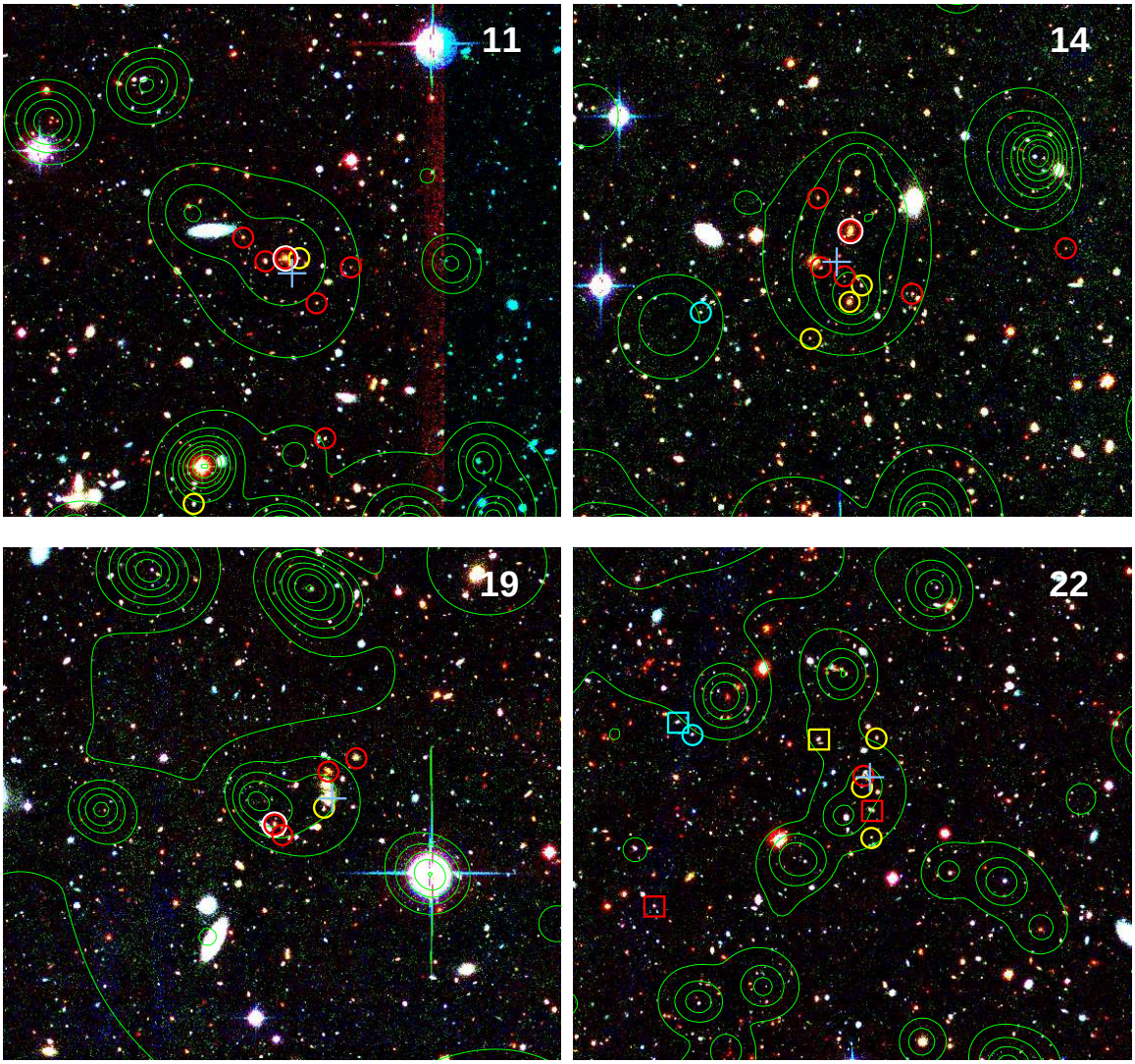

Figure 3.9: Top left: RGB image of cluster 11. Members are in different colours, according to theirs stellar population: red for old, yellow for a majority of old stars with some star formation, cyan for star-forming. The BCG is identified by a white circle. The X-ray contours in green are logarithmically distributed in ten levels between the maximum and minimum emission observed in a 7×7 arcmin^2 box around the X-ray source. A blue cross marks the centre of the X-ray best fit model. Top right: RGB image of cluster 14. Bottom left: Image of cluster 19. Bottom right: Image of candidate cluster 22. The two large-scale structures are differentiated by symbols: squares for the structure at $z = 1.046$ and circle for the one at $z = 1.092$.

3.5 Discussion

3.5.1 Two structures in candidate cluster 22

Candidate cluster 22 is a good example of why spectroscopic observation are required to confirm the nature of candidate clusters. While generally reliable, photometric redshifts do not allow one to distinguish between two independant structures close in redshift (e.g. Willis et al. 2020). Assuming WMAP9 cosmology ($H_0 = 69.32$ km s^{-1} Mpc^{-1}, $\Omega_m = 0.2865$, and $\Omega_\Lambda = 0.7135$, see Hinshaw et al. 2013) similar to the one used in Trudeau et al. (2020), the comoving radial distance between the two structures in candidate 22 can be computed. This distance is 110 Mpc (Wright 2006), which is approximatively the distance between the Milky Way and the Coma cluster (Thomsen et al. 1997; Kavelaars et al. 2000). Thus, it can be safely assumed that the two structures are not related.

In order to determine which structure is the most likely to be associated with the X-ray emission, the projected distances between the structures members and the X-ray centroid were computed. On average, the projected separation between structure 1 members and the X-ray centroid is 565 kpc, and the median is 542 kpc. For structure 2, the average separation is 251 kpc, with a median of 163 kpc. These distances, together with the photometric redshift of 1.08 computed for this candidate, suggest that the X-ray emission is more likely associated with structure 2. However, it must be stressed that with only four (structure 1) and five (structure 2) confirmed galaxies, the projected separation of either structure is very sensitive to individual measurements and thus remains an insufficient argument to conclude that structure 2 is a cluster of galaxies.

3.5.2 Comparison with photometric redshifts

To further investigate the relationship between photometric and spectroscopic redshifts, each spectroscopic redshift was matched with a photometric counterpart from the VIDEO catalogue (Jarvis et al. 2013, see also Adams et al. 2020 for the version of the catalogue used here). Figure 3.10 shows the relationship between VIDEO photometric redshifts and GMOS spectroscopic redshifts for the four candidate clusters. Quantitatively, Adams et al. (2020) estimate the reliability of VIDEO photometric redshifts with the Normalised Median Absolute Deviation, (NMAD) which they define as $1.48|z_{phot} - z|/(1+z)$. For the the part of the XXL-North field covered by VIDEO, they found a NMAD of 0.031. Among the galaxies spectroscopically confirmed in Section 3.4, the NMAD is slightly lower: 0.022. This could be explained by the fact that the observed galaxy are mostly massive ellipti-

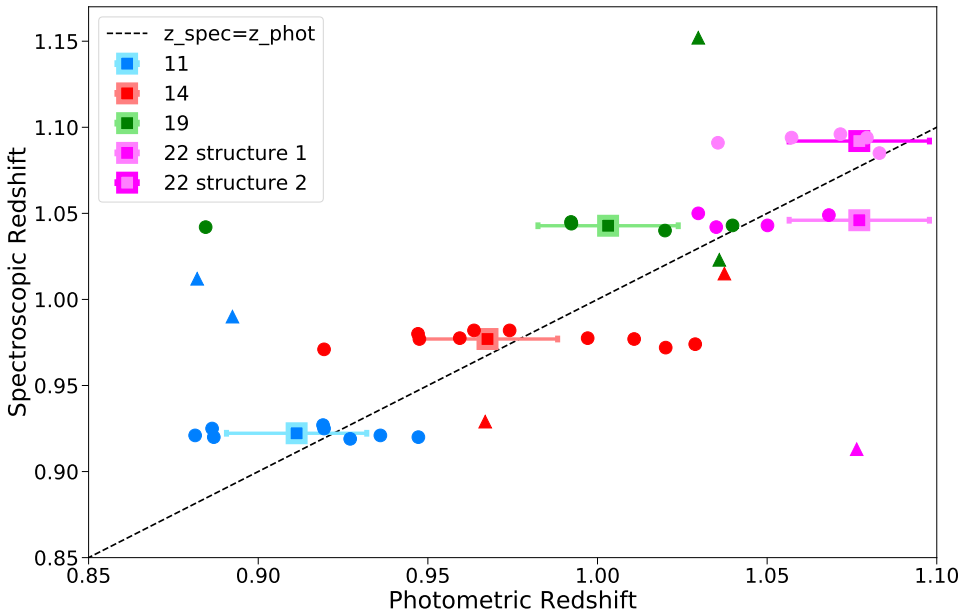

Figure 3.10: Comparison between the photometric and spectroscopic redshifts of the targeted galaxies, colour-coded by field. The circles indicate the spectroscopic members and the triangles show the foreground or background galaxies. The big squares highlight the relationship between the clusters photometric redshifts, as calculated in Trudeau et al. (2020), and their mean spectroscopic redshifts. Note that one of the background galaxies in cluster 19 field-of-view was omitted, because its spectroscopic redshift is 1.3375.

cals galaxies at $z \sim 1$, while VIDEO sample was constructed to cover the range $0 \geq z \geq 4$ (Jarvis et al. 2013). Photometric redshifts generally perform better for bright, red galaxies characteristic of those targeted in the present chapter.

Despite this lower deviation value, Figure 3.10 shows that it is impossible to discriminate candidate cluster 22 two structures based on photometric redshifts alone. Futhermore, neither the average nor the median of $(z_{phot} - z)/(1 + z)$ (no absolute value) are equal to zero. They correspond respectively to -0.011 and -0.007, which is small, but might indicate a slight tendency for the photometric redshift to underestimate the spectroscopic redshift. Indeed, all the spectroscopic redshifts of the confirmed clusters are slightly greater than the expected redshifts computed in (Trudeau et al. 2020).

3.5.3 Star formation histories

While the primary goal of these spectroscopic observations was to confirm clusters, they can also be used to gain insight into the star formation histories of the bright cluster members. The majority of the spectroscopic features used for confirming galaxy redshifts are age-dependent. For example, the CaII K and H lines, visible in most of my confirmed galaxies, are associated with evolved stellar population (Rose 1985). Conversely, the [OII] and [OIII] emission lines doublets are associated with current star formation (e.g. Poggianti et al. 1999, 2004; Trager et al. 2000; Dressler et al. 2004).

As explained in Section 3.4.1, depending of the exact star formation history, Balmer lines can be in emission, absorption or sometimes both (e.g. Dressler & Gunn 1983; Trager et al. 2000; Rosa-Gonzlez et al. 2002; Kong et al. 2003). The deepest Balmer lines are typically observed in young (about 0.5 to 1 Gyr) stellar populations (Rabin 1982; Kong et al. 2003), but can be contaminated by star formation. Hβ and Hγ are especially subject to partial filling(Trager et al. 2000; Dressler et al. 2004; Poggianti et al. 2004). Thus, Hδ is usually considered the best indicator of recent, but not current star formation (Dressler & Gunn 1983; Poggianti & Barbaro 1997).

To characterize the star formation of my galaxies, I divide them into three broad categories:

- Evolved galaxies: These are evolved galaxies with a redshift based on the K, H and/or G absorption lines. No [OII] or [OIII] emission is detected.

- Intermediate galaxies:These galaxies display a combination of K, H and/or G lines, either with [OII] and/or [OIII] emission line doublets, or with at least two Balmer absorption lines partially filled by emission. These systems are interpreted as a majority of old stars with some weak star formation.

- Actively star-forming galaxies: The spectra of these galaxies feature [OII] and/or [OIII] emission line doublets but no evidence of K, H or G absorption lines. This implies that the light of these galaxies is dominated by a young stellar component.

This classification does not take into account the Balmer lines to classify the evolved or active galaxies. However, I note that in most passive galaxies (see Figure 3.6 for some example) the Balmer line appears to be entirely in absorption. There are two passive galaxies in cluster 14 where there might a partial filling of Hβ without any convincing indication that the other Balmer lines are affected. However, both spectra have signal-to-noise ratio close to or below 5 and thus this Hβ 'filling' could be nothing more than noise.

In Figure 3.9, the classification of each cluster or structure member is indicated by a red, yellow or blue symbol. The vast majority of the cluster members belong either to the passive or intermediate population, with only three member galaxies classified as actively star-forming. These three galaxies exhibit prominent Balmer emission lines (Hβ, Hγ and Hδ) with only the most energetic Balmer transitions (Hζ and Hη) in absorption. The topmost panel of Figure 3.7 shows an example of active galaxy. Such emission lines are indicative of a vigorous star formation, but do not exclude the presence of an underlying older component (e.g. Westera et al. 2004).

Furthermore, an examination of Figure 3.9 shows that these active galaxies lie at larger projected separation from the X-ray centroids than the passive or intermediate galaxies, in agreement with the generally accepted idea that the fraction of star-forming galaxies in clusters increases away from the core (e.g. Raichoor & Andreon 2012; Alberts et al. 2014; Pintos-Castro et al. 2019). However, there is no evidence that the intermediate galaxies are farther from the core than passive galaxies.

Intermediate galaxies present features typical of old galaxies, with [OII] and [OIII] lines, which are indicative of recent star formation. In most of these galaxies, emission and absorption Balmer lines coexist, sometimes within a single line, as shown in the bottom-most panel of Figure 3.7. Intermediate galaxies are thus still star-forming, but their star formation is weak, unable to dominate their spectra.

In Trudeau et al. (2020), galaxies were classified as red or blue, depending on their colour. To determine where the intermediate galaxies fall within this classification, I made the CMD diagram of the photometric cluster members, indicating the spectroscopic member by red, cyan or yellow square, depending on their classification. These CMD are presented in Figure 3.11.

As expected, evolved members lie above or on the predicted red sequence colour (see Section 2.4.1 in Trudeau et al. 2020, for an explanation of how it is computed), while active members inhabit the blue cloud. The only exceptions are the members of structure 1 in candidate cluster 22, which lie below the main sequence, regardless of their classifications. This suggest that the number of star-forming galaxies might be overestimated in candidate cluster 22.

Intermediate members lie either among the red sequence or the blue cloud, depending on their exact star-formation rate. This shows that the use of colour to discriminate between star-forming and quenched members is a useful but incomplete characterisation method, as it fail to capture the difference between quenched and weakly star-forming members.

In most $z \sim 1$ clusters, star formation is mostly present in lower mass members (e.g.

Raichoor & Andreon 2012; Behroozi et al. 2013; Alberts et al. 2014; Pintos-Castro et al. 2019), with the most massive members being already quenched. The presence of a significant fraction of star-forming (albeit weakly) bright members in these cluster cores suggests that they are less evolved and have thus collapsed later than more massive clusters (e.g. Rennehan et al. 2020).

3.5.4 BCG spectra

In Trudeau et al. (2020), BCGs were identified and classified as blue or red on the basis of broad-band photometry. With spectroscopic data now in hand it is possible to check if those initial BCG classification were reliable. The BCG candidates in clusters 11 and 14 were considered as 'red', and the BCG candidate of cluster 19 was classified as blue. At the exception of candidate cluster 22, where no convincing BCG was found, every BCG has been confirmed as a cluster member in the GMOS observations.

Figure 3.12 presents each BCG spectrum. None of the BCGs selected in Trudeau et al. (2020) present evidence of ongoing star formation: [OII] or [OIII] emission lines are absent and, when present, Balmer lines are in absorption. In the topmost panel, the BCG of cluster 11 possesses a prominent Hβ absorption, which would be a sign of recent star formation (i.e. 0.5 to 1 Gyr ago; see Rabin 1982; Dressler & Gunn 1983; Poggianti & Barbaro 1997) if the Hγ and Hδ line were not too weak to be identified. Alternatively, there is a weak iron line at 4890 Å (Willis et al. 2001), which could be blended with the Hβ line.

Conversely, although an inconveniently placed chip gap masks the location of the Hβ line in candidate BCG of cluster 19 (bottommost panels of Figures 3.6 and 3.12), Hγ and Hδ are present and noticeable. This suggest that a part of the stellar population of this BCG has recently formed, which might explain its bluer colour. It must be stressed however that a measurement of the equivalent width of Hδ would be needed to confirm this hypothesis.

Finally, the BCG of cluster 14 (middle panel of Figure 3.12), which is classified as red, features barely noticeable Balmer lines, with the exception of Hη. This also indicates an evolved stellar population, with no recent star formation.

Overall, none of the three spectra presented in Figure 3.12 is significantly different from the others, with only marginal indication that the blue one might have experienced some star formation at a later time than the red ones. Whether the absence of star formation in the BCG of cluster 19 is representative of the stellar population of other blue BCGs remains to be proved.

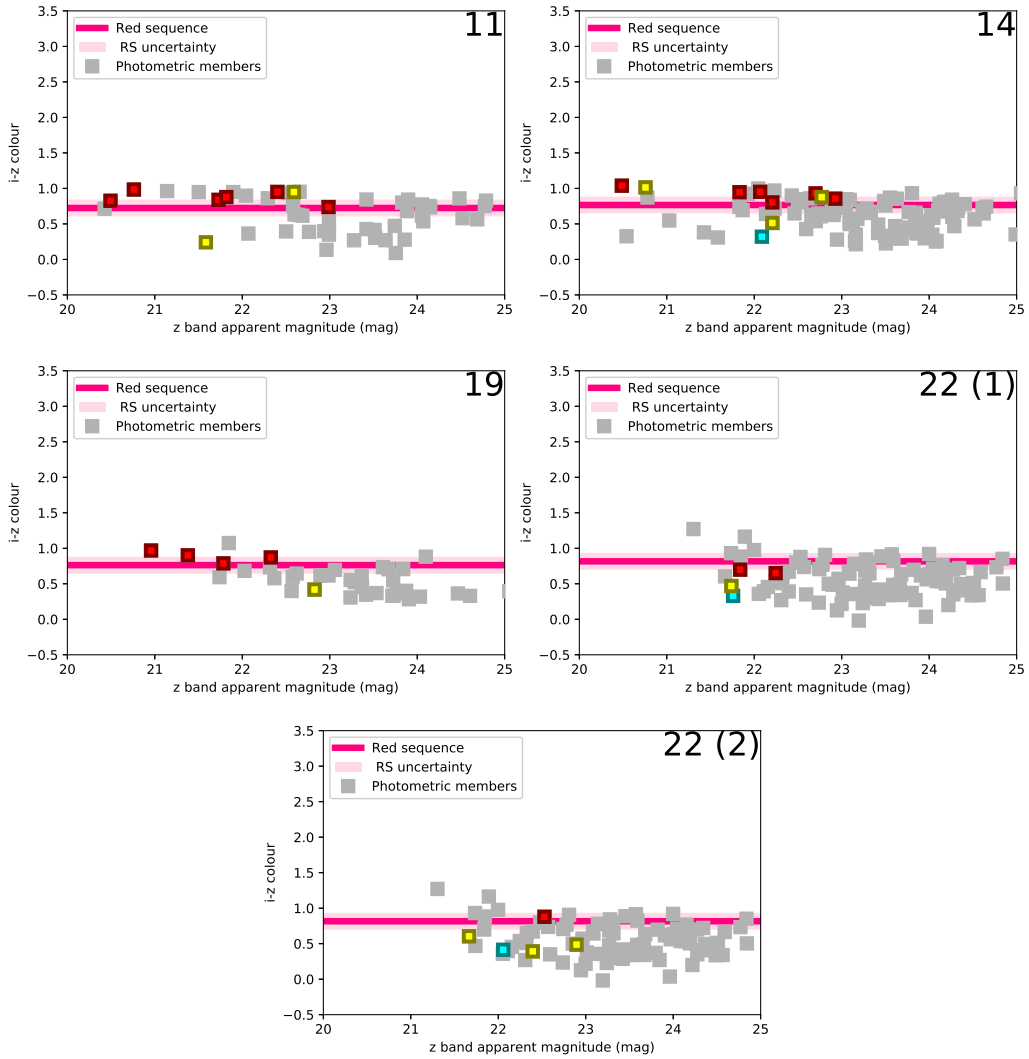

Figure 3.11: Top left: CMD diagram of cluster 11, with the spectroscopic member indicated in red (quiescent), yellow (old stellar population with some star formation) and cyan (star formation). The cluster photometric members are indicated by grey square, and the modelled red sequence colour (see Section 2.4.1 in Trudeau et al. 2020) is indicated in pink. Top right: CMD diagram of cluster 14. Centre left CMD diagram of cluster 19. Centre right: CMD diagram of structure 1 in candidate cluster 22. Bottom: CMD diagram of structure 2.

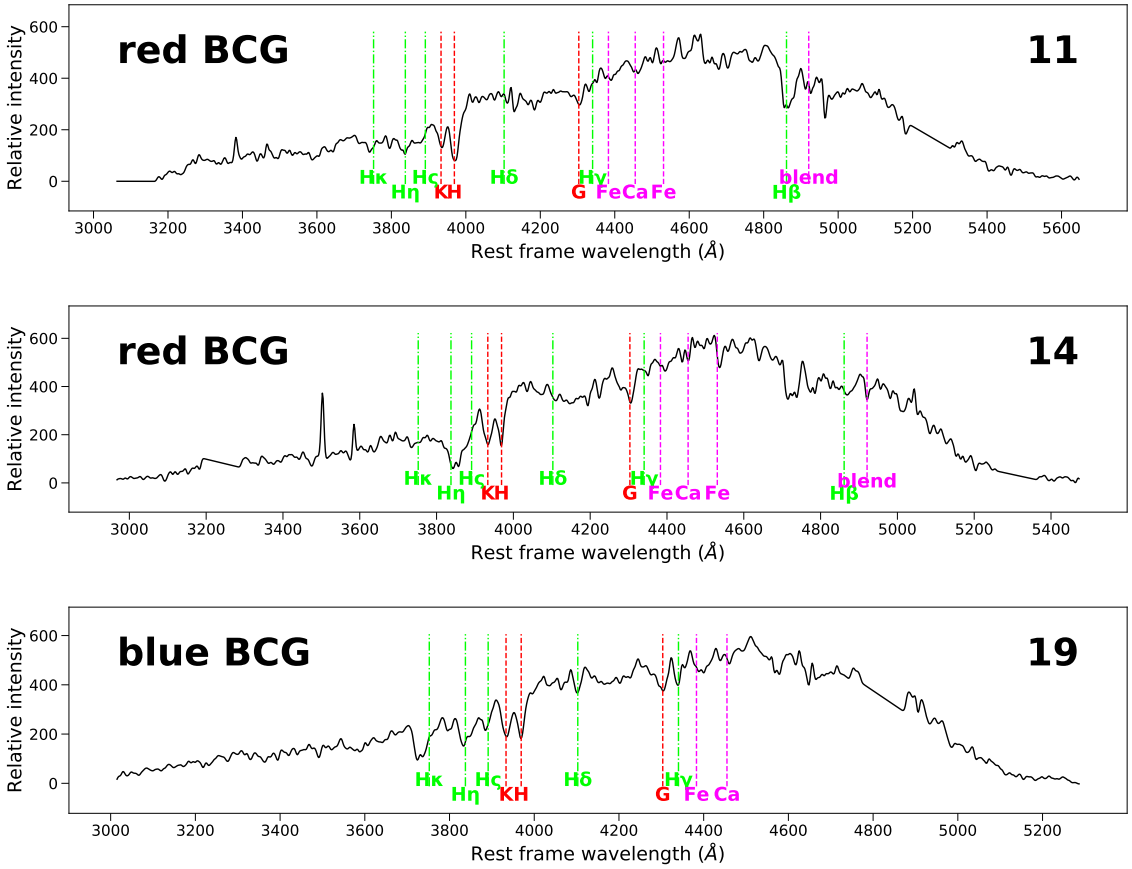

Figure 3.12: The three BCGs. Emission and absorption lines are identified as in Figures 3.6 and 3.7. Top: Spectrum of slit 1 in cluster 11 at $z = 0.92$. Middle: Spectrum of slit 6 in cluster 14, ($z = 0.9775$). Bottom: The BCG of cluster 19, i.e. slit 10 ($z = 1.043$). All are class 1 spectra.

3.6 Conclusion

3.6.1 Future work

The stellar population analysis presented here is qualitative: it could be further improved by incorporating the photometric and spectroscopic data into a SED-fitting code or by measuring the equivalent widths of the the [OII], H, K, and Hδ lines (e.g. Poggianti & Barbaro 1997; Mansheim et al. 2017). For both endeavours, higher signal-to-noise ratio spectra would be preferable, albeit this might be difficult to justify to a time allocation committee.

Of the 35 candidate clusters presented in Trudeau et al. (2020), 21 remain unconfirmed. Of these, 13 possess photometric redshifts below or around 1.2 and could thus be confirmed using GMOS or another ground-based multi-object spectrograph. As demonstrated in this chapter, low-resolution spectra are sufficient to confirm most of these sources, and the additional spectra could be used to perform an analysis of the stellar population of X-ray clusters with a more statistically significant sample. This analysis would be interesting in the context were very few studies that investigates colour bimodality and quenching in clusters were done with X-ray selected clusters. Most studies rely either on optically and infrared-selected clusters (e.g. Jian et al. 2018; Muzzin et al. 2012) or mixed samples (e.g. Old et al. 2020), despite tentative evidence that, unlike optically selected clusters, X-ray clusters do not always possess a prominent red sequence (Donahue et al. 2002; Willis et al. 2018).

More spectroscopic data could also form the basis of a spectroscopic analysis of the BCGs at $z \sim 1$ in X-ray selected clusters. There is evidence of moderate star formation in some high-redshift BCGs (Webb et al. 2015b) with possibly a transition in the triggering mechanism around $z \sim 0.8$ (McDonald et al. 2016). Further observation of clusters with blue BCG might allow to identify the mechanism involved at higher redshift, which remains poorly understood. Finally, more confirmed clusters would be a way to spot interesting targets, which could be further understood through follow-up studies. An example of such a study is presented in the following chapter.

3.6.2 Summary

Using spectroscopic nod-and-shuffle observation from GMOS, I have confirmed the redshift of three galaxy clusters. The fourth targeted candidate is composed of two independent structures, with no unambiguous indication that would permit the association of one or both of them with the extended X-ray emission.

Data were reduced using pyRAF version 2.1.15. The main steps of the data reduction process can be described as such:

1. For each object, the science frames were added together. The two blocks of charge resulting from the nod-and-shuffle observations were subtracted, creating an image with coupled positive and negative traces.

2. Each double science trace was cut from the main image, using a gradient image generated from the flat-fields to locate the traces.

3. Each trace was wavelength-calibrated, using the main emission line of a CuAr discharge lamps.

4. Each wavelength-calibrated negative trace was multiplied by -1 and summed along the slit axis. The positive traces were also summed and then each pair of traces was summed together to create an a one-dimension spectrum. The spectra of 43 of the 47 targeted objects were extracted. The few spectra that were not extracted are either absent or otherwise problematic.

5. The resulting spectra were Gaussian-filtered to reduce the noise levels.

In each spectrum, the H and K CaII doublet, the G Fraunhofer line, the [OII] and/or the [OIII] doublets were identified to determine the spectroscopic redshift. The spectroscopic redshift was then further confirmed by identifying some of the main Balmer lines and if possible several weaker calcium and iron absorption lines. Of the 43 objects with extracted redshift, 39 galaxies possess reliable redshifts. Three spectra belong to Milky Way's stars.

Starting with each galaxy spectrum in the field-of-view of a candidate cluster, I was able to identify cluster members using a recursive computation: at each step, the galaxy possessing the most discrepant radial velocity is discarded, until the greatest difference between the median and the velocities is less than three times the bi-weight scale. A cluster is considered confirmed if at least three member galaxies are located inside the X-ray emission and if no competing structure is identified. As three of the four targeted candidate clusters are now confirmed, the observing programs GS-2019B-Q-314 and GN-2019B-Q-326 were a success.

A comparison with the photometric-based analysis made in Trudeau et al. (2020) was made. Although the photometry and spectroscopy are globally consistent, the spectroscopy allowed the identification of members with weak star formation, a population that was overlooked by the photometric analysis.

Acknowledgements

Based on observations obtained at the international Gemini Observatory, a program of NSFs NOIRLab, which is managed by the Association of Universities for Research in Astronomy (AURA) under a cooperative agreement with the National Science Foundation on behalf of the Gemini Observatory partnership: the National Science Foundation (United States), National Research Council (Canada), Agencia Nacional de Investigación y Desarrollo (Chile), Ministerio de Ciencia, Tecnología e Innovación (Argentina), Ministério da Ciência, Tecnologia, Inovações e Comunicações (Brazil), and Korea Astronomy and Space Science Institute (Republic of Korea). Acquired through the Gemini Observatory Archive at NSFs NOIRLab and processed using the Gemini IRAF package.

Chapter 4

Linking the members star formation histories to the cluster mass assembly in the z = 1.98 galaxy cluster XLSSC 122

The material presented in this Chapter is accepted for publication in Monthly Notices of the Royal Astronomical Society under the title The XXL survey XLIX: linking the members star formation histories to the cluster mass assembly in the z=1.98 galaxy cluster XLSSC 122. The authors were A. Trudeau, J.P. Willis, D. Rennehan, R. E. A. C. Canning, A. C. C. Carnall, B. Poggianti, E. Noordeh and M. Pierre. I made the data analysis and wrote the article. Jon Willis reduced the HST data with the help of Rebecca Canning and Emil Noordeh. Douglas Rennehan queried the MultiDark Planck 2 simulations database to find dark matter haloes comparable in mass to XLSSC 122.

Abstract

The most massive protoclusters virialize to become clusters at $z \sim 2$, which is also a critical epoch for the evolution of their member galaxies. XLSSC 122 is a $z = 1.98$ galaxy cluster with 37 spectroscopically confirmed members. We aim to characterize their star formation histories and to put them in the context of the cluster accretion history. We measure their photometry in 12 bands and create a PSF-matched catalogue of the cluster members. We employ BAGPIPES to fit star formation histories characterized by exponentially decreasing star-forming rates. Stellar masses, metal and dust contents are also treated as free parameters. The oldest stars in the red-sequence galaxies display a range of ages, from 0.5 Gyr to

over ∼3 Gyrs. Characteristic times are between ∼0.1 and ∼0.3 Gyr, and the oldest members present the longest times. Using MultiDark Planck 2 dark matter simulations, we calculate the assembly of XLSSC 122-like haloes, weighted by the age posteriors of the oldest members. We found that 74% of these haloes were less than 10% assembled at the onset of star formation, declining to 67% of haloes when such galaxies had formed 50% of their z=1.98 stellar masses. When 90% of their stellar masses were formed, 75% of the haloes were less than 30% assembled. The star formation histories of the red-sequence galaxies seem consistent with episodes of star formation with short characteristic times. Onset and cessation of star formation in the oldest galaxies are both likely to precede XLSSC 122 virialization.

Keywords: galaxies: clusters: general – galaxies: clusters: individual: XLSSC 122 – galaxies: evolution – galaxies: high-redshift – galaxies: star formation

4.1 Introduction

Clusters of galaxies are the most massive gravitationally bound structures in the Universe. At optical and near infrared wavelengths, they appear as overdensities of galaxies (Abell 1958), hence the name. However, they are dark matter dominated objects (∼85 per cent of the mass) with stars accounting for less than 3 per cent of their total masses (e.g. Gonzalez et al. 2013; Sanderson et al. 2013; Chiu et al. 2016). The bulk of their baryonic mass budgets is formed by a hot X-ray emitting gas called the intracluster medium.

Galaxy cluster progenitors are loosely bound, unvirialised overdensities of galaxies called protoclusters (Chiang et al. 2013; Muldrew et al. 2015; Lovell et al. 2018), which typically exhibit elevated star-forming rates (SFRs) and large amounts of cold gas (e.g. Behroozi et al. 2013; Cucciati et al. 2014; Chiang et al. 2017; Oteo et al. 2018; Miller et al. 2018). These structures can be found as early as $z \sim 7-8$ (Ishigaki et al. 2016; Hu et al. 2021), although more records exist for protoclusters at reshifts close to $z \sim 6.5$ (Franck & McGaugh 2016; Calvi et al. 2019; Chanchaiworawit et al. 2019; Harikane et al. 2019; Higuchi et al. 2019). The number of these structures listed in the literature increases at lower redshifts (e.g. Toshikawa et al. 2014; Wang et al. 2016; Jiang et al. 2018; Kubo et al. 2019, 2021; Shi et al. 2019, 2021; Long et al. 2020; Calvi et al. 2021; Kalita et al. 2021).

Like clusters, protoclusters grow by merging with other structures (e.g. Behroozi et al. 2013; Wu et al. 2013; Muldrew et al. 2015; Klypin et al. 2016; Werner et al. 2022). Theoretically, the difference between clusters and protoclusters is that clusters are virialized (e.g. Chiang et al. 2013; Muldrew et al. 2015; Lovell et al. 2018). The epoch of the transi-

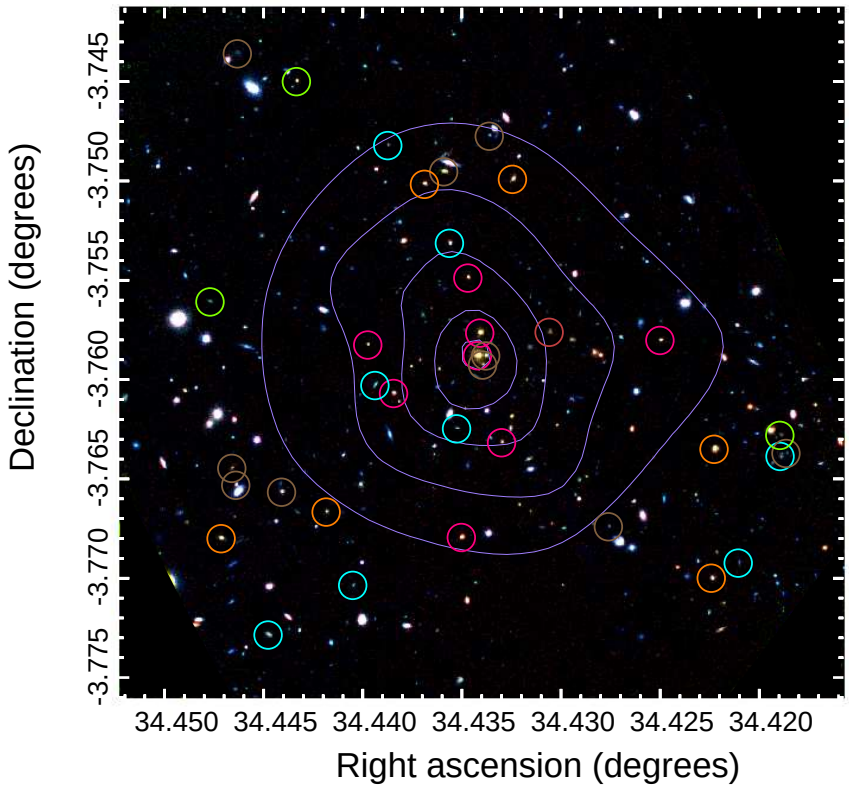

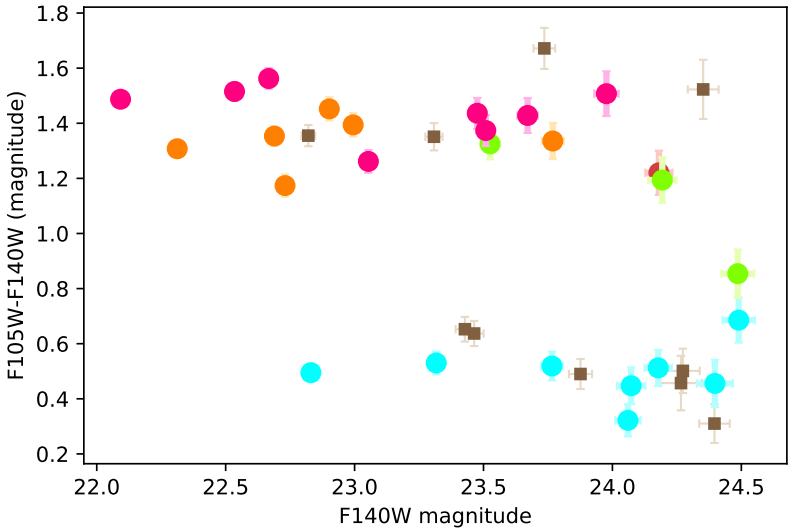

Figure 4.1: *Top*: Colour image of XLSSC 122, made with three bands: *F105W* (blue), *F140W* (green), and K_s (red). X-ray contours are drawn in violet. Spectroscopic members of the cluster are indicated by coloured circles. Colours refer to different ages (see Section 4.3.3): pink for the oldest members, orange for the old ones, green for the young galaxies and cyan for the star-forming members. A dust-rich member is indicated in red. Members with poor fits (see the bronze members in Section 4.3.2) are indicated in brown and not included in our analysis. *Bottom*: CMD diagram on XLSSC 122 members, using the same colour code.

tion from protoclusters to clusters varies with their masses: the most massive overdensities collapse first, around $z \sim 1.5-2$ (Chiang et al. 2013, 2017; Rennehan et al. 2020); the less massive ones might collapse as late as $z = 0$. However, authors usually rely on observables to distinguish between protoclusters and clusters: a cluster should present an X-ray emitting intracluster medium and/or a red sequence (Papovich et al. 2010; Gobat et al. 2011; Andreon et al. 2014; Muldrew et al. 2015).

The red sequence is the line formed on a colour-magnitude diagram (CMD) by the reddest galaxies. Most of these galaxies are quenched, i.e. they ceased most of their star formation at least 0.5 Gyr before the epoch of observation. Quenching is an evolutionary process affected by stellar mass and environment: in every environment, massive galaxies tend to be more quenched (e.g. Poggianti et al. 2006; Peng et al. 2010, 2012; Woo et al. 2013; Fossati et al. 2017; Kawinwanichakij et al. 2017; Jian et al. 2018; Lemaux et al. 2019). At $z \lesssim 1$, denser environments tend to increase the percentage of quenched galaxies for all masses (e.g. Balogh et al. 2004; Peng et al. 2010, 2012; Woo et al. 2013; Knobel et al. 2015; Balogh et al. 2016; Kawinwanichakij et al. 2017; Jian et al. 2018; Cora et al. 2019; Lemaux et al. 2019; Pintos-Castro et al. 2019), although the effect seems more dramatic on low mass galaxies. At high redshifts, several studies suggest that the galaxy quenched fraction is already enhanced in dense environments (e.g. Nantais et al. 2017; Lemaux et al. 2019; Strazzullo et al. 2019), but the strength of this enhancement seems to depend on the host halo mass-scale (Cerulo et al. 2016; Lemaux et al. 2019). Clusters of galaxies provide a gradient of dense environments, from the packed cores to the more scarcely populated outskirts (Balogh et al. 2000; Poggianti et al. 2008; Raichoor & Andreon 2012; Aguerri et al. 2018; Pintos-Castro et al. 2019; Werner et al. 2022) and are thus an ideal laboratory to understand how galaxy evolution is affected by environment at high redshifts.

Star formation in overdensities peaks at $z \sim 3$, earlier than in the field (e.g. Behroozi et al. 2013; Chiang et al. 2017; Muldrew et al. 2018). This is also the epoch where the first signatures of quenching are expected (Poggianti et al. 2006; Lovell et al. 2018; Muldrew et al. 2018) a prediction supported by the recent observations of quenched galaxies in $z \sim 3$ protoclusters (e.g. Shi et al. 2019, 2021; Kalita et al. 2021; Kubo et al. 2021). The epoch between $z \sim 2$ and $z \sim 1.5$ represents a transition time with the coexistence of several quiescent and starbursting massive galaxies in clusters (e.g. Strazzullo et al. 2013; Andreon et al. 2014; Fassbender et al. 2014; Webb et al. 2015a; Cooke et al. 2016; Coogan et al. 2018). Later, at $z < 1$, the evolution of the quenching fraction in clusters is mostly driven by intermediate and low-mass members (e.g. Bower et al. 1992; Poggianti et al. 2006; Raichoor & Andreon 2012; Behroozi et al. 2013; Alberts et al. 2014; Aguerri et al. 2018;

Pintos-Castro et al. 2019), the more massive galaxies being already quenched.

XLSSC 122 is a $z = 1.98$ galaxy cluster with 37 spectroscopically confirmed members (Willis et al. 2020) and a mass of $(6.3 \pm 1.5) \times 10^{13} M_{\odot}$ (Mantz et al. 2018, hereafter referred as XXL Paper XVII). It is thus an interesting target to probe a critical epoch for both cluster assembly and members' evolution. The intracluster medium of XLSSC 122 is detected as an extended X-ray emission and also as a Sunayev-Zel'dovich decrement (Mantz et al. 2014, also referred as XXL Paper V and XXL Paper XVII). Recently, Willis et al. (2020) found that XLSSC 122 has a prominent red sequence, with less luminous, less clustered blue cloud members. Figure 4.1 summarizes these observations: the top panel shows a three-coloured image of XLSSC 122, with the members highlighted and the X-ray contours overlaid; the bottom panel presents the colour-magnitude diagram of those members.

In this paper, we use Spectral Energy Distribution (SED) modelling to reconstruct the star formation histories of XLSSC 122 members and compare them with the cluster assembly. Both seem to be linked (Poggianti et al. 2006; Muldrew et al. 2018; Behroozi et al. 2019) but the mass scale of the haloes in which the firsts passive galaxy were quenched is unclear. Section 4.2 presents the building of the multiwavelength catalogue used to model the member SEDs. Section 4.3 presents the detail of this modelling and its main results, which are discussed and compared with the cluster assembly in Section 4.4. A summary of our main findings is given in Section 4.5. We assume $H_0 = 70$ km s^{-1}Mpc^{-1} with $\Omega_m = 0.3$ and $\Omega_\Lambda = 0.7$. Hence, at $z = 1.98$ the age of the Universe is 3.26 Gyrs and one arcsec corresponds to 8.38 kpc.

4.2 Construction of a multiwavelength catalogue

Our catalogue (available in the supplementary material online) contains 12 bands, which includes two *Hubble Space Telescope* (*HST*) images (*F105W* and *F140W*) and seven images coming from publicly available surveys. We direct the reader towards Willis et al. (2020) for a description of the data reduction process for the *HST* Wide-Field Camera 3 images. Y, J and K_s-band images were taken by the High Acuity Wide field K-band Imager (HAWK-I) mounted on the Very Large Telescope (VLT; Pirard et al. 2004; Casali et al. 2006; Kissler-Patig et al. 2008; Siebenmorgen et al. 2011). We also use observations from the Canada-France-Hawaii Telescope Legacy Survey (CFHTLS; Gwyn 2012), in the u, g, r and first generation i band. CFHTLS z-band image is heavily affected by fringing; we replaced it with z-band observations from the Hyper Suprime Camera Subaru Strategic

Program (HSC-SSP; Aihara et al. 2018a,b). We do not use other HSC-SSP observations as, surprisingly, an estimate of the depths based on the SExtractor noises showed that the corresponding CFHTLS observations are deeper. We completed the catalogue with *I1* and *I2* images taken by the Infrared Array Camera (IRAC), as part of the *Spitzer* Wide Infrared Extragalatic Survey (SWIRE).

Our catalogue consists of 37 entries, one for each spectroscopic member of XLSSC 122. These members were selected to be brighter than a magnitude of 25.5, measured within a 0.8 arcsec-wide aperture in the *F140W* filter (Willis et al. 2020). At $z = 1.98$, the *F140W* filter probes the SED beyond the 4000 Å break, making the sample selection relatively independant of the galaxy star-formation history. We note however that the *F140W* magnitude might be influenced by the presence of strong emission or absorption lines such as [OIII], H β or H γ, resulting in a weak bias towards star-forming galaxies in the faintest part of our sample.

4.2.1 Source extraction and aperture selection

Table 4.1: Summary of the sizes and properties of the applied apertures. The third column presents the percentage of the average flux densities within the apertures.

Band	Aperture diameter (arcsec)	Flux within 5σ detection (%)	(mag)
u	2.66	82 ± 5	25.9
g	2.45	83 ± 4	26.1
r	1.81	77 ± 4	25.9
i	2.13	78 ± 3	25.6
z	1.81	77 ± 5	25.0
Y	1.81	85 ± 6	24.8
F105W[a]	1.02	-	26.87
J	2.13	81 ± 4	24.2
F140W	1.02	77.8 ± 0.8	25.96
K_s	1.38	80 ± 2	24.3
I1[b]	3.73	78 ± 3	23.2
I2[b]	4.26	82 ± 3	22.5

[a] Since they have similar PSFs, we assumed that the best aperture for the convolved *F105W* image is equivalent to the best aperture for *F140W*.
[b] Apertures and percentages are based on the point source growth curves.

Source Extraction was performed with SExtractor version 2.5.0 (Bertin & Arnouts 1996). SExtractor detects the *F140W* sources using a pixel-based inverse variance weighting (IVM) and weights the photometry with the root mean square (RMS) variation per pixel. To facilitate source matching, *F105W* photometry is computed in dual image mode, using *F140W* as the detection image. These bands probe the SED before and after the 4000 Å break respectively. Thus, red-sequence galaxies are usually brighter in the *F140W* image, which motivates our choice to select it as our reference image for aperture corrections.

The *F105W* image is convolved with a Moffat kernel (Moffat 1969) to match its resolution with the *F140W*-band resolution. A suitable aperture for the *HST* images is selected by locating the confirmed members of XLSSC 122 in the *F140W* image. Their average growth curve is computed using 10 apertures between 0.18 and 2.28 arcsec in diameter. We apply strict contamination criteria: any members with neighbours brighter than its magnitude minus 3 (i.e. brighter than 6.4 per cent of its flux density) and closer than twice the full width at half maximum (FWHM) of the contaminating source is not included in the computation. We also did not include the Brightest Cluster Galaxy (BCG) and the three members closest to it in the aperture calculation, as they might be contaminated by intracluster light. However, we keep the BCG and ID 657 in the silver sample of our SED fitting results (see Section 4.3.2 and following). We aim to include about 80 per cent of the flux density within the chosen aperture. Thus, for the *HST* images, we selected the 1.02 arcsec aperture as the most suitable one (see Table 4.1).

We noticed a systematic astrometric offset between the *HST* images and their ground-based or *Spitzer* counterpart. Thus, we compute an astrometric correction of the first order using 200 sources, which were selected to possess *F140W* magnitudes similar to those of XLSSC 122 members. Each band photometry is computed in dual image mode, using the K_s band as the detection image. This choice was motivated by two considerations. First, SExtractor dual image mode can be used only on images with the same pixel size, which means that some bands must be resampled. Compared to *HST*, HAWK-I pixel size is closer to the original CFHT, HSC and IRAC pixel sizes. Secondly, sources can be reliably matched between the *F140W* and K_s band: 90 per cent of the 200 sources used for astrometry matching have separations inferior to 0.24 arcsec between these two bands.

The aperture sizes of the ground-based images are chosen as described above, but with test apertures between 0.64 and 5.11 arcsec, which are better adapted to the resolutions of these bands. Results are shown in Table 4.1. However, due to the lower resolution of *Spitzer* IRAC, we are unable to find a sufficient number of isolated XLSSC 122 members

to compute an average member growth curve for *I1* and *I2*. We thus assume that they are unresolved and choose apertures containing approximately 80 per cent of the flux density of a point source. The IRAC data are also subject to colour-dependent flat-field errors. We account for them by increasing the IRAC flux density errors by 10 per cent of the flux density values, added in quadrature.

4.2.2 Correction factors

To account for the difference in resolution between the *HST* images and the other data, we apply aperture correction factors. We base our computations on the Newman et al. (2012) method: we convolve our *F140W* image with different Moffat kernels. Then, we select the convolved images possessing the closest point spread function (PSF) to the ground-based and IRAC images by comparing the average growth curves of their point sources.

The aperture correction factors are computed object-by-object, by comparing the galaxy flux density in the original *F140W* image to its flux density in the convolved image. Thus, for band X, the correction factor a_X and the corrected flux density $F_{X,corr}$ are given by:

$$a_X = \frac{F_{140W}}{F_{140W,X}} \tag{4.1}$$

and,

$$F_{X,corr} = a_X F_X, \tag{4.2}$$

where F_{140W} is the flux density of the considered source in the *F140W* image, measured in a 1.02 arcsec aperture, and $F_{140W,X}$ is the flux density in the convolved image, measured within the aperture selected for band X. F_X is the flux density measured in band X. Since we are interested in 37 galaxies only, all within a single image, we deemed it preferable to compute correction factors for every cluster member rather than one per band as Newman et al. (2012) did. Furthermore, correction factors are more spread per band than they are per object. To account for possible small differences between the convolved and ground-based image PSFs, we add in quadrature 5 per cent of the correction factor value to its errors.

4.3 Results

4.3.1 SED modelling

We perform the SED modelling with the python-based package Bayesian Analysis of Galaxies for Physical Inference and Parameter EStimation (BAGPIPES) version 0.8.4 (Carnall et al. 2018). BAGPIPES is a Bayesian SED modelling and fitting code, that generates SED models based on Bruzual & Charlot (2003) stellar population models and explores the parameters space with MultiNest (Feroz & Hobson 2008; Feroz et al. 2009, 2019; Buchner 2014) a nestled sampling algorithm. We use uniform priors. The merit function quantifying the match between a model and the photometric data is evaluated by the following likelihood (Carnall et al. 2018):

$$\ln(\mathscr{L}) = -0.5\sum_i \ln\left(2\pi\sigma_i^2\right) - 0.5\sum_i \frac{\left(f_i - f_{m,i}\right)^2}{\sigma_i^2}, \tag{4.3}$$

where f_i are the observed flux densities (in μJy), σ_i their errors, and $f_{m,i}$ are the flux densities predicted by the tested model.

We assume a simple star formation history, described by five free parameters. Two describe an exponentially decreasing star-forming rate: the age of the oldest stars and the characteristic time (τ). The other free parameters control the dust extinction (A_v), following a Calzetti et al. (2000) extinction curve, the metallicity (Z), and the logarithm of the total stellar mass formed, expressed in solar units. Prior intervals displayed in Table 4.2 are uniformly weighted. Redshifts are set to the values measured by Willis et al. (2020) and each MultiNest run is initiated with a thousand live points.

Table 4.2: List of the parameter priors, expressed in term of minimum and maximum allowed values.

Parameter	Unit	Minimum	Maximum
Age	Gyr	0.01	3.26[a]
τ	Gyr	0.01	3.26[a]
A_v	mag	0	2.5
Z	$Z_\odot$	0	5
Mass	$\log\left(\frac{M}{M_\odot}\right)$	9	13

[a] Age of the Universe at z=1.98.

4.3.2 Assessing the fit quality

We assess the quality of the resulting fits with the following criteria:

1. The number of degrees of freedom in the fit must be one or more. This effectively means that a member must be detected in at least six bands.

2. There should be flux measurements in both *HST* bands (*F105W* and *F140W*). These two bands put the furthest constrains on the fit, as they are the deepest and probe the SED before and after the 4000 Å break.

3. The most likely SED model must have a reduced χ^2 (χ^2_ν) inferior to 6. For a fit with seven degrees of freedom (i.e. with detections in every band), $\chi^2_\nu = 6$ corresponds to a difference of 5σ between the fit and the data points.

These criteria are met by 26 members, which are highlighted by coloured circles and dots in Figure 4.1. The 11 other members, called 'bronze members', are indicated in brown and are not included in our analysis.

For those 26 members, we define another criterion, meant to distinguish between those with well-behaved photometric data (gold members) and those where contamination by nearby sources might make the photometry less reliable:

4. When assembling the aperture corrected photometry of members, we flagged photometric data that might be blended with another object, or significantly polluted by the light of a neighbouring detection. We require a good fit to have no photometric data points flagged, with the exception of the two IRAC data points, which tend to be systematically contaminated because of their resolution.

4.3.3 Age and characteristic time

We find that the ages of the oldest stars in XLSSC 122 form a continuum: the peaks of the age distributions (i.e. the modal ages) vary from less than 0.2 Gyr to close to the age of the Universe (3.26 Gyrs at z=1.98). Red-sequence members all have short characteristic times ($\lesssim$ 0.3 Gyr), in contrast to poorly constrained τ displayed by most of the blue cloud members. We define four main categories of members, based on the medians of the age and characteristic time posteriors:

1. Very old members: display median ages above 1.75 Gyrs.

2. Old members: display median ages between 0.75 and 1.75 Gyrs.

3. Young members: display ages younger than 0.75 Gyr, with median τ shorter than 1 Gyr.

4. Star-forming members: display ages younger than 0.75 Gyr, with median τ greater or equal to 1 Gyr.

Throughout this paper, we will refer to the members of the very old, old and young age categories as the evolved members. The age categories of each member are presented in Table 4.3 along with their coordinates, redshift, *F140W* magnitude and quality category. For convenience, we adopt Willis et al. (2020) IDs. Figures 4.2 to 4.5 show the posterior distributions of ages and characteristic times, as well as their degeneracies. Four examples of a complete set of parameters distributions and degeneracies are given in the Appendix 4.5.

The oldest members, presented in Figure 4.2, are characterised by relatively broad age posterior distributions, with the 1σ confidence region usually covering the interval between 1.5 and 3 Gyrs. Characteristic time posterior distribution are consistent with $\tau \lesssim 0.5$ Gyr, although they tend to be broader than for other evolved members, due to the degeneracies with the age distributions. In the top panel of Figure 4.1, these members are concentrated within the cluster core: the average projected distance to the BCG is 147 kpc (for the old, young and star-forming members the average distances are respectively 380, 473, and 347 kpc). In contrast to this, old members, shown in Figure 4.3 present various intermediate posterior distributions between the broad age posteriors of the oldest members and the peaked ones of the young members. The τ distributions suggest short characteristic times, usually approximately equal or smaller than 0.3 Gyr. Both the young and star-forming members (Figures 4.4 and 4.5) are younger than 0.75 Gyr. Young and star-forming members are differentiated by the shape of their τ posterior distributions: shorter than 0.2 Gyr and degenerate with the age distribution for the young members; very poorly constrained and independent from the age distribution (or any other fitted parameters) for the star-forming members. Their location on the CMD diagram are also different: the star-forming members populate the blue cloud while the young members reside in the red sequence, with the exception of ID 522.

Table 4.3: Member ID, position, quality of the fit and age categories. The medians of the age, characteristic time and stellar mass distributions are also presented.

ID[a]	RA[b] (deg)	Dec [b] (deg)	Redshift[a]	*F140W* magnitude	Quality	Age class	Median age (Gyr)	Median τ (Gyr)	Median mass[c] ($\log_{10}(M/M_{\odot})$)
526	34.4342	-3.7588	1.98	22.09 ± 0.02	silver	very old	2.24	0.28	11.20
451	34.4223	-3.7635	1.98	22.31 ± 0.02	gold	old	1.29	0.24	10.92
657	34.4341	-3.7577	1.98	22.53 ± 0.02	silver	very old	2.33	0.27	11.02
295	34.4353	-3.7680	1.99	22.67 ± 0.02	gold	very old	2.49	0.34	11.00
1032	34.4325	-3.7499	1.98	22.69 ± 0.02	gold	old	1.64	0.09	10.74
240	34.4224	-3.7700	1.98	22.73 ± 0.03	gold	old	0.96	0.06	10.47
1064	34.4359	-3.7495	1.99	22.82 ± 0.03	bronze	-	-	-	-
917	34.4356	-3.7531	1.96	22.83 ± 0.03	gold	star-forming	0.15	2.03	10.01
298	34.4472	-3.7680	1.99	22.90 ± 0.03	gold	old	0.93	0.07	10.60
1050	34.4369	-3.7502	1.98	22.99 ± 0.03	gold	old	1.68	0.12	10.73
606	34.4385	-3.7607	1.97	23.05 ± 0.03	silver	very old	2.31	0.47	10.76
236	34.4516	-3.7703	1.98	23.30 ± 0.07	bronze	-	-	-	-
642	34.4338	-3.7588	2.04	23.31 ± 0.03	bronze	-	-	-	-
145	34.4448	-3.7729	1.98	23.32 ± 0.03	gold	star-forming	0.03	1.94	9.74
372	34.4441	-3.7657	1.96	23.43 ± 0.04	bronze	-	-	-	-

Table 4.3: Member ID, position, quality of the fit and age categories. The medians of the age, characteristic time and stellar mass distributions are also presented.

ID[a]	RA[b] (deg)	Dec [b] (deg)	Redshift[a]	*F140W* magnitude	Quality	Age class	Median age (Gyr)	Median τ (Gyr)	Median mass[c] ($\log_{10}(M/M_{\odot})$)
402	34.4464	-3.7653	1.97	23.46 ± 0.04	bronze	-	-	-	-
734	34.4250	-3.7580	2.00	23.48 ± 0.04	gold	very old	1.86	0.12	10.60
845	34.4347	-3.7549	1.98	23.51 ± 0.04	gold	very old	2.47	0.28	10.43
1220	34.4434	-3.7450	1.98	23.53 ± 0.04	silver	young	0.68	0.07	10.10
493	34.4330	-3.7632	1.96	23.67 ± 0.04	silver	very old	2.21	0.17	10.52
649	34.4340	-3.7593	2.00	23.74 ± 0.04	bronze	-	-	-	-
603	34.4394	-3.7603	1.98	23.77 ± 0.04	gold	star-forming	0.34	1.80	9.72
345	34.4419	-3.7667	1.99	23.77 ± 0.04	silver	old	1.62	0.33	10.12
1141	34.4336	-3.7478	1.96	23.88 ± 0.04	bronze	-	-	-	-
730	34.4398	-3.7583	1.99	23.98 ± 0.05	gold	very old	2.30	0.44	10.52
547	34.4353	-3.7625	1.96	24.06 ± 0.05	gold	star-forming	0.14	1.88	9.24
452	34.4190	-3.7639	1.97	24.07 ± 0.06	silver	star-forming	0.60	1.82	9.63
229	34.4405	-3.7704	1.98	24.18 ± 0.05	silver	star-forming	0.16	1.75	9.46
726	34.4306	-3.7576	1.97	24.18 ± 0.05	gold	dusty[d]	2.22	1.55	10.60
806	34.4477	-3.7561	1.98	24.19 ± 0.05	gold	young	0.63	0.11	9.71

Table 4.3: Member ID, position, quality of the fit and age categories. The medians of the age, characteristic time and stellar mass distributions are also presented.

ID[a]	RA[b] (deg)	Dec [b] (deg)	Redshift[a]	*F140W* magnitude	Quality	Age class	Median age (Gyr)	Median τ (Gyr)	Median mass[c] ($\log_{10}(M/M_{\odot})$)
1253	34.4463	-3.7436	2.02	24.27 ± 0.08	bronze	-	-	-	-
466	34.4187	-3.7637	1.98	24.27 ± 0.07	bronze	-	-	-	-
428	34.4466	-3.7645	1.98	24.35 ± 0.06	bronze	-	-	-	-
329	34.4276	-3.7674	1.97	24.40 ± 0.06	bronze	-	-	-	-
263	34.4211	-3.7692	1.98	24.40 ± 0.07	silver	star-forming	0.19	1.93	9.50
522	34.4190	-3.7628	1.96	24.49 ± 0.06	silver	young	0.41	0.06	9.53
1125	34.4387	-3.7482	2.00	24.49 ± 0.06	silver	star-forming	0.32	2.03	9.63

[a] IDs and spectroscopic redshifts are from Willis et al. (2020).

[b] Positions are based on the *F140W* band astrometry.

[c] This is the current stellar mass, while the fitted free parameter is the total stellar mass formed during the star formation history.

[d] The only galaxy that does not fit into a category. See Appendix 4.5 for more details.

We note however that while the exponentially decreasing modelling provides an easy-to-interpret overview of the star formation history in XLSCC 122 members, detailed star formations histories are likely to be more complex and varied (e.g. Sparre et al. 2015; Leja et al. 2019; Tacchella et al. 2022). For example, mergers might generate more complex star formation histories. Massive clusters members are often the product of dry or wet mergers (Brodwin et al. 2013; Cattaneo et al. 2013; Cooke et al. 2015; Wagner et al. 2015) which might bring together galaxies with different star formation histories, or, in the case of wet mergers, trigger a temporary increase of the star-forming rate.

Another element to consider is the impact of the assumed prior on to the recovered star formation histories. For example, Carnall et al. (2019a) show that simple τ-models, such as the ones employed here, struggle to recover constant or rising star formation rates, which might explain why the characteristic times of our star-forming members are so poorly constrained. To overcome the limitations of simple τ-models, several ideas have been proposed: delayed τ-models (e.g. Pacifici et al. 2013; Simha et al. 2014), log-normal models (e.g. Diemer et al. 2017), double power laws (e.g. Carnall et al. 2018) or non-parametric modelling (e.g. Iyer et al. 2019; Leja et al. 2019) constitute a non-exhaustive list.

4.3.4 Testing the dependence upon the assumed star formation model

In order to assess the dependence of our results on the assumed star formation history, we tested the effect of a change of the model. BAGPIPES offers six basic parametric star formation histories, ranging from a total of four to six free parameters (assuming that the stellar mass, the metal and dust contents are allowed to vary). More complex models can be build by combining several parametric models together (for more detail, see Sections 3.1.2 and 4.2 of Carnall et al. 2018). However, given the quality of our data, a six-parameter model such as a double power law (Behroozi et al. 2013; Carnall et al. 2018) tends to generate poorly constrained results, especially for the less luminous members of the red sequence.

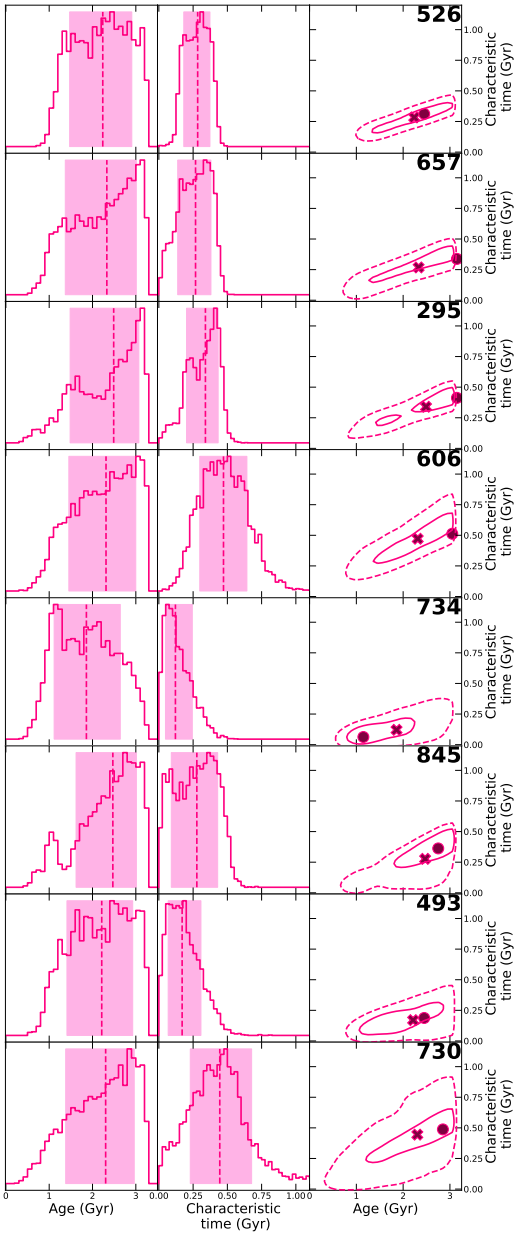

Figure 4.2: *Left*: Posterior distributions of the age of the oldest stars for every member classified as very old. The dashed lines are the distribution medians and the shaded regions correspond to the intervals between the 16th and 84th percentiles. *Centre*: Posterior distributions for the characteristic time. *Right*: Smoothed 1 and 2σ contours for the degeneracy between age and τ. The distributions medians and modes are represented by Xs and dots respectively. Each member ID is shown on the top right corner of its degeneracy plot.

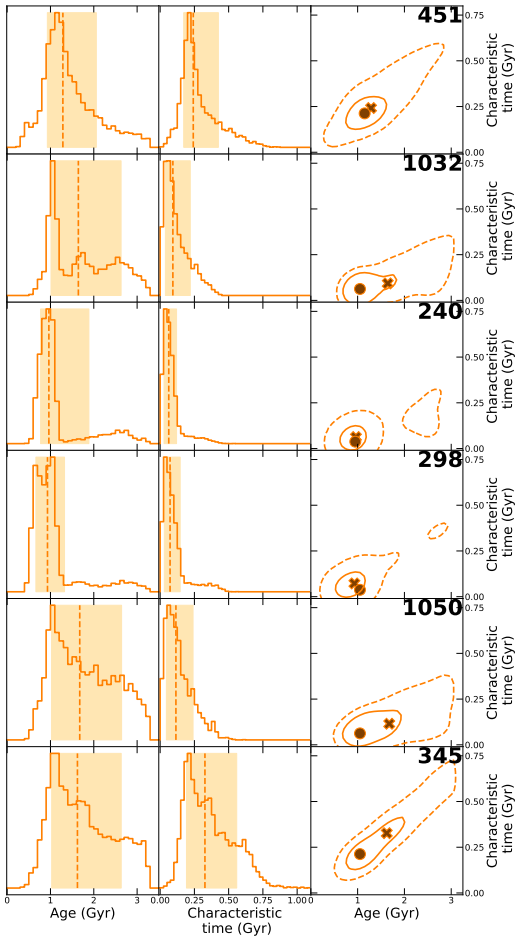

Figure 4.3: Posterior distributions of the ages and characteristic times of the old members, along with their degeneracies. Lines and contours definition are given in Figure 4.2.

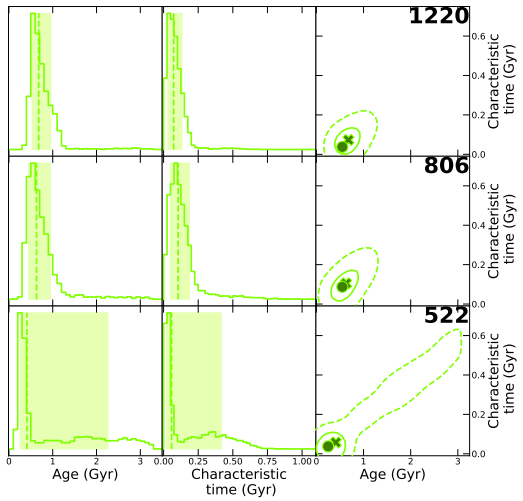

Figure 4.4: Posterior distributions of the ages and characteristic times of the young members, along with their degeneracies. Lines and contours definition are given in Figure 4.2.

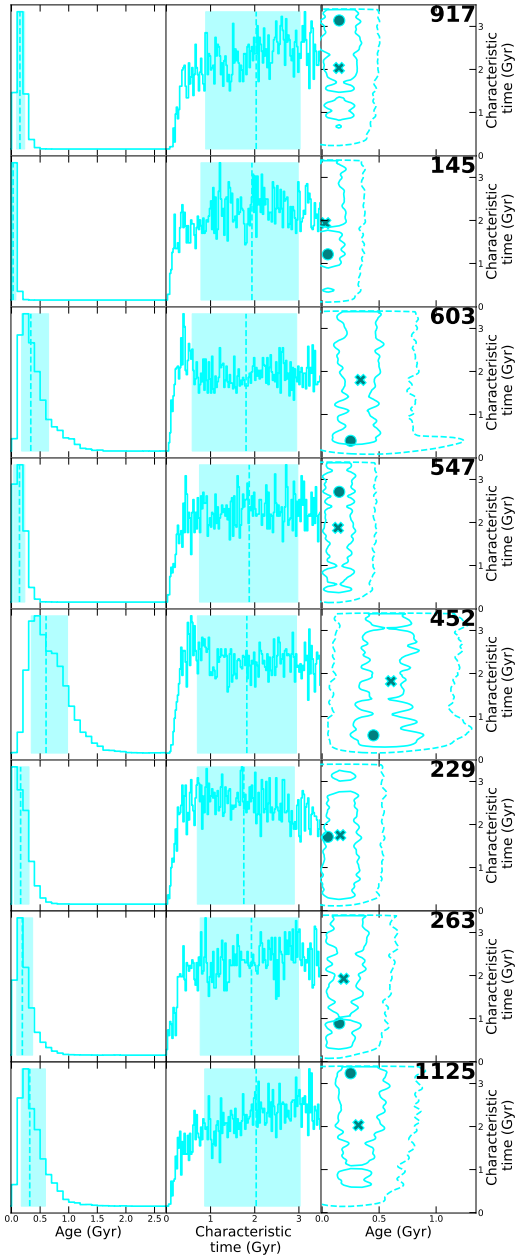

Figure 4.5: Posterior distributions of the ages and characteristic times of the star-forming members, along with their degeneracies. Lines and contours definition are given in Figure 4.2.

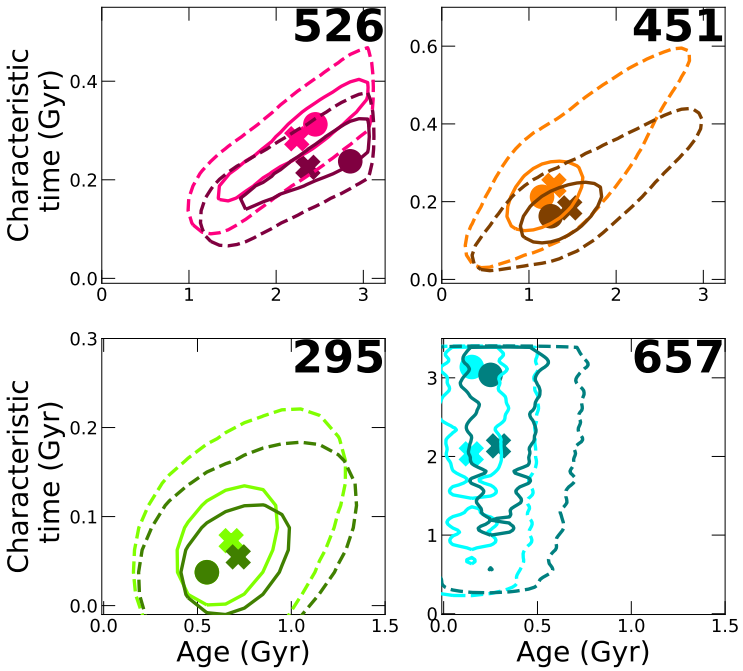

Figure 4.6: Comparison between the age-characteristic time degeneracies of the simple and delayed τ-models, for representative members of the four age categories. The simple τ-model degeneracies follow the colour scheme introduced in Figure 4.1 (pink for very old, orange for old, green for young, and cyan for star-forming) with the delayed τ-model degeneracies overlaid in darker colours. The 1 and 2σ degeneracies are represented by full and dashed contours respectively.

With the exception of the constant, rectangularly shaped star formation history and the currently used τ-model, all of the five parameters models available rely on the assumption that the star formation declines more slowly than it rises. Among those, the delayed τ-model has the form:

$$\mathrm{SFR(t)} \propto \begin{cases} (t-t_0)e^{-(t-t_0)/\tau} & \text{if } t \geq t_0 \\ 0 & \text{else} \end{cases} \tag{4.4}$$

where t_0 is the formation time of the oldest stars and τ is the characteristic time, or

$$\mathrm{SFR(a)} \propto \begin{cases} (a_0-a)e^{-(a_0-a)/\tau} & \text{if } a \leq a_0 \\ 0 & \text{else} \end{cases} \tag{4.5}$$

when expressed in term of ages. In this latter form, a_0 is the age of the oldest stars.

The similarities between the parameters of the simple and delayed τ-model allow us to compare the results of the two models directly. The results of such a comparison are

presented in Figure 4.6 for four representative galaxies. For the evolved members, the distributions of the age of oldest stars remain similar between the models but the characteristic times of the delayed model are slightly shifted towards lower values. For the star-forming members, we observe a shift towards higher ages.

This behaviour can be understood if one notes that the SED photometric data essentially constrains the duration and last epoch of major star formation in any model fit. The passive nature of the evolved members places a firm constraint on the age at which star formation must end in these systems. The delayed τ-model differs from the simple τ-model in that the star formation rate takes an amount of time equivalent to the value of τ to rise from zero star formation to a maximum value, from which it then declines. As the SED photometric data constrains the duration of star formation in the fitted model, the effect of adding this early time behaviour to the model (effectively an additional τ of rising star formation) is compensated for in the fitting procedure by reducing the overall τ value of the model. In this sense the slightly different results generated by the two star formation models can be understood. Each model generates fits of equivalent statistical merit and, with no direct evidence available to constrain the form of the SFR(t), we adopt the simple τ-model as our baseline model yet note the minor numerical differences between the two models that propagate through our later analyses as they arise in the paper.

4.3.5 Mock photometry fits for two population SEDs

To explore the effects upon the SED fitting process of the presence of more than one stellar population in a galaxy, we created mock observations characterised by two episodes of star formation with exponentially declining star-forming rates. We then fitted them with a simple τ-model, as described in Section 4.3.1. The first episode starts 2 Gyrs ago and possesses a characteristic time of 300 Myr; the other begins 150 Myr ago and has $\tau = 2$ Gyrs. The contribution of the second episode varies from 2 to 40 per cent of the total stellar mass formed, which is fixed to 10^{11} $M_{\odot}$. Metallicity is set to $Z_{\odot}$ and dust extinction to 0.8 magnitude. Photometric errors are estimated by calculating the average photometric errors of the very old and star-forming members. Those averages are multiplied by the fraction of 'old' and 'young' components and then summed. Figures are presented in Appendix 4.5. We found that when the younger component accounts for 4 per cent or more of the total stellar mass, the recovered τ posterior is poorly constrained, like in the star-forming members. Additionally, when the younger component represents $\gtrsim 20$ per cent of the stellar mass, the recovered median age starts to be consistent with our criterion for star-forming

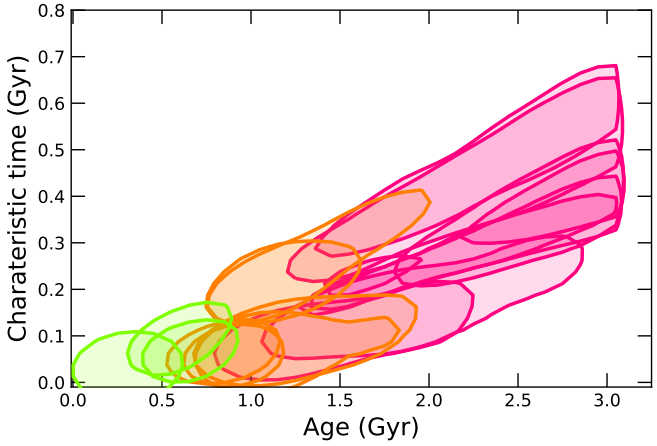

Figure 4.7: The 1σ degeneracies between age and characteristic time, for each evolved member. Same colour scheme as before.

members.

This allow us to place further constraints on the stellar population of each age category. Very old members contain less than 4 per cent of young stars: otherwise the confidence interval of their characteristic time posterior would be 1 Gyr broad or more. For the same reason, old and young members are unlikely to host significant populations of newly formed stars. In contrast, star-forming member members might possess up to 80 per cent of older stars.

4.4 Discussion

4.4.1 XLSSC 122 star formation history and its implications

The bottom panel of Figure 4.1 shows that the colour bimodality observed in XLSSC 122 corresponds to different star formation histories for the red sequence and the blue cloud. The former displays ages varying from approximately 0.5 to 3 Gyrs and short characteristic time-scales while the latter is more uniform, with ages younger than ~ 0.6 Gyr and, at the exception of ID 522, poorly constrained characteristic times.

This relative homogeneity might be explained by different factors. Several authors (e.g. Li & Han 2007; Carnall et al. 2019a) found that parametric stellar population models tend to be biased towards younger stellar ages, especially if more than one population are present. Our own tests, presented in Section 4.3.5, show that above a certain percentage of

young stars, it becomes very difficult to determine whether an older component is present or not. Thus, we cannot determine if our star-forming members experienced a prolonged star formation activity.

For the red-sequence members, the characteristic time distributions are short and relatively well-constrained. This observation argues against the occurrence of more than one major epoch of star formation per galaxy, despite the variety of ages observed. We note however that the oldest galaxies age posteriors are broad. This might either indicate the presence of two or several evolved stellar populations close in ages, perhaps brought together by mergers (e.g. Cooke et al. 2015), or arises from the difficulty of constraining the ages of evolved stellar populations, especially when the available observations place only limited constrains on the metallicity and dust content (e.g. Conroy 2013; Carnall et al. 2020, see also the examples of full parametric distributions in Appendix 4.5). The inclusion of near-infrared and/or mid-infrared data with a good resolution (Conroy 2013; Carnall et al. 2019b) would help us to further constrain the fits; photometric or spectroscopic observations from the newly launched *James Webb Space Telescope* would be ideal in that regard. More realistically, medium-bandwidth photometry in the H and J filters (e.g. Straatman et al. 2016) would increase our coverage of the SED close to the 4000 Å break.

Figure 4.7 shows the 1σ degeneracy between age and characteristic time, for the evolved members. There is a distinct trend: the younger the member the shorter the characteristic time. This observation suggests an increase of the quenching efficiency with time, possibly due to the cluster mass increase over time. There is a mixed set of precedents: some authors find an increase of quenching efficiency with time in high-redshift groups and clusters (e.g. Nantais et al. 2016, 2017; Kawinwanichakij et al. 2017) while others found a decrease (e.g. Balogh et al. 2016; Foltz et al. 2018) or a constant efficiency (e.g. Lemaux et al. 2019). These discrepant measurements might point towards a dependence of the quenching efficiency on the halo mass, i.e. larger structures being more effective in quenching galaxies than groups (e.g. Peng et al. 2010, 2012; Balogh et al. 2016; Foltz et al. 2018), although this is again controversial (e.g. Fossati et al. 2017).

4.4.2 Link with the cluster assembly history

To investigate XLSSC 122 assembly history, we select 500 dark matter haloes in the MultiDark Planck 2 simulation (Klypin et al. 2016), with M_{500} masses between $4.3 \times 10^{13}\ M_{\odot}$ and $8.3 \times 10^{13}\ M_{\odot}$ at $z = 1.98$. This mass interval is centred on our best estimate of the XLSSC 122 mass, $6.3 \times 10^{13}\ M_{\odot}$, and is likely to encompass its true mass as it is slightly

larger than the 1σ confidence interval $\pm 1.5 \times 10^{13}\ M_{\odot}$. We then determine the percentage of its $z = 1.98$ mass accreted by each halo at any earlier epochs. We organize the results by intervals of 10 per cent, from less than 10 per cent to more than 90 per cent assembled. Figure 4.8 shows the evolution with time of the fraction of haloes that are less than 50 per cent assembled.

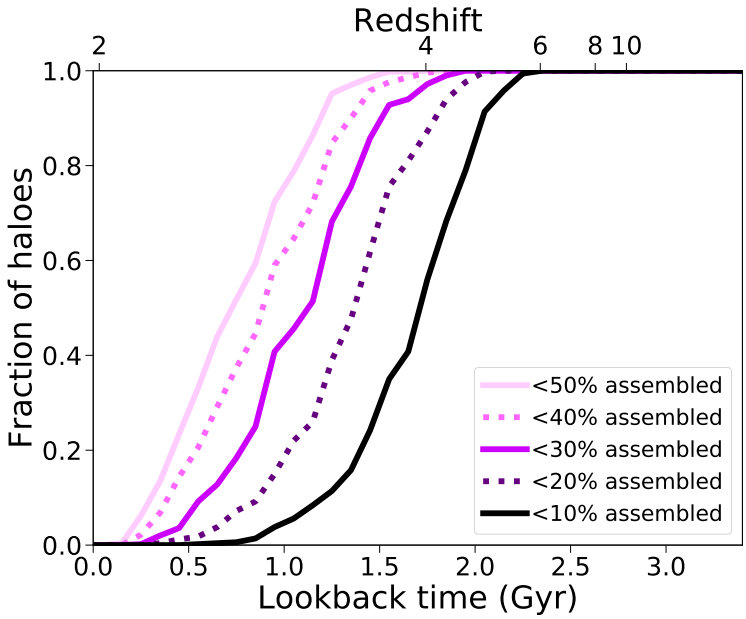

Figure 4.8: Evolution with the time of the fraction of the XLSSC 122-like simulated haloes that are less than 10% assembled, 10 to 20% assembled, etc. Simulated haloes assemblies are colour-coded, from black (less than 10% assembled) to pale lilac (more than 50%) assembled

Before $z = 6$ (2.34 Gyrs before $z = 1.98$), none of the dark matter haloes had accreted more than 10 per cent of its z=1.98 mass, in contrast to the wide range of accreted fractions possible at $z = 3.5$ (1.48 Gyrs before $z = 1.98$). This variety of accreted fractions at later times is representative of the variety of the assembly histories: some haloes will reach their final mass via multiples minor merging events, while others will experience a few major mergers, sometimes accreting more than 30 per cent of their $z = 1.98$ masses in a single time step.

The left panel of Figure 4.9 presents a comparison between the age posterior distribution of the BCG (a_0) with the time at which each simulated halo becomes at least 10 per cent assembled. The 10 per cent assembly times for the simulated haloes correspond roughly to the younger half of the posterior distribution, showing that the onset of star formation occurred long before virialization.

We then quantitatively compare the fitted star formation histories of the member galaxies with the mass assembly histories of the simulated haloes by weighting them by the age posterior. For example, the weighted fraction of haloes that have accreted less than 10 per cent of their $z = 1.98$ masses is given by:

$$f_{form,<10\%} = \sum_t P_{age}(t) \times f_{<10\%}(t), \tag{4.6}$$

where $P_{age}(t)$, the probability that star formation started at time t, is given by the value at t of the normalized age posterior of the galaxy. The term $f_{<10\%}(t)$ is the fraction of simulated haloes that have accreted less than 10 per cent of their $z = 1.98$ masses at t. We can similarly compute $f_{form,10-20\%}$, the weighted fraction of haloes that have accreted between 10 and 20 per cent of their mass, and so on. Table 4.4 shows the weighted fraction of haloes that have accreted less than 10, 20, 30 or 40 per cent of their masses at the time of the onset of the star formation in the very old cluster members. The bottom line shows that, on average, 74 per cent of the haloes had accreted less than 10 per cent of their mass when the very old members began to form their stars.

The τ-model used to determine the star formation histories does not allow us to directly determine a quenching time. Instead, we use the time-scales at which cluster members formed 50 and 90 per cent of their stellar masses as proxies to place this event in the cluster accretion history. To calculate t_X, the time when a fraction X of the stellar mass was formed, one must solve the following equation:

$$\int_{t_0}^{t_X} \mathrm{SFR}dt = X \int_{t_0}^{t_{obs}} \mathrm{SFR}dt, \tag{4.7}$$

where t_0 is the formation time of the oldest stars and t_{obs} the epoch at which we observe the galaxy. Thus, the age posterior is given by $a_0 = t_{obs} - t_0$. Due to the simplicity of the τ-model this equation has an analytical solution:

$$t_X - t_0 = -\tau ln[Xe^{-(t_{obs}-t_0)/\tau} - X + 1]. \tag{4.8}$$

We then define $a_X = t_{obs} - t_X$ the time since a fraction X of the star were formed, and reorganise the equation to get:

$$a_X = \tau ln[Xe^{-(a_0)/\tau} - X + 1] + a_0. \tag{4.9}$$

The central and right panels of Figure 4.9 compare the times at which each simulated halo becomes at least 10 per cent assembled to respectively the $a_{0.5}$ and $a_{0.9}$ 'posteriors' for

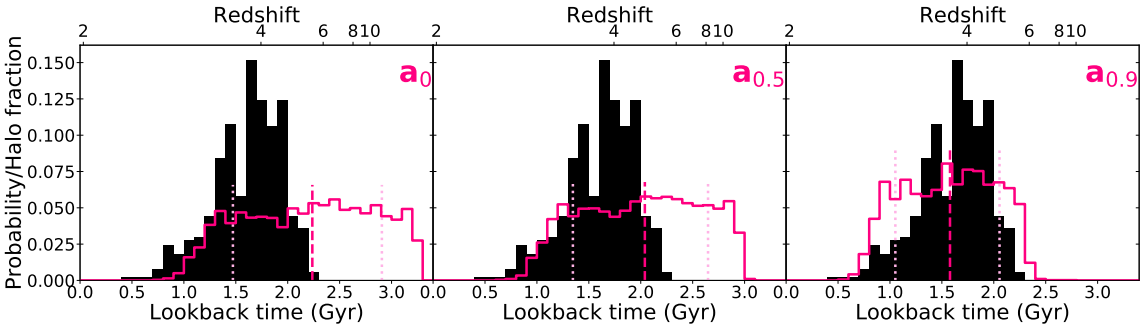

Figure 4.9: *Left*: Comparison between the time at which each simulated halo becomes 10 per cent assembled or more (black histogram) and the posterior of the age of the oldest stars in the BCG. The posterior is traced in pink, and its median is indicated by a pink dashed line. The dotted light pink lines show the edges of its 1σ confidence interval. *Centre*: Comparison between the time at which each halo becomes 10 per cent assembled and the distribution corresponding to the time-scale at which the BCG formed 50 per cent of its stellar mass (i.e. $a_{0.5}$). *Right*: Comparison between the time at which each halo becomes 10 per cent assembled and the $a_{0.9}$ distribution.

the BCG. The BCG acquires 90 per cent of its stellar mass on approximately the same time-scale for the simulated haloes to become 10 per cent assembled.

By replacing $P_{age}(t)$ in Equation 4.6 by probabilities drawn from the $a_{0.5}$ and $a_{0.9}$ posteriors, we compute the fraction of haloes less than 10 per cent assembled when the first galaxies had formed 50 or 90 per cent of their stellar masses. Results are given in Tables 4.5 and 4.6. We thus determine that 67 per cent of the haloes had accreted 10 per cent of their masses when the oldest members had 50 per cent of their own stellar masses formed. Although there is more variability than for the onset of star formation, we also compute

Table 4.4: Cumulative fractions of XLSSC 122 haloes that are <10% assembled, <20% assembled, etc., integrated over the age distributions of the oldest members.

ID	<10%	<20%	<30%	<40%
526	0.75	0.87	0.94	0.97
657	0.74	0.85	0.91	0.95
295	0.78	0.88	0.93	0.96
606	0.75	0.86	0.92	0.95
734	0.60	0.74	0.84	0.91
845	0.81	0.88	0.92	0.95
493	0.72	0.84	0.91	0.95
730	0.75	0.85	0.91	0.94
Average	0.74	0.85	0.91	0.95

Table 4.5: Cumulative fraction of XLSSC 122-like haloes that are partially assembled, integrated over the time distributions corresponding to the formation of 50% of the stellar masses of the oldest members.

ID	<10%	<20%	<30%	<40%	<50%
526	0.68	0.83	0.91	0.95	0.98
657	0.69	0.81	0.89	0.93	0.96
295	0.73	0.84	0.90	0.94	0.96
606	0.64	0.78	0.87	0.92	0.95
734	0.56	0.71	0.82	0.89	0.93
845	0.77	0.86	0.91	0.94	0.96
493	0.68	0.81	0.89	0.94	0.96
730	0.64	0.77	0.86	0.91	0.94
Average	0.67	0.80	0.88	0.93	0.96

Table 4.6: Cumulative fraction of XLSSC 122-like haloes that are partially assembled, integrated over the time distributions corresponding to the formation of 90% of the stellar masses of the oldest members.

ID	<10%	<20%	<30%	<40%	<50%	<60%	<70%
526	0.43	0.65	0.79	0.87	0.93	0.96	0.98
657	0.50	0.67	0.80	0.87	0.92	0.95	0.97
295	0.50	0.68	0.80	0.87	0.91	0.94	0.97
606	0.18	0.39	0.58	0.71	0.79	0.85	0.90
734	0.44	0.62	0.75	0.84	0.89	0.93	0.96
845	0.55	0.74	0.84	0.90	0.94	0.96	0.97
493	0.53	0.70	0.81	0.88	0.93	0.95	0.97
730	0.25	0.44	0.59	0.70	0.77	0.83	0.88
Average	0.42	0.61	0.75	0.83	0.89	0.92	0.95

that when 90 per cent of the first galaxies stellar masses were in place, 42 per cent of the simulated haloes had accreted less than 10 per cent of their masses. This percentage rises to 74 per cent for the haloes that are less than 30 per cent assembled.

Changing the assumed star formation history to a delayed τ-model tends to decrease the values of the $a_{0.5}$ and $a_{0.9}$ distributions. However the impact is limited: with a delayed τ-model, an average of 69 per cent of the simulated haloes had accreted 30 per cent of their masses when the oldest members had 90 per cent of their own stellar masses formed. Appendix 4.5 presents further assembly predictions for this model, and a comparison of the a_0, $a_{0.5}$ and $a_{0.9}$ posteriors obtained for the BCG with the two star formation histories.

Our results suggest that the oldest members in XLSSC 122 formed and were quenched in the protocluster stage, in agreement with previous attempts to link star formation history and overdensity evolution (e.g. Poggianti et al. 2006; Muldrew et al. 2018; Werner et al. 2022). Our conclusions are also supported by recent observations of $z \sim 3$ protoclusters already harbouring quenched galaxies (e.g. Shi et al. 2019, 2021; Kalita et al. 2021; Kubo et al. 2021), which might have formed around $z \sim 4$ (e.g. Long et al. 2020).

4.5 Summary

We have constructed a photometric catalogue to study the galaxy population of XLSSC 122, a mature galaxy cluster at $z = 1.98$. Our catalogue contains aperture-corrected flux densities for 37 spectroscopically confirmed members in 12 bands, covering the near ultraviolet to the mid-infrared. The stellar populations of 26 of these members were modelled with a exponentially decreasing star-forming rate. Although we also treated the mass, the metallicity and the dust extinction as free parameters, we focus our analysis on to the age of the oldest stars and the characteristic time.

We found that the red sequence galaxies exhibit a variety of ages, spanning from 0.5 to 3.26 Gyrs old, which is the age of the Universe at this redshift. Their characteristic times are all short, usually $\lesssim 0.3$ Gyr, and are thus consistent with a short duration of the star formation. In contrast, all but one of the blue cloud members display poorly constrained τ and young ages. This suggests these objects are still building a significant amount of their stellar masses, but we are unable to determine whether they possess an older stellar population or not.

Age and τ appear to be linked among the evolved members, with younger galaxies featuring shorter characteristic times than the older ones. We suggest that quenching efficiency increases with the mass of the cluster, but there is no consensus in the literature on

that subject.

Finally, we use 500 dark matter haloes from the MultiDark Planck 2 simulations to reconstruct the mass assembly history of XLSSC 122, allowing us to put constrains on the cluster state when its oldest members formed their first stars, and when they had 50 per cent and 90 per cent of their stellar masses in place. We found that, for the oldest galaxies, 74 per cent of the simulated haloes had accreted less than 10 per cent of their $z = 1.98$ masses at the time of the star formation onset. When the oldest galaxies had 50 per cent of their stellar masses formed, 67 per cent of the haloes are less than 10 per cent assembled. Similarly, 90 per cent of the oldest members stellar masses were in place, 75 per cent of the haloes were less than 30 per cent assembled. These probabilities allow us to determine that some of the first galaxies in XLSSC 122 where very likely quenched before the cluster virialization, in agreement with the recent discovery of quenched galaxies in $z \sim 3$ protoclusters.

Acknowledgements

The authors wish to thank Lucio Chiappetti for his careful review of the manuscript. AT is supported by the Natural Sciences and Engineering Research Council of Canada (NSERC) Postgraduate Scholarship-Doctoral Program. JPW acknowledges support from the Natural Sciences and Engineering Research Council of Canada Discovery Grant program. DR acknowledges the support of the Natural Sciences and Engineering Research Council of Canada , funding reference number 534263. REAC and EN acknowledge support from NASA grant number HST-GO-15267.002-A. ACC would like to thank the Leverhulme Trust for their support via the Leverhulme Early Career Fellowship scheme. EN acknowledges support from *Chandra* award GO0-21088X (proposal 21700167). MP acknowledges long-term support from the Centre National d'Etudes Spatiales (CNES). XXL is an international project based around an *XMM-Newton* Very Large Programme surveying two 25 deg^2 extragalactic fields at a depth of $\sim 6 \times 10^{-15}$ erg cm^{-2} s^{-1} in the [0.5-2] keV band for point-like sources. The XXL website is `http://irfu.cea.fr/xxl`.

Data availability

The data underlying this article are available at `https://www.cadc-ccda.hia-iha.nrc-cnrc.gc.ca/en/megapipe/` (CFHTLS; *u*, *g*, *r* and *i* bands) and `http://archive.eso.org/wdb/wdb/adp/phase3_main/form?collection_name=HAWKI` (VLT HAWK-I; *Y*, *J* and

K_s bands). HSC-SSP z-band data can be found at `https://hsc-release.mtk.nao.ac.jp/das_cutout/pdr2/` and IRAC data are available at `https://irsa.ipac.caltech.edu/data/SPITZER/SWIRE/`. All *HST* data presented in this paper are publicly available in the *Hubble* Legacy Archive (`https://hla.stsci.edu/`). The programme number is 15267.

Notes on individual galaxies

The BCG

Unlike some other high-redshift BCGs (e.g. Webb et al. 2015b; Bonaventura et al. 2017; Cooke et al. 2019), ID 526 does not exhibit any signs of recent star formation. Its age distribution (see Figure 4.2) is typical of a very old galaxy, albeit with slightly more probability towards 1 to 2 Gyrs than others, and its short characteristic time is inconsistent with the presence on a small population of young stars.

ID 726

ID 726 (presented in Figure 4.10) is the only reliable fit that does not enter into any of the four main age categories. Although its age distribution corresponds to a very old member, its characteristic time is poorly constrained and its dust content is markedly higher than in any other fit. Together with its irregular shape (see the top panel of Figure 4.1), this might suggest that ID 726 has undergone (or is still experiencing) an highly obscured star-forming episode.

ID 522

ID 522 characteristics place it between the young and the star-forming members: it is younger and bluer than any other evolved member (see Figure 4.4 and the bottom panel of Figure 4.1). However, unlike the other blue cloud members its characteristic time is very short and well-constrained, which could mean that ID 522 recently transitioned from star-forming to quenched. We thus classified it as a young members.

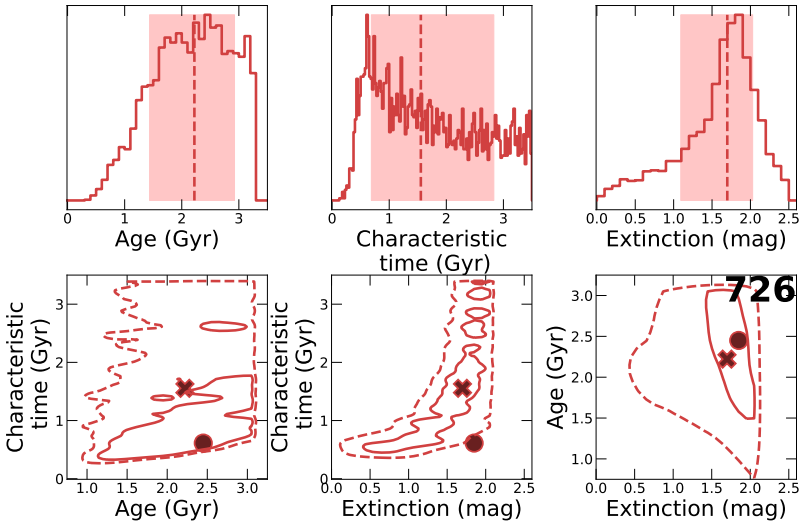

Figure 4.10: *Top*: Age, τ and dust extinction posterior distribution for ID 726, a dust-rich galaxy. *Bottom*: Age-τ, A_v-τ and Age-A_v, degeneracy plots for ID 726. Medians, modes and 1 and 2σ contours are presented following the same convention as in Figure 4.2.

Examples of full parameters distributions

Figures 4.11 to 4.14 present the full results of the fits for four XLSSC 122 members: the BCG, ID 451, ID 806 (members of the red sequence; Figure 4.11, 4.12 and 4.13 respectively) and ID 917 (in the blue cloud; 4.14). Each column shows the impact of one free parameter on the fits: the top panel displays the posterior distribution, and the subsequent panels show the degeneracies between this parameter and the others.

Mock photometry plots

Figure 4.15 shows the results of the mock photometry tests presented in Section 4.3.5: simulated galaxies containing an evolved and a young stellar populations. The percentage of the simulated galaxies masses corresponding to young stars is indicated on the top of each plot. Even a small percentage of young stars has a significant impact on the characteristic time distribution, suggesting that the evolved members in our sample are unlikely to experience a significant amount of star formation.

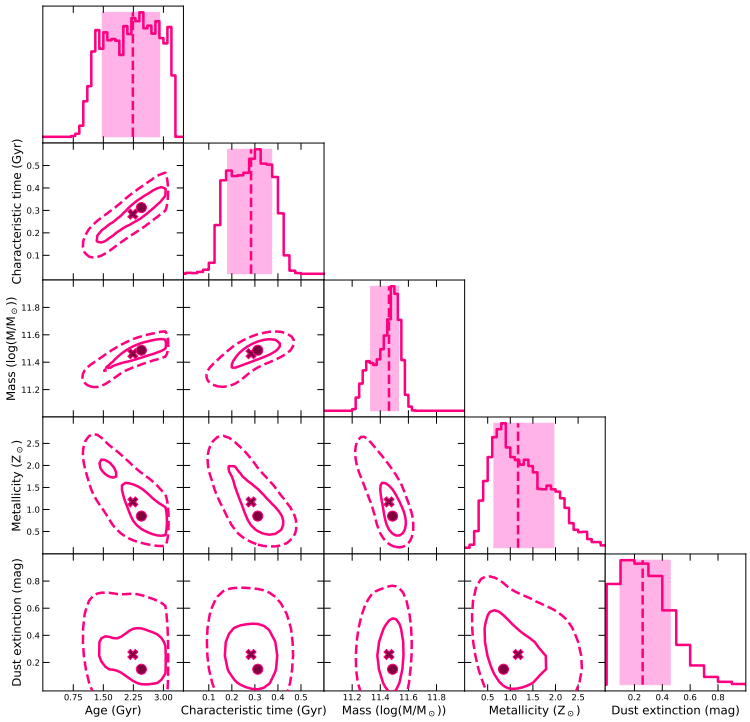

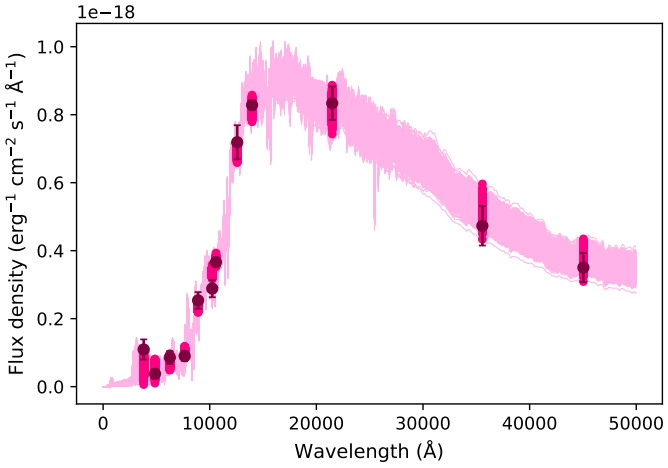

Figure 4.11: *Top*: A corner plot showing the results of the BCG fits, i.e. every parameter distribution and degeneracies. On the panels showing posterior distributions, the distances between the 16th and 84th percentiles (i.e. the 1σ confidence region) are coloured and the medians are highlighted by dashed lines. On the panels illustrating degeneracies, the 1 and 2σ contours are shown. Modes and medians are respectively denoted by dots and Xs. *Bottom*: Comparison between the BCG flux density measurements (f_λ) and their best fits. The shaded region corresponds to the fits between the 16th and 84th percentiles and the highlighted spots correspond to the theoretical flux densities measurements associated with those fits. Observed flux densities are represented as dark dots.

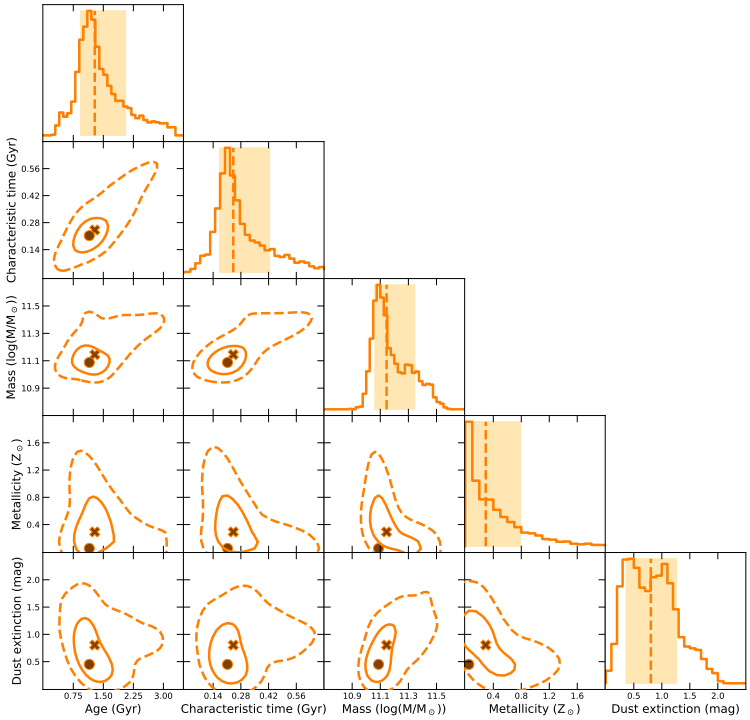

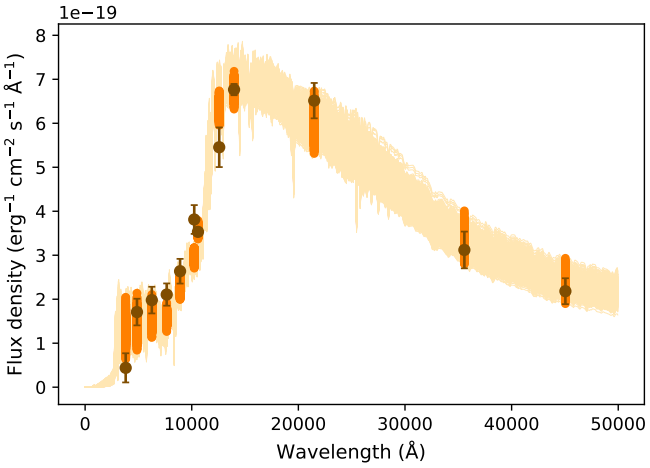

Figure 4.12: *Top*: ID 451 corner plot. *Bottom*: ID 451 best fits. See the previous Figure for an explanation of the symbols.

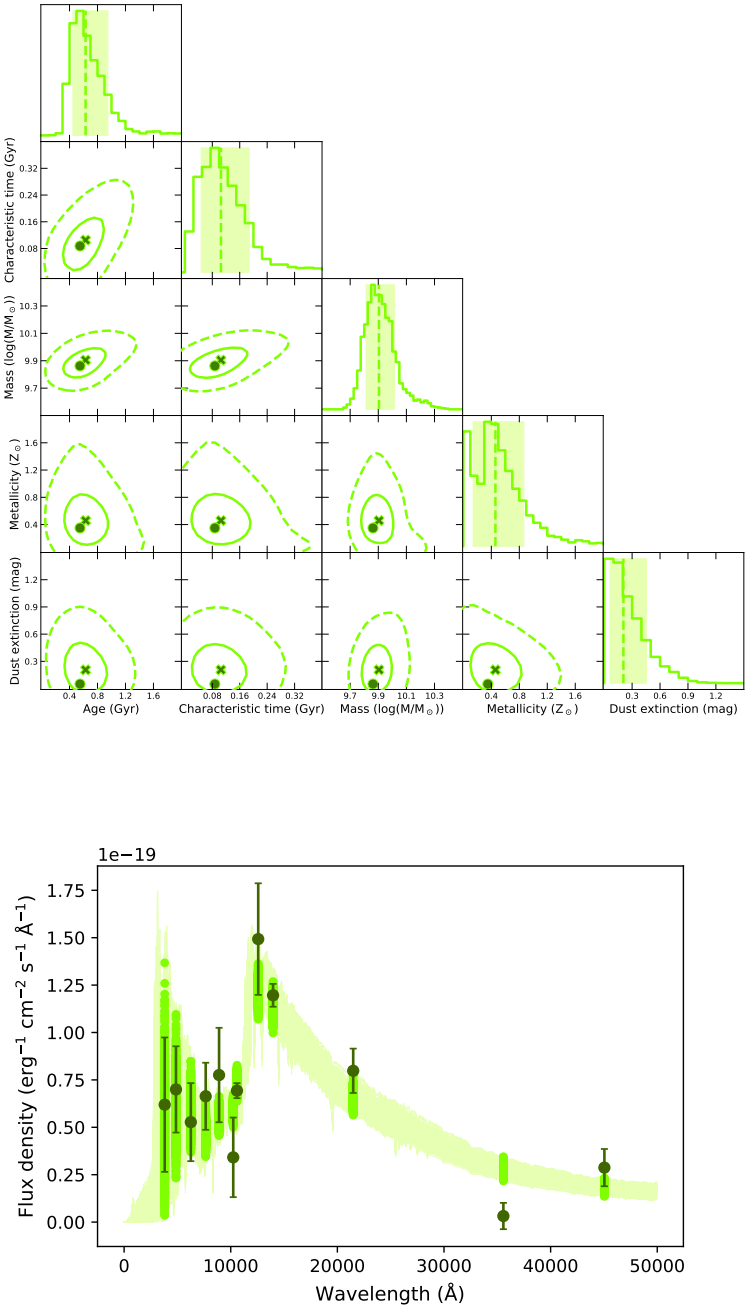

Figure 4.13: *Top*: ID 806 corner plot. *Bottom*: ID 806 best fits. See Figure 4.11 for an explanation of the symbols.

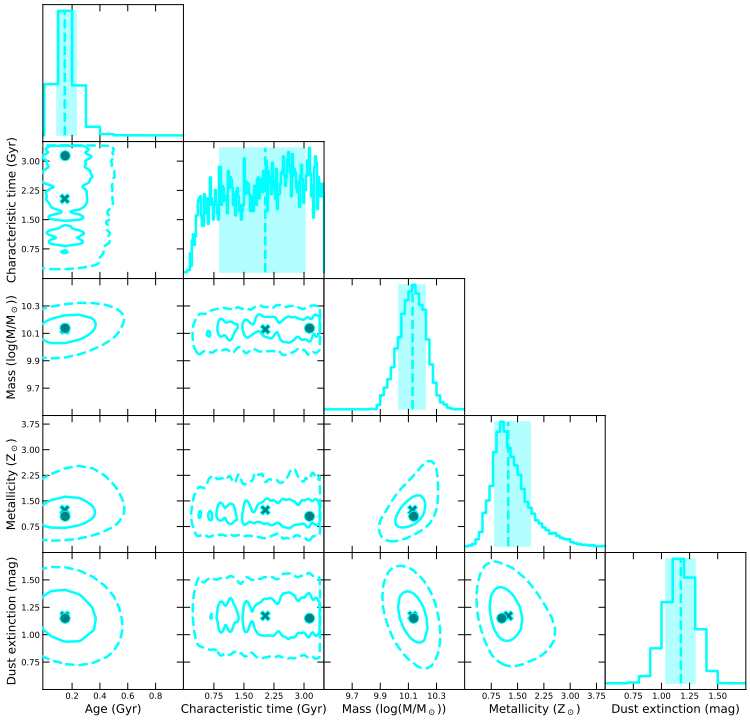

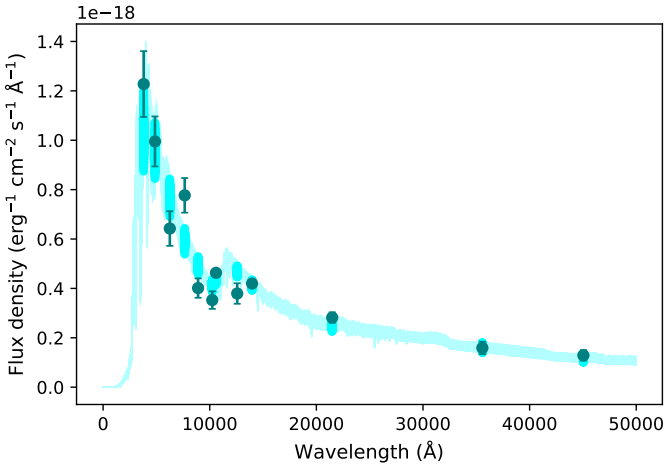

Figure 4.14: *Top*: ID 917 corner plot. *Bottom*: ID 917 best fits. See Figure 4.11 for an explanation of the symbols.

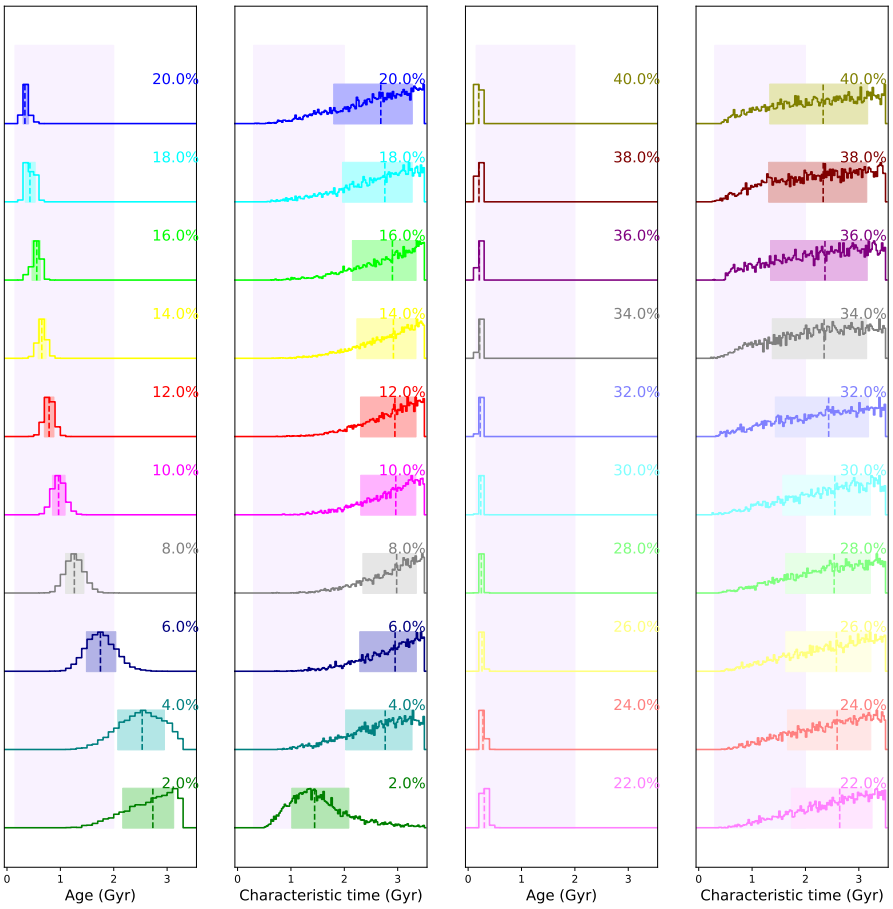

Figure 4.15: The age and characteristic time distributions obtained by fitting the mock photometry presented in Section 4.3.5. The percentages on top of each distribution indicate how much of the stellar mass was produced by the ongoing episode of star formation. Dashed lines indicate medians. The coloured regions highlight the 1σ intervals associated with each distribution and the pale lilac shades indicate the difference between the parameters used to create the old and young components of the mock photometry.

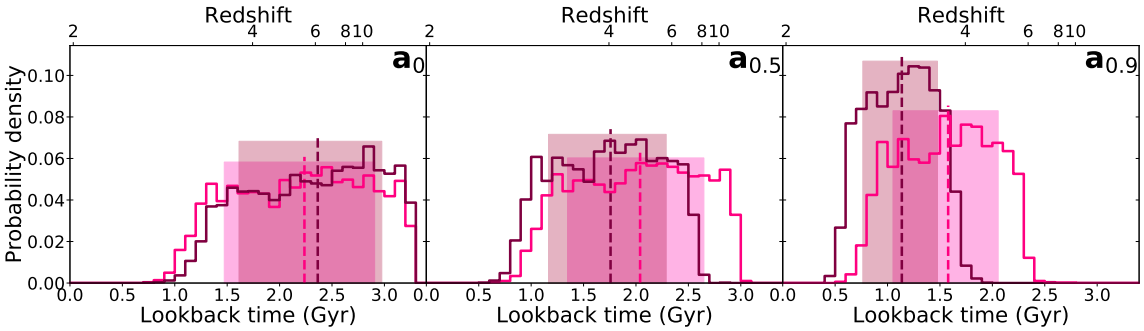

Figure 4.16: *Left*: Comparison between the a_0 posteriors (i.e. the age of the oldest stars) of the simple τ-model, in pink, and the delayed τ-model, in burgundy, for the BCG. The dashed lines are the distribution medians and the shaded regions correspond to the intervals between the 16th and 84th percentiles. *Centre*: Comparison between the distributions corresponding to the time-scale at which the BCG formed 50 per cent of its stellar mass (i.e. $a_{0.5}$) for the simple and delayed τ-models. *Right*: Comparizon between the $a_{0.9}$ distributions of the simple and delayed τ-models.

The cluster assembly history with a delayed τ-model

For the delayed τ-model, the equivalent of Equation 4.9 is:

$$a_X = a_0 + \tau + W_{-1}\left(\frac{-1}{\tau e}((1-X)\tau + X(a_0+\tau)e^{-a_0/\tau})\right), \tag{4.10}$$

where W_{-1} is one of the branches of the Lambert W-function. Figure 4.16 displays comparisons between the a_0, $a_{0.5}$ and $a_{0.9}$ posteriors of the simple and delayed τ-models, for the BCG. The a_0 posteriors, corresponding to the age of the oldest stars, are very similar. However, the different star formation history, combined with a slightly shorter characteristic time generate an $a_{0.9}$ distribution slightly younger and more peaked than the one corresponding to the regular τ-model. Tables 4.7, 4.8, and 4.9 present our assembly predictions for XLSSC 122-like halo, assuming a delayed τ-model.

Table 4.7: Cumulative fractions of XLSSC 122 haloes that are <10% assembled, <20% assembled, etc., integrated over the age distributions of the oldest members, assuming a delayed τ-model.

ID	<10%	<20%	<30%	<40%
526	0.80	0.91	0.96	0.98
657	0.74	0.85	0.92	0.96
295	0.79	0.88	0.93	0.96
606	0.76	0.87	0.92	0.96
734	0.62	0.77	0.87	0.92
845	0.82	0.89	0.93	0.96
493	0.73	0.85	0.91	0.95
730	0.74	0.84	0.90	0.94
Average	0.75	0.86	0.92	0.95

Table 4.8: Cumulative fraction of XLSSC 122-like haloes that are partially assembled, integrated over the time distributions corresponding to the formation of 50% of the stellar masses of the oldest members, assuming a delayed τ-model.

ID	<10%	<20%	<30%	<40%	<50%
526	0.67	0.83	0.91	0.96	0.98
657	0.63	0.77	0.87	0.92	0.96
295	0.67	0.80	0.88	0.93	0.95
606	0.55	0.72	0.82	0.89	0.93
734	0.54	0.71	0.82	0.89	0.93
845	0.74	0.85	0.90	0.94	0.96
493	0.65	0.79	0.87	0.92	0.95
730	0.54	0.70	0.81	0.87	0.91
Average	0.62	0.77	0.86	0.92	0.95

Table 4.9: Cumulative fraction of XLSSC 122-like haloes that are partially assembled, integrated over the time distributions corresponding to the formation of 90% of the stellar masses of the oldest members, assuming a delayed τ-model.

ID	<10%	<20%	<30%	<40%	<50%	<60%	<70%
526	0.34	0.59	0.76	0.86	0.92	0.95	0.97
657	0.36	0.58	0.73	0.83	0.89	0.93	0.96
295	0.33	0.57	0.73	0.82	0.88	0.92	0.95
606	0.10	0.27	0.46	0.61	0.72	0.79	0.86
734	0.40	0.59	0.73	0.83	0.89	0.93	0.96
845	0.46	0.68	0.81	0.88	0.92	0.95	0.97
493	0.48	0.66	0.78	0.86	0.91	0.94	0.96
730	0.16	0.34	0.51	0.63	0.72	0.79	0.85
Average	0.33	0.54	0.69	0.79	0.86	0.90	0.94

Chapter 5

Conclusions

5.1 Summary

In this dissertation, the galaxy populations of distant, X-ray selected clusters of galaxies were studied. Stellar ages and quenching levels of the most luminous galaxies in these clusters were shown to be diverse, from galaxies that were formed and quenched long before a redshift of 2 to others that are still forming stars at $z \sim 0.8$.

Chapter 2 presents the search for distant overdensities of galaxies associated with deep, 46 ks X-ray observations (Chen et al. 2018). A sample of 35 candidate clusters at $z \gtrsim 0.8$ was found, among which 15 candidates are new detections and 10 others were previously detected but never spectroscopically confirmed. Most of the 15 new detections appear to be either low mass or high redshift clusters, which might explain why they were not detected by the previous cluster surveys that covered this area of the sky (Olsen et al. 2007; Finoguenov et al. 2010; Durret et al. 2011; Wen & Han 2011; Licitra et al. 2016; Adami et al. 2018). A preliminary analysis based on photometric data (Jarvis et al. 2013; Adams et al. 2020) shows that these candidate clusters possess a wide variety of quenching levels. Candidate BCGs display a variety of $J - K_s$ colours, suggesting diverse star formation histories.

This dissertation chapter brings additional tentative evidence that the galaxy populations of X-ray selected galaxy clusters are more diverse than the ones found in optically or infrared-selected clusters (e.g. Donahue et al. 2002; Willis et al. 2018), an important result in constrast to most studies of quenching in distant clusters, which were realised with infrared-selected (e.g. Brodwin et al. 2013; Alberts et al. 2014; Nantais et al. 2017; Pintos-Castro et al. 2019) or mixed samples (e.g. the GOGREEN survey, see Balogh et al. 2017,

and associated publications). This sample is also of interest for the XXL survey cosmological analysis (Pierre et al. 2016). Since cluster-based cosmological studies need cluster samples to be as complete and pure as possible, a comparatively deep subsample of clusters can provide information about the type of clusters missed by the main 10 ks sample and how they can be accounted for.

Chapter 3 presents spectroscopic observations of four candidate clusters at $z \sim 1$, selected from the Chapter 2 sample. Multi-object spectroscopy was performed on Gemini North and South with GMOS, following an observing method called Nod-and-Shuffle spectroscopy. Data were reduced with PYRAF with the exception of the spectral extraction, which was performed with a custom-written routine. Spectroscopic redshifts were determined by visual examination of the spectra and are based on the identification of the CaII H and K absorption doublet and/or the [OII] unresolved emission doublet. Redshifts are then further secured by the identification of the Balmer lines and of the [OIII] doublet when present. With theses redshifts, three of the four observed candidate clusters were confirmed as true galaxy clusters. The remaining overdensity is a superposition of physically unrelated structures

A comparison of the spectroscopic redshifts with photometric redshifts from the VIDEO catalogue (Jarvis et al. 2013; Adams et al. 2020) reveals that VIDEO redshifts are generally accurate for bright $z \sim 1$ galaxies. However, they are not precise enough to allow one to recognize a superposition of unrelated structures as such, thus illustrating the need for spectroscopic observations to build a pure sample of galaxy clusters. Additionally, the spectroscopic observations bring an important perspective on the quenching analysis performed in Chapter 2. Of particular interest is the existence of a population of galaxies hosting an evolved stellar population with weak star formation, which appear to be an intermediate between the quenched and star-forming galaxies of Chapter 2.

Chapter 4 presents a detailed study of the galaxy populations of XLSSC 122, a X-ray selected galaxy cluster at $z = 1.98$ with 37 spectroscopically confirmed members (Willis et al. 2020). Images in 12 photometric bands, covering the near ultraviolet to the mid infrared, were used in the analysis. Flux densities were extracted with SEXTRACTOR 2.5.0 (Bertin & Arnouts 1996), using circular apertures selected to contain approximately 80% of the flux density of an average cluster member. Differences in the image resolutions were accounted for by the calculation of aperture correction factors.

These data were then used to perform a Spectral Energy Distribution (SED) fitting with BAGPIPES. SED fitting allows one to reconstruct the star-formation history of a galaxy, assuming that the star formation rate followed a certain pattern. Here the pattern used is an

exponentially declining star formation rate, expressed in term of the age of the oldest stars and the characteristic time, with three other free parameters controlling the stellar mass, the metallicity and the dust content.

Results show that the age of the oldest stars varies within the red sequence, from about 0.5 Gyr to 2 Gyrs or more. Characteristic times are short ($\lesssim 0.5$ Gyr) and correlate with the age of the oldest stars. The longest characteristic times belong to the galaxies with the oldest stars, suggesting that the environment became more efficient in quenching galaxies over time, possibly because of the cluster's growth.

To investigate the cluster growth, 500 dark-matter haloes from the MultiDark Planck 2 simulations (Klypin et al. 2016) were selected on the basis of their XLSSC 122-like masses at $z = 1.98$. Compared with the age posterior distributions of the oldest galaxies, the merger history of these simulated haloes suggest that XLSSC 122 had most likely accreted less than 10% of its $z = 1.98$ mass at the time of the star formation onset. When 90% of the stellar masses of the oldest galaxies were in place, XLSSC 122 had most likely accreted less than 30% of its mass. Never before had the link between the assembly history of a observed cluster quantitatively linked to the star formation histories of its members.

These results suggest that within distant X-ray selected clusters, the member galaxies display varied star-formation histories. The host cluster mass and accretion history seem to impact the star formation history of its members, suggesting that a detailed characterization of a galaxy environment is needed to comprehend the phenomena that shaped it.

5.2 Future work

Much of the recent work done on galaxy populations in clusters has been in the form of large scale surveys (e.g. Wilson et al. 2006; Alberts et al. 2014; Balogh et al. 2017; Pintos-Castro et al. 2019) and plans for future observatories such as Euclid (e.g. Euclid Collaboration et al. 2019) suggest more large-scale surveys in the future. While such surveys are useful for studying environmental quenching from a statistical point of view and for discovering interesting objects, most objects in large samples tend to be poorly characterized. I am thus interested in studying the co-evolution of cluster members and their environment with complementary approaches: the building of a medium-sized but well characterized cluster sample or detailed studies of very well characterized individual clusters. A few examples of future projects are presented below.

5.2.1 Exploring quenching in clusters with spectroscopy

As demonstrated in Chapter 2, at $z \sim 1$ the quenching of massive galaxies in clusters is still incomplete. The sample built in this Chapter displays a wide variety of quenching levels, suggesting that there might be some intrinsic variability in the number of quenched galaxies in clusters. The spectroscopic analysis performed in Chapter 3 suggests the existence of a population of intermediate galaxies which host a majority of evolved stars with some weak star formation activity.

Thus, I would like to carry on the work undertaken in these Chapters and use spectroscopic observations to confirm the remaining 13 candidate clusters at $z \sim 1$ in Trudeau et al. (2020, see also e.g. Muzzin et al. 2009; Khullar et al. 2019). This would generate a sample of up to 16 confirmed X-ray selected clusters, which would have the potential of providing a less biased view of quenching in clusters at $z \gtrsim 0.8$ than the large infrared-selected and mixed cluster samples used for this kind of analysis before (Donahue et al. 2002; Wilson et al. 2006; Balogh et al. 2017, 2021; Willis et al. 2018), yet with less sensitivity to small number statistics than studies focussing on a small number of high redshift clusters (e.g. Nantais et al. 2017; Foltz et al. 2018; Strazzullo et al. 2019). The spectroscopic information obtained to confirm the clusters could be in used in combination with the photometric information in the VIDEO catalogue (Jarvis et al. 2013; Adams et al. 2020) to perform detailed modelling of the star formation histories of the cluster members (Belli et al. 2019, 2021; Carnall et al. 2019b; Saracco et al. 2019; Estrada-Carpenter et al. 2020; Webb et al. 2020).

5.2.2 Star formation histories of the BCGs and the link with their environment

This detailed spectro-photometric modelling would also be useful to explore the stellar populations responsible of the variety of $J - K_s$ BCG colours, an investigation especially interesting considering that the fuelling mechanism of star formation in high-redshift BCGs is poorly understood (McDonald et al. 2016; Webb et al. 2015b). To understand the role environment played in shaping the stellar population of blue BCGs, further observations would be necessary: Sunayev-Zel'dovich or deeper X-rays observations would determine whether the intracluster medium structures are consistent with a residual cooling flow or not (Hlavacek-Larrondo et al. 2020; Kéruzoré et al. 2020; Ricci et al. 2020; Ruppin et al. 2021), and millimetric observations would determine the size and the kinematics of eventual cold

gas reservoirs (Daddi et al. 2010; Decarli et al. 2016; Webb et al. 2017; Noble et al. 2019; Castignani et al. 2020).

5.2.3 The impact of a cluster merger on its member galaxies

Clusters of galaxies grow by merging with smaller structures (Gunn & Gott 1972; Press & Schechter 1974). Cluster mergers are therefore relatively common, as they are a direct consequence of this hierarchical growth. In this dissertation, Chapter 4 explores the link between cluster members and star-formation indirectly by comparing cluster mass-scale and the star-formation timescale of its members. I would like to explore this link more directly by conducting detailed SED modellings of the galaxies within a high-redshift cluster merger. Despite the existence of several well characterised clusters at $z \sim 1$ (Jee et al. 2014; Ruppin et al. 2020; Di Mascolo et al. 2021), most of the work on this topic has been focussed on the low to moderate-redshift regime ($z \lesssim 0.5$). Futhermore, even at low redshift, cluster members appears to be affected by cluster mergers, although whether star formation is enhanced or suppressed seems to depend of the stage and the axis of the merger (see e.g. Miller & Owen 2003; Hwang & Lee 2009; Ma et al. 2010; Shim et al. 2011; Deshev et al. 2017; Stroe & Sobral 2021).

There is abundant literature on quenching and environment, but very little of it explores how the evolution of their environment shapes galaxies in clusters. This dissertation has laid the groundwork for a exploration of the links between the evolution of member galaxies and the changes in their environment.

Bibliography

2022a, Gemini Observatory, http://www.gemini.edu

2022b, GMOS Data Reduction Cookbook (v2.0), https://noirlab.edu/science/programs/csdc/usngo/gmos-cookbook/index.html

Abell, G. O. 1958, The Astrophysical Journal Supplement Series, 3, 211

Adami, C., Biviano, A., Durret, F., & Mazure, A. 2005, Astronomy & Astrophysics, 443, 17

Adami, C., Biviano, A., & Mazure, A. 1998, Astronomy & Astrophysics, 331, 439

Adami, C., Durret, F., Mazure, A., et al. 2007, Astronomy & Astrophysics, 462, 411

Adami, C., Giles, P., Koulouridis, E., et al. 2018, Astronomy & Astrophysics, 620, A5, (XXL Paper XX)

Adams, N. J., Bowler, R. A. A., Jarvis, M. J., et al. 2020, Monthly Notices of the Royal Astronomical Society, 494, 1771

Aguerri, J. A. L., Agulli, I., & Méndez-Abreu, J. 2018, Monthly Notices of the Royal Astronomical Society, 477, 1921

Aihara, H., Arimoto, N., Armstrong, R., et al. 2018a, Publications of the Astronomical Society of Japan, 70, S4

Aihara, H., Armstrong, R., Bickerton, S., et al. 2018b, Publications of the Astronomical Society of Japan, 70, S8

Alberts, S., Pope, A., Brodwin, M., et al. 2014, Monthly Notices of the Royal Astronomical Society, 437, 437

Anders, E. & Grevesse, N. 1989, Geochimica et Cosmochimica Acta, 53, 197

Andreon, S. 2002, Astronomy & Astrophysics, 382, 821

Andreon, S., Newman, A. B., Trinchieri, G., et al. 2014, Astronomy & Astrophysics, 565, A120

Andreon, S., Valtchanov, I., Jones, L. R., et al. 2005, Monthly Notices of the Royal Astronomical Society, 359, 1250

Angulo, R. E., Springel, V., White, S. D. M., et al. 2012, Monthly Notices of the Royal Astronomical Society, 426, 2046

Arnaud, M., Pratt, G. W., Piffaretti, R., et al. 2010, Astronomy & Astrophysics, 517, A92

Arnouts, S., Cristiani, S., Moscardini, L., et al. 1999, Monthly Notices of the Royal Astronomical Society, 310, 540

Baldry, I. K., Glazebrook, K., Brinkmann, J., et al. 2004, The Astrophysical Journal, 600, 681

Balogh, M. L., Baldry, I. K., Nichol, R., et al. 2004, The Astrophysical Journal Letters, 615, L101

Balogh, M. L., Gilbank, D. G., Muzzin, A., et al. 2017, Monthly Notices of the Royal Astronomical Society, 470, 4168

Balogh, M. L. & McGee, S. L. 2010, Monthly Notices of the Royal Astronomical Society, 402, L59

Balogh, M. L., McGee, S. L., Mok, A., et al. 2016, Monthly Notices of the Royal Astronomical Society, 456, 4364

Balogh, M. L., Navarro, J. F., & Morris, S. L. 2000, The Astrophysical Journal, 540, 113

Balogh, M. L., van der Burg, R. F. J., Muzzin, A., et al. 2021, Monthly Notices of the Royal Astronomical Society, 500, 358

Barnes, D. J., Vogelsberger, M., Kannan, R., et al. 2018, Monthly Notices of the Royal Astronomical Society, 481, 1809

Barrena, R., Biviano, A., Ramella, M., Falco, E. E., & Seitz, S. 2002, Astronomy & Astrophysics, 386, 816

Beers, T. C., Flynn, K., & Gebhardt, K. 1990, The Astronomical Journal, 100, 32

Behroozi, P., Wechsler, R. H., Hearin, A. P., & Conroy, C. 2019, Monthly Notices of the Royal Astronomical Society, 488, 3143

Behroozi, P. S., Wechsler, R. H., & Conroy, C. 2013, The Astrophysical Journal, 770, 57

Bekki, K. 1999, The Astrophysical Journal Letters, 510, L15

Bell, E. F., van der Wel, A., Papovich, C., et al. 2012, The Astrophysical Journal, 753, 167

Belli, S., Contursi, A., Genzel, R., et al. 2021, The Astrophysical Journal, 909, L11

Belli, S., Genzel, R., Förster Schreiber, N. M., et al. 2017, The Astrophysical Journal Letters, 841, L6

Belli, S., Newman, A. B., & Ellis, R. S. 2019, The Astrophysical Journal, 874, 17

Bellstedt, S., Lidman, C., Muzzin, A., et al. 2016, Monthly Notices of the Royal Astronomical Society, 460, 2862

Bernardi, M., Hyde, J. B., Sheth, R. K., Miller, C. J., & Nichol, R. C. 2007, The Astronomical Journal, 133, 1741

Berrier, J. C., Stewart, K. R., Bullock, J. S., et al. 2009, The Astrophysical Journal, 690, 1292

Bertin, E. & Arnouts, S. 1996, Astronomy & Astrophysics Supplement Series, 117, 393

Best, P. N., von der Linden, A., Kauffmann, G., Heckman, T. M., & Kaiser, C. R. 2007, Monthly Notices of the Royal Astronomical Society, 379, 894

Bildfell, C., Hoekstra, H., Babul, A., & Mahdavi, A. 2008, Monthly Notices of the Royal Astronomical Society, 389, 1637

Bilton, L. E., Hunt, M., Pimbblet, K. A., & Roediger, E. 2019, Monthly Notices of the Royal Astronomical Society, 490, 5017

Blandford, R. D. & Payne, D. G. 1982, Monthly Notices of the Royal Astronomical Society, 199, 883

Blanton, M. R., Hogg, D. W., Bahcall, N. A., et al. 2003, The Astrophysical Journal, 594, 186

Bleem, L. E., Stalder, B., de Haan, T., et al. 2015, The Astrophysical Journal Supplement Series, 216, 27

Böhringer, H., Schuecker, P., Guzzo, L., et al. 2001, Astronomy & Astrophysics, 369, 826

Bonaventura, N. R., Webb, T. M. A., Muzzin, A., et al. 2017, Monthly Notices of the Royal Astronomical Society, 469, 1259

Bower, R. G., Lucey, J. R., & Ellis, R. S. 1992, Monthly Notices of the Royal Astronomical Society, 254, 601

Bradt, H., Mayer, W., Naranan, S., Rappaport, S., & Spada, G. 1967, The Astrophysical Journal Letters, 150, L199

Brodwin, M., Stanford, S. A., Gonzalez, A. H., et al. 2013, The Astrophysical Journal, 779, 138

Brough, S., Proctor, R., Forbes, D. A., et al. 2007, Monthly Notices of the Royal Astronomical Society, 378, 1507

Bruzual, G. & Charlot, S. 2003, Monthly Notices of the Royal Astronomical Society, 344, 1000

Buchner, J. 2014, arXiv:astro-ph/1407.5459

Burns, J. O., Hallman, E. J., Gantner, B., Motl, P. M., & Norman, M. L. 2008, The Astrophysical Journal, 675, 1125

Butcher, H. & Oemler, Jr., A. 1978, The Astrophysical Journal, 219, 18

Butcher, H. & Oemler, Jr., A. 1984, The Astrophysical Journal, 285, 426

Byram, E. T., Chubb, T. A., & Friedman, H. 1966, Science, 152, 66

Cai, Z., Fan, X., Peirani, S., et al. 2016, The Astrophysical Journal, 833, 135

Calvi, R., Dannerbauer, H., Arrabal Haro, P., et al. 2021, Monthly Notices of the Royal Astronomical Society, 502, 4558

Calvi, R., Rodríguez Espinosa, J. M., Mas-Hesse, J. M., et al. 2019, Monthly Notices of the Royal Astronomical Society, 489, 3294

Calzetti, D., Armus, L., Bohlin, R. C., et al. 2000, The Astrophysical Journal, 533, 682

Carlstrom, J. E., Holder, G. P., & Reese, E. D. 2002, Annual Review of Astronomy and Astrophysics, 40, 643

Carnall, A. C., Leja, J., Johnson, B. D., et al. 2019a, The Astrophysical Journal, 873, 44

Carnall, A. C., McLure, R. J., Dunlop, J. S., et al. 2019b, Monthly Notices of the Royal Astronomical Society, 490, 417

Carnall, A. C., McLure, R. J., Dunlop, J. S., & Davé, R. 2018, Monthly Notices of the Royal Astronomical Society, 480, 4379

Carnall, A. C., Walker, S., McLure, R. J., et al. 2020, Monthly Notices of the Royal Astronomical Society, 496, 695

Carroll, B. W. & Ostlie, D. A. 2007, An Introduction to Modern Astrophysic, 2nd edn. (San Francisco: Pearson Addison Weasley)

Casali, M., Pirard, J.-F., Kissler-Patig, M., et al. 2006, in Society of Photo-Optical Instrumentation Engineers (SPIE) Conference Series, Vol. 6269, Society of Photo-Optical Instrumentation Engineers (SPIE) Conference Series, ed. I. S. McLean & M. Iye, 62690W

Castignani, G., Combes, F., Salomé, P., & Freundlich, J. 2020, Astronomy & Astrophysics, 635, A32

Cattaneo, A., Woo, J., Dekel, A., & Faber, S. M. 2013, Monthly Notices of the Royal Astronomical Society, 430, 686

Cerulo, P., Couch, W. J., Lidman, C., et al. 2017, Monthly Notices of the Royal Astronomical Society, 472, 254

Cerulo, P., Couch, W. J., Lidman, C., et al. 2016, Monthly Notices of the Royal Astronomical Society, 457, 2209

Champagne, J. B., Decarli, R., Casey, C. M., et al. 2018, The Astrophysical Journal, 867, 153

Chanchaiworawit, K., Guzmán, R., Salvador-Solé, E., et al. 2019, The Astrophysical Journal, 877, 51

Chen, C.-T. J., Brandt, W. N., Luo, B., et al. 2018, Monthly Notices of the Royal Astronomical Society, 478, 2132

Chen, Y., Reiprich, T. H., Böhringer, H., Ikebe, Y., & Zhang, Y.-Y. 2007, Astronomy & Astrophysics, 466, 805

Chiang, Y.-K., Overzier, R., & Gebhardt, K. 2013, The Astrophysical Journal, 779, 127

Chiang, Y.-K., Overzier, R. A., Gebhardt, K., & Henriques, B. 2017, The Astrophysical Journal, 844, L23

Chiappetti, L., Fotopoulou, S., Lidman, C., et al. 2018, Astronomy & Astrophysics, 620, A12, (XXL Paper XXVII)

Chiu, I., Mohr, J., McDonald, M., et al. 2016, Monthly Notices of the Royal Astronomical Society, 455, 258

Cirasuolo, M., McLure, R. J., Dunlop, J. S., et al. 2010, Monthly Notices of the Royal Astronomical Society, 401, 1166

Clerc, N., Sadibekova, T., Pierre, M., et al. 2012, Monthly Notices of the Royal Astronomical Society, 423, 3561

Cole, S., Aragon-Salamanca, A., Frenk, C. S., Navarro, J. F., & Zepf, S. E. 1994, Monthly Notices of the Royal Astronomical Society, 271, 781

Colless, M., Ellis, R. S., Taylor, K., & Hook, R. N. 1990, Monthly Notices of the Royal Astronomical Society, 244, 408

Conroy, C. 2013, Annual Review of Astronomy and Astrophysics, 51, 393

Conroy, C. & Gunn, J. E. 2010, The Astrophysical Journal, 712, 833

Conroy, C., Gunn, J. E., & White, M. 2009, The Astrophysical Journal, 699, 486

Coogan, R. T., Daddi, E., Sargent, M. T., et al. 2018, Monthly Notices of the Royal Astronomical Society, 479, 703

Cooke, E. A., Hatch, N. A., Rettura, A., et al. 2015, Monthly Notices of the Royal Astronomical Society, 452, 2318

Cooke, E. A., Hatch, N. A., Stern, D., et al. 2016, The Astrophysical Journal, 816, 83

Cooke, K. C., Kartaltepe, J. S., Tyler, K. D., et al. 2019, The Astrophysical Journal, 881, 150

Cora, S. A., Hough, T., Vega-Martínez, C. A., & Orsi, . A. 2019, Monthly Notices of the Royal Astronomical Society, 483, 1686

Cresci, G., Marconi, A., Zibetti, S., et al. 2015, Astronomy & Astrophysics, 582, A63

Croton, D. J., Springel, V., White, S. D. M., et al. 2006, Monthly Notices of the Royal Astronomical Society, 365, 11

Cucciati, O., Zamorani, G., Lemaux, B. C., et al. 2014, Astronomy & Astrophysics, 570, A16

Cuillandre, J. C., Fort, B., Picat, J. P., et al. 1994, Astronomy & Astrophysics, 281, 603

Daddi, E., Bournaud, F., Walter, F., et al. 2010, The Astrophysical Journal, 713, 686

Dannerbauer, H., Lehnert, M. D., Emonts, B., et al. 2017, Astronomy & Astrophysics, 608, A48

Darvish, B., Scoville, N. Z., Martin, C., et al. 2020, The Astrophysical Journal, 892, 8

Davies, R. I. 2007, Monthly Notices of the Royal Astronomical Society, 375, 1099

Davies, R. L., Förster Schreiber, N. M., Übler, H., et al. 2019, The Astrophysical Journal, 873, 122

De Lucia, G. & Blaizot, J. 2007, Monthly Notices of the Royal Astronomical Society, 375, 2

De Lucia, G., Kauffmann, G., Springel, V., et al. 2004, Monthly Notices of the Royal Astronomical Society, 348, 333

De Lucia, G., Weinmann, S., Poggianti, B. M., Aragón-Salamanca, A., & Zaritsky, D. 2012, Monthly Notices of the Royal Astronomical Society, 423, 1277

Decarli, R., Walter, F., Aravena, M., et al. 2016, The Astrophysical Journal, 833, 70

Deshev, B., Finoguenov, A., Verdugo, M., et al. 2017, Astronomy & Astrophysics, 607, A131

Di Mascolo, L., Mroczkowski, T., Perrott, Y., et al. 2021, Astronomy & Astrophysics, 650, A153

Diemer, B., Sparre, M., Abramson, L. E., & Torrey, P. 2017, The Astrophysical Journal, 839, 26

Donahue, M., de Messières, G. E., O'Connell, R. W., et al. 2011, The Astrophysical Journal, 732, 40

Donahue, M., Scharf, C. A., Mack, J., et al. 2002, The Astrophysical Journal, 569, 689

Donzelli, C. J., Muriel, H., & Madrid, J. P. 2011, The Astrophysical Journal Supplement Series, 195, 15

Dressler, A. 1978, The Astrophysical Journal, 223, 765

Dressler, A. & Gunn, J. E. 1983, The Astrophysical Journal, 270, 7

Dressler, A., Oemler, Jr., A., Poggianti, B. M., et al. 2013, The Astrophysical Journal, 770, 62

Dressler, A., Oemler, Jr., A., Poggianti, B. M., et al. 2004, The Astrophysical Journal, 617, 867

Dunn, R. J. H. & Fabian, A. C. 2008, Monthly Notices of the Royal Astronomical Society, 385, 757

Durret, F., Adami, C., Cappi, A., et al. 2011, Astronomy & Astrophysics, 535, A65

Eckert, D., Molendi, S., & Paltani, S. 2011, Astronomy & Astrophysics, 526, A79

Edwards, L. O. V., Salinas, M., Stanley, S., et al. 2020, Monthly Notices of the Royal Astronomical Society, 491, 2617

Egami, E., Misselt, K. A., Rieke, G. H., et al. 2006, The Astrophysical Journal, 647, 922

Einstein, A. 1936, Science, 84, 506

Estrada-Carpenter, V., Papovich, C., Momcheva, I., et al. 2020, The Astrophysical Journal, 898, 171

Euclid Collaboration, Adam, R., Vannier, M., et al. 2019, Astronomy & Astrophysics, 627, A23

Fabian, A. C. 1994, Annual Review of Astronomy and Astrophysics, 32, 277

Fabian, A. C. 2012, Annual Review of Astronomy and Astrophysics, 50, 455

Fabian, A. C., Celotti, A., Blundell, K. M., Kassim, N. E., & Perley, R. A. 2002, Monthly Notices of the Royal Astronomical Society, 331, 369

Faccioli, L., Pacaud, F., Sauvageot, J.-L., et al. 2018, Astronomy & Astrophysics, 620, A9, (XXL Paper XXIV)

Farouki, R. & Shapiro, S. L. 1981, The Astrophysical Journal, 243, 32

Fassbender, R., Nastasi, A., Santos, J. S., et al. 2014, Astronomy & Astrophysics, 568, A5

Felten, J. E., Gould, R. J., Stein, W. A., & Woolf, N. J. 1966, The Astrophysical Journal, 146, 955

Feroz, F. & Hobson, M. P. 2008, Monthly Notices of the Royal Astronomical Society, 384, 449

Feroz, F., Hobson, M. P., & Bridges, M. 2009, Monthly Notices of the Royal Astronomical Society, 398, 1601

Feroz, F., Hobson, M. P., Cameron, E., & Pettitt, A. N. 2019, The Open Journal of Astrophysics, 2, 10

Finner, K., James Jee, M., Webb, T., et al. 2020, The Astrophysical Journal, 893, 10

Finoguenov, A., Watson, M. G., Tanaka, M., et al. 2010, Monthly Notices of the Royal Astronomical Society, 403, 2063

Fluetsch, A., Maiolino, R., Carniani, S., et al. 2019, Monthly Notices of the Royal Astronomical Society, 483, 4586

Foltz, R., Wilson, G., Muzzin, A., et al. 2018, The Astrophysical Journal, 866, 136

Foreman-Macke, D., Sick, J., & Johnson, B. 2014, python-fsps: Python bindings to FSPS (v0.1.1), `https://zenodo.org/record/12157#.XoewBS97SqB`

Forman, W., Kellogg, E., Gursky, H., Tananbaum, H., & Giacconi, R. 1972, The Astrophysical Journal, 178, 309

Förster Schreiber, N. M., Übler, H., Davies, R. L., et al. 2019, The Astrophysical Journal, 875, 21

Fossati, M., Wilman, D. J., Mendel, J. T., et al. 2017, The Astrophysical Journal, 835, 153

Fotopoulou, S. & Paltani, S. 2018, Astronomy & Astrophysics, 619, A14

Franck, J. R. & McGaugh, S. S. 2016, The Astrophysical Journal, 833, 15

Garling, C. T., Peter, A. H. G., Kochanek, C. S., Sand, D. J., & Crnojević, D. 2020, Monthly Notices of the Royal Astronomical Society, 492, 1713

Gavazzi, R. & Soucail, G. 2007, Astronomy & Astrophysics, 462, 459

Gendron-Marsolais, M., Hlavacek-Larrondo, J., Martin, T. B., et al. 2018, Monthly Notices of the Royal Astronomical Society, 479, L28

Genzel, R., Förster Schreiber, N. M., Rosario, D., et al. 2014, The Astrophysical Journal, 796, 7

Giacconi, R. 2003, Reviews of Modern Physics, 75, 995

Giacconi, R., Kellogg, E., Gorenstein, P., Gursky, H., & Tananbaum, H. 1971, The Astrophysical Journal, 165, L27

Gioia, I. M., Maccacaro, T., Schild, R. E., et al. 1990, The Astrophysical Journal Supplement Series, 72, 567

Gladders, M. D. & Yee, H. K. C. 2000, The Astronomical Journal, 120, 2148

Gladders, M. D. & Yee, H. K. C. 2005, The Astrophysical Journal Supplement Series, 157, 1

Glazebrook, K. & Bland-Hawthorn, J. 2001, Publications of the Astronomical Society of the Pacific, 113, 197

Gobat, R., Daddi, E., Onodera, M., et al. 2011, Astronomy & Astrophysics, 526, A133

Gonzalez, A. H., Sivanandam, S., Zabludoff, A. I., & Zaritsky, D. 2013, The Astrophysical Journal, 778, 14

Gottlöber, S., Klypin, A., & Kravtsov, A. V. 2001, The Astrophysical Journal, 546, 223

Granato, G. L., De Zotti, G., Silva, L., Bressan, A., & Danese, L. 2004, The Astrophysical Journal, 600, 580

Green, T. S., Edge, A. C., Stott, J. P., et al. 2016, Monthly Notices of the Royal Astronomical Society, 461, 560

Groenewald, D. N. & Loubser, S. I. 2014, Monthly Notices of the Royal Astronomical Society, 444, 808

Guglielmo, V., Poggianti, B. M., Vulcani, B., et al. 2018, Astronomy & Astrophysics, 620, A7, (XXL Paper XXII)

Gunn, J. E. & Gott, III, J. R. 1972, The Astrophysical Journal, 176, 1

Gursky, H., Solinger, A., Kellogg, E. M., et al. 1972, The Astrophysical Journal Letters, 173, L99

Gwyn, S. D. J. 2012, The Astronomical Journal, 143, 38

Hamana, T., Miyazaki, S., Kashikawa, N., et al. 2009, Publications of the Astronomical Society of Japan, 61, 833

Harikane, Y., Ouchi, M., Ono, Y., et al. 2019, The Astrophysical Journal, 883, 142

Hart, M. 2019, The Astronomical Journal, 157, 221

Hashimoto, T., Laporte, N., Mawatari, K., et al. 2018, Nature, 557, 392

Hatch, N. A., De Breuck, C., Galametz, A., et al. 2011a, Monthly Notices of the Royal Astronomical Society, 410, 1537

Hatch, N. A., Kurk, J. D., Pentericci, L., et al. 2011b, Monthly Notices of the Royal Astronomical Society, 415, 2993

Herrera-Camus, R., Tacconi, L., Genzel, R., et al. 2019, The Astrophysical Journal, 871, 37

Higuchi, R., Ouchi, M., Ono, Y., et al. 2019, The Astrophysical Journal, 879, 28

Hinshaw, G., Larson, D., Komatsu, E., et al. 2013, The Astrophysical Journal Supplement Series, 208, 19

Hlavacek-Larrondo, J., Fabian, A. C., Edge, A. C., et al. 2013, Monthly Notices of the Royal Astronomical Society, 431, 1638

Hlavacek-Larrondo, J., Fabian, A. C., Edge, A. C., et al. 2012a, Monthly Notices of the Royal Astronomical Society, 421, 1360

Hlavacek-Larrondo, J., Fabian, A. C., Edge, A. C., & Hogan, M. T. 2012b, Monthly Notices of the Royal Astronomical Society, 424, 224

Hlavacek-Larrondo, J., McDonald, M., Benson, B. A., et al. 2015, The Astrophysical Journal, 805, 35

Hlavacek-Larrondo, J., Rhea, C. L., Webb, T., et al. 2020, The Astrophysical Journal, 898, L50

Hogg, D. W., Blanton, M. R., Eisenstein, D. J., et al. 2003, The Astrophysical Journal Letters, 585, L5

Hopkins, P. F., Quataert, E., & Murray, N. 2012, Monthly Notices of the Royal Astronomical Society, 421, 3522

Hu, W., Wang, J., Infante, L., et al. 2021, Nature Astronomy, 5, 485

Hubble, E. P. 1922, The Astrophysical Journal, 56

Hubble, E. P. 1925, The Astrophysical Journal, 62

Hudson, D. S., Mittal, R., Reiprich, T. H., et al. 2010, Astronomy & Astrophysics, 513, A37

Hung, C.-L., Casey, C. M., Chiang, Y.-K., et al. 2016, The Astrophysical Journal, 826, 130

Hwang, H. S. & Lee, M. G. 2009, Monthly Notices of the Royal Astronomical Society, 397, 2111

Ilbert, O., Arnouts, S., McCracken, H. J., et al. 2006, Astronomy & Astrophysics, 457, 841

Ilbert, O., Capak, P., Salvato, M., et al. 2009, The Astrophysical Journal, 690, 1236

Ishigaki, M., Ouchi, M., & Harikane, Y. 2016, The Astrophysical Journal, 822, 5

Iyer, K. G., Gawiser, E., Faber, S. M., et al. 2019, The Astrophysical Journal, 879, 116

Jaffé, Y. L., Poggianti, B. M., Moretti, A., et al. 2018, Monthly Notices of the Royal Astronomical Society, 476, 4753

Jarvis, M. J., Bonfield, D. G., Bruce, V. A., et al. 2013, Monthly Notices of the Royal Astronomical Society, 428, 1281

Jee, M. J., Hughes, J. P., Menanteau, F., et al. 2014, The Astrophysical Journal, 785, 20

Jetha, N. N., Hardcastle, M. J., Babul, A., et al. 2008, Monthly Notices of the Royal Astronomical Society, 384, 1344

Jian, H.-Y., Lin, L., Oguri, M., et al. 2018, Publications of the Astronomical Society of Japan, 70, S23

Jiang, L., Wu, J., Bian, F., et al. 2018, Nature Astronomy, 2, 962

Kaiser, N., Squires, G., & Broadhurst, T. 1995, The Astrophysical Journal, 449, 460

Kalita, B. S., Daddi, E., D'Eugenio, C., et al. 2021, The Astrophysical Journal Letters, 917, L17

Kavelaars, J. J., Harris, W. E., Hanes, D. A., Hesser, J. E., & Pritchet, C. J. 2000, The Astrophysical Journal, 533, 125

Kawinwanichakij, L., Papovich, C., Quadri, R. F., et al. 2017, The Astrophysical Journal, 847, 134

Kéruzoré, F., Mayet, F., Pratt, G. W., et al. 2020, Astronomy & Astrophysics, 644, A93

Khullar, G., Bleem, L. E., Bayliss, M. B., et al. 2019, The Astrophysical Journal, 870, 7

Kissler-Patig, M., Pirard, J.-F., Casali, M., et al. 2008, Astronomy & Astrophysics, 491, 941

Klypin, A., Yepes, G., Gottlöber, S., Prada, F., & He, S. 2016, Monthly Notices of the Royal Astronomical Society, 457, 4340

Knobel, C., Lilly, S. J., Woo, J., & Kovač, K. 2015, The Astrophysical Journal, 800, 24

Kodama, T., Tanaka, I., Kajisawa, M., et al. 2007, Monthly Notices of the Royal Astronomical Society, 377, 1717

Kong, X., Charlot, S., Weiss, A., & Cheng, F. Z. 2003, Astronomy & Astrophysics, 403, 877

Kormendy, J. & Ho, L. C. 2013, Annual Review of Astronomy and Astrophysics, 51, 511

Kubo, M., Toshikawa, J., Kashikawa, N., et al. 2019, The Astrophysical Journal, 887, 214

Kubo, M., Umehata, H., Matsuda, Y., et al. 2021, The Astrophysical Journal, 919, 6

Kuiper, E., Hatch, N. A., Miley, G. K., et al. 2011, Monthly Notices of the Royal Astronomical Society, 415, 2245

Kuiper, E., Venemans, B. P., Hatch, N. A., Miley, G. K., & Röttgering, H. J. A. 2012, Monthly Notices of the Royal Astronomical Society, 425, 801

Laine, S., van der Marel, R. P., Lauer, T. R., et al. 2003, The Astronomical Journal, 125, 478

Lange, J. U., van den Bosch, F. C., Hearin, A., et al. 2018, Monthly Notices of the Royal Astronomical Society, 473, 2830

Larson, R. B., Tinsley, B. M., & Caldwell, C. N. 1980, The Astrophysical Journal, 237, 692

Lauer, T. R., Postman, M., Strauss, M. A., Graves, G. J., & Chisari, N. E. 2014, The Astrophysical Journal, 797, 82

Lavoie, S., Willis, J. P., Démoclès, J., et al. 2016, Monthly Notices of the Royal Astronomical Society, 462, 4141, (XXL Paper XV)

Lea, S. M., Silk, J., Kellogg, E., & Murray, S. 1973, The Astrophysical Journal Letters, 184, L105

Lee, K.-G., Hennawi, J. F., Stark, C., et al. 2014a, The Astrophysical Journal Letters, 795, L12

Lee, K.-G., Hennawi, J. F., White, M., Croft, R. A. C., & Ozbek, M. 2014b, The Astrophysical Journal, 788, 49

Lee, Y., Rey, S.-C., Hilker, M., Sheen, Y.-K., & Yi, S. K. 2016, The Astrophysical Journal, 822, 92

Leja, J., Carnall, A. C., Johnson, B. D., Conroy, C., & Speagle, J. S. 2019, The Astrophysical Journal, 876, 3

Lemaux, B. C., Tomczak, A. R., Lubin, L. M., et al. 2019, Monthly Notices of the Royal Astronomical Society, 490, 1231

Li, Z. & Han, Z. 2007, Astronomy & Astrophysics, 471, 795

Licitra, R., Mei, S., Raichoor, A., Erben, T., & Hildebrandt, H. 2016, Monthly Notices of the Royal Astronomical Society, 455, 3020

Lidman, C., Suherli, J., Muzzin, A., et al. 2012, Monthly Notices of the Royal Astronomical Society, 427, 550

Lilly, S. J., Cowie, L. L., & Gardner, J. P. 1991, The Astrophysical Journal, 369, 79

Lin, H. W., McDonald, M., Benson, B., & Miller, E. 2015, The Astrophysical Journal, 802, 34

Lin, Y.-T. & Mohr, J. J. 2004, The Astrophysical Journal, 617, 879

Logan, C. H. A., Maughan, B. J., Bremer, M. N., et al. 2018, Astronomy & Astrophysics, 620, A18, (XXL Paper XXXIII)

Łokas, E. L. & Mamon, G. A. 2003, Monthly Notices of the Royal Astronomical Society, 343, 401

Long, A. S., Cooray, A., Ma, J., et al. 2020, The Astrophysical Journal, 898, 133

Lonoce, I., Longhetti, M., Maraston, C., et al. 2015, Monthly Notices of the Royal Astronomical Society, 454, 3912

Lonoce, I., Maraston, C., Thomas, D., et al. 2020, Monthly Notices of the Royal Astronomical Society, 492, 326

Loubser, S. I., Babul, A., Hoekstra, H., et al. 2016, Monthly Notices of the Royal Astronomical Society, 456, 1565

Loubser, S. I., Sánchez-Blázquez, P., Sansom, A. E., & Soechting, I. K. 2009, Monthly Notices of the Royal Astronomical Society, 398, 133

Lovell, C. C., Thomas, P. A., & Wilkins, S. M. 2018, Monthly Notices of the Royal Astronomical Society, 474, 4612

Lubin, L. M., Oke, J. B., & Postman, M. 2002, The Astronomical Journal, 124, 1905

Lumb, D. H., Schartel, N., & Jansen, F. A. 2012, Optical Engineering, 51, 011009

Lutovinov, A. A., Vikhlinin, A., Churazov, E. M., Revnivtsev, M. G., & Sunyaev, R. A. 2008, The Astrophysical Journal, 687, 968

Ma, C. J., Ebeling, H., Marshall, P., & Schrabback, T. 2010, Monthly Notices of the Royal Astronomical Society, 406, 121

Madau, P. 1995, The Astrophysical Journal, 441, 18

Madau, P. & Dickinson, M. 2014, Annual Review of Astronomy and Astrophysics, 52, 415

Mansheim, A. S., Lemaux, B. C., Dawson, W. A., et al. 2017, The Astrophysical Journal, 834, 205

Mantz, A. B., Abdulla, Z., Allen, S. W., et al. 2018, Astronomy & Astrophysics, 620, A2, (XXL Paper XVII)

Mantz, A. B., Abdulla, Z., Carlstrom, J. E., et al. 2014, The Astrophysical Journal, 794, 157, (XXL Paper V)

Markevitch, M. & Vikhlinin, A. 2007, Physics Reports, 443, 1

McDonald, M., Bayliss, M., Benson, B. A., et al. 2012, Nature, 488, 349

McDonald, M., Benson, B., Veilleux, S., Bautz, M. W., & Reichardt, C. L. 2013, The Astrophysical Journal Letters, 765, L37

McDonald, M., McNamara, B. R., van Weeren, R. J., et al. 2015, The Astrophysical Journal, 811, 111

McDonald, M., Stalder, B., Bayliss, M., et al. 2016, The Astrophysical Journal, 817, 86

McDonald, M., Swinbank, M., Edge, A. C., et al. 2014, The Astrophysical Journal, 784, 18

McGee, S. L., Balogh, M. L., Bower, R. G., Font, A. S., & McCarthy, I. G. 2009, Monthly Notices of the Royal Astronomical Society, 400, 937

McIntosh, D. H., Guo, Y., Hertzberg, J., et al. 2008, Monthly Notices of the Royal Astronomical Society, 388, 1537

McIntosh, D. H., Wagner, C., Cooper, A., et al. 2014, Monthly Notices of the Royal Astronomical Society, 442, 533

McNamara, B. R., Kazemzadeh, F., Rafferty, D. A., et al. 2009, The Astrophysical Journal, 698, 594

McNamara, B. R. & Nulsen, P. E. J. 2007, Annual Review of Astronomy and Astrophysics, 45, 117

McNamara, B. R. & Nulsen, P. E. J. 2012, New Journal of Physics, 14, 055023

McNamara, B. R. & O'Connell, R. W. 1989, The Astronomical Journal, 98, 2018

Menanteau, F., Hughes, J. P., Sifón, C., et al. 2012, The Astrophysical Journal, 748, 7

Merritt, D. 1985, The Astrophysical Journal, 289, 18

Mignone, A., Rossi, P., Bodo, G., Ferrari, A., & Massaglia, S. 2010, Monthly Notices of the Royal Astronomical Society, 402, 7

Mihos, J. C. & Hernquist, L. 1994, The Astrophysical Journal Letters, 425, L13

Miller, J. S. A., Bolton, J. S., & Hatch, N. 2019, Monthly Notices of the Royal Astronomical Society, 489, 5381

Miller, N. A. & Owen, F. N. 2003, The Astronomical Journal, 125, 2427

Miller, T. B., Chapman, S. C., Aravena, M., et al. 2018, Nature, 556, 469

Miyazaki, S., Hamana, T., Ellis, R. S., et al. 2007, The Astrophysical Journal, 669, 714

Miyazaki, S., Hamana, T., Shimasaku, K., et al. 2002, The Astrophysical Journal Letters, 580, L97

Mo, H., van den Bosh, F., & White, S., eds. 2010, Galaxy Formation and Evolution (Cambridge: Cambridge University Press)

Moffat, A. F. J. 1969, Astronomy & Astrophysics, 3, 455

Moore, B., Katz, N., & Lake, G. 1996, The Astrophysical Journal, 457, 455

Moore, B., Lake, G., Quinn, T., & Stadel, J. 1999, Monthly Notices of the Royal Astronomical Society, 304, 465

Motl, P. M., Hallman, E. J., Burns, J. O., & Norman, M. L. 2005, The Astrophysical Journal Letters, 623, L63

Muldrew, S. I., Hatch, N. A., & Cooke, E. A. 2015, Monthly Notices of the Royal Astronomical Society, 452, 2528

Muldrew, S. I., Hatch, N. A., & Cooke, E. A. 2018, Monthly Notices of the Royal Astronomical Society, 473, 2335

Muzzin, A., Wilson, G., Yee, H. K. C., et al. 2012, The Astrophysical Journal, 746, 188

Muzzin, A., Wilson, G., Yee, H. K. C., et al. 2009, The Astrophysical Journal, 698, 1934

Nantais, J. B., Muzzin, A., van der Burg, R. F. J., et al. 2017, Monthly Notices of the Royal Astronomical Society, 465, L104

Nantais, J. B., Rettura, A., Lidman, C., et al. 2013, Astronomy & Astrophysics, 556, A112

Nantais, J. B., van der Burg, R. F. J., Lidman, C., et al. 2016, Astronomy & Astrophysics, 592, A161

Newman, A. B., Ellis, R. S., Bundy, K., & Treu, T. 2012, The Astrophysical Journal, 746, 162

Noble, A. G., Muzzin, A., McDonald, M., et al. 2019, The Astrophysical Journal, 870, 56

Nulsen, P. E. J., Jones, C., Forman, W. R., et al. 2007, in Heating versus Cooling in Galaxies and Clusters of Galaxies, ed. H. Böhringer, G. W. Pratt, A. Finoguenov, & P. Schuecker, 210

O'Dea, C. P., Baum, S. A., Privon, G., et al. 2008, The Astrophysical Journal, 681, 1035

O'Dea, K. P., Quillen, A. C., O'Dea, C. P., et al. 2010, The Astrophysical Journal, 719, 1619

Oemler, Jr., A. 1976, The Astrophysical Journal, 209, 693

O'Hara, T. B., Mohr, J. J., & Guerrero, M. A. 2004, The Astrophysical Journal, 604, 604

Old, L. J., Balogh, M. L., van der Burg, R. F. J., et al. 2020, Monthly Notices of the Royal Astronomical Society, 493, 5987

Olsen, L. F., Benoist, C., Cappi, A., et al. 2007, Astronomy & Astrophysics, 461, 81

Oppenheimer, B. D. & Davé, R. 2006, Monthly Notices of the Royal Astronomical Society, 373, 1265

Oppenheimer, B. D., Davé, R., Kereš, D., et al. 2010, Monthly Notices of the Royal Astronomical Society, 406, 2325

Ostriker, J. P. & Tremaine, S. D. 1975, The Astrophysical Journal Letters, 202, L113

Oteo, I., Ivison, R. J., Dunne, L., et al. 2018, The Astrophysical Journal, 856, 72

Overzier, R. A. 2016, Astronomy & Astrophysics Review, 24, 14

Pacaud, F., Pierre, M., Refregier, A., et al. 2006, Monthly Notices of the Royal Astronomical Society, 372, 578

Pacifici, C., Kassin, S. A., Weiner, B., Charlot, S., & Gardner, J. P. 2013, The Astrophysical Journal, 762, L15

Papovich, C., Momcheva, I., Willmer, C. N. A., et al. 2010, The Astrophysical Journal, 716, 1503

Pavesi, R., Riechers, D. A., Sharon, C. E., et al. 2018, The Astrophysical Journal, 861, 43

Peng, Y., Maiolino, R., & Cochrane, R. 2015, Nature, 521, 192

Peng, Y.-j., Lilly, S. J., Kovač, K., et al. 2010, The Astrophysical Journal, 721, 193

Peng, Y.-j., Lilly, S. J., Renzini, A., & Carollo, M. 2012, The Astrophysical Journal, 757, 4

Pierre, M., Clerc, N., Maughan, B., et al. 2012, Astronomy & Astrophysics, 540, A4

Pierre, M., Pacaud, F., Adami, C., et al. 2016, Astronomy & Astrophysics, 592, A1, (XXL Paper I)

Pierre, M., Pacaud, F., Duc, P.-A., et al. 2006, Monthly Notices of the Royal Astronomical Society, 372, 591

Pierre, M., Valtchanov, I., Altieri, B., et al. 2004, Journal of Cosmology and Astroparticle Physics, 2004, 011

Pintos-Castro, I., Yee, H. K. C., Muzzin, A., Old, L., & Wilson, G. 2019, The Astrophysical Journal, 876, 40

Pipino, A., Kaviraj, S., Bildfell, C., et al. 2009, Monthly Notices of the Royal Astronomical Society, 395, 462

Pirard, J.-F., Kissler-Patig, M., Moorwood, A., et al. 2004, in Society of Photo-Optical Instrumentation Engineers (SPIE) Conference Series, Vol. 5492, Ground-based Instrumentation for Astronomy, ed. A. F. M. Moorwood & M. Iye, 1763–1772

Planck Collaboration, Ade, P. A. R., Aghanim, N., et al. 2013, Astronomy & Astrophysics, 554, A140

Plionis, M., López-Cruz, O., & Hughes, D., eds. 2008, A pan-chromatic view of clusters of galaxies and the large-scale structure, Lecture notes in physics, 740 (Dordrecht: Springer)

Poggianti, B. M. & Barbaro, G. 1997, Astronomy & Astrophysics, 325, 1025

Poggianti, B. M., Bridges, T. J., Komiyama, Y., et al. 2004, The Astrophysical Journal, 601, 197

Poggianti, B. M., Desai, V., Finn, R., et al. 2008, The Astrophysical Journal, 684, 888

Poggianti, B. M., Fasano, G., Omizzolo, A., et al. 2016, The Astronomical Journal, 151, 78

Poggianti, B. M., Gullieuszik, M., Tonnesen, S., et al. 2019, Monthly Notices of the Royal Astronomical Society, 482, 4466

Poggianti, B. M., Smail, I., Dressler, A., et al. 1999, The Astrophysical Journal, 518, 576

Poggianti, B. M., von der Linden, A., De Lucia, G., et al. 2006, The Astrophysical Journal, 642, 188

Polletta, M., Tajer, M., Maraschi, L., et al. 2007, The Astrophysical Journal, 663, 81

Postman, M., Lubin, L. M., Gunn, J. E., et al. 1996, The Astronomical Journal, 111, 615

Pratt, G. W., Croston, J. H., Arnaud, M., & Böhringer, H. 2009, Astronomy & Astrophysics, 498, 361

Press, W. H. & Schechter, P. 1974, The Astrophysical Journal, 187, 425

Quai, S., Pozzetti, L., Moresco, M., et al. 2019, Monthly Notices of the Royal Astronomical Society, 490, 2347

Rabin, D. 1982, The Astrophysical Journal, 261, 85

Rafferty, D. A., McNamara, B. R., & Nulsen, P. E. J. 2008, The Astrophysical Journal, 687, 899

Rafferty, D. A., McNamara, B. R., Nulsen, P. E. J., & Wise, M. W. 2006, The Astrophysical Journal, 652, 216

Ragone-Figueroa, C., Granato, G. L., Ferraro, M. E., et al. 2018, Monthly Notices of the Royal Astronomical Society, 479, 1125

Raichoor, A. & Andreon, S. 2012, Astronomy & Astrophysics, 543, A19

Raimundo, S. I., Vestergaard, M., Koay, J. Y., et al. 2019, Monthly Notices of the Royal Astronomical Society, 486, 123

Randall, S. W., Jones, C., Markevitch, M., et al. 2009, The Astrophysical Journal, 700, 1404

Randall, S. W., Nulsen, P. E. J., Jones, C., et al. 2015, The Astrophysical Journal, 805, 112

Rawle, T. D., Edge, A. C., Egami, E., et al. 2012, The Astrophysical Journal, 747, 29

Rennehan, D., Babul, A., Hayward, C. C., et al. 2020, Monthly Notices of the Royal Astronomical Society, 493, 4607

Ricci, M., Adam, R., Eckert, D., et al. 2020, Astronomy & Astrophysics, 642, A126, (XXL Paper XLIV)

Ricci, M., Benoist, C., Maurogordato, S., et al. 2018, Astronomy & Astrophysics, 620, A13, (XXL Paper XXVIII)

Roettiger, K., Loken, C., & Burns, J. O. 1997, The Astrophysical Journal Supplement Series, 109, 307

Rosa-Gonzlez, D., Terlevich, E., & Terlevich, R. 2002, Monthly Notices of the Royal Astronomical Society, 332, 283

Rose, J. A. 1985, The Astronomical Journal, 90, 1927

Rossetti, M., Gastaldello, F., Eckert, D., et al. 2017, Monthly Notices of the Royal Astronomical Society, 468, 1917

Rossetti, M., Gastaldello, F., Ferioli, G., et al. 2016, Monthly Notices of the Royal Astronomical Society, 457, 4515

Rubin, V. C., Ford, Jr., W. K., & Thonnard, N. 1980, The Astrophysical Journal, 238, 471

Ruppin, F., McDonald, M., Bleem, L. E., et al. 2021, The Astrophysical Journal, 918, 43

Ruppin, F., McDonald, M., Brodwin, M., et al. 2020, The Astrophysical Journal, 893, 74

Sadibekova, T., Pierre, M., Clerc, N., et al. 2014, Astronomy & Astrophysics, 571, A87

Salpeter, E. E. 1955, The Astrophysical Journal, 121, 161

Sanders, J. S., Fabian, A. C., Taylor, G. B., et al. 2016, Monthly Notices of the Royal Astronomical Society, 457, 82

Sanderson, A. J. R., O'Sullivan, E., Ponman, T. J., et al. 2013, Monthly Notices of the Royal Astronomical Society, 429, 3288

Saracco, P., La Barbera, F., Gargiulo, A., et al. 2019, Monthly Notices of the Royal Astronomical Society, 484, 2281

Sarazin, C. L. 1986, Reviews of Modern Physics, 58, 1

Schneider, P. 1996, Monthly Notices of the Royal Astronomical Society, 283, 837

Scholtz, J., Harrison, C. M., Rosario, D. J., et al. 2020, Monthly Notices of the Royal Astronomical Society, 492, 3194

Schombert, J. M. 1986, The Astrophysical Journal Supplement Series, 60, 603

Schombert, J. M. 1987, The Astrophysical Journal Supplement Series, 64, 643

Schombert, J. M. 1988, The Astrophysical Journal, 328, 475

Sembach, K. R. & Tonry, J. L. 1996, The Astronomical Journal, 112, 797

Sereno, M. 2016, Monthly Notices of the Royal Astronomical Society, 455, 2149

Sereno, M., Fedeli, C., & Moscardini, L. 2016, Journal of Cosmology and Astroparticle Physics, 01, 042

Shi, K., Lee, K.-S., Dey, A., et al. 2019, The Astrophysical Journal, 871, 83

Shi, K., Toshikawa, J., Lee, K.-S., et al. 2021, The Astrophysical Journal, 911, 46

Shim, H., Im, M., Lee, H. M., et al. 2011, The Astrophysical Journal, 727, 14

Siebenmorgen, R., Carraro, G., Valenti, E., et al. 2011, The Messenger, 144, 9

Silk, J. 1976, The Astrophysical Journal, 208, 646

Simha, V., Weinberg, D. H., Conroy, C., et al. 2014, arXiv:astro-ph/1404.0402

Sparre, M., Hayward, C. C., Springel, V., et al. 2015, Monthly Notices of the Royal Astronomical Society, 447, 3548

Springel, V., White, S. D. M., Jenkins, A., et al. 2005, Nature, 435, 629

Springel, V., White, S. D. M., Tormen, G., & Kauffmann, G. 2001, Monthly Notices of the Royal Astronomical Society, 328, 726

Stark, C. W., White, M., Lee, K.-G., & Hennawi, J. F. 2015, Monthly Notices of the Royal Astronomical Society, 453, 311

Steinhauser, D., Schindler, S., & Springel, V. 2016, Astronomy & Astrophysics, 591, A51

Stott, J. P., Collins, C. A., Burke, C., Hamilton-Morris, V., & Smith, G. P. 2011, Monthly Notices of the Royal Astronomical Society, 414, 445

Stott, J. P., Edge, A. C., Smith, G. P., Swinbank, A. M., & Ebeling, H. 2008, Monthly Notices of the Royal Astronomical Society, 384, 1502

Stott, J. P., Hickox, R. C., Edge, A. C., et al. 2012, Monthly Notices of the Royal Astronomical Society, 422, 2213

Straatman, C. M. S., Spitler, L. R., Quadri, R. F., et al. 2016, The Astrophysical Journal, 830, 51

Strateva, I., Ivezić, v., Knapp, G. R., et al. 2001, The Astronomical Journal, 122, 1861

Strazzullo, V., Gobat, R., Daddi, E., et al. 2013, The Astrophysical Journal, 772, 118

Strazzullo, V., Pannella, M., Mohr, J. J., et al. 2019, Astronomy & Astrophysics, 622, A117

Stroe, A. & Sobral, D. 2021, The Astrophysical Journal, 912, 55

Sunyaev, R. A. & Zel'dovich, I. B. 1980a, Annual Review of Astronomy and Astrophysics, 18, 537

Sunyaev, R. A. & Zel'dovich, I. B. 1980b, Monthly Notices of the Royal Astronomical Society, 190, 413

Sunyaev, R. A. & Zel'dovich, Y. B. 1970, Comments on Astrophysics and Space Physics, 2, 66

Sunyaev, R. A. & Zel'dovich, Y. B. 1972, Comments on Astrophysics and Space Physics, 4, 173

Tacchella, S., Conroy, C., Faber, S. M., et al. 2022, The Astrophysical Journal, 926, 134

Tanaka, M., De Breuck, C., Venemans, B., & Kurk, J. 2010, Astronomy & Astrophysics, 518, A18

Thomsen, B., Baum, W. A., Hammergren, M., & Worthey, G. 1997, The Astrophysical Journal, 483, L37

Tonnesen, S. 2019, The Astrophysical Journal, 874, 161

Toshikawa, J., Kashikawa, N., Overzier, R., et al. 2014, The Astrophysical Journal, 792, 15

Trager, S. C., Faber, S. M., Worthey, G., & González, J. J. 2000, The Astronomical Journal, 119, 1645

Tremaine, S. D. & Richstone, D. O. 1977, The Astrophysical Journal, 212, 311

Treu, T., Ellis, R. S., Kneib, J.-P., et al. 2003, The Astrophysical Journal, 591, 53

Trinh, C. Q., Ellis, S. C., Bland-Hawthorn, J., et al. 2013, Monthly Notices of the Royal Astronomical Society, 432, 3262

Trudeau, A., Garrel, C., Willis, J., et al. 2020, Astronomy & Astrophysics, 642, A124, (XXL Paper XLII)

Trussler, J., Maiolino, R., Maraston, C., et al. 2020, Monthly Notices of the Royal Astronomical Society, 491, 5406

Tudorica, A., Hildebrandt, H., Tewes, M., et al. 2017, Astronomy & Astrophysics, 608, A141

Tyson, J. A., Valdes, F., Jarvis, J. F., & Mills, Jr., A. P. 1984, The Astrophysical Journal Letters, 281, L59

Tyson, J. A., Valdes, F., & Wenk, R. A. 1990, The Astrophysical Journal Letters, 349, L1

Umetsu, K., Sereno, M., Lieu, M., et al. 2020, The Astrophysical Journal, 890, 148

Valtchanov, I., Pierre, M., & Gastaud, R. 2001, Astronomy & Astrophysics, 370, 689

Valtchanov, I., Pierre, M., Willis, J., et al. 2004, Astronomy & Astrophysics, 423, 75

Vantyghem, A. N., McNamara, B. R., Edge, A. C., et al. 2017, The Astrophysical Journal, 848, 101

Veilleux, S., Cecil, G., & Bland-Hawthorn, J. 2005, Annual Review of Astronomy and Astrophysics, 43, 769

Venemans, B. P., Röttgering, H. J. A., Miley, G. K., et al. 2007, Astronomy & Astrophysics, 461, 823

Vikhlinin, A., McNamara, B. R., Forman, W., et al. 1998, The Astrophysical Journal, 502, 558

Visvanathan, N. & Sandage, A. 1977, The Astrophysical Journal, 216, 214

Von Der Linden, A., Best, P. N., Kauffmann, G., & White, S. D. M. 2007, Monthly Notices of the Royal Astronomical Society, 379, 867

Wagner, C. R., Brodwin, M., Snyder, G. F., et al. 2015, The Astrophysical Journal, 800, 107

Wang, T., Elbaz, D., Daddi, E., et al. 2016, The Astrophysical Journal, 828, 56

Webb, K., Balogh, M. L., Leja, J., et al. 2020, Monthly Notices of the Royal Astronomical Society, 498, 5317

Webb, T., Noble, A., DeGroot, A., et al. 2015a, The Astrophysical Journal, 809, 173

Webb, T. M. A., Lowenthal, J., Yun, M., et al. 2017, The Astrophysical Journal Letters, 844, L17

Webb, T. M. A., Muzzin, A., Noble, A., et al. 2015b, The Astrophysical Journal, 814, 96

Weisskopf, M. C. 1999, arXiv:astro-ph/9912097

Wen, Z. L. & Han, J. L. 2011, The Astrophysical Journal, 734, 68

Werner, S. V., Hatch, N. A., Muzzin, A., et al. 2022, Monthly Notices of the Royal Astronomical Society, 510, 674

West, M. J., Jones, C., & Forman, W. 1995, The Astrophysical Journal Letters, 451, L5

Westera, P., Cuisinier, F., Telles, E., & Kehrig, C. 2004, Astronomy & Astrophysics, 423, 133

Wetzel, A. R., Tinker, J. L., & Conroy, C. 2012, Monthly Notices of the Royal Astronomical Society, 424, 232

Wetzel, A. R., Tinker, J. L., Conroy, C., & van den Bosch, F. C. 2013, Monthly Notices of the Royal Astronomical Society, 432, 336

White, S. D. M. 1976, Monthly Notices of the Royal Astronomical Society, 174, 19

White, S. D. M. & Rees, M. J. 1978, Monthly Notices of the Royal Astronomical Society, 183, 341

Willis, J. P., Canning, R. E. A., Noordeh, E. S., et al. 2020, Nature, 577, 39

Willis, J. P., Clerc, N., Bremer, M. N., et al. 2013, Monthly Notices of the Royal Astronomical Society, 430, 134

Willis, J. P., Hewett, P. C., & Warren, S. J. 2001, Monthly Notices of the Royal Astronomical Society, 325, 1002

Willis, J. P., Pacaud, F., Valtchanov, I., et al. 2005, Monthly Notices of the Royal Astronomical Society, 363, 675

Willis, J. P., Ramos-Ceja, M. E., Muzzin, A., et al. 2018, Monthly Notices of the Royal Astronomical Society

Wilson, G., Muzzin, A., Lacy, M., et al. 2006, arXiv:astro-ph/0604289

Wilson, G., Muzzin, A., Yee, H. K. C., et al. 2009, The Astrophysical Journal, 698, 1943

Wittman, D., Dell'Antonio, I. P., Hughes, J. P., et al. 2006, The Astrophysical Journal, 643, 128

Wittman, D., Margoniner, V. E., Tyson, J. A., et al. 2003, The Astrophysical Journal, 597, 218

Wittman, D., Tyson, J. A., Margoniner, V. E., Cohen, J. G., & Dell'Antonio, I. P. 2001, The Astrophysical Journal Letters, 557, L89

Woo, J., Carollo, C. M., Faber, S. M., Dekel, A., & Tacchella, S. 2017, Monthly Notices of the Royal Astronomical Society, 464, 1077

Woo, J., Dekel, A., Faber, S. M., & Koo, D. C. 2015, Monthly Notices of the Royal Astronomical Society, 448, 237

Woo, J., Dekel, A., Faber, S. M., et al. 2013, Monthly Notices of the Royal Astronomical Society, 428, 3306

Wright, E. L. 2006, Publications of the Astronomical Society of the Pacific, 118, 1711

Wu, H.-Y., Hahn, O., Wechsler, R. H., Mao, Y.-Y., & Behroozi, P. S. 2013, The Astrophysical Journal, 763, 70

Zel'dovich, Y. B. & Sunyaev, R. A. 1969, Astrophysics and Space Science, 4, 301